Department Chemie
der Technischen Universität München

Optimal Control, Partial Alignment and More: The Design Of Novel Tools for NMR Spectroscopy of Small Molecules

Kyryl Kobzar

Vollständiger Abdruck der von der Fakultät Chemie der Technischen Universität München zur Erlangung des akademischen Grades eines

Doktors der Naturwissenschaften

genehmigten Dissertation

Im Traum, im letzten Morgentraume stand ich heut auf einem Vorgebirge, - jenseits der Welt, hielt eine Wage und *wog* die Welt.< ... >

Messbar für Den, der Zeit hat, wägbar für einen guten Wäger, erfliegbar für starke Fittiche, errathbar für göttliche Nüsseknacker: also fand mein Traum die Welt< ... >

Wie sicher schaute mein Traum auf diese endliche Welt, nicht neugierig, nicht altgierig, nicht fürchtend, nicht bittend: -

- als ob ein voller Apfel sich meiner Hand böte, ein reifer Goldapfel, mit kühl-sanfter sammtener Haut: - so bot sich mir die Welt: -

- als ob ein Baum mir winke, ein breitästiger, starkwilliger, gekrümmt zur Lehne und noch zum Fussbrett für den Wegmüden: so stand die Welt auf meinem Vorgebirge: -

- als ob zierliche Hände mir einen Schrein entgegentrügen, - einen Schrein offen für das Entzücken schamhafter verehrender Augen: also bot sich mir heute die Welt entgegen: -

- nicht Räthsel genug, um Menschen-Liebe davon zu scheuchen, nicht Lösung genug, um Menschen-Weisheit einzuschläfern: - ein menschlich gutes Ding war mir heut die Welt, der man so Böses nachredet!

F. W. Nietzsche *"Also sprach Zarathustra"*

Abstract

The NMR spectroscopy is a constantly changing field, with both hardware and methodology developing in concert and influencing each other. The constantly increasing magnetic field strengths of modern spectrometers bring an advantage of better signal-to-noise ratios and increased resolution, but make even basic tasks, like the uniform excitation of one-dimensional ^{13}C spectra, to a technical challenge. Also the sample preparation gets more and more sophisticated, as for example with the exciting development in the field of partially oriented molecules where arbitrary scaling of alignment poses a fundamental problem. Finally, the development of novel pulse sequence techniques, the ßoftwareöf NMR spectroscopy, will always be a central aspect in modern NMR. All these fields have been addressed with various approaches in this thesis. Optimal control of spin dynamics is shown to be a highly efficient mathematical tool for the design of all kind of complex pulses like broadband excitation, inversion, or universal rotation pulses, or "pattern pulses" with almost unlimited flexibility in their offset and rf-amplitude profiles. In a separate series of projects, various polymer gels have been produced chemically as orienting media without lower limit of alignment. With the introduction of such media a significant improvement of alignment scalability could be achieved, which opens the possibility of measuring anisotropic NMR-parameters to a wide range of small to medium-sized organic molecules. Within the projects, a number of new and significantly improved pulse sequences has been developed as well as several simulation programs which are briefly described.

Zusammenfassung

Die NMR-Spektroskopie ist ein sich stetig wandelndes Gebiet mit Weiterentwicklungen in Hardware und Methodik, die sich gegenseitig beeinflussen. Die immer weiter ansteigenden Magnetfeldstärken moderner Spektrometer bringen die Vorteile eines besseren Signal-zu-Rausch-Verhältnisses und höherer Auflösung, machen aber auch ganz einfache Aufgaben wie z.B. die gleichmäßige Anregung in eindimensionalen ^{13}C-Spektren zu einer technischen Herausforderung. Auch die Probenpräparation wird immer anspruchsvoller, so z.B. auf dem Gebiet der partiell orientierten Moleküle, in dem eine stufenlose Skalierbarkeit der Orientierung ein fundamentales Problem darstellt. Schließlich wäre da noch die Entwicklung neuer Pulssequenzen, der "NMR-Software", die eine zentrale Rolle in der modernen NMR-Spektroskopie spielt. All diese Aspekte wurden in der vorliegenden Arbeit in verschiedenen Ansätzen behandelt. So wurde gezeigt, dass optimale Steuerungstheorie angewendet auf spindynamische Prozesse ein effizientes mathematisches Werkzeug ist, um alle Arten komplexer Pulse zu entwerfen, wie z.B. Breitbandanregungs- und -inversionspulse, universelle Rotationspulse oder "Pattern-Pulse" mit fast unbegrenzter Flexibilität in ihren Offset- und Radiofrequenzamplituden-Abhängigkeiten. In einer Reihe anderer Projekte wurden Polymergele als Medien ohne unteres Limit in ihrem Orientierungsvermögen hergestellt. Durch die Einführung solcher Orientierungsmedien konnte die Skalierbarkeit der Ausrichtung signifikant verbessert werden, was die Messung anisotrope NMR-Parameter kleiner bis mittelgroßer organischer Moleküle ermöglicht. Innerhalb dieser Projekte wurden eine Reihe neuer und deutlich verbesserter Pulssequenzen und einige Simulationsprogramme entwickelt, die kurz beschrieben werden.

Parts of this thesis have already been published:

1. **Easy and scalable method for the partial alignment of organic molecules for measuring residual dipolar couplings.** B.Luy, K.Kobzar, H.Kessler (2004) *Angew. Chem.* **116**, 1112-1115; *Angew. Chem.Int.Ed.* **43**, 1092-1094.

2. **Exploring the limits of broadband excitation and inversion pulses.** K. Kobzar, T. E. Skinner, N. Khaneja, S. J. Glaser, B. Luy (2004) *J.Magn.Reson.* **170**, 236-243.

3. **Stretched Poly(vinyl acetate) Gels as NMR Alignment Media for the Measurement of Residual Dipolar Couplings in Polar Organic Solvents.** J. C. Freudenberger, S. Knör, K. Kobzar, D. Heckmann, T. Paululat, H. Kessler, B. Luy (2005) *Angew. Chem.* **117**, 427-430; *Angew. Chem.Int.Ed.* **44**, 423-426.

4. **Stretched gelatin gels as chiral alignment media capable to discriminate enantiomers.** K. Kobzar, H. Kessler, B. Luy (2005) *Angew. Chem.* **117**, 3205-3207; *Angew. Chem.Int.Ed.* **44**, 3145-3147.

5. **Pattern pulses: Design of arbitrary excitation profiles as a function of pulse amplitude and offset.** K. Kobzar, B. Luy, N.Khaneja, S.J. Glaser (2005) *J.Magn.Reson.* **173**, 229-235.

6. **Orientational Properties of Stretched Polystyrene Gels in Organic Solvents and the Suppression of Their Residual ^{1}H-NMR Signals** B. Luy, K. Kobzar, S.Knör, D. Heckmann, J. Furrer, H. Kessler (2005) *J. Am. Chem. Soc.* **127**, 6459-6465.

7. **RDC as a new NMR-parameter for peptides.** H. Kessler, B. Luy, K. Kobzar, J. C. Freudenberger, S. Knör, D. Heckmann, J. Klages (2005) *Biopolymers* **80**, 500.

8. **Construction of universal rotations from point-to-point transformations** B. Luy, K. Kobzar, T. E. Skinner, N. Khaneja, S. J. Glaser (2005) *J.Magn.Reson.* **176**, 179-186.

9. **Optimal control design of constant amplitude phase-modulated pulses: Application to calibration-free broadband excitation** T. E. Skinner, K. Kobzar, B. Luy, R. Bendall, W. Bermel, N. Khaneja, S. J. Glaser (2006) *J.Magn.Reson.* **179**, 241-249.

10. **Spin state selective Hadamard encoding during transfer periods using multiple selective CW-HCP** K. Kobzar, B. Luy (2007) *J.Magn.Reson.* **186**, 228-237.

11. **Analyses, extensions and comparison of three experimental schemes for measuring ($^{n}J_{CH} + D_{CH}$)-couplings at natural abundance** K. Kobzar, B. Luy (2007) *J.Magn.Reson.* **186**, 131-141.

Contents

List of Figures

List of Tables

Introduction and scope of the work

The progress in NMR seems to be unstoppable and the state of staleness simply didn't have a chance to establish in this exciting field: one just starts to think that there is a passing moment to take a breather and in this very moment new groundbreaking developments emerge in some place of already quite vast field of modern NMR spectroscopy. A constant flow of new ideas (begged, borrowed or stolen, whatsoever [1]) doesn't seize to occupy the minds of NMR spectroscopists.

One such idea is the idea to apply the formalism of optimal control theory (a relatively old mathematical formalism, widely used in engineering and economics) to the design of very basic building blocks of NMR spectroscopy: RF-pulses. Chapter 1 of the actual work is concerned with this topic. The general optimization procedure for a single spin is described and applied to manipulate the ensembles of uncoupled spins with a high degree of control. With the aid of the optimization procedure some very general NMR problems could be investigated, like the limits of broadband excitation and inversion in ensembles of uncoupled spins (Section 1.3.3). The algorithm allows to search for optimal pulses within limited search spaces, producing pulses with very special properties best suited for particular NMR applications. In Section 1.5 the unprecedented flexibility provided by the optimization procedure allowed to create pulses with very peculiar excitation profiles, so-called "pattern pulses". The optimization of another type of pulses of more direct practical use is presented in the following section - so-called universal rotation pulses. We could successfully apply the optimal control algorithm to create this kind of pulses, which allow the direct exchange of hard pulses by the optimized ones in any conventional pulse sequence (c.f. Section 1.7), but also found an easy procedure to create such pulses from usual point-to-point pulses utilizing very general symmetry properties (Section 1.6). The detailed analysis of the optimized universal rotation pulses showed that such symmetry properties are a general feature in this class of pulses. Equipped with all neccesary tools, we could apply the optimized pulses to two very commonly used NMR experiments, HSQC and HMBC, which significantly improved their performance (Section 1.8).

The second part of this work is dedicated to the development of new alignment media for use in high-resolution NMR spectroscopy. The measurements in aligned media are nowadays among the hottest topics in NMR. The re-introduction of dipolar interactions, otherwise averaged out in usual isotropic samples, reveals quite an amount of structural information, and hence, since few years has significantly changed the field of biomolecular NMR and is going to do this with NMR of small molecules. Until recently, the use of this technique for the small molecules was very limited due to the fact, that only very

few alignment media were available for typical organic solvents. Here, new media are introduced: polystyrene (Section 2.2) and poly(vinyl acetate) (Section 2.3) anisotropically swollen and stretched can be used as alignment media for a large range of organic solvents. In addition, gelatin gels swollen and stretched in water were introduced as an alignment media to measure residual dipolar couplings. Due to the chiral character of its structure, it can also be used to discriminate enantiomers with the aid of RDCs, as shown in Section 2.4. The practical aspects of applicability of these media are investigated, the problems emerging with it and the ways to overcome these. But the application of the technique to small molecules also requires new tools to access as many residual dipolar couplings as possible. Section 2.5 therefore describes various improved approaches for measuring long-range heteronuclear RDCs.

Chapter 3 occupies with another topic being highly popular these days which is based on a very old idea - Hadamard spectroscopy. Hadamard spectroscopy today represents an alternative to conventional Fourier transform spectroscopy. Typically, the selective inversion of several narrow frequency bands is achieved by tailored inversion pulses in place of t_1-evolution periods. However, band-selective inversion can also be achieved during coherence transfer steps, thereby shortening the period during which the magnetization is in the transverse plane. Using CW heteronuclear cross-polarization (CW-HCP) as an example for highly selective coherence transfer, the implementation of Hadamard encoding within a transfer step is presented. Transfer characteristics, the preparation of multiple frequency selective CW-HCP and the possibility of acquiring spin state selective spectra are discussed in detail.

The software developed in the course of this work is described in the Appendix, as well as some of the pulse programs for Bruker Avance spectrometers.

Chapter 1

Optimizations

> Was ist gut? - Alles, was das Gefühl der Macht, den Willen
> zur Macht, die Macht selbst im Menschen erhöht.
> Was ist schlecht? - Alles, was aus der Schwäche stammt.
> Was ist Glück? - Das Gefühl davon, daß die Macht wächst,
> daß ein Widerstand überwunden wird.
>
> Friedrich W. Nietzsche, "Der Antichrist"
>
> Do what thou wilt shall be the whole of the Law.
>
> Aleister Crowley, "The Book of the Law"

1.1 Introduction

Since the introduction of pulsed Fourier-Transformation NMR spectroscopy, radiofrequency pulses have become the most essential, the indispensable building block of literally every NMR experiment. Some time later experimental imperfections, inherently connected to the non-ideality and hence limited performance of RF-pulses, have become apparent. Attempts to improve the situation were undertaken very soon by applying series of pulses (so called *composite pulses*) either designed by purely intuitive approach or, later, by numerical optimizations. When it was realized, that not only the phases of individual pulses can be changed (which is the case for composite pulses), but also the amplitudes, a whole new field of so called *shaped pulses* was invented. The use of shaped pulses opened completely new perspectives in NMR, connected with selective or band-selective excitation/inversion achieved by such pulses, but it also allowed much larger flexibility in the design of very basic RF-pulses. From this moment on, the 'only' problem in designing better pulses was to find an appropriate algorithm and enough computational power. But this appeared to be quite a significant problem. In principle, finding an RF pulse, which satisfies certain conditions imposed by the researcher (providing excitation, inversion or some other rotation over a given range of offsets, whatsoever), is nothing else but a usual

mathematical problem of finding an extremum of a multidimensional function. One has
to be able to calculate a value of this function (we will call it a *cost* or *performance func-
tion*) in every point of space, as well as gradients with respect to every variable. Then
it's just a matter of applying routine mathematical tools to find an extremum. However,
for every realistic problem in NMR such an approach is absolutely unfeasible in terms of
the amount of calculations involved. So, while direct optimization is not possible, many
different algorithms were proposed, none providing a general approach, but rather being
limited to some family of either pulse shapes or treated problems.

In contrast, an approach based on optimal control theory, a mathematical formal-
ism widely used for various kind of applications from engineering to economics and first
applied in NMR for the optimization of band- selective pulses in MRI [2–4], brought a
way to perform a general optimization with an enormously reduced number of required
calculations. In this procedure a gradient towards better performing parameters is cal-
culated efficiently based on an analytical formula that allows a significant increase in the
number of independently optimized parameters. Because of the high efficiency of the
algorithm the space of possible pulse shapes used in the optimization is not restricted to
any pulse family. In spin systems where the theoretical limits of quantum evolution were
known [5–11], numerical algorithms based on principles of optimal control theory, provide
pulse sequences which approach the physical limits [12–14].

1.2   Gradient ascent pulse engineering

1.2.1   Optimal control theory

Optimal control theory is a mathematical field that is concerned with control policies that
can be deduced using optimization algorithms [15,16]. In other words, this theory provides
a way to find such controls for a given dynamic system, which drive it from initial state
to a target one in a most efficient way (time- efficient, fuel-efficient, whatsoever). It is
based on a classical Euler-Lagrange formalism, developed by Leonhard Euler and Joseph-
Louis Lagrange in the 1750s and being the major formula of the calculus of variations. It
provides a way to solve for functions which extremize a given cost functional. It states,
that given a functional $\mathcal{L}(t, \boldsymbol{x}(t), \boldsymbol{u}(t))$ with continuous first and second derivatives, any
function f which extremizes the cost functional

$$\mathcal{J}[x] = \int_{t_0}^{t_1} \mathcal{L}[t, \boldsymbol{x}(t), \boldsymbol{u}(t)]dt, \tag{1.1}$$

must also satisfy the ordinary differential equation

$$\frac{\partial \mathcal{L}}{\partial \boldsymbol{x}} - \frac{d}{dt}\frac{\partial \mathcal{L}}{\partial \boldsymbol{u}} = 0. \tag{1.2}$$

It is analogous to the result from calculus that a function attains its extreme values
when its derivative vanishes. In classical mechanics, where the formalism was originally

invented, the functional $\mathcal{L}$ is the Lagrange operator, $\boldsymbol{u} = d\boldsymbol{x}/dt$, $\boldsymbol{x}(t_0)$ and $\boldsymbol{x}(t_1)$ are fixed, and the curves $\boldsymbol{x}(t)$ and $\boldsymbol{u}(t)$ are required to be continuous. The necessary condition that such a curve is an optimal curve is that the variation $\delta\mathcal{J}$ at all points of the path are equal to zero, which results in equation 1.2.

The optimal control theory generalizes this formalism to other kinds of functionals and typically includes in addition to the "running" cost function $\mathcal{L}$ a final cost term $\Phi[\boldsymbol{x}(t_1)]$, which depends on the state in which the system ends up:

$$\mathcal{J}[x] = \int_{t_0}^{t_1} \mathcal{L}[t, \boldsymbol{x}(t), \boldsymbol{u}(t)]dt + \Phi[\boldsymbol{x}(t_1)], \tag{1.3}$$

where $\boldsymbol{x}(t)$ represents the state of the system, while $\boldsymbol{u}(t)$ represents controls to be optimized.

A more significant generalization for the development of optimal control theory is the removal of the restriction that $\boldsymbol{u}$ be continuous. For practical NMR applications, the RF amplitude, phase, and/or frequency must be allowed to make discontinuous jumps.

Additional constraints, which can be imposed on points of the optimizing curve, of the form $g(\boldsymbol{x}) = c$, are included in the formalism by introducing Lagrange multipliers λ_j for each constraint equation g_j, which transforms the equation 1.3 for $\mathcal{L}$ to a similar one for the function

$$h = \mathcal{L} - \sum_j \lambda_j g_j. \tag{1.4}$$

1.2.2 Transfer between Hermitian operators

The basic theoretical ideas behind the application of the optimal control theory to the problem of pulse design are fixed in [13]. As the general case consider the transfer between Hermitian operators in the absence of relaxation. The state of the spin system is characterizes by the density operator $\rho(t)$, and its equation of motion is the Liouville-von Neumann equation [17]

$$\dot{\rho}(t) = -i\left[\left(\mathcal{H}_0 + \sum_{k=1}^{m} u_k(t)\mathcal{H}_k\right), \rho(t)\right], \tag{1.5}$$

where $\mathcal{H}_0$ is the free evolution Hamiltonian, $\mathcal{H}_k$ are the radiofrequency (rf) Hamiltonians corresponding to the available control fields and $u(t) = (u_1(t), u_2(t), \ldots, u_m(t))$ represents the vector of amplitudes that can be changed and which is referred to as control vector. The problem is to find the optimal amplitudes $u_k(t)$ of the rf fields that steer a given initial density operator $\rho(0) = \rho_0$ in a specified time T to a density operator $\rho(T)$ with maximum overlap to some desired target operator C. For Hermitian operators ρ_0 and C, this overlap may be measured by the standard inner product

$$\langle C | \rho(T) \rangle = tr\{C^\dagger \rho(T)\}. \tag{1.6}$$

Hence, the performance index Φ_0 of the transfer process can be defined as

$$\Phi_0 = \langle C | \rho(T) \rangle \tag{1.7}$$

In the following we will assume that the chosen transfer time T is discretized in N equal steps of duration $\Delta = T/N$ and during each step the control amplitudes u_k are constant, i.e. during the jth step the amplitude $u_k(t)$ of the kth control Hamiltonian is given by $u_k(j)$ (see Fig. 1.1). The time-evolution of the spin system during a time step j is given by the propagator

$$U_j = exp\left\{ -i\Delta t \left(\mathcal{H}_0 + \sum_{k=1}^{m} u_k(j)\mathcal{H}_k \right) \right\} \tag{1.8}$$

The final density operator at time $t = T$ is

$$\rho(T) = U_N \cdots U_1 \rho_0 U_1^\dagger \cdots U_N^\dagger, \tag{1.9}$$

and the performance function Φ_0 (Eq. 1.7) to be maximized can be expressed as

$$\Phi_0 = \langle C | U_N \cdots U_1 \rho_0 U_1^\dagger \cdots U_N^\dagger \rangle. \tag{1.10}$$

Using the definition of the inner product (Eq. 1.6) and the fact that the trace of a product is invariant under cyclic permutations of the factors, this can be rewritten as

$$\Phi_0 = \langle \underbrace{U_{j+1}^\dagger \cdots U_N^\dagger C U_N \cdots U_{j+1}}_{\lambda_j} | \underbrace{U_j \cdots U_1 \rho_0 U_1^\dagger \cdots U_j^\dagger}_{\rho_j} \rangle, \tag{1.11}$$

where ρ_j is the density operator $\rho(t)$ at time $t = j\Delta t$ and λ_j is the backward propagated target operator C at the same time $t = j\Delta t$. Let us see how the performance Φ_0 changes when we perturb the control amplitude $u_k(j)$ at time step j to $u_k(j) + \delta u_k(j)$. From Eq. 1.8, the change in U_j to first order in $\delta u_k(j)$ is given by

$$\delta U_j = -i\Delta t \delta u_k(j) \bar{\mathcal{H}}_k U_j \tag{1.12}$$

with

$$\overline{\mathcal{H}}_k \Delta t = \int_0^{\Delta t} U_j(\tau) H_k U_j(-\tau) \mathrm{d}\tau \tag{1.13}$$

and

$$U_j(\tau) = exp\left\{ -i\tau \left(\mathcal{H}_0 + \sum_{k=1}^{m} u_k(j)\mathcal{H}_k \right) \right\}. \tag{1.14}$$

This follows from the standard formula

$$\frac{\mathrm{d}}{\mathrm{d}x} e^{A+xB}|_{x=0} = e^A \int_0^1 e^{A\tau} B e^{-A\tau} \mathrm{d}\tau. \tag{1.15}$$
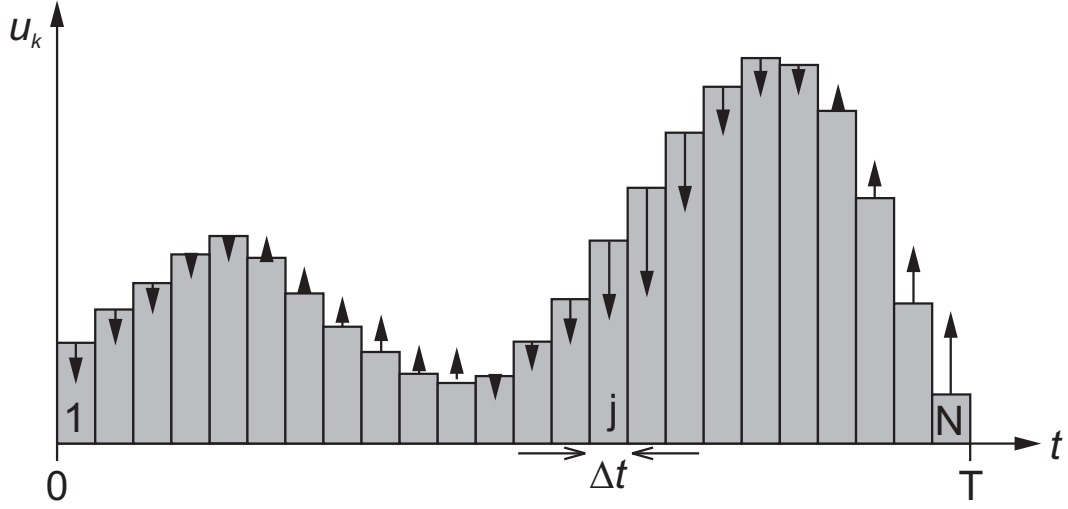
Figure 1.1: Schematic representation of a control amplitude $u_k(t)$, consisting of N steps of duration $\Delta t = T/N$. During each step j, the control amplitude $u_k(j)$ is constant. The vertical arrows represent gradients $\delta\Phi_0/\delta u_k(j)$, indicating how each amplitude $u_k(j)$ should be modified in the next iteration to improve the performance function Φ_0

For small Δt (when $\Delta t \ll \| \mathcal{H}_0 + \sum_{k=1}^{m} u_k(j)\mathcal{H}_k \|^{-1}$), $\overline{H}_k \approx H_k$ and using Eqs. 1.11 and 1.12 we find to first order in Δt

$$\frac{\delta\Phi_0}{\delta u_k(j)} = -\langle\lambda_j|i\Delta t[\mathcal{H}_k, \rho_j]\rangle. \tag{1.16}$$

We increase the performance function Φ_0 if we choose

$$u_k(j) \rightarrow u_k(j) + \epsilon\frac{\delta\Phi_0}{\delta u_k(j)}, \tag{1.17}$$

where ϵ is a small step size. This forms the basis of the following algorithm, the so-called *gradient ascent pulse engineering* (GRAPE):

1. Guess initial controls $u_k(j)$.

2. Starting from ρ_0, calculate $\rho_j = U_j \cdots U_1\rho_0 U_1^\dagger \cdots U_N^\dagger$ for all $j \leq N$.

3. Starting from $\lambda_N = C$, calculate $\lambda_j = U_{j+1}^\dagger \cdots U_N^\dagger C U_N \cdots U_{j+1}$ for all $j \leq N$.

4. Evaluate $\delta\Phi_0/\delta u_k(j)$ and update the $m \times N$ control amplitudes $u_k(j)$ according to Eq. 1.17.

5. With these as new controls, go to step 2.

The algorithm is terminated if the change in the performance index Φ_0 is smaller than a chosen threshold value. Clearly, since the algorithm is based on a gradient ascent procedure, there is no guarantee that it will converge to a global minimum. However, at each step the algorithm moves in the direction of increasing performance (see Fig. 1.1), so we can be assured that it converges to control amplitudes that are extremal points of the desired performance function. To expedite the process of this convergence, we can adopt standard conjugate gradient methods [15].

The important advantages of the optimal control related approach are best highlighted by comparing the GRAPE algorithm to conventionally used numerical difference methods to calculate the gradient $\delta\Phi_0/\delta u_k(j)$ by computing Φ_0 for the given pulse sequence $u_k(j)$ as well as for small variations of all $m \times N$ control amplitudes. For example, for $N = 500$ and $m = 4$, the conventional approach would require to calculate 2001 full time evolutions of the density operator from $t = 0$ to T. In contrast, the GRAPE approach to calculate the same gradient $\delta\Phi_0/\delta u_k(j)$ only requires two full time evolutions (one to propagate ρ_0 from $t = 0$ to T and one to back-propagate λ_N from $t = T$ to 0), i.e., it is orders of magnitude faster. This makes it possible to efficiently optimize NMR pulse sequences in much larger parameter spaces. As conventional approaches were typically limited to a few dozens of control variables, a typical strategy was to restrict the optimization to certain pulse families, such as composite pulses with a limited number of flip and phase angles [18,19], Gaussian pulse cascades [20], spline functions [21], or Fourier expansions [22]. In contrast, the GRAPE algorithm allows for much higher flexibility as the number of pulse parameters to be optimized can be orders of magnitude larger compared to conventional approaches.

1.2.3 Application to an ensemble of non-interacting spins

In general, the implementation of the above algorithm implies manipulations with $2^N \times 2^N$ spin-state and rotation matricies for a N-spin case. Not only the matrix multiplications are quite time consuming operations, but much more so are the matrix diagonalization procedures, required to calculate the evolution of a state for every $u_k(j)$ step. But in the case of an ensemble of non-interacting spins the calculations can be significantly simplified if performed in three dimensional real space, where the rotations of spins are governed by Bloch equations, so that there is no need in operations with matrices.

For optimal control of a system of non-interacting spins in NMR, the goal is to find the trajectory for the magnetization vector $\boldsymbol{M}(t)$ that optimizes a suitably chosen cost functional $\mathcal{J}$. In units of angular frequency (rad/s) and in terms of two available control fields $u_x(t)$ and $u_y(t)$, the effective RF field in the rotating frame is

$$\begin{aligned}
\boldsymbol{\omega}_e &= \omega_1(t)[\cos\phi(t)\hat{\boldsymbol{x}} + \sin\phi(t)\hat{\boldsymbol{y}}] + \Delta\omega(t)\hat{\boldsymbol{z}} = \\
&= u_x(t) + u_y(t) + \Delta\omega(t)\hat{\boldsymbol{z}} = \\
&= \boldsymbol{\omega}_{\text{rf}}(t) + \Delta\omega(t)\hat{\boldsymbol{z}}
\end{aligned} \tag{1.18}$$

which encompasses any desired modulation of the amplitude ω_1, phase ϕ, and frequency offset $\Delta\omega$ of the pulse. The possible trajectories $\boldsymbol{M}(t)$ are constrained to satisfy the Bloch

equation

$$\dot{\boldsymbol{M}} = \boldsymbol{\omega_e} \times \boldsymbol{M}, \tag{1.19}$$

which therefore introduces three Lagrange multipliers λ_j. The three constant functions g_j in Eq. 1.4 are then simply the components of the vector

$$\boldsymbol{g} = \boldsymbol{\omega_e} \times \boldsymbol{M}. \tag{1.20}$$

Since $\boldsymbol{\omega_e}(t)$ controls the evolution of $\boldsymbol{M}(t)$, the goal of finding the optimum trajectory is the same as finding the optimal RF sequence to apply to the sample. Given an initial state $\boldsymbol{M}(t_0)$ and a desired final or target state $\boldsymbol{F}$ at the end of the pulse, we want to optimize

$$\mathcal{J}[\boldsymbol{M}] = \int_{t_0}^{t_p} \mathcal{L}[t, \boldsymbol{M}(t), \boldsymbol{\omega_e}(t)]dt + \Phi[\boldsymbol{M}(t_p)] \tag{1.21}$$

over the interval $[t_0, t_p]$. Including the Bloch equation constraints on $\boldsymbol{M}$, the requirement $\delta \mathcal{J} = 0$ (which is the case, when the functional $\mathcal{J}$ is extremized) implies

$$\dot{\boldsymbol{\lambda}} = -\partial h / \partial \boldsymbol{M} \tag{1.22}$$

with initial condition

$$\boldsymbol{\lambda}(t_p) = \partial \Phi / \partial \boldsymbol{M} \tag{1.23}$$

for the time evolution of $\boldsymbol{\lambda}$, and

$$\partial h(t) / \partial \boldsymbol{\omega_e}(t) = 0, \tag{1.24}$$

at all points of the optimal trajectory, which provides a means for adjusting the RF controls. By analogy with the Hamiltonian formalism of classical mechanics, $\boldsymbol{M}$ and $\boldsymbol{\lambda}$ are conjugate variables, since

$$\dot{\boldsymbol{M}} = \boldsymbol{\omega_e} \times \boldsymbol{M} = \partial h / \partial \boldsymbol{\lambda} \tag{1.25}$$

according to equations 1.4 and 1.20.

For all of the applications discussed later here, the running cost, given by the function $\mathcal{L}$ in Eq. 1.21, was set equal to zero. We then find that the optimization of the final cost $\mathcal{J} = \Phi[\boldsymbol{M}(t_p)]$ has an especially simple geometrical interpretation for the particular choice

$$\Phi = \boldsymbol{M}(t_p) \cdot \boldsymbol{F}, \tag{1.26}$$

which quantifies the degree to which $\boldsymbol{M}(t_p) = \boldsymbol{F}$, and where $\boldsymbol{F}$ is just the state, we want our system to reach at the end of the control system, the target state. In this case, Eq. 1.4 becomes

$$h = \boldsymbol{\lambda} \cdot (\boldsymbol{\omega_e} \times \boldsymbol{M}) = \boldsymbol{\omega_e} \cdot (\boldsymbol{M} \times \boldsymbol{\lambda}). \tag{1.27}$$

And from Eq. 1.23 we get particularly simple relation:

$$\boldsymbol{\lambda}(t_p) = \boldsymbol{F}. \tag{1.28}$$

The conditions that must be satisfied at each time for the cost to be maximized are

$$\dot{\boldsymbol{M}} = \boldsymbol{\omega_e} \times \boldsymbol{M}, \tag{1.29}$$

$$\dot{\boldsymbol{\lambda}} = \boldsymbol{\omega_e} \times \boldsymbol{\lambda}, \tag{1.30}$$

$$\frac{\partial h}{\partial \boldsymbol{\omega_e}} = \boldsymbol{M} \times \boldsymbol{\lambda} = 0. \tag{1.31}$$

Note here, that while the magnetization $\boldsymbol{M}$ is defined for a time moment t_0, the variable $\boldsymbol{\lambda}$, which is not just conjugate to $\boldsymbol{M}$, but also has identical equation of motion, is defined by Eq. 1.28 at time moment t_p, at the end of a sequence.

   This provides us with all necessary tools for an optimization. As illustrated in Fig. 1.2, a sequence which transforms $\boldsymbol{M}(t_0)$ forward in time to the desired target state $\boldsymbol{F}$ therefore transforms $\boldsymbol{\lambda}(t_p) = \boldsymbol{F}$ backwards in time to $\boldsymbol{M}(t_0)$. For the optimal pulse, we then have $\boldsymbol{M}_{opt}(t) = \boldsymbol{\lambda}_{opt}(t)$, which satisfies the stationary condition given by Eq. 1.31. For a non-optimal pulse, $(\boldsymbol{M} \times \boldsymbol{\lambda})$ at each point of the two trajectories gives the proportional adjustment to make in the control field $\boldsymbol{\omega_e}(t)$. And the procedure for optimizing the cost can be incorporated in the following algorithm:

1. Choose an initial RF sequence $\boldsymbol{\omega_e}^{(0)}$.

2. Evolve $\boldsymbol{M}$ forward in time from the predefined initial state $\boldsymbol{M}(t_0)$.

3. Evolve $\boldsymbol{\lambda}$ backwards in time from the predefined target state $\boldsymbol{F}$.

4. $\boldsymbol{\omega_e}^{(k+1)}(t) \longrightarrow \boldsymbol{\omega_e}^{(k)}(t) + \epsilon[\boldsymbol{M}(t) \times \boldsymbol{\lambda}(t)]$

5. Repeat steps 2 - 4 until a desired convergence of Φ is reached.

Since the Bloch equation governs the evolution of both vectors, $\boldsymbol{M}$ and $\boldsymbol{\lambda}$, and represents an instantaneous rotation about $\boldsymbol{\omega_e}(t)$, which preserves both the length of these vectors and angle between them, step 3 can be replaced by

3′ Calculate $\boldsymbol{M}(t_p) \times \boldsymbol{\lambda}(t_p)$ and evolve this vector backwards in time.

   which eliminates repeated calculation of $(\boldsymbol{M} \times \boldsymbol{\lambda})$ at each t in step 4.

   Provided we have a m-component control field (for a usual RF-pulse $m = 2$, which are x- and y-components or amplitude and phase), digitized in n time increments, the cost function to be optimized is a function of $N = mn$ variables. Many methods exist for finding an extremum (minimum or maximum) of an N-dimensional function (see, for example, [23]). Typically, they utilize various strategies for stepping downhill (uphill) until a minimum (maximum) of the function is reached. A general function, with no closed form analytical expression for calculating the gradient (i.e., the direction of steepest descent), which is the case for a general NMR RF-pulse, can require on the order of N evaluations to take a single step towards the extremum. Each evaluation of the cost function we want
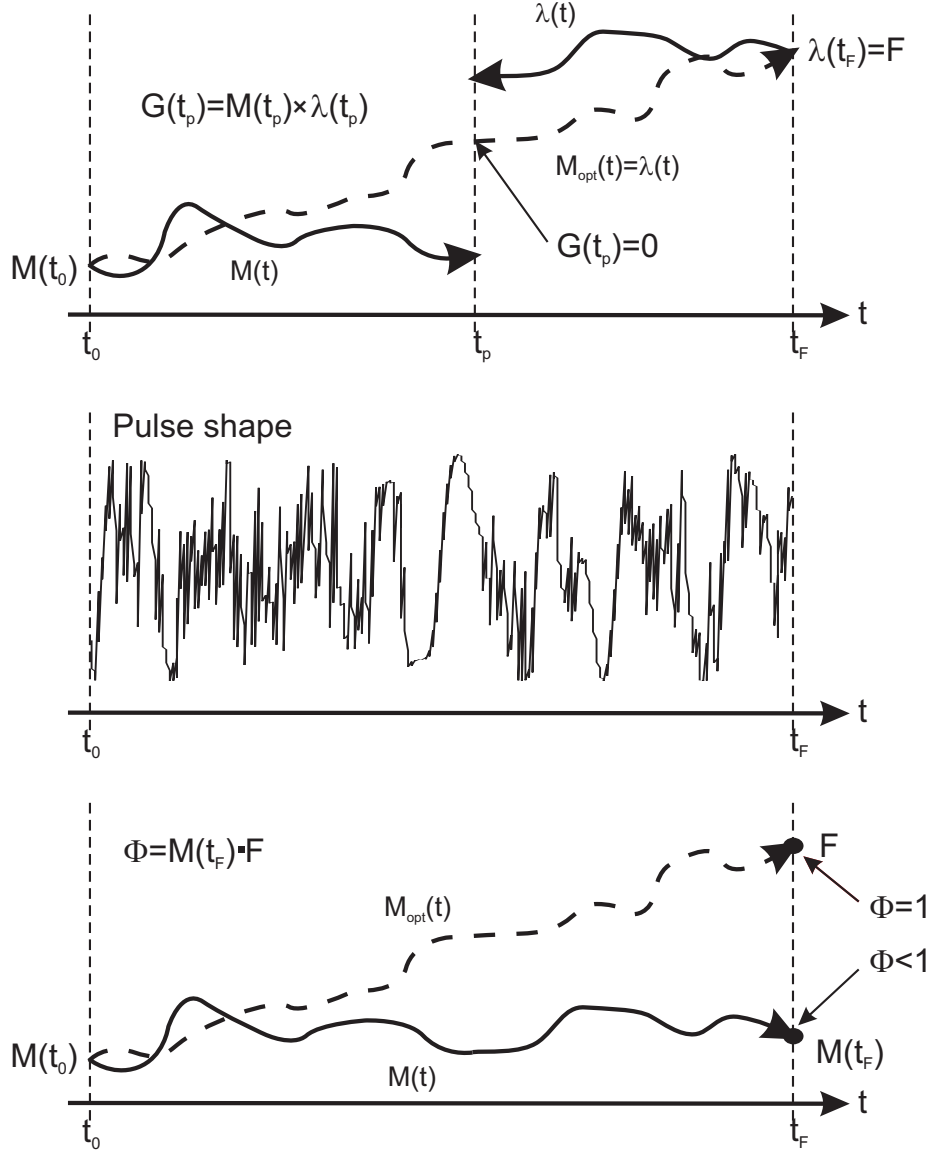
Figure 1.2: Optimization scheme. For a given RF sequence $\boldsymbol{\omega}_e(t)$ (middle), the initial state $\boldsymbol{M}(t_0)$ evolves to some final state $\boldsymbol{M}(t_F)$ through a sequence of intermediate states, shown schematically as the solid line connecting $\boldsymbol{M}(t_0)$ and $\boldsymbol{M}(t_F)$ (bottom). If this final state $\boldsymbol{M}(t_F)$ is not the same, as the defined target state $\boldsymbol{F}$, the quality factor $\Phi < 0$. To calculate the gradients at a given point of the pulse shape the initial state $\boldsymbol{M}(t_0)$ is evolved towards this time point, as well as the desired final target state $\boldsymbol{F}$, which is equal to the Lagrange multiplier term $\boldsymbol{\lambda}(t_p)$ according to Eqs. 1.23 and 1.26, is evolved backwards in time towards this time point (top). The cross product of the two states at this time point gives the proportional adjustment to make for the control fields $\boldsymbol{\omega}_e(t)$. The separate paths for $\boldsymbol{M}(t)$ and $\boldsymbol{\lambda}(t)$ become equal for the optimized RF sequence $\boldsymbol{\omega}_{opt}(t)$ that drives $\boldsymbol{M}(t_0)$ to $\boldsymbol{\lambda}(t_p) = \boldsymbol{F}$.

to optimize requires, in turn, a time evolution of the initial state over the sequence of control fields. By contrast, optimal control theory requires only the two evolutions shown in Fig. 1.2 to determine the best direction to step and improve the cost. It provides therefore an enormous efficiency gain compared to traditional procedures and opens the door to a host of problems that otherwise might be too demanding computationally to be tractable.

1.2.4   Synthesis of unitary transformations

Two important classes of composite and shaped pulses are point-to-point rotations (PP pulses) and universal rotations (UR pulses). PP pulses (also denoted class B2 pulses [18]) are designed to rotate a magnetization vector from a given initial direction as closely as possible to a desired final direction, e.g. from the z axis to the x axis for excitation or from z to $-z$ for inversion pulses. In contrast, UR pulses (also denoted class A pulses [18], constant rotation pulses [19], general rotation pulses [24], plane rotation pulses [25] or simply universal pulses [26]) are designed to induce an effective rotation with a defined direction of the rotation axis and a defined rotation angle not only for a given initial vector orientation but for any arbitrary initial vector. Applications where UR pulses are required include refocusing and mixing pulses in two-dimensional experiments. The *de novo* design of UR pulses is generally assumed to be considerably harder than the design of robust PP pulses.

First, we consider the problem to create in a given time T a desired unitary propagator is also considered in [13]. The equation of motion for the propagator of a closed quantum system is

$$\dot{U} = -i\left(\mathcal{H}_0 + \sum_{k=1}^{m} u_k(t)\mathcal{H}_k\right)U. \tag{1.32}$$

At $t = 0$, the initial propagator is $U(0) = 1$.

First, we consider the problem to approach a desired propagator U_F by applying a pulse sequence $u_j(t)$ such that at the final time

$$||U_F - U(T)||^2 = ||U_F||^2 - 2\text{Re}\langle U_F|U(T)\rangle + ||U(T)||^2 \tag{1.33}$$

is minimized, which is equivalent to maximizing $\text{Re}\langle U_F|U(T)\rangle$. Hence, we can define the performance function to be optimized by the pulse sequence as

$$
\begin{aligned}
\Phi_0 &= \text{Re}\langle U_F|U(T)\rangle \\
&= \text{Re}\langle U_F|U_N\cdots U_1\rangle \\
&= \text{Re}\langle \underbrace{U_{j+1}^\dagger\cdots U_N^\dagger U_F}_{P_j}|\underbrace{U_j\cdots U_1}_{X_j}\rangle.
\end{aligned}
\tag{1.34}
$$

and the corresponding gradient $\delta\Phi_0/\delta u_k(j)$ to first order in Δt is given by

$$\frac{\delta\Phi_0}{\delta u_k(j)} = -\text{Re}\langle P_j|i\Delta t\mathcal{H}_k X_j\rangle. \tag{1.35}$$

While the performance index Φ_0 may be of theoretical interest, for practical applications, it is sufficient to approach the target propagator U_F only up to an arbitrary phase factor $exp\{i\phi\}$ and

$$||U_F - e^{i\phi}U(T)||^2 = ||U_F||^2 - 2\text{Re}\langle U_F|e^{i\phi}U(T)\rangle + ||U(T)||^2 \qquad (1.36)$$

is to be minimized for choice of ϕ, which is equivalent to maximizing the performance function

$$\begin{aligned}
\Phi_1 &= |\langle U_F|U(T)\rangle|^2 \\
&= \langle U_F|U_N\cdots U_1\rangle\langle U_1\cdots U_N|U_F\rangle \\
&= \langle P_j|X_j\rangle\langle X_j|P_j\rangle
\end{aligned} \qquad (1.37)$$

with the operators X_J and P_j as defined in Eq. 1.34. The corresponding gradient $\delta\Phi_1/\delta u_k(j)$ to first order in Δt is given by

$$\begin{aligned}
\frac{\delta\Phi_1}{\delta u_k(j)} &= -\langle P_j|X_j\rangle\langle i\Delta t\mathcal{H}_kX_j|P_j\rangle - \langle P_j|i\Delta t\mathcal{H}_kX_j\rangle\langle X_j|P_j\rangle \\
&= -2\text{Re}\{\langle P_j|i\Delta\mathcal{H}_ktX_j\rangle\langle X_j|P_j\rangle\}.
\end{aligned} \qquad (1.38)$$

1.2.5 Unitary rotations in an ensemble of uncoupled spins

As in the case of point-to-point transformations in an ensemble of non-interacting spins, where calculations can be simplified by using three-dimensional rotations instead of matrix manipulations, the optimization of unitary transformations can be simplified as well.

Normally, for the description of three-dimensional rotations the use of the Eulerian angles α, β, γ is well established [27–30]. And, as a matter of fact, all of the optimizations of point-to point transformations throughout this work were performed with the use of the Eulerian angles. But as elegant as the formal definition may be, it is cumbersome to picture the result of a physical rotation with given values of the Eulerian angles or to predict the result of two successive rotations given by two different sets of angles. A description of rotations more readily acceptable to average human intuition than the Eulerian angles would require specification of the three directional cosines l_{xx}, l_{yy}, l_{zz} of the rotation axes, the rotation angle θ, and a composition rule for the evaluation of successive rotations around different axes. Then, without leaving the realm governed by simple Bloch equations, we only have to assure that the net effect of the optimized pulse would be the rotation with identical rotation axes and rotation angles on every offset within the defined performance range.

Such a formalism has already been established by W. R. Hamilton in 1843 [31] in connection with an extension of the vector calculus. The four variables l_{xx}, l_{yy}, l_{zz}, and θ are related to the four elements of a *quaternion* on which Hamilton wrote his last major opus [32]. All the formulas necessary for our calculations, the relationship of the quaternion elements to the Eulerian angles, the directional cosines of the rotation axis, and the respective rotation angle are reviewed in [33].

   Starting with a general description of three dimensional rotations, the Eulerian angles α, β, γ can be replaced by a different set of variables such as the elements of a 2×2 unitary matrix with determinant 1 [30]

$$u = \left[\begin{array}{cc} a & b \\ -b^* & a^* \end{array}\right],$$ (1.39)

where $|a|^2 + |b|^2 = 1$. Since a and b are complex, this leaves three independent parameters corresponding to the three Eulerian angles. A positive rotation of coordinates x, y, z achieved by the matrix u is given as

$$\left[\begin{array}{cc} z' & x' - iy' \\ x' + iy' & -z' \end{array}\right] = u \left[\begin{array}{cc} z & x - iy \\ x + iy & -z \end{array}\right] u^{-1},$$ (1.40)

where the elements of u are related to the Eulerian angles by [30]

$$a = \cos\frac{\beta}{2}e^{i(\alpha+\gamma)/2},$$

$$b = \sin\frac{\beta}{2}e^{-i(\alpha-\gamma)/2}.$$ (1.41)

   In this form u is identified as the rotation matrix of a spin $1/2$. The appearance of half angles expresses the two-fold homomorphism between the 2×2 rotation matrices and the group of three-dimensional pure rotations: The Eulerian angles are determined within multiples of 2π but the half angles are determined only within multiples of π. Since all trigonometric functions and complex exponentials change sign when the argument is changed by π, the matrix u suffers a sign ambiguity. This, however, does not affect the outcome of the transformation 1.40, since the transformation is quadratic in the rotation matrix.

   Considering successive rotations in the following, the rotation matrix u_2 will be evaluated which combines a rotation u_0 followed by a rotation u_1, in an axis fixed coordinate frame

$$u_2 = u_0 u_1.$$ (1.42)

The resulting elements are given by

$$\left[\begin{array}{cc} a_2 & b_2 \\ -b_2^* & a_2^* \end{array}\right] = \left[\begin{array}{cc} a_0 a_1 - b_0 b_1^* & a_0 b_1 + b_0 a_1^* \\ -b_0^* a_1 - a_0^* b_1^* & -b_0^* b_1 + a_0^* a_1^* \end{array}\right].$$ (1.43)

It is now convenient to rewrite 1.43 in terms of the real and imaginary parts of a and b:

$$a = D + iC,$$

$$b = B + iA,$$ (1.44)

where from 1.41

$$A = -\sin\frac{\beta}{2}\sin\frac{\alpha - \gamma}{2}, \quad B = \sin\frac{\beta}{2}\cos\frac{\alpha - \gamma}{2},$$

$$C = \cos\frac{\beta}{2}\sin\frac{\alpha + \gamma}{2}, \quad D = \cos\frac{\beta}{2}\cos\frac{\alpha + \gamma}{2}.$$ (1.45)

The four terms A, B, C and D form a quaternion. Since they are interrelated by

$$A^2 + B^2 + C^2 + D^2 = 1 \tag{1.46}$$

the four quaternion elements correspond to three independent variables.

From 1.43 and 1.44 the elements of the quaternion of the composite rotation are derived in terms of the quaternion elements of the first and the second rotation

$$\begin{bmatrix} A_2 \\ B_2 \\ C_2 \\ D_2 \end{bmatrix} = \begin{bmatrix} +D_1 & -C_1 & +B_1 & +A_1 \\ +C_1 & +D_1 & -A_1 & +B_1 \\ -B_1 & +A_1 & +D_1 & +C_1 \\ -A_1 & -B_1 & -C_1 & +D_1 \end{bmatrix} \cdot \begin{bmatrix} A_0 \\ B_0 \\ C_0 \\ D_0 \end{bmatrix}. \tag{1.47}$$

The usefulness of quatemions is based on the connection of the quaternion elements to the rotation angle θ and the directional cosines l_{xx}, l_{yy}, l_{zz} of the rotation axis. The quaternion elements A, B, C and D can be expressed in these terms [33] as follows:

$$\begin{aligned} A &= l_{xx}\sin\theta/2, \\ B &= l_{yy}\sin\theta/2, \\ C &= l_{zz}\sin\theta/2, \\ D &= \cos\theta/2. \end{aligned} \tag{1.48}$$

In the case of an ensemble of non-interacting spins, where two control fields $u_x(t)$ and $u_y(t)$ have to be optimized, this can be rewritten as

$$\begin{aligned} A(j) &= u_x(j)\,\sin\{\theta(j)/2\}, \\ B(j) &= u_y(j)\,\sin\{\theta(j)/2\}, \\ C(j) &= \Delta\omega\,\sin\{\theta(j)/2\}, \\ D(j) &= \cos\{\theta(j)/2\} \end{aligned} \tag{1.49}$$

for every digit j, with offset $\Delta\omega$ and rotation angle $\theta(j)$ expressed as

$$\theta(j) = \Delta t \cdot \sqrt{u_x^2(j) + u_y^2(j) + (\Delta\omega)^2}. \tag{1.50}$$

It has to be noticed that these quaternion elements describe positive rotations of co-ordinates. The quaternion elements for positive rotations of functions are obtained by replacing θ by $-\theta$, because rotations of coordinates and rotations of functions correspond to inverse operations [30]. In agreement with Eq. 1.45 this produces a change of sign for A, B, and C.

The performance index of the transfer process can then be expressed (cf. Eqs. 1.34), as

$$\Phi_0 = A_F \cdot A(T) + B_F \cdot B(T) + C_F \cdot C(T) + D_F \cdot D(T), \tag{1.51}$$

and the corresponding gradients to first order in Δt are given by

$$\frac{\delta \Phi_0}{\delta u_x(j)} = -A_P D_X - B_P C_X + C_P B_X + D_P A_X,$$

$$\frac{\delta \Phi_0}{\delta u_y(j)} = A_P C_X - B_P D_X - C_P A_X + D_P B_X, \qquad (1.52)$$

where indexes X and P correspond to quaternion representations of operators X_j and P_j in Eqs. 1.34.

Whereas for the performance function Φ_1 (cf. Eq. 1.37) one can write:

$$\Phi_1 = [A_F \cdot A(T) + B_F \cdot B(T) + C_F \cdot C(T) + D_F \cdot D(T)]^2, \qquad (1.53)$$

and the corresponding gradients to first order in Δt are given by

$$\frac{\delta \Phi_0}{\delta u_x(j)} = (-A_P D_X - B_P C_X + C_P B_X + D_P A_X)(A_P A_X + B_P B_X + C_P C_X + D_P D_X)$$

$$\frac{\delta \Phi_0}{\delta u_y(j)} = (A_P C_X - B_P D_X - C_P A_X + D_P B_X)(A_P A_X + B_P B_X + C_P C_X + D_P D_X) \; (1.54)$$

Similary to the section 1.2.3, where for an ensemble of non-interacting spins the full quantum mechanical description could be reduced to vector rotations in three-dimensional space, we here reduced the full quantum mechanical description to rotations of four-component vectors, sufficient to describe an ensemble of non-interacting spins.

Equipped now with all necessary equations, we can modify the basic GRAPE algorithm to perform optimizations of unitary rotations. This will take the following form:

1. Guess initial controls $u_k(j)$.

2. Starting from $U(0) = 1$, calculate $U_j = U_j U_{j-1} \cdots U_1$ for all $j \leq N$.

3. Starting from $U_F = C$, calculate $\lambda_j = U_{j+1}^\dagger \cdots U_N^\dagger C$ for all $j \leq N$.

4. Evaluate $\delta \Phi_0 / \delta u_k(j)$ and update the $m \times N$ control amplitudes $u_k(j)$ according to Eq. 1.17.

5. With these as new controls, go to step 2.

1.3 Broadband excitation and inversion

Modern high resolution NMR spectrometers with very high magnetic fields result in large offset ranges that have to be covered by modern pulse sequences. Especially ^{13}C and ^{19}F nuclei with their large offset ranges pose problems to conventional hard pulses. But also weak ^{15}N pulses of common triple resonance probeheads, for example, make it impossible to cover the whole nitrogen spectrum of uniformly labeled nucleic acids. The increased offset ranges could in principle be covered by stronger hard pulses, but high spectrometer frequencies close to 1 GHz limit the technically available maximum rf-amplitude. An effective alternative to the hard pulse for covering the necessary bandwidth therefore is urgently needed.

The development of cryogenic probe heads allows NMR-measurements with significantly improved signal to noise ratios. However, the large temperature gradient in such a probehead leads to a coil design with significantly increased B_1-field inhomogeneity compared to conventional probeheads. As a consequence the sensitivity gain due to the cryogenic cooling is reduced with every uncompensated pulse. With robust pulses that are compensated for strong variations in rf-amplitude this loss in sensitivity could be strongly reduced. Optimal control theory is an ideal tool for the design of such pulses.

In the algorithm described above, the initial state for an excitation pulse $\boldsymbol{M}(t_0) = \hat{\boldsymbol{z}}$ and the target state $\boldsymbol{F} = \hat{\boldsymbol{x}}$, while for inversion pulse the target state $\boldsymbol{F} = -\hat{\boldsymbol{z}}$. Since no pulse can effectively excite or invert an infinite range of offsets, one needs to define a range of offset of interest and chose a number of points, say k, over this offset range, where the performance of the pulse will be checked. Furthemore, one can be interested in getting a pulse, which tolerates miscalibration. therefore, the amplitude can be calculated as $\omega_1(t) = \alpha \omega_1^0(t)$ for a set of l scaling factors α. So, for a range of chemical shift offset, and also a range of non-ideal RF fields, the cost function Φ is calculated for every offset and every RF scaling factor α ($N = kl$ points altogether) and the *average* cost $\langle \Phi \rangle$ is then used as the performance criterion of the pulse:

$$\langle \Phi \rangle = \frac{1}{n_{\text{off}} \ n_{\text{rf}}} \sum_{i=1}^{n_{\text{off}}} \sum_{j=1}^{n_{\text{rf}}} \alpha_{\text{rf}}^{(i)} \alpha_{\text{off}}^{(j)} \boldsymbol{M}_{ij}(t_p) \cdot \boldsymbol{F}, \qquad (1.55)$$

where α_{rf} and α_{off} are eventual weighting factors, $i = 1..n_{\text{off}}$ being the offsets and $j = 1..n_{\text{rf}}$ the scaled rf-amplitudes calculated for each pulse of length t_p, e.g. to include the effects of rf-inhomogeneity or rf-amplitude misadjustments. Similarly, the value of $\boldsymbol{M} \times \boldsymbol{\lambda}$ is calculated for every combination of resonance offset and RF field, and the average of all these values, $\langle \boldsymbol{M} \times \boldsymbol{\lambda} \rangle$, is used in step (3'). Since frequency modulation is equivalent to phase modulation, with $\Delta\omega(t) = d\phi(t)/dt$, only amplitude and phase modulations were considered in the current implementation of the algorithm. The value of $\Delta\omega$ in Eq. 1.18 is then time-independent. and gives the chemical shift of the irradiated spin. Since one cannot apply a RF pulse with z component, only the transverse or (x,y) components of $\boldsymbol{\omega}_e$ are modified in step 4. This effectively ignores the information contained in the z component of $\boldsymbol{M} \times \boldsymbol{\lambda}$ for optimizing the cost. The stepsize, ϵ, can be chosen sufficiently small to ensure the solution always tends steadily towards the optimum, but

this can be overly time-consuming, involving many unnecessarily small steps during some iterations. Instead, the largest step providing improvement in the cost is determined at each iteration by bracketing the optimal step size among three values and using a simple 1D line minimization routine [23]. The efficiency of the optimization is further enhanced using a conjugate gradient method to determine the step direction.

1.3.1   First application to broadband excitation

For the first application of the optimal control theory to the problem of broadband excitation reported in [34], the average $\langle \boldsymbol{M} \times \boldsymbol{\lambda} \rangle$, calculated using steps 2 and $(3')$, was calculated over a combination of 81 resonance offsets in the range ± 20 kHz, incremented by 500 Hz, and 5 RF scalings given by $\alpha = (0.95, 0.975, 1.0, 1.025, 1.05)$. The RF values were weighted according to a Gaussian distribution $exp[-(1-\alpha)^2/(2\sigma^2)]$, with $\sigma = 0.042$ giving a full width at half-maximum (FWHM) of 0.1, or 10% of the nominal RF value. The resonance offsets were weighted equally. The two RF control fields $(\omega_1)_x$ and $(\omega_1)_y$ were digitized in 0.5 μs steps over the 2ms pulse length. RF inhomogeneity in the amplitude $\omega_1(t)$ was incorporated by scaling the ideal RF amplitude $\omega_1^0(t)$ according to $\omega_1(t) = \alpha\omega_1^0(t)$ for constant factors α. So, the optimized cost function had a total of 8000 independent control parameters (4000 time digits, 2 components each) to be optimized over 405 possible combinations of RF scale factor and resonance offset, which for traditional optimization methods would present a formidable challenge.

The optimal control algorithm, implemented according to the design criteria of the previous section, converged to the excitation pulse displayed in Fig. 1.3. The algorithm requires less than 30 min of CPU time to generate the pulse on a 1.5GHz Pentium IV processor.

The seemingly random appearance of the pulse belies its function: each increment of the pulse delivers the precise RF amplitude and phase required to maximize the final x magnetization over the target ranges in RF inhomogeneity and resonance offset for the given (random) initial RF waveform. The inverse transformation $I_x \rightarrow I_z$ can be obtained by applying the time-reversed pulse, with each phase incremented by 180°. The theoretical performance of the pulse, assuming simple Bloch equation evolution of the irradiated spins (as in the optimization procedure), is illustrated in Fig. 1.4. Contours of x magnetization, M_x, are plotted in the upper panel as functions of resonance offset and RF inhomogeneity. The phase of the excited magnetization is shown similarly in the lower panel. Over a $\pm 5\%$ variation in the nominal RF delivered by the coil and resonance offsets of ± 20 kHz, the excited magnetization M_x is at least 99.5% of the initial z magnetization, $\boldsymbol{M}_0$.

For this pulse a commonly used figure-of-merit (FOM), defined as the total excitation bandwidth satisfying the benchmark divided by the peak RF amplitude, is equal to 2.3, which is comparable to the best values of the previous broadband excitation pulses, with the exception of the 12 ms ABSTRUSE pulse [35], which gives a much higher FOM at the price of increased vulnerability to J-coupling and relaxation effects. The FOM, however, provides no measure for the uniformity of the performance as a function of changing RF
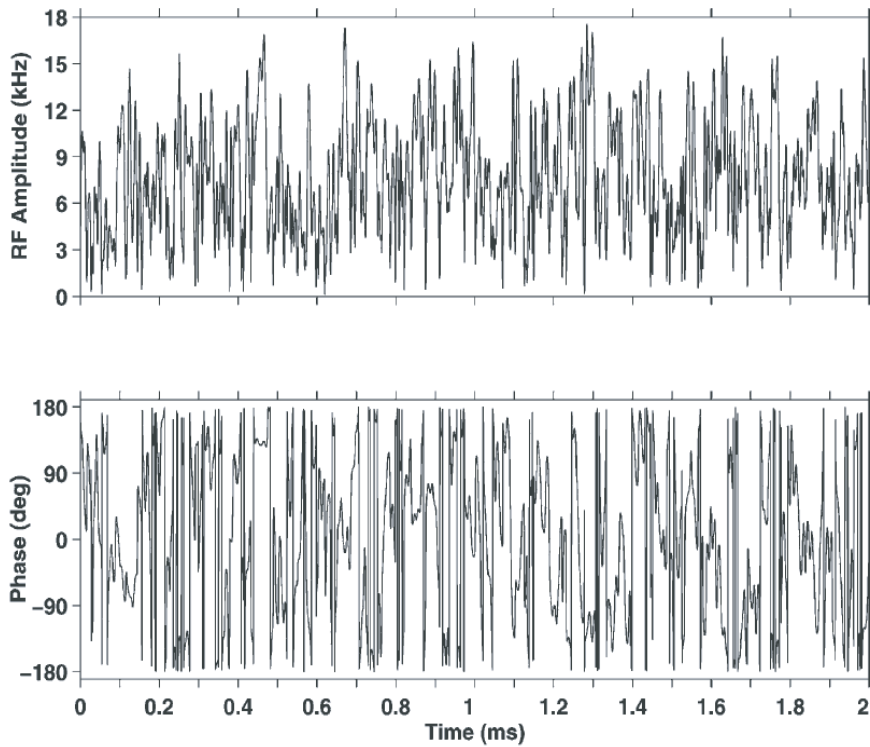
Figure 1.3: Broadband excitation pulse. The deceptively "random" appearance in pulse amplitude (upper panel) and phase (lower panel) as a function of time efficiently chore-ographs the transformation $I_z \rightarrow I_x$ over a 40 kHz range of resonance offsets with moderate tolerance to RF miscalibration (see Fig. 1.4). The pulse length was fixed at 2 ms, result-ing in a maximum RF amplitude for the pulse of 17.5 kHz. A 2 ms pulse of constant 8.5 kHz RF amplitude would have the same power requirements as the pulse shown. Figure taken from [34].
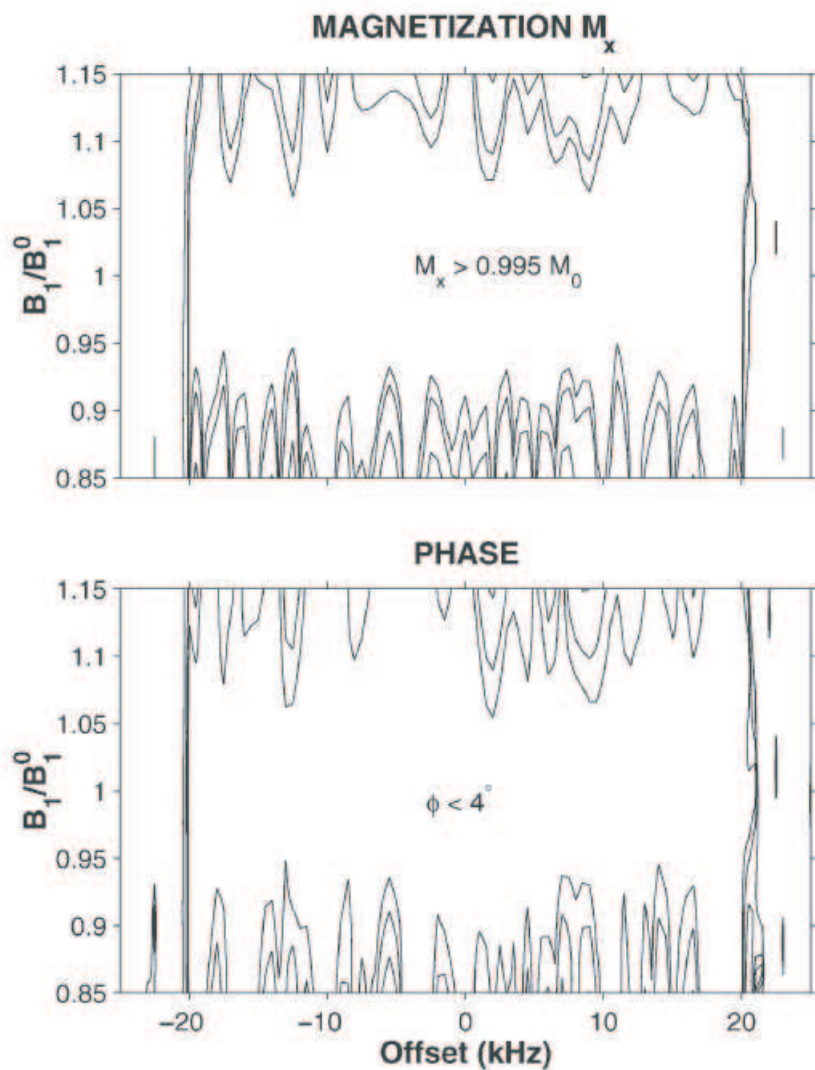
Figure 1.4: Simulated performance of the optimized pulse of Fig. 1.3. Starting with initial z magnetization $\boldsymbol{M}_0$, the magnitude M_x (upper panel) and phase ϕ (lower panel) of the excited magnetization is plotted as a function of resonance offset and RF field B_1, represented as a fraction of the nominal field B_1^0. Contour lines displayed for M_x are [0.995, 0.99, 0.96], and those for the phase of the excited magnetiztion are [4°, 8°, 16°]. Figure taken from [34].

calibration or homogeneity.

The longer an excitation pulse is, the more important the potential effects of J-coupling during the pulse, and 2ms is sufficiently long that this could be a significant concern. However, it was shown on simulations as well as experimentally [34], that for a heteronuclear systems the performance of the pulse is essentially the same, as it is for a single spin shown in Fig. 1.4.

1.3.2   Limiting the pulse amplitude

Although the 2ms pulse for the broadband excitation optimized by means of optimal control theory, (BEBOP), described just above, performs extremely well, shorter pulses are also desirable in order to minimize relaxation effects. At the same time, peak RF amplitude must remain below probe limits (e.g., available for ^{13}C spectroscopy). In the procedure described above the maximum amplitude of the RF controls was not explicitly constrained – a chosen pulse length and convergence factor for terminating the algorithm resulted in an unspecified maximum pulse amplitude. This is, however, unpractical, while any attempt to optimize a shorter pulse in order to eventually improve its relaxation properties will inevitably result in final amplitude driven up by the algorithm to always higher values in order to achieve convergence. By decreasing the length of a pulse we wish to optimize at some point we will reach the situation, where for every optimization attempt with all possible starting sequences the produced peak amplitude will be so high, that any practical application of such a pulse on real spectrometers will be just impossible. So, one has to change the algorithm in a way, that only pulses with amplitudes below some limit can be produced. In other words we need to limit the space of allowed control amplitudes, so that $\omega_1(t) < \omega_{max}$ for every t.

The procedure for optimizing the cost, subject to the constraint that the RF amplitude at each time, $\omega_1(t)$, be no greater than a chosen maximum amplitude ω_{max}, is incorporated in the following algorithm [36]:

1. Choose an initial RF sequence $\boldsymbol{\omega}_e^{(0)}$.

2. Evolve $\boldsymbol{M}$ forward in time from the predefined initial state $\boldsymbol{M}(t_0)$.

3. Calculate $\boldsymbol{M}(t_p) \times \boldsymbol{\lambda}(t_p)$ and evolve it backwards in time.

4. $\boldsymbol{\omega}_e^{(k+1)}(t) \longrightarrow \boldsymbol{\omega}_e^{(k)}(t) + \epsilon[\boldsymbol{M}(t) \times \boldsymbol{\lambda}(t)]$.

5. For any $\omega_1(t) > \omega_{max}$, set $\omega_1(t) \rightarrow \omega_{max}$.

6. Repeat steps 2 - 5 until a desired convergence of Φ is reached.

The RF clipping in step 5 is implemented by adjusting $(\omega_1)_x$ and $(\omega_1)_y$ to satisfy the constraint on maximum RF amplitude without changing the phase of ω_1

This modified algorithm was implemented in [36] with all parameters set to the same values as in [34], only the length of the pulse was set to a shorter value of 500μs. But this
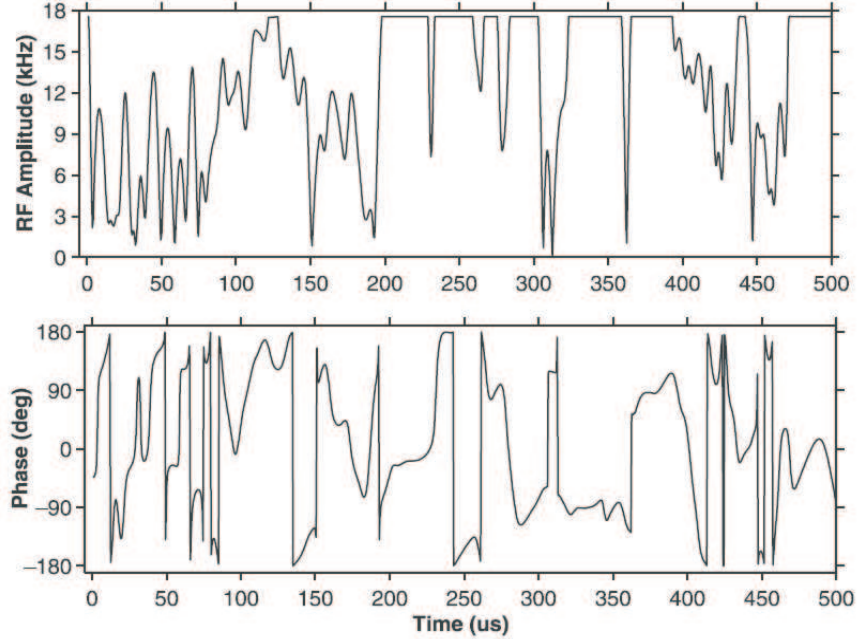
Figure 1.5: Broadband excitation pulse obtained using the optimal control algorithm described in the text. Application of pulse amplitude (upper panel) and phase (lower panel) produces the transformation $I_z \rightarrow I_x$ over a 40 kHz range of resonance offsets with tolerance to RF miscalibration sufficient for typical high-resolution NMR probes (see Fig. 1.6). The maximum RF amplitude was limited to 17.5 kHz by clipping whenever the amplitude exceeded this value, forcing the algorithm to search for another solution. A 500 μs pulse of constant 13.5 kHz RF amplitude would have the same power requirements as the pulse shown. Figure taken from [36].

time the maximal possible RF amplitude was constrained to 17.5 kHz, a value of reached peak amplitude in previous implementation of the algorithm. The amplitude and phase of the resulting excitation pulse, digitized in 0.5 μs increments, are plotted as a function of time in Fig. 1.5 for comparison with the earlier result. The figure clearly shows the cutoff for the maximum RF amplitude, resulting in a constant amplitude of 17.5 kHz during extended periods of the pulse.

The theoretical performance of the pulse, assuming simple Bloch equation evolution of the irradiated spins (as in the optimization procedure), is illustrated in Fig. 1.6. Contours of x magnetization, M_x, are plotted in the upper panel as functions of resonance offset and RF inhomogeneity. The phase of the excited magnetization is shown similarly in the lower panel. Over a $\pm 5\%$ variation in the nominal RF delivered by the coil and resonance offsets of ± 20 kHz, the excited magnetization M_x is still at least 99.5% of the initial z magnetization, $\boldsymbol{M}_0$, but the phase is now less than 2°, compared to 4° for the 2 ms pulse. The 99% contours cover almost a $\pm 15\%$ variation in nominal RF, and the phase
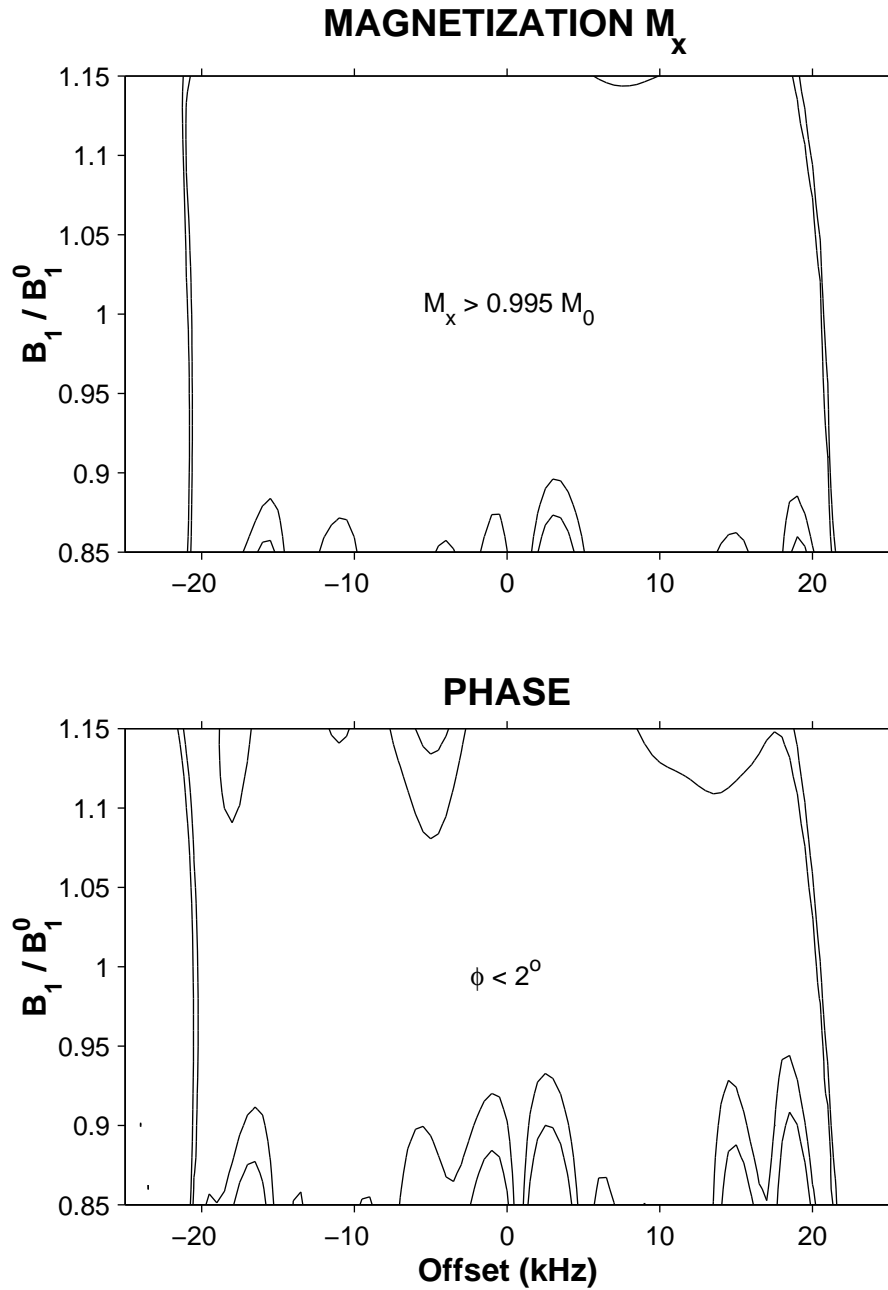
Figure 1.6: Simulated performance of the optimized pulse of Fig. 1.5. Starting with initial z magnetization $\boldsymbol{M}_0$, the magnitude M_x (upper panel) and phase ϕ (lower panel) of the excited magnetization are plotted as a function of resonance offset and RF field B_1, represented as a fraction of the nominal field B_1^0. Contour lines displayed for M_x are [0.995, 0.99], and those for the phase of the excited magnetization are [2°, 4°], demonstrating practically ideal performance even beyond the range of RF ($\pm 5\%$) and resonance offset (± 20 kHz) variations considered in the optimal control implementation. Figure taken from [36].

of the final magnetization is on the order of only 4° over this larger RF range, operating over the same 40 kHz bandwidth. The nearly ideal pulse performance illustrated in Fig. 1.6 indicates that there is some latitude within the constraints of the design criteria for further shortening the pulse length, since perfect performance may not be necessary.

1.3.3   Exploring the limits of broadband excitation and inversion

As we see, the optimal control theory is a powerful tool, which allows one to design RF pulses covering large offset ranges and showing significant degree of tolerance against miscalibration. Nonetheless, all attempts to optimize pulses so far were just a kind of blind search, the pulse parameters were chosen more or less arbitrarily with the hope, that this choice will allow the algorithm to produce reasonably performing pulses. Depending on demands one wants the pulse to meet, such a search for optimal parameters can be a rather time consuming procedure, while every change will require a full optimization run in order to see whether a sufficiently good pulse can be produced under these conditions. It will be therefore quite useful to know the minimal necessary conditions, like duration and peak RF amplitude, a pulse should meet in order to produce a desired degree of excitation or inversion for a given range of offsets and given tolerance to RF power miscalibration. More to say, once we know, that for certain spin systems, where the theoretical limits of quantum evolution were known [5–11], numerical algorithms based on principles of optimal control theory, provide pulse sequences which approach the physical limits [12–14], then such search can pretend on some generality and show the estimates to the physical limits for robust broadband excitation and inversion. In particular we want to specify upper limits for the minimum durations of pulses as a functions of bandwidths and RF variation.

For this purpose a systematic study of the pulse performance was performed with tools of optimal control theory. Sets of excitation and inversion pulses were calculated for bandwidths of 10, 20, 30, 40, and 60 kHz considering both ideal rf amplitude (scale factor of 1) and a variation of ± 20 percent in the factor used to scale the rf amplitudes. Also sets of pulses for a fixed bandwidth of 20 kHz with variations of ϑ of ± 10, ± 20, ± 30, and ± 40 percent in rf scale factor were optimized to test robustness against B_1-field inhomogeneity. In all cases, the nominal (unscaled) rf-amplitude was limited to 10 kHz using the method described in the previous section. For each set, pulse lengths t_p were varied in ranges as listed in Table 1.1. Generally, pulse durations were incremented until the quality factor Φ exceeded 0.995. Each chosen bandwidth was divided into equal increments, with $n_{\text{off}} = 100$ for 10 kHz bandwidth, $n_{\text{off}} = 200$ for bandwidths of 20, 30, and 40 kHz and $n_{\text{off}} = 300$ for 60 kHz bandwidth. n_{rf} was chosen equal to 5 with equidistant percentage amplitude changes whenever variations in rf-amplitude were included in the calculations. The time digitization for the optimized shapes was 0.5 μs in all cases.

One hundred randomized starting pulses were generated to start 100 optimizations for each data point in Figs. 1.8 and 1.9. As with all gradient-based optimizations, the optimal control algorithm can terminate at a local, rather than the global, extremum. The pulse found by the algorithm depends on the (random) pulse chosen to start the procedure. However, in contrast to conventional optimization procedures, a significant

Table 1.1: Constraints used for BEBOP and BIBOP optimizations

rf-limit (kHz)	$\Delta\nu^a$ (kHz)	n_{off}	ϑ^b (%)	t_p excitation (μs)	t_p inversion (μs)
10	10	100	—	2.5 - 85	2.5 - 122.5
10	20	200	—	2.5 - 142.5	2.5 - 182.5
10	30	200	—	2.5 - 217.5	2.5 - 247.5
10	40	200	—	2.5 - 267.5	2.5 - 312.5
10	60	300	—	2.5 - 422.5	2.5 - 457.5
10	20	200	$\pm$ 10	2.5 - 247.5	2.5 - 242.5
10	20	200	$\pm$ 20	2.5 - 337.5	2.5 - 307.5
10	20	200	$\pm$ 30	2.5 - 442.5	2.5 - 352.5
10	20	200	$\pm$ 40	2.5 - 667.5	2.5 - 417.5
10	5	100	$\pm$ 20	30 - 60	40 - 115
10	10	200	$\pm$ 20	50 - 125	50 - 170
10	20	200	$\pm$ 20	100 - 190	85 - 212.5
10	30	300	$\pm$ 20	150 - 285	200 - 250
10	40	300	$\pm$ 20	180 - 405	265 - 385
10	50	300	$\pm$ 20	200 - 540	

^{a}) $\Delta\nu$ is defined as the excitation/inversion bandwidth used in the optimization. ^{b}) ϑ is the range of rf amplitude scaling incorporated in the optimization.

percentage of the optimal control trials converges to similar values, even in cases with tight constraints. In addition, the quality factors cited as establishing limits on pulse performance are very high, approaching the ideal value of one (see Fig. 1.7 and Fig. 1.13). Any potential improvement in these limits will therefore be relatively small.

The convergence of every single optimization was very fast ranging from seconds for the shortest pulses to tens of minutes for the longest ones with larger n_{off} and n_{rf} on a single AMD Athlon 1500+ processor Linux-based PC.

The results of the optimizations of excitation and inversion pulses are shown in Figs. 1.8 and 1.9, respectively: The performance of the optimized pulses described by the quality factor $\mathbf{\Phi}$ is given as a function of pulse length on a linear scale in Figs. 1.8 A, D and 1.9 A, D. A logarithmic scale is used in Figs. 1.8 B, E and 1.9 B, E to show the differences at longer pulse durations more clearly. As expected, higher demands in terms of bandwidth or tolerance to rf-amplitude variation lead to reduced quality factors that can, however, be compensated by increased pulse lengths. In all cases pulses with more than 99.5 percent excitation or inversion over the entire offset and rf-amplitude ranges could be found for unexpectedly short pulse durations of significantly less than 700 μs. A question of considerable practical interest is the minimum pulse length needed to achieve an excitation or inversion of a given quality. This information is shown in Figs. 1.8 C, F and 1.9 C, F.
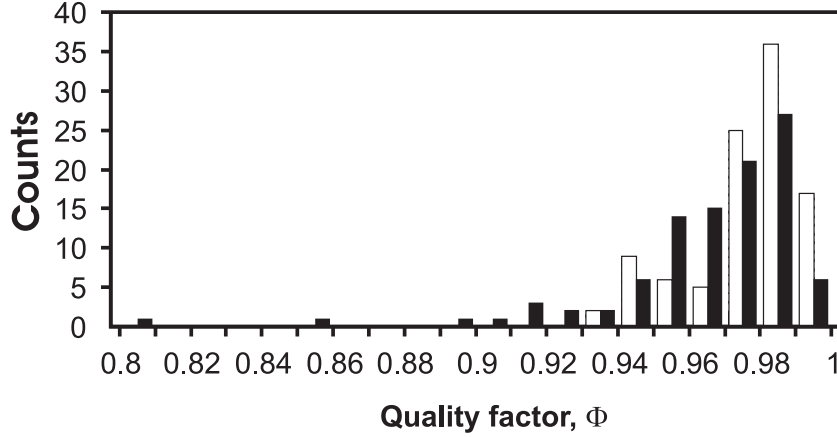
Figure 1.7: Histogram distribution of quality factors Φ obtained for 100 optimizations for excitation pulses of 20 kHz bandwidth, of 300 μs duration, and ± 20 % rf-variation (open bars); 600 μs duration and ± 40 % variation in rf-amplitude (black bars). A significant percentage of the optimizations is close to the maximum quality factors of 0.9955 and 0.9957, respectively.

The relation between the duration and bandwidth is roughly linear for both types of pulses for the investigated offset and rf ranges.

The dependence of the quality factor on the pulse duration is not a single round curve, but shows a step or wave-like behavior (c.f. Figs. 1.8 A,D and 1.9 A,D). A more detailed analysis reveals that steps are related to specific pulse families of optimal pulses. Representatives of such pulse families are shown in Fig. 1.7 for excitation. For very short pulses, optimal control theory found that hard pulses with constant amplitude and phase provided the best performance. For longer pulses, the algorithm introduced 180° phase shifts resulting in pulses very similiar to phase-alternating composite pulses with one, two, and three phase jumps. If the pulse length increases further, the phase jumps 'morph' into more continuous phase changes. As was shown in [36], even longer pulses will have significant amplitude modulation, interspersed with periods of maximum rf amplitude. If the pulse is sufficiently long, the amplitude will not necessarily reach the rf limit [34]. The pulse families shown in Fig. 1.7 each correspond to a 'step' in Fig. 1.8 A,D.

Pulses optimized for inversion all show constant rf-amplitude over the entire length, but the observed step-like behavior still corresponds to certain pulse patterns. As for excitation, hard pulses and pulses with a single 180° phase jump give best results for very short pulse durations and bandwidths up to 30 kHz. E.g. for a bandwidth of 20 kHz and assuming no variation in rf amplitude, Fig. 1.11 B shows the numerically optimized pulse with a total duration of 67.5 μs, which represents a phase-alternating composite pulse $\{52^\circ_x, 191^\circ_{-x}\}$. For this bandwidth, such two-component phase-alternating pulses of the general form $\{\alpha_x, \ \beta_{-x}\}$ are found to be optimal for pulse durations between 52.5 and 72.5 μs. In this range, the flip angle β of the numerically found optimal pulses is
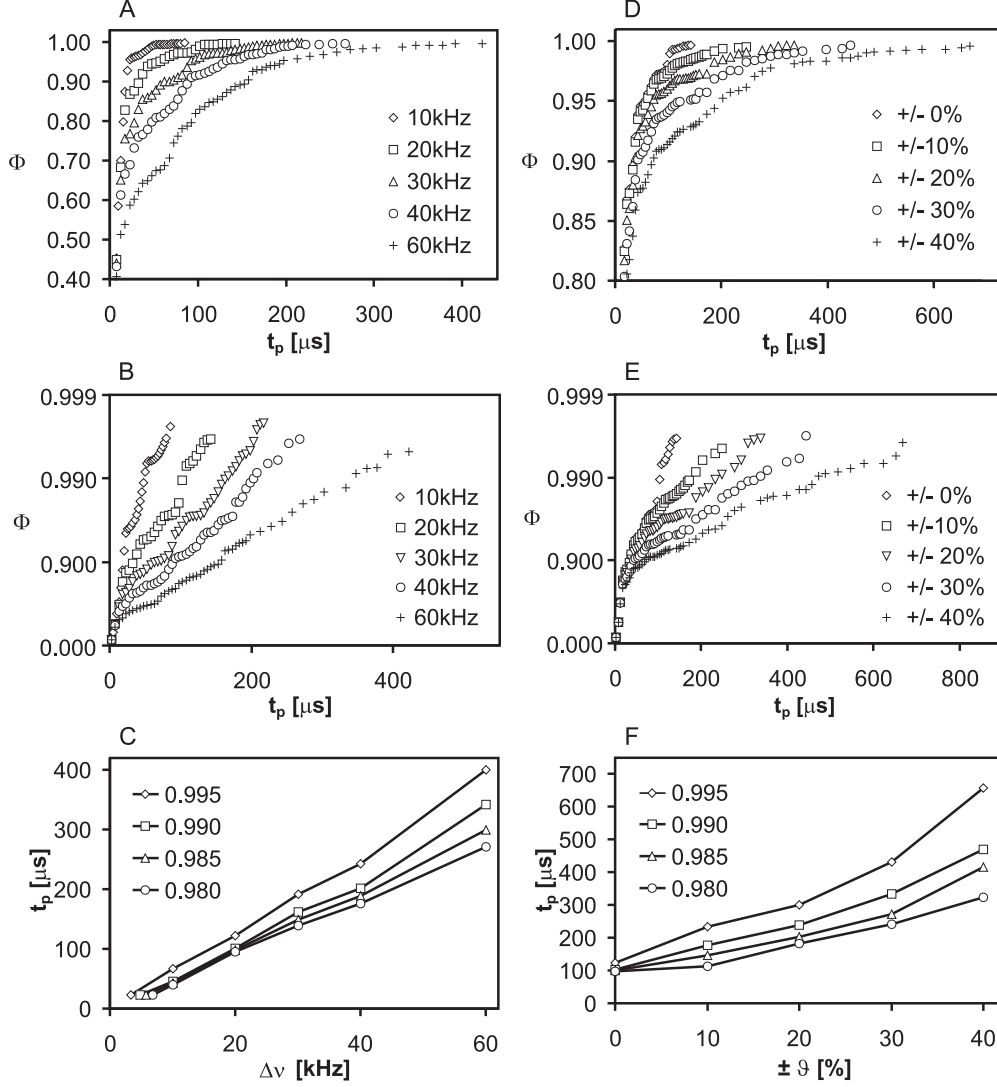
Figure 1.8: Maximum quality factors reached for broadband excitation pulses (BE-BOP) with rf-amplitude limited to 10 kHz under various optimization constraints. The maximum quality factors Φ with respect to pulse duration is given for the five different bandwidths $\Delta\nu$ equal to 10 kHz, 20 kHz, 30 kHz, 40 kHz, and 60 kHz on a linear (A) and logarithmic scale (B). In C, the pulse lengths for quality factors of 0.98, 0.985, 0.99, and 0.995 are plotted as a function of the desired bandwidth and provide an estimate for the minimum pulse duration needed for specific requirements. The maximum quality factors Φ with respect to rf-variation are shown for no variation and rf-ranges ϑ of ±10 %, ±20 %, ±30 %, and ±40 % on a linear (D) and logarithmic scale (E) for a fixed bandwidth of 20 kHz. In (F), the minimum pulse duration t_p are shown as a function of the rf variation $\pm\vartheta$ for quality factors $\Phi = 0.98$, 0.985, 0.99, and 0.995.

Figure 1.9: Maximum quality factors reached for broadband inversion pulses (BIBOP) with rf-amplitude limited to 10 kHz under various optimization constraints. Again, maximum quality factors Φ with respect to pulse duration are given for the five different bandwidths $\Delta\nu$ equal to 10 kHz, 20 kHz, 30 kHz, 40 kHz, and 60 kHz on a linear (A) and logarithmic scale (B). In C, the pulse lengths for quality factors of 0.98, 0.985, 0.99, and 0.995 are plotted as a function of the desired bandwidth and provide an estimate for the minimum pulse duration needed for specific requirements. The maximum quality factors Φ with respect to rf-variation are shown for no variation and rf-ranges ϑ of ± 10 %, ± 20 %, ± 30 %, and ± 40 % on a linear (D) and logarithmic scale (E) for a fixed bandwidth of 20 kHz. In (F), the minimum pulse duration t_p are shown as a function of the rf variation $\pm\vartheta$ for quality factors $\Phi = 0.98$, 0.985, 0.99, and 0.995.

Figure 1.10: Amplitude and Phase for optimized excitation pulses of various durations found in the optimization for a bandwidth of 30 kHz and no rf-variation. Although no restrictions to the pulse shape were made, phase-alternating composite pulses are found for pulse durations of up to 82.5 μs (pulses shown in A-D correspond to 63°_y, $\{29^\circ_{-y}, 88^\circ_y\}$, $\{32^\circ_y, 85^\circ_{-y}, 126^\circ_y\}$, and $\{29^\circ_{-y}, 68^\circ_y, 88^\circ_{-y}, 112^\circ_y\}$, while smooth phase-modulations were found for longer pulses.

approximated by $\beta \approx \alpha + 145^\circ$. Hence, the overall on-resonance flip angle ($\alpha - \beta$) of these pulses is only about 145° for this family of short pulses, which achieve the best possible *average* inversion over the full 20 kHz offset range. For a bandwidth of 30 kHz, two-component phase-alternating pulses $\{\alpha_x, \beta_{-x}\}$ are found for durations between 52.5 and 62.5 μs with $\beta \approx \alpha + 125^\circ$. For a bandwidth of 10 kHz, two-component phase-alternating pulses are found for durations between 52.5 and 87.5 μs with $\beta \approx \alpha + 165^\circ$, e.g. for a duration of 87.5 μs, the numerically optimized pulse is $\{76^\circ_x, 239^\circ_{-x}\}$, which is similar to the well known pulse $\{90^\circ_x, 270^\circ_{-x}\}$ [37, 38]. For longer pulse durations and broader bandwidths, a pulse family with smoothly modulated phase is found to be superior to phase-alternating composite pulses (c.f. Fig. 1.11 C-E for a bandwidth of 20 kHz). The number of modulations in the phase marks different subclasses that again correspond to slight steps in Fig. 1.9 A, D. Although no symmetry constraints were imposed in the optimization, pulses of this class are perfectly symmetric around the pulse center. In Fig. 1.12 the phase and frequency of three such pulses is shown. The central smooth frequency sweep is strongly reminiscent of adiabatic pulses, which have a high degree of tolerance to rf inhomogeneity or miscalibration. However, the class of pulses derived here has constant maximum amplitude and therefore shows very low adiabaticity at the pulse edges. Instead, a pronounced frequency swing is observed that seems to achieve a similar effect as the amplitude modulation at the edges of adiabatic pulses. In general, the optimized pulses are similar to BIP pulses derived in [39] with only slightly improved inversion properties.

For comparison of the BEBOP and BIBOP pulses with already known excitation and inversion pulses we calculated the quality factor $\mathbf{\Phi}$ for a large number of short published pulses. In all cases we set the maximum rf-amplitude to 10 kHz for consistent results. In addition, we set up comparisons without considering rf-amplitude variation and con-
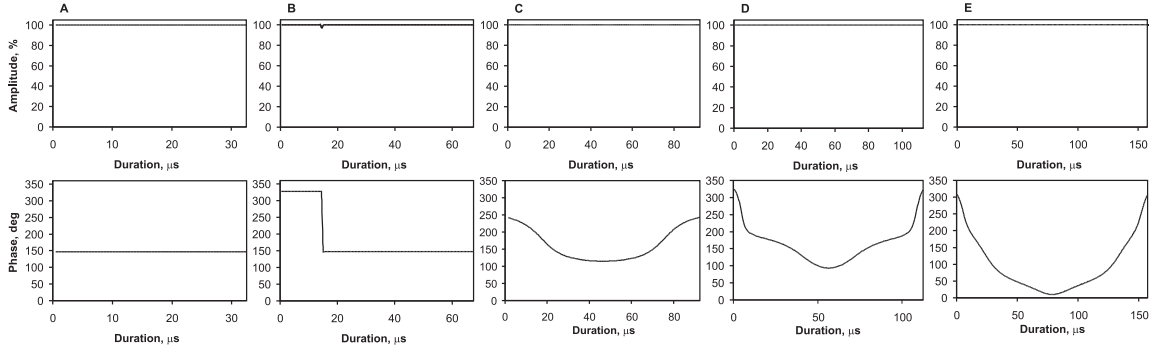
Figure 1.11: Amplitude and phase behavior for optimal inversion pulses of various durations found for an optimization bandwidth of 20 kHz and no rf-variation. Constant amplitude pulses were obtained for all pulse lengths. While hard and phase-alternating composite pulses appear to be optimal for very short durations (pulses shown in A,B correspond to 112.5°_x and $\{52^\circ_x, 191^\circ_{-x}\}$), a symmetric class of pulses with smooth phase modulations seems to be optimal for pulse lengths longer than 70 μs.

sidering a variation ϑ of ± 20 %. For all pulses we numerically determined the maximum bandwidth in which the quality factor $\mathbf{\Phi}$ reaches 0.98. In detail, composite pulses we used for comparison were taken from [18, 40, 41] for excitation and from [18, 41–45] for inversion. In addition we derived optimum sech/tanh and tanh/tan adiabatic pulses for several bandwidths as described in [46] and implemented most of the BIP inversion pulses [39]. The results are shown in Fig. 1.13: In the case of excitation no pulse reaches the performance of BEBOP pulses, considering variations in rf-amplitude none of the tested pulses does reach a quality factor of 0.98 (Fig. 1.13 A,B). In the case of broadband inversion, only the $90_y 240_x 90_y$ pulse [18] achieves the limit when no rf-variation is considered (Fig. 1.13 C). As shown in Fig. 1.13 D, the BIP pulses [39] closely approach the limits found by our algorithm if rf-amplitude variations of ± 20 % are included in the calculations.

Some of the limitations to the applicability of the presented BEBOP and BIBOP pulses should be pointed out. All pulses are optimized starting with initial $\pm M_z$ magnetization. The pulse is not defined for any other starting magnetization. However, if a BEBOP pulse shall be used to transfer M_x magnetization to M_z, the time reversed pulse shape can be used. In addition, as with most other optimized excitation and inversion pulses, BEBOP and BIBOP pulses do not result in uniform unitary rotations. Initial magnetization components different from M_z will not be transfered the same way as a hard pulse would do. BIBOP pulses therefore cannot be used as refocussing pulses. The refocussing of a single transverse magnetization component (e.g. $-M_x$) can be achieved by the application of two pulses, first a time-reversed and 180° phase shifted BEBOP pulse and then the original BEBOP pulse. In this case the magnetization component is refocussed in two steps: $-M_x \rightarrow M_z \rightarrow M_x$.

BEBOP and BIBOP pulses are, of course, scalable in the same way as conventional pulses. A pulse applied with twice the rf-amplitude will have half the duration and cover
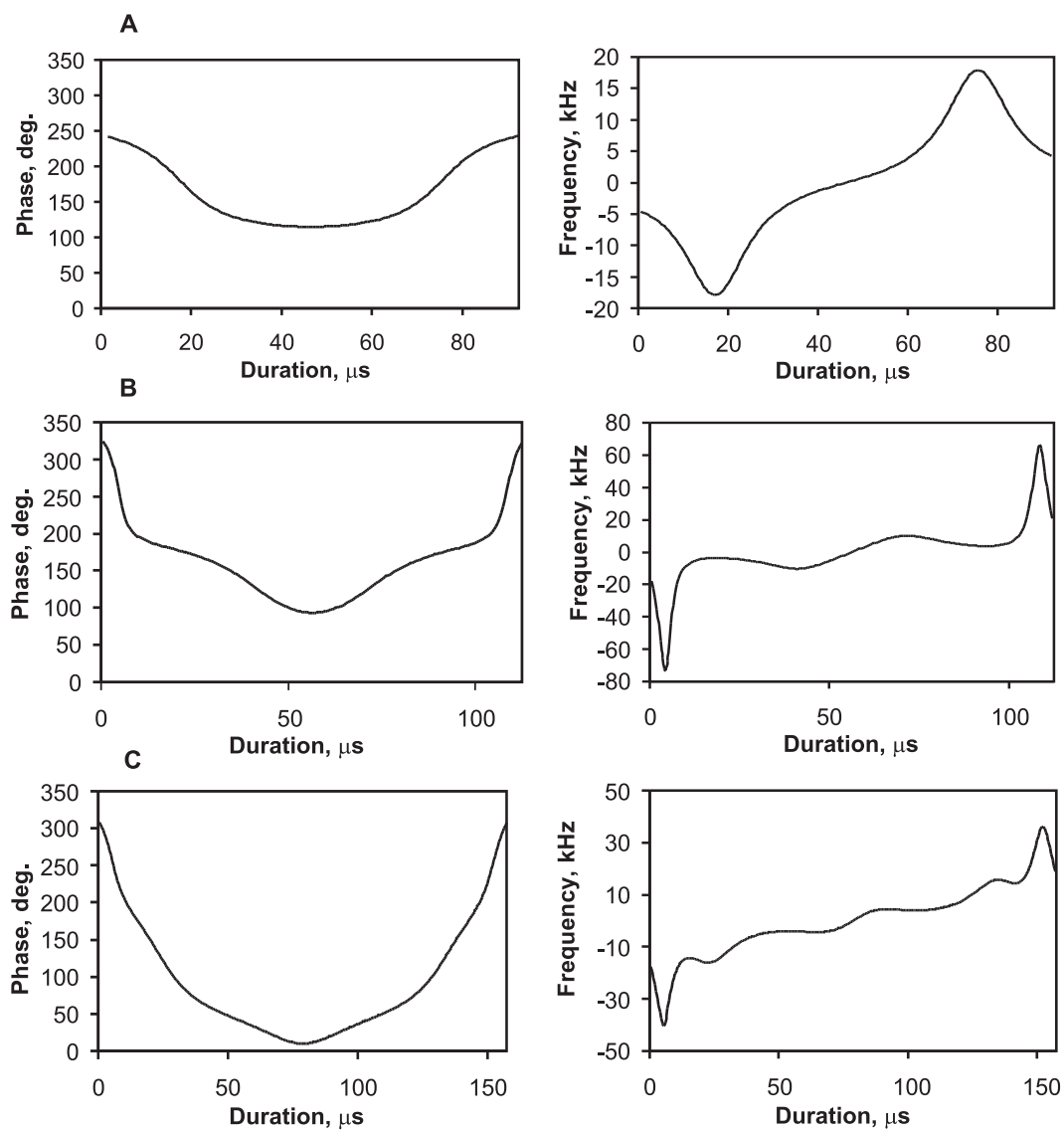
Figure 1.12: The phase behavior of the pulses shown in Fig. 1.11 C-E has been converted to frequency modulation for comparison. A symmetric non-linear frequency sweep is observed. While the frequency sweep observed in the pulse center is reminiscent of adiabatic pulses, the swings at the pulse edges are not of high adiabaticity.
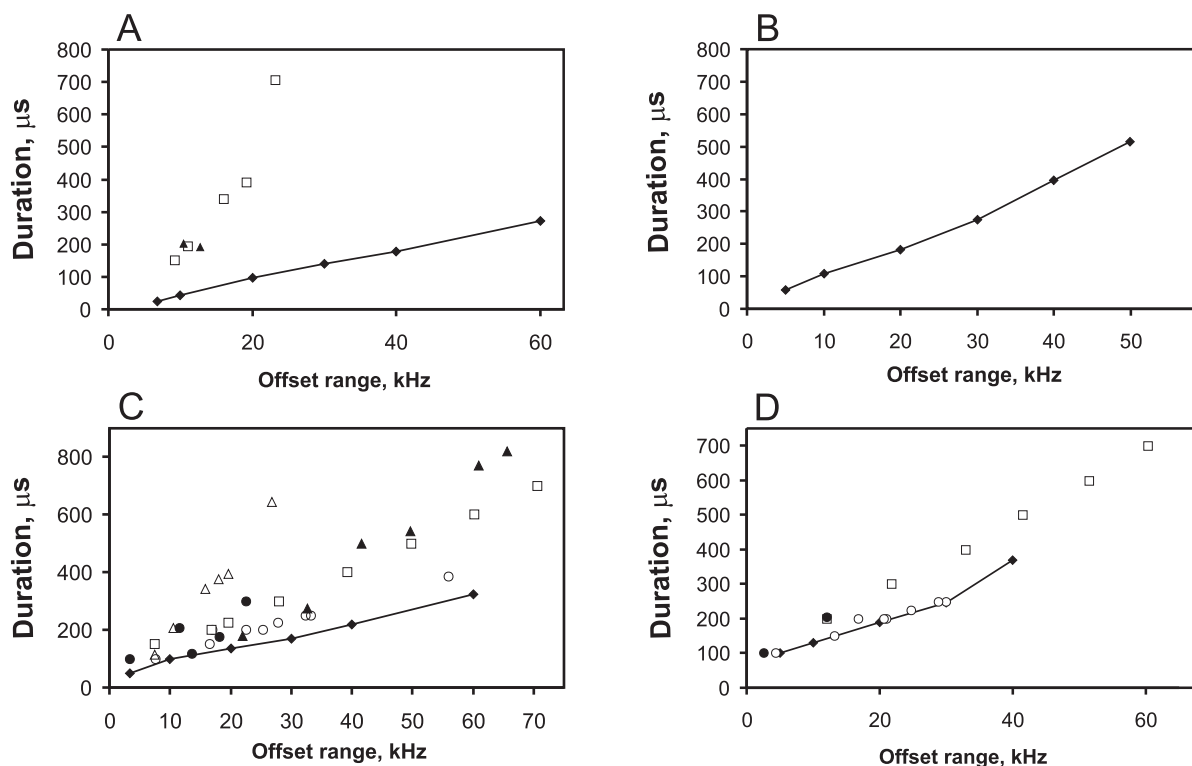
Figure 1.13: Comparison of the maximum bandwidths with a quality factor Φ of 0.98 for previously reported broadband excitation (A,B) and inversion pulses (C,D) relative to BEBOP and BIBOP pulses obtained here. BEBOP and BIBOP pulses are indicated by filled diamonds which are connected by solid lines. (A) For excitation, BEBOP pulses were compared with pulses from [41] (squares) and other pulses cited in [47] from original references [18, 40] (filled triangles). (B) By taking a rf-variation of ± 20 % into account, none of the composite pulses reached a quality factor of 0.98. (C) Inversion pulses compared to BIBOP were taken from [44] (filled triangles), [41] (open triangles), [39] (open circles), [46] (open squares), and other inversion pulses cited in [47] from original references [18, 42, 43, 45]. Only a $90_y 240_x 90_y$ pulse reaches the performance of BIBOP pulses. (D) The same comparison including ± 20 % rf-variation. Only few composite pulses, adiabatic and BIP pulses reach a quality factor of 0.98. The shapes of the BIP pulses [39] are almost identical to the optimum BIBOP pulses.

twice the bandwidth of the original pulse with the same robustness with respect to relative variations of the rf-amplitude. The data presented will therefore be useful as an estimate for most pulse requirements.

Besides practical aspects on the application of pulses in modern spectroscopy some theoretical aspects of this study should be noted. The length of a well B_1-field compensated excitation pulse exceeds the time of an equally well compensated inversion pulse. We therefore conclude that a controlled phase in the transverse plane in the presence of B_1-field inhomogeneity is a rather difficult task especially if the bandwidth exceeds the maximum allowed rf-amplitude. Compensation for variation in rf-amplitude introduces phase modulation already for pulses of the length of a hard 90° pulse and amplitude modulation for slightly longer pulses. It seems that the phase-alternating composite pulses obtained from broadband studies therefore are a result of the bandwidth only, while B_1-compensation could be better achieved by smooth phase and amplitude changes.

Finally, for relatively short inversion pulses a symmetric class of pulses with constant amplitude appears to be optimal. The pulses show a frequency sweep similar to adiabatic pulses in the center but a distinct 'frequency swing' at the pulse edges and closely resemble the BIP pulses [39].

1.3.4 Constant amplitude pulses

The BEBOP pulses obtained to date and demonstrated above exhibit nearly ideal performance, but their rapid and extreme amplitude jumps can require some monitoring and adjustment of system hardware, primarily with regard to amplifier linearity and accurate output of the waveform generators. It was demonstrated that this is not a problem for modern NMR-consoles with linearized amplifiers and fast amplitude and phase switching times. For NMR-spectrometers equipped with non-linearized amplifiers, however, constant amplitude pulses would be more convenient. In addition, encouraged by the success of optimal control theory in designing broadband pulses with outstanding performance, we therefore consider a problem which has been resistent to a successful solution: nearly calibration-free broadband excitation. To accomodate the majority of ^{13}C probes in use, the pulse should operate equally well for a peak RF output anywhere in the range 10–20 kHz (25–12.5 μs pulse width).

As was shown above, for a given bandwidth and tolerance to RF variability, an optimal control algorithm which allows amplitude and phase modulation and limits the maximum RF amplitude produces a purely phase-modulated pulse when the pulse length is reduced below a certain level – the algorithm pins the RF to its maximum allowed value at all times during the pulse in attempting to optimize pulse performance. For longer pulse lengths, the algorithm is able to converge to a solution using lower, time-variable values of the amplitude without having to consider larger RF values. Instead of reducing pulse length by trial-and-error until constant amplitude pulses are found, it is more efficient to derive them directly. The algorithm described above only needs to be slightly modified to perform such kind of task. For a constant amplitude phase-modulated pulse, ω_1 in Eq. 1.18 is time-independent and the only control is the phase, ϕ. Plugging $\boldsymbol{\omega}_e$ from Eq. 1.18
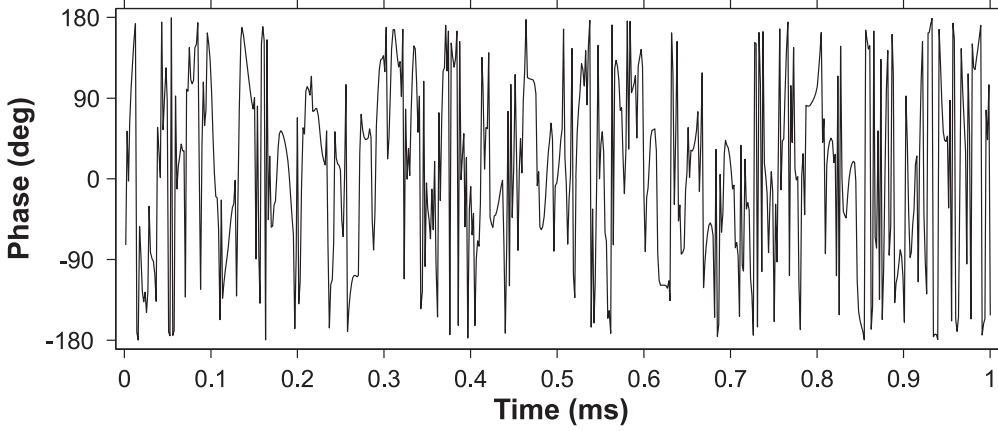
Figure 1.14: Phase modulation of the constant amplitude 1 ms PM-BEBOP pulse. This pulse performs the point-to-point transformation $I_z \rightarrow I_x$ over a 50 kHz range of resonance offsets for constant RF amplitude set anywhere in the range 10 - 20 kHz

into Eq. 1.27 and setting $\partial h/\partial \phi = 0$ gives, together with the previous conditions on the evolution of $\boldsymbol{M}$ and $\boldsymbol{\lambda}$, the same requirements to optimize the cost, as in Eqs 1.29, 1.30, while instead of Eq. 1.31 we now have

$$\boldsymbol{\omega}_{\mathrm{rf}} \cdot \left(\boldsymbol{\lambda} M_z - \boldsymbol{M} \lambda_z \right) = 0. \tag{1.56}$$

The algorithm, modified with accordance to this condition, now has the following form:

1. Choose an initial RF sequence $\boldsymbol{\omega}_e^{(0)}$.

2. Evolve $\boldsymbol{M}$ forward in time from the predefined initial state $\boldsymbol{M}(t_0)$.

3. Evolve $\boldsymbol{\lambda}$ backwards in time from the predefined target state $\boldsymbol{F}$.

4. $\boldsymbol{\omega}_e^{(k+1)}(t) \longrightarrow \boldsymbol{\omega}_e^{(k)}(t) + \epsilon \boldsymbol{\omega}_{\mathrm{rf}} \cdot \left(\boldsymbol{\lambda} M_z - \boldsymbol{M} \lambda_z \right)$

5. Repeat steps 2 - 4 until a desired convergence of Φ is reached.

Since the optimization is performed over a range of chemical-shift offsets and variations in the peak RF calibration, the gradient used in step 4 is averaged over the entire range.

Pulse performance, in general, depends on the pulse duration, with pulses of sufficient length giving the optimal control algorithm the flexibility to obtain practically ideal results in many cases. In addition, as shown in the previous section, excitation (and inversion) efficiency undergoes a steep drop in performance below a minimum pulse length, which depends on the parameters defining the optimization. Increasing pulse length significantly above this minimum provides only marginal improvement, so the shortest pulse that provides acceptable performance is the goal. Choosing 2 ms for the pulse length initially and optimizing with the new algorithm provided a pulse that transforms 99.9% of initial

z magnetization to within 1.5° of the x-axis over a resonance offset range of 50 kHz for a constant RF amplitude anywhere in the range 1020 kHz. This nearly ideal performance can be traded for shorter pulse length. Since performance drops rapidly for shorter pulses, we find that overdigitizing the initial waveform used in the optimal control procedure gives the algorithm additional flexibility in finding the best solution. Every other point of the resulting pulse is used as the initial input for generating a new pulse, and this procedure is continued until a minimal digitization with acceptable performance is reached. For a 1 ms pulse length, 320,000 random phases were input initially ($\sim$3 ns per time step). Such a large number of parameters would be extremely difficult, if not impossible, to optimize using conventional methods. This breeder pulse resulted in the final 625-point pulse shown in Fig. 1.14.

Experimental excitation profiles were implemented on Bruker Avance spectrometers equipped with SGU units for RF control and linearized amplifiers. For testing the performance of the phase modulated BEBOP pulses a sample of 99.96% D_2O was doped with $CuSO_4$ to a final T_1 relaxation time of $\sim$500 ms. To reduce effects of B_1-field inhomogeneity, approximately 40 μl of this solution was placed in a Shigemi limited volume tube. The maximum RF amplitude was calibrated using a square shaped pulse. Offset profiles were then obtained by varying the offset of the shaped pulses from -27 kHz to 27 kHz in steps of 1 kHz. In order to also monitor the B_1-field dependence of the pulses, the experiments were repeated with $\pm$1, $\pm$2, and $\pm$3 dB attenuation relative to a central RF amplitude, corresponding to RF amplitudes of 10.0, 11.2, 12.6, 14.1, 15.8, 17.8, and 20.0 kHz. The results are shown in Fig. 1.15. The experimental data represent a considerable improvement over the maximum attainable performance of a phase-corrected hard pulse, opening the door to practically calibration-free excitation pulses.
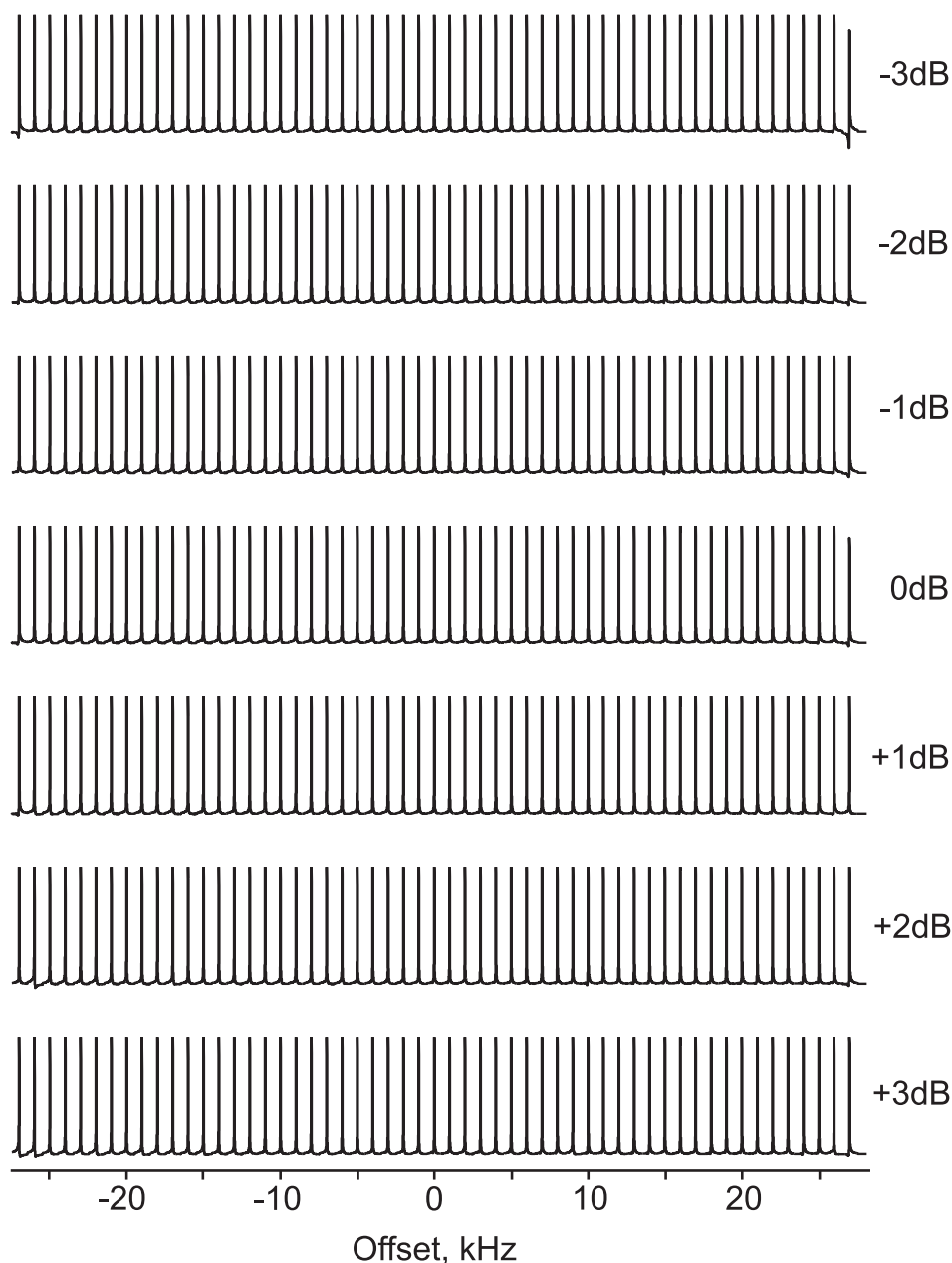
Figure 1.15: Excitation profiles for the residual HDO signal in a sample of 99.96% D_2O are displayed as a function of resonance offset (1 kHz increments) and RF power levels applied using the 1 ms PM-BEBOP pulse of Fig. 1.14. The pulse with nominal RF amplitude of 15 kHz was applied with constant amplitudes of 10 kHz (+3 dB), 11.2 kHz (+2 dB), 12.6 kHz (+1 dB), 14.1 kHz (0 dB), 15.8 kHz (-1 dB), 17.8 kHz (-2 dB), and 20 kHz (-3 dB). The experimental performance of the pulse is in excellent agreement with theory, producing practically perfect excitation, $M_x > 0.99\,M_0$, over ± 25 kHz for RF variability within 6 dB ($\pm 33.3\%$) of the nominal value.

1.4 Power limited pulses

1.4.1 Theory

Fundamental limitations comes to the fore, whenever one wants to apply a train of rf-pulses, which is indispensable in most pulse sequences used in modern applications of NMR spectroscopy. Such essential building blocks of many pulse sequences as spin lock, homo- and heteronuclear Hartmann-Hahn transfer or any kind of decoupling sequence are nothing else than more or less long pulse trains. Whenever one uses such elements in a pulse sequence, extreme care should be taken when setting their power level in order not to damage the probehead or amplifier.

It is therefore of utmost importance to optimize pulses or pulse trains, which provide the best available performance for e.g. excitation or inversion for a given average rf-power.

The algorithm described in previous sections only needs to be slightly modified to perform this task. The procedure for optimizing the cost, subject to the constraint that the average rf-power of the pulse be no greater than a chosen maximum power is very similar to that for optimizing pulses with limited rf-amplitude (see paragraph 1.3.2), with the only significant difference, that the root mean square value ω_{rms} of the piecewise constant rf-amplitude has to be calculated for the pulse shape as a whole and is checked to be less then the predefined limit:

1. Choose an initial rf sequence $\boldsymbol{\omega}_e^{(0)}$.

2. Evolve $\boldsymbol{M}$ forward in time from the predefined initial state $\boldsymbol{M}(t_0)$.

3. Calculate $\boldsymbol{M}(t_p) \times \boldsymbol{\lambda}(t_p)$ and evolve it backwards in time.

4. $\boldsymbol{\omega}_e^{(k+1)}(t) \longrightarrow \boldsymbol{\omega}_e^{(k)}(t) + \epsilon[\boldsymbol{M}(t) \times \boldsymbol{\lambda}(t)]$.

5. Calculate $\omega_{rms} = \sqrt{\frac{\sum_{i=1}^{n} \omega_i^2(t)}{n}}$

6. If $\omega_{rms} > \omega_{rms}^{def}$, with ω_{rms}^{def} as the defined limit of the root mean square power, then for every $\omega_1(t)$ set $\omega_1(t) \rightarrow \omega_1(t) \cdot \frac{\omega_{rms}^{def}}{\omega_{rms}}$,

7. Repeat steps 2 - 6 until a desired convergence of Φ is reached.

Since the optimization is performed over a range of chemical-shift offsets and variations in peak rf calibration, the gradient used in step 4 is averaged over the entire range.

1.4.2 Optimizations

As was calculated in Section 1.3.3 for the case of pulses with limited rf-amplitude, it would also be useful for pulses with limited average rf-power to know the minimal necessary conditions, like duration and average rf-amplitude, a pulse should meet in order to produce a desired degree of excitation or inversion for a given range of offsets and given tolerance

Table 1.2: Constraints used for optimizations of pulses with limited average rf-power

$\Delta\nu^a$ (kHz)	ϑ^b (%)	t_p excitation (μs)	t_p inversion (μs)
10	—	5 - 45	5 - 105
20	—	5 - 65	5 - 155
30	—	5 - 85	5 - 205
40	—	5 - 105	5 - 265
50	—	5 - 125	5 - 325
10	$\pm$ 10	5 - 95	5 - 135
10	$\pm$ 20	5 - 135	5 - 155
10	$\pm$ 30	5 - 185	5 - 195
10	$\pm$ 40	5 - 235	5 - 245
20	$\pm$ 10	5 - 125	5 - 175
20	$\pm$ 20	5 - 185	5 - 225
20	$\pm$ 30	5 - 255	5 - 295
20	$\pm$ 40	5 - 375	5 - 345
30	$\pm$ 10	5 - 175	5 - 255
30	$\pm$ 20	5 - 245	5 - 305
30	$\pm$ 30	5 - 345	5 - 325
30	$\pm$ 40	5 - 405	5 - 355

^{a}) $\Delta\nu$ is defined as the excitation/inversion bandwidth used in the optimization. ^{b}) ϑ is the range of rf-amplitude scaling incorporated in the optimization.

to rf-power miscalibration. For this purpose a systematic study of the pulse performance was performed with tools of optimal control theory. Sets of excitation and inversion pulses were calculated for bandwidths of 10, 20, 30, 40, and 50 kHz considering ideal rf-amplitude (scale factor of 1). Also sets of pulses for bandwidths of 10, 20 and 30 kHz with variations of ϑ of $\pm$10, $\pm$20, $\pm$30, and $\pm$40 percent in rf scale factor were optimized to test robustness against B_1-field inhomogeneity. In all cases, the root mean square average rf-amplitude was limited to 10 kHz using the method described above. For each set, pulse lengths t_p were varied in ranges as listed in Table 1.2. Generally, pulse durations were incremented until the quality factor $\mathbf{\Phi}$ exceeded 0.995. Each chosen bandwidth was divided into equal increments, with $n_{\text{off}} = 100$. n_{rf} was chosen equal to 5 with equidistant percentage amplitude changes whenever variations in rf-amplitude were included in the calculations. The time digitization for the optimized shapes was 0.5 μs in all cases. One hundred randomized starting pulses were generated to start 100 optimizations for each data point in Figs. 1.16 and 1.17. Like in the case of pulses with limited rf-amplitudes, the convergence of every single optimization was very fast ranging from seconds for the shortest pulses to tens of minutes for the longest ones with larger n_{off} and n_{rf} on a single AMD Athlon 1500+ processor Linux-based PC.

The results of the optimizations of excitation and inversion pulses are shown in Figs.
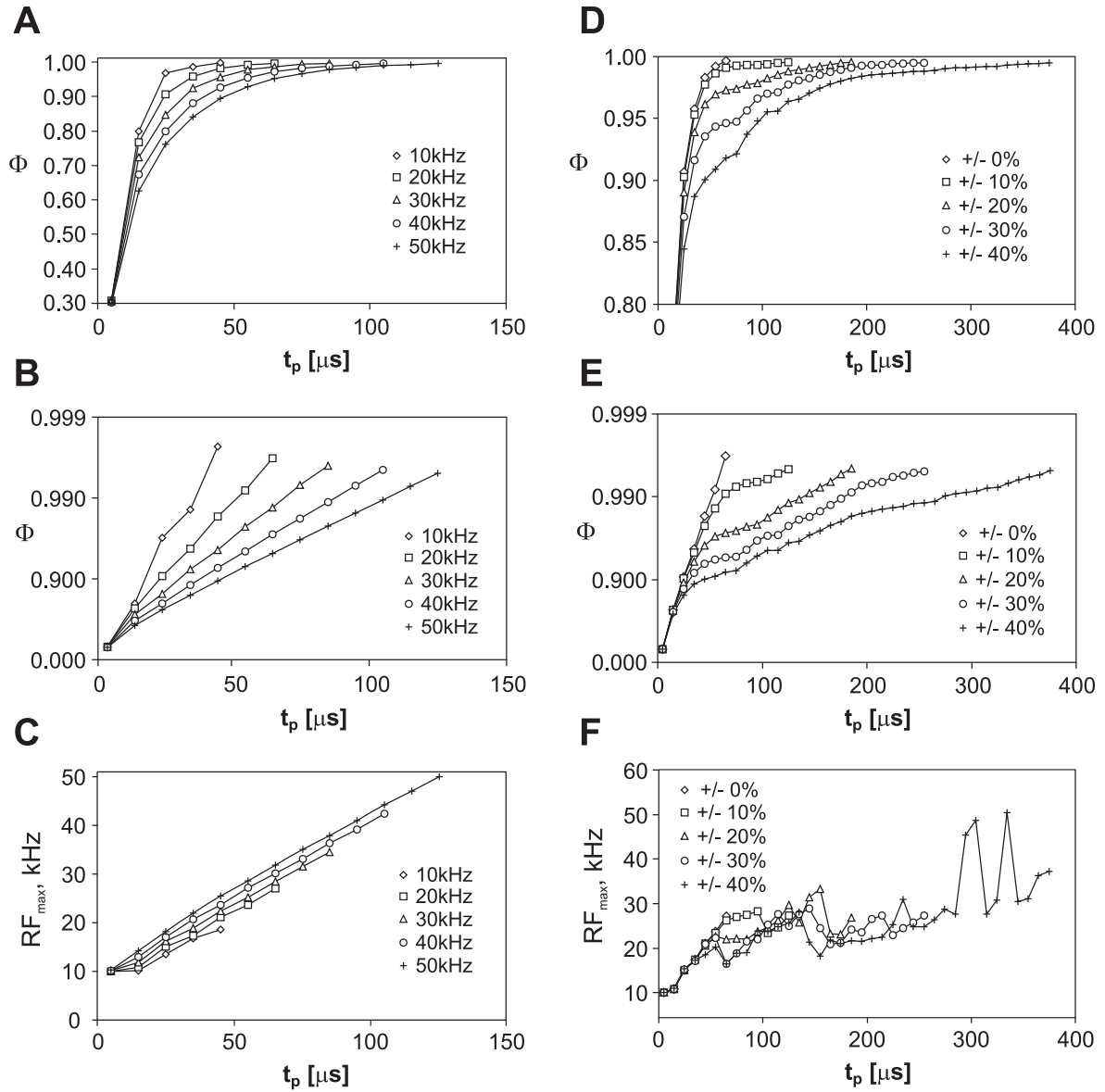
Figure 1.16: Maximum quality factors reached for broadband excitation pulses with *average* rf-power limited to 10 kHz under various optimization constraints. The maximum quality factors Φ with respect to pulse duration is given for the five different bandwidths $\Delta\nu$ equal to 10 kHz, 20 kHz, 30 kHz, 40 kHz, and 50 kHz on a linear (A) and logarithmic scale (B). In C, the values of peak rf-power of corresponding pulses are plotted as a function of pulse length. The maximum quality factors Φ with respect to rf-variation are shown for no variation and rf-ranges ϑ of ± 10 %, ± 20 %, ± 30 %, and ± 40 % on a linear (D) and logarithmic scale (E) for a fixed bandwidth of 20 kHz. In (F),the values of peak rf-power of corresponding pulses are plotted as a function of pulse length.

Figure 1.17: Maximum quality factors reached for broadband inversion pulses with *average* rf-power limited to 10 kHz under various optimization constraints. The maximum quality factors Φ with respect to pulse duration is given for the five different bandwidths $\Delta\nu$ equal to 10 kHz, 20 kHz, 30 kHz, 40 kHz, and 50 kHz on a linear (A) and logarithmic scale (B). In C, the values of peak rf-power of corresponding pulses are plotted as a function of pulse length. The maximum quality factors Φ with respect to rf-variation are shown for no variation and rf-ranges ϑ of ±10 %, ±20 %, ±30 %, and ±40 % on a linear (D) and logarithmic scale (E) for a fixed bandwidth of 20 kHz. In (F),the values of peak rf-power of corresponding pulses are plotted as a function of pulse length.

Figure 1.18: Amplitude and Phase for optimized excitation pulses of various durations with limited power deposition found in the optimization for a bandwidth of 30 kHz and 10% rf-variation. Pulses very similar to the polychromatic pulses [48] were found in all optimizations.

1.16 and 1.17, respectively: The performance of the optimized pulses described by the quality factor **Φ** is given as a function of pulse length on a linear scale in Figs. 1.16 A, D and 1.17 A, D. A logarithmic scale is used in Figs. 1.16 B, E and 1.17 B, E to show the differences at longer pulse durations more clearly. Figs. 1.16 C, F and 1.17 C, F show peak rf-amplitudes in corresponding pulses. As expected, higher demands in terms of bandwidth or tolerance to rf-amplitude variation lead to reduced quality factors that can, however, be compensated by increased pulse lengths. The relation between duration and bandwidth is roughly linear for both types of pulses for the investigated offset and rf ranges.

In contrast to optimizations with limited rf-amplitude, in the case of limited *average* amplitudes the dependence of the quality factor on the pulse duration shows a step or wave-like behavior only for excitation pulses with large toleration to rf-inhomogeneity (c.f. Fig. 1.16 D). In all other cases the corresponding dependencies are all smooth curves. This might suggest, in contrast to the considerations in Section 1.3.3, that all pulses resulting in such optimizations should belong to a single pulse family with eventual exception of pulses optimized to tolerate large rf-inhomogeneities. The detailed inspection of pulse shapes, some typical representatives of which are shown in Fig. 1.18 for excitation, shows that they indeed all belong to a single pulse family, even the pulses optimized to tolerate large rf-inhomogeneities. The shortest pulses, looking very similar to conventional hard pulses with only slight modulation in amplitude, might at first glance appear different compared to longer pulses. However, a closer look reveals, that they all have shapes similar to the left half of a sinc curve: the shortest pulses being only a small piece of it, with longer pulses accomodating longer "tails" of it. With even longer pulse lengths the phase jumps become smoothened and amplitudes get finer modulations. The sinc shape of the pulses resembles that of polychromatic pulses for wideband excitation described in [48], which, however, were designed without any constraints in power deposition.

Detailed investigation of shapes produced for inversion pulses (c.f. Fig. 1.19) reveals,
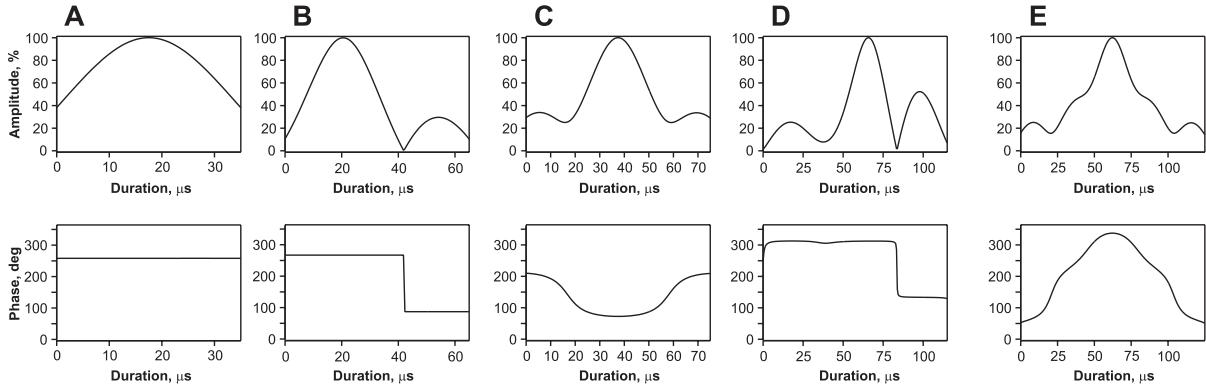
Figure 1.19: Amplitude and phase behavior for optimal inversion pulses of various durations with limited power deposition found for an optimization bandwidth of 30 kHz and 10% rf-variation. Two major pulse classes are observed: phase-alternating pulses and pulses with smooth adiabatic-like phase, in both cases with smoothly varying amplitudes.

that basically only two families emerge. One family consists of pulses with few periods with constant phase with every such period having smoothly modulated amplitude, as a rule with one distinct maximum in the center of the period. The other family resembles inversion pulses optimized in section 1.3.3 (c.f. Fig. 1.11) and the so-called BIP pulses [39] with smoothly modulated amplitudes. The pulses of the second family are very similar to pulses derived in [49] for optimized decoupling at low power levels with essentialy identical requirements. Interesting is, that the two pulse families are not chracteristic for certain pulse length regions, like they are for pulses with limited rf-amplitude, causing their stepwise appearance of the performance curve. The representatives of both families can be met among pulses of any length.

Figures 1.20 and 1.21 show the performance curves of power limited pulses with those of pulses optimized with limited amplitudes and same average power. Clearly, the pulses with limited average rf-amplitude are generally better performing. The maximum difference is achieved for excitation pulses with large offsets. The differences for inversion pulses are generally less prominent. The introduction of rf-inhomogeneity further reduces the differences in performance.
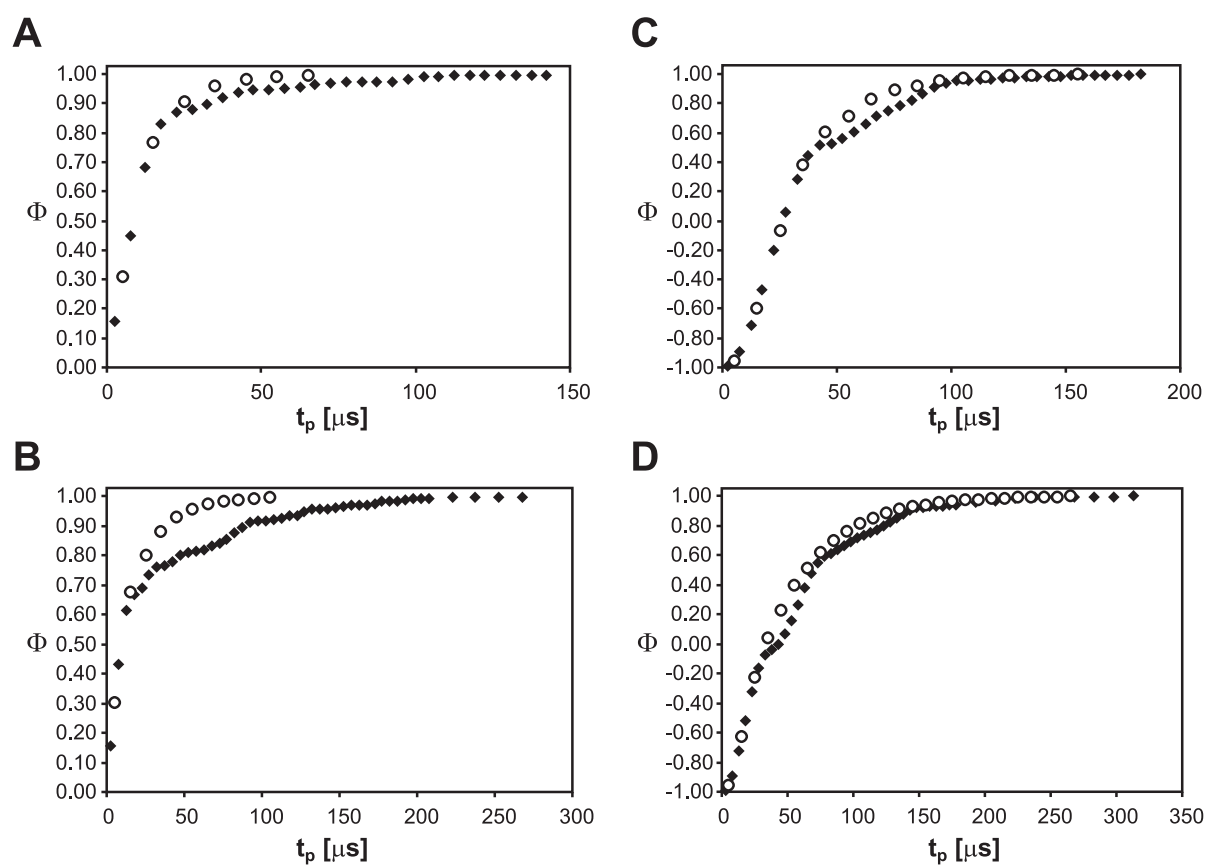
Figure 1.20: Comparison of maximum quality factors of power limited pulses (circles) with quality factors of pulses optimized with limited rf-amplitude (filled diamonds, same as in Figs. 1.8 and 1.9) for excitation (A, B) and inversion (C, D) pulses and offset ranges of 20 kHz (A, C) and 40 kHz (B, D).
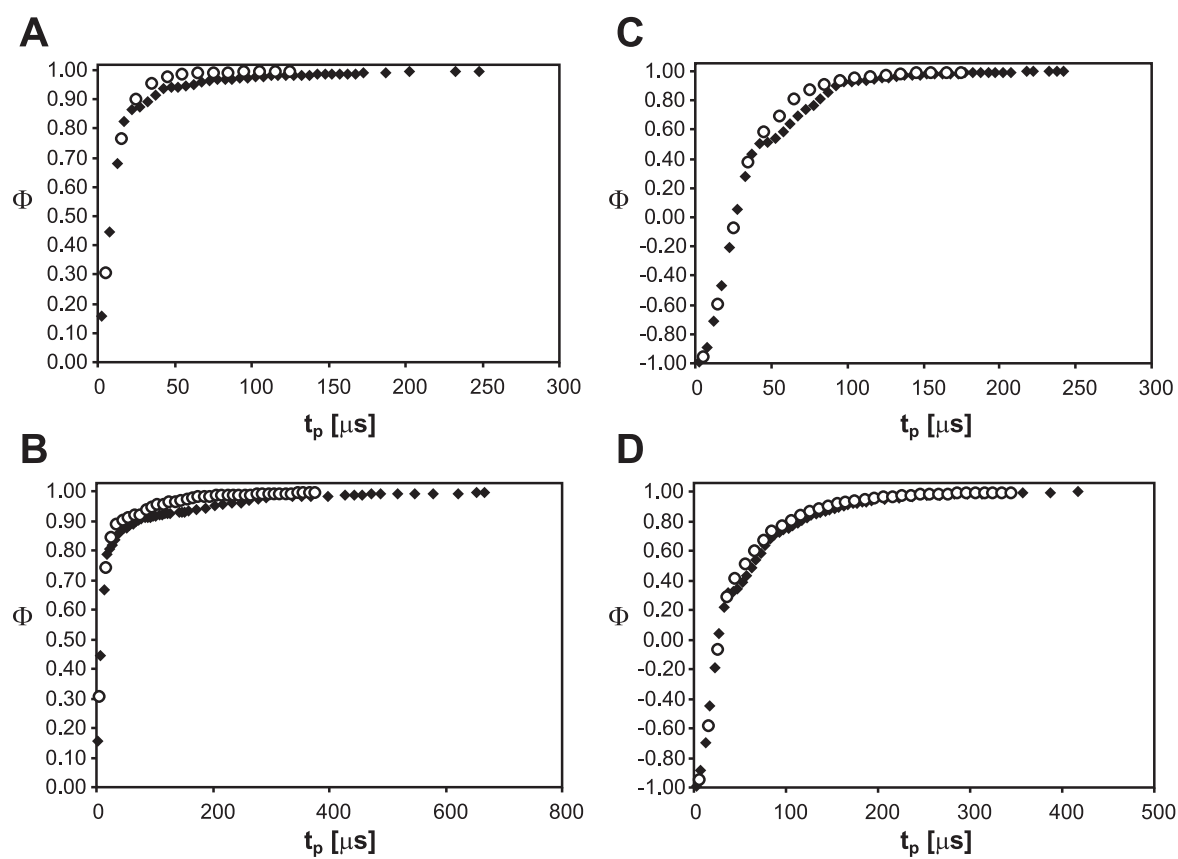
Figure 1.21: Comparison of maximum quality factors of power limited pulses (circles) with quality factors of pulses optimized with limited rf-amplitude (filled diamonds, same as in Figs. 1.8 and 1.9) for excitation (A, B) and inversion (C, D) pulses and rf-inhomogeneity ranges of $\pm 10\%$ (A, C) and $\pm 40\%$ (B, D).

1.5   Pattern pulses

Radiofrequency pulses with the only effect of effective excitation or inversion of some range of chemical shift offsets are by no means the only kind of pulses used in modern NMR. Pulses with specifically defined excitation or inversion profiles have a long history in NMR [18,19,50–53]. Not only pulses which are broadband with respect to offset and/or rf amplitude, but also selective and band-selective pulses have found numerous applications in NMR spectroscopy and imaging. A particularly powerful approach for the design of such pulses is based on principles of optimal control theory [2,13,15,54], which make it possible to optimize a large number of pulse-sequence parameters very efficiently. We managed to design the pulses which create arbitrary excitation patterns as a function of offset and rf amplitude.

1.5.1   Theory

Here, we use essentially the same algorithm as described in section 1.3.2 and restrict the following discussion to excitation pulses that create x magnetization if applied to initial z magnetization. However, the results can be immediately generalized to other pulses, such as saturation or inversion pulses. (In fact, the design of selective inversion pulses is generally considered to be an easier problem than the design of selective excitation pulses [51,55].)

For conventional pulses, the desired excitation profile as a function of offset (ν_0) and rf amplitude (ν_1) typically has the form of a rectangle. The width $\Delta\nu_0$ of this rectangular profile corresponds to the bandwidth of frequency offsets to be covered, whereas the height $\Delta\nu_1$ of the rectangle specifies the range of rf amplitudes ν_1 for which the pulse is expected to be functional. For example, for a broadband excitation pulse which is also robust with respect to rf amplitude variations due to pulse miscalibration or due to rf inhomogeneity, both $\Delta\nu_0$ and $\Delta\nu_1$ should be large, see e.g. [34,36,51,55–57]. In contrast, for offset-selective or rf amplitude-selective pulses, $\Delta\nu_0$ or $\Delta\nu_1$ should be small, respectively [19,51,55,58–66]. However, as shown below, it is possible to create much more sophisticated patterns of excitation as a function of ν_0 and ν_1.

In Fig. 1.22 A-D, a series of simple test patterns is shown. In these examples, the test patterns were specified as the desired orientation of the target magnetization vector M_t after the pulse (white: $M_t = (1,0,0)$, black: $M_t=(0,0,1)$) on a grid of N_0 equally spaced offsets ν_0 between -5 kHz and $+5$ kHz (but ± 10 kHz in Fig. 1 B) and N_1 equally spaced rf amplitudes ν_1 between 6 kHz and 14 kHz. Here, the $N_0 \times N_1$ grid of offsets and rf amplitudes, for which the desired M_x component was specified, was chosen to be 40×16 (Fig. 1.22 A), 105×10 (Fig. 1.22 B), and 40×10 (Fig. 1.22 C, D).

Fig. 1.22 A represents an excitation profile that is band-selective with respect to rf amplitude (9 kHz $\leq \nu_1 \leq$ 11 kHz) and broadband with respect to offset (-5 kHz $\leq \nu_0 \leq$ 5 kHz). Conversely, Fig. 1.22 B represents a profile that is narrowband with respect to offset (-1 kHz $\leq \nu_0 \leq$ 1 kHz) and broadband with respect to rf amplitude (6 kHz $\leq \nu_1 \leq$ 14 kHz). Figures 1.22 C and D represent more general excitation patterns that cannot be

specified by a rectangular excitation region with bandwidths $\Delta\nu_0$ and $\Delta\nu_1$. The pattern in Fig. 1.22 C corresponds to a pulse that excites spins at different offsets, depending on the rf amplitude. In particular, here the desired excitation freqency ν_0 was proportional to ν_1. Conversely, the pattern in Fig. 1.22 D excites x magnetization for all combinations of ν_0 and ν_1 in the given range, except for offsets that are proportional to the rf amplitude.

For these target patterns, we optimized rf pulses using the general optimal control based gradient ascent strategy with the cost [57]

$$\Phi = \sum_{\nu_0} \sum_{\nu_1} \| \boldsymbol{M}_t(\nu_0, \nu_1) - \boldsymbol{M}_f(\nu_0, \nu_1) \|^2, \qquad (1.57)$$

where $\boldsymbol{M}_f$ is the final magnetization vector after a given pulse, $\boldsymbol{M}_t$ is the target vector, as specified in Fig. 1.22 A-D. Other cost functions can, in principle, be used as well. In general, larger pulse durations result in larger flexibility of the achievable excitation pattern. We have chosen pulse durations of 2, 3, 5, and 5 ms. Each pulse was digitized in steps of 0.5 μs and the x and y amplitudes of all subpulses were optimized [34,36]. For example, for a pulse duration of 5 ms, this corresponds to 20000 optimization parameters. The amplitude and phase functions $s(t)$ and $\phi(t)$ of the resulting pulses are shown in Figs. 1.23 A-D. The performance of the optimized pulses was first analyzed by simulating the excitation profiles numerically for the same range of offsets and rf amplitudes as in Figs. 1.22 A-D (but on a finer grid of 100×21 combinations of ν_0 and ν_1). In all cases, a reasonable match is found between desired and simulated excitation profiles.

The examples shown in Fig. 1.22 suggest that the power and flexibility of the optimum control gradient ascent algorithm will allow to create arbitrary excitation patterns, provided the specified pulse duration is suffiently long. As a non-trivial test case, we specified the more complex pattern shown in Fig. 1.24. Here, the target pattern was defined on a grid of $N_0 = 120$ equally spaced offsets ν_0 between $\pm$ 10 kHz and $N_1 = 20$ equally spaced rf amplitudes between 6 kHz and 14 kHz. A pulse with a duration of 5 ms was optimized (data not shown), which created the simulated excitation pattern shown in Fig. 1.24 B. Analogously, some other complicated excitation patterns were successfully realized, as Figs 1.25, 1.26 show.

1.5.2 Experimental

The new pattern pulses were tested experimentally using a sample of 99.96% D_2O doped with $CuSO_4$ to a final T_1 relaxation time of $\sim$ 500 ms. To reduce effects of B_1 field inhomogeneity, approximately 40 μl of this solution was placed in a Shigemi limited volume tube. The experiments were performed on a Bruker DMX 900 spectrometer equipped with modern SGU units for RF control and linearized amplifiers.

We used two different approaches to acquire the experimental ν_0-ν_1 pattern of a given pulse. In the first approach, which, for example, was used to acquire excitation profiles on Fig. 1.26 B, a spectrum of the sample is acquired for each combination of ν_0 and ν_1. The resulting peak amplitude as a function of offset and rf amplitude respresents the experimental excitation pattern. For example, for N_0=41 offset values and N_1=20
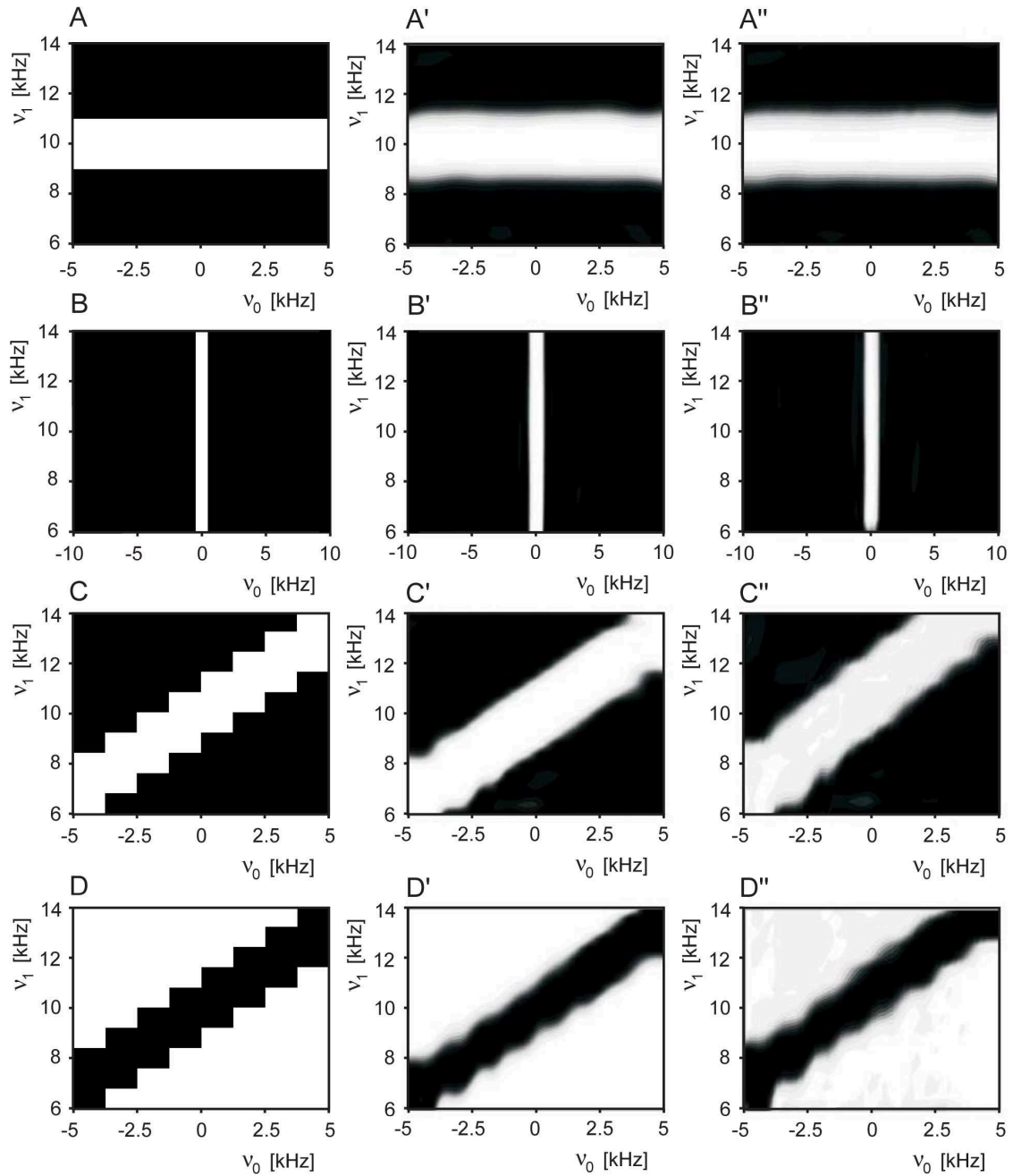
Figure 1.22: Simple target patterns as a function of offset ν_0 and maximum rf amplitude ν_1 are shown in A-D. For initial z magnetization, the desired orientation of the target magnetization vector $\boldsymbol{M}_t$ after the pulse is color coded: (white: $\boldsymbol{M}_t = (1,0,0)$, black: $\boldsymbol{M}_t = (0,0,1)$). For the corresponding optimized pulses shown in Fig. 2, simulated (A'-D') and experimental (A''-D'') excitation profiles are presented, where the grey scale of the contour plots represents the actual x component of the final magnetization vector after the pulse (white: $M_x = 1$, black: $M_x = 0$).
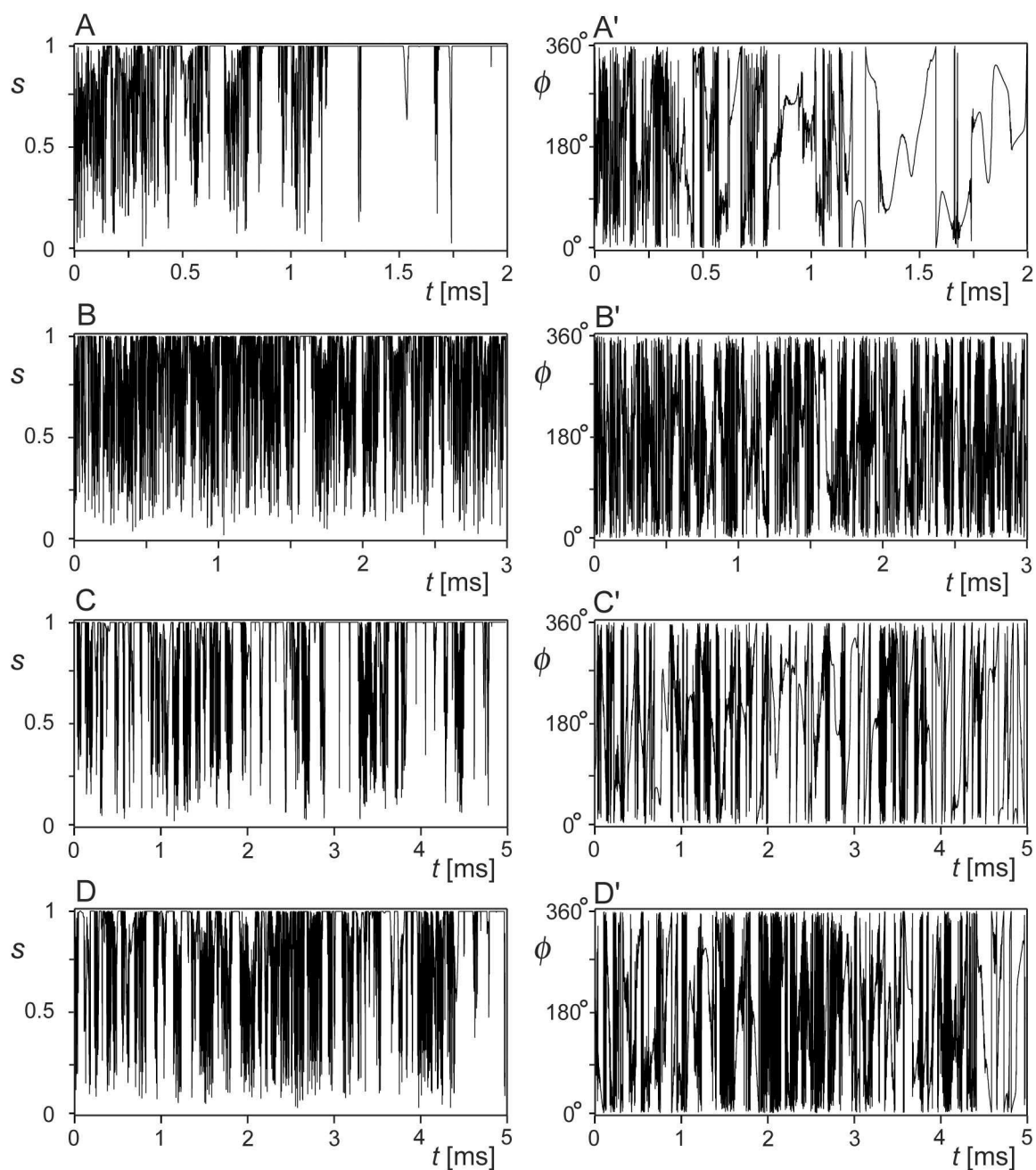
Figure 1.23: Pulse amplitude and phase functions $s(t)$ and $\phi(t)$ of shaped pulses optimized to approach the target patterns shown in Fig. 1.22 A-D.
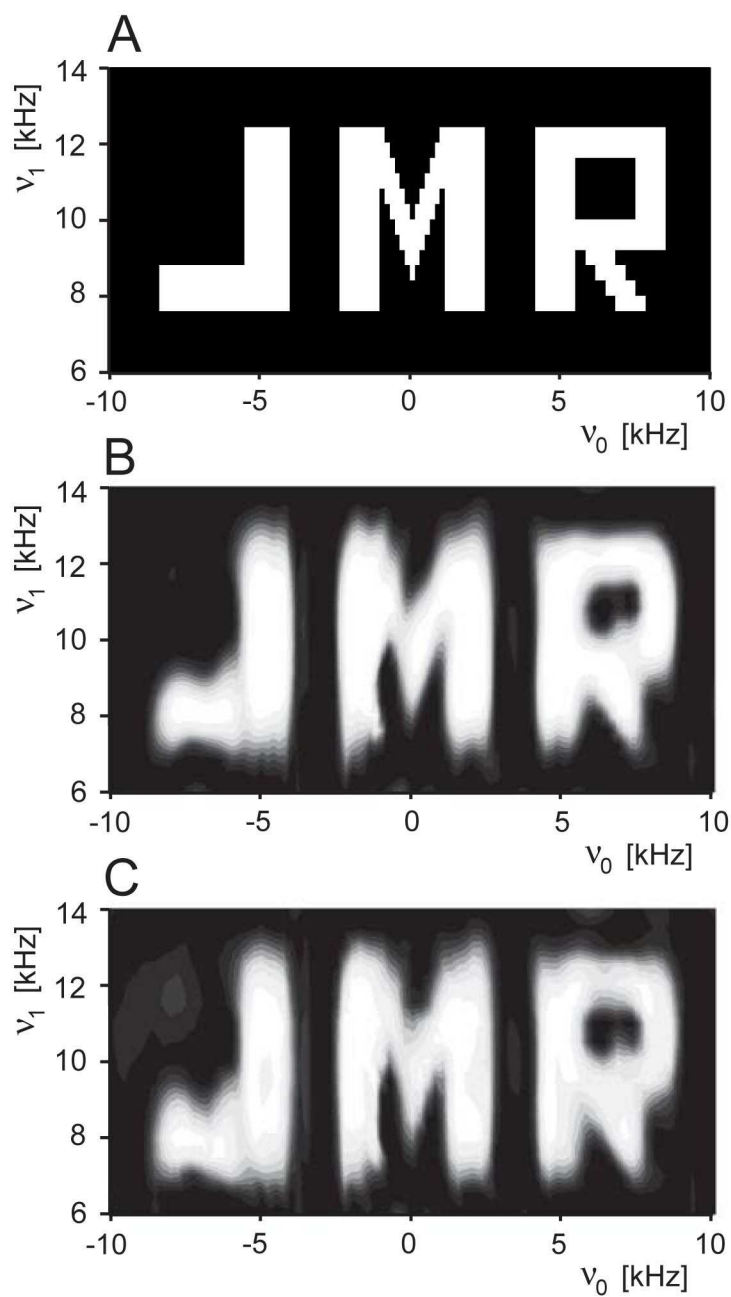
Figure 1.24: More complex target excitation pattern (A) and the corresponding simulated (B) and experimental (C) excitation profile of an optimized pulse.
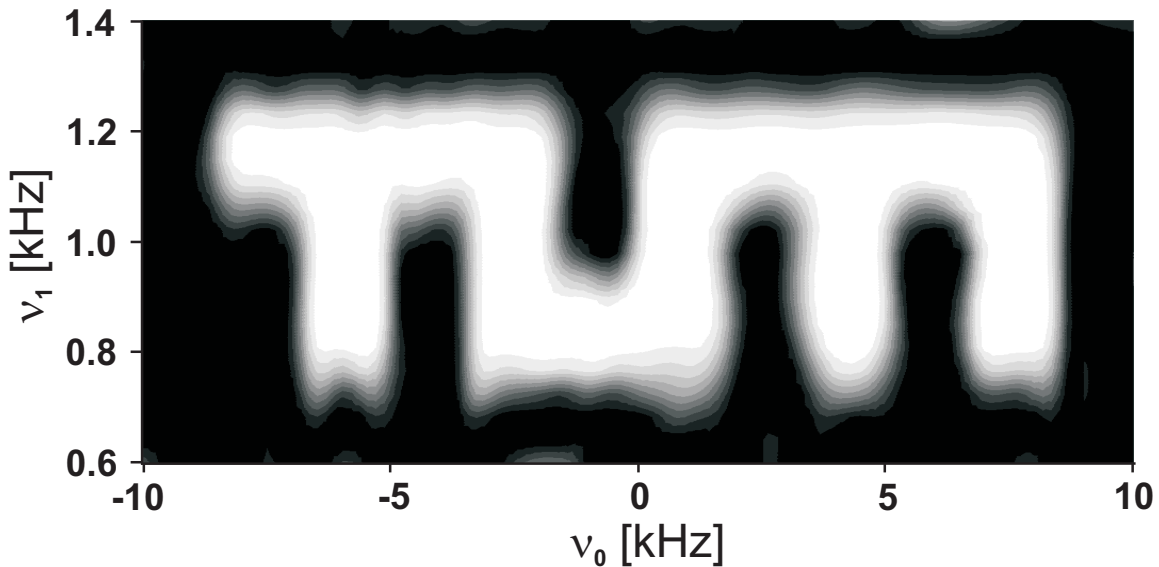
Figure 1.25: Simulated excitation profile of yet another optimized pulse with complex target excitation pattern.

different rf amplitude settings, this requires the acquisition of $N_0 N_1 = 820$ scans. Hence, with a typical delay of 1 s between scans, the acquisition of a detailed two-dimensional excitation pattern requires about 14 minutes.

Alternatively, for each rf amplitude ν_1, the response of the spins can be simultaneously acquired for a desired offset range in a single shot by performing the experiments in the presence of a B_0 field gradient [67, 68]. As we were interested only in the x component of the final magnetization vectors, we used the following variant of the single shot experiment, which is insensitive to imperfect gradient switching (c.f. Fig. 1.28). The experiment exploits the excellent broadband excitation characteristics of BEBOP pulses [34, 36], which have been calibrated and tested on our spectrometer before. Here, we used a BEBOP pulse with a maximum rf amplitude of $\nu_1 = 17.5$ kHz and a duration of 125 μs [57], which transforms z magnetization to x magnetization over a bandwidth of 40 kHz. (For actual calibration experiments, a more robust pulse, such as the 500 μs BEBOP pulse should be used, which is insensitive to ν_1 variations of about $\pm$ 2 dB [36]). Immediately after the shaped pulse of interest is applied to the sample, the resulting x magnetization is flipped to the z axis by a time-reversed BEBOP pulse. Any remaining transverse magnetization is defocused by the gradient during a delay $\delta = 1.2$ ms and finally the stored z magnetization is brought back to the x axis by the BEBOP pulse and is detected. Fourier transformation of the FID yields the excitation profile of the shaped pulse of interest. The single shot approach for each ν_1 setting significantly reduces the time required to measure the experimental excitation pattern as a function of ν_0 and ν_1, e.g. in the example given above, the time is reduced from 14 minutes to only 20 seconds. A disadvantage of the single-shot approach is that distorted patterns can result if B_0
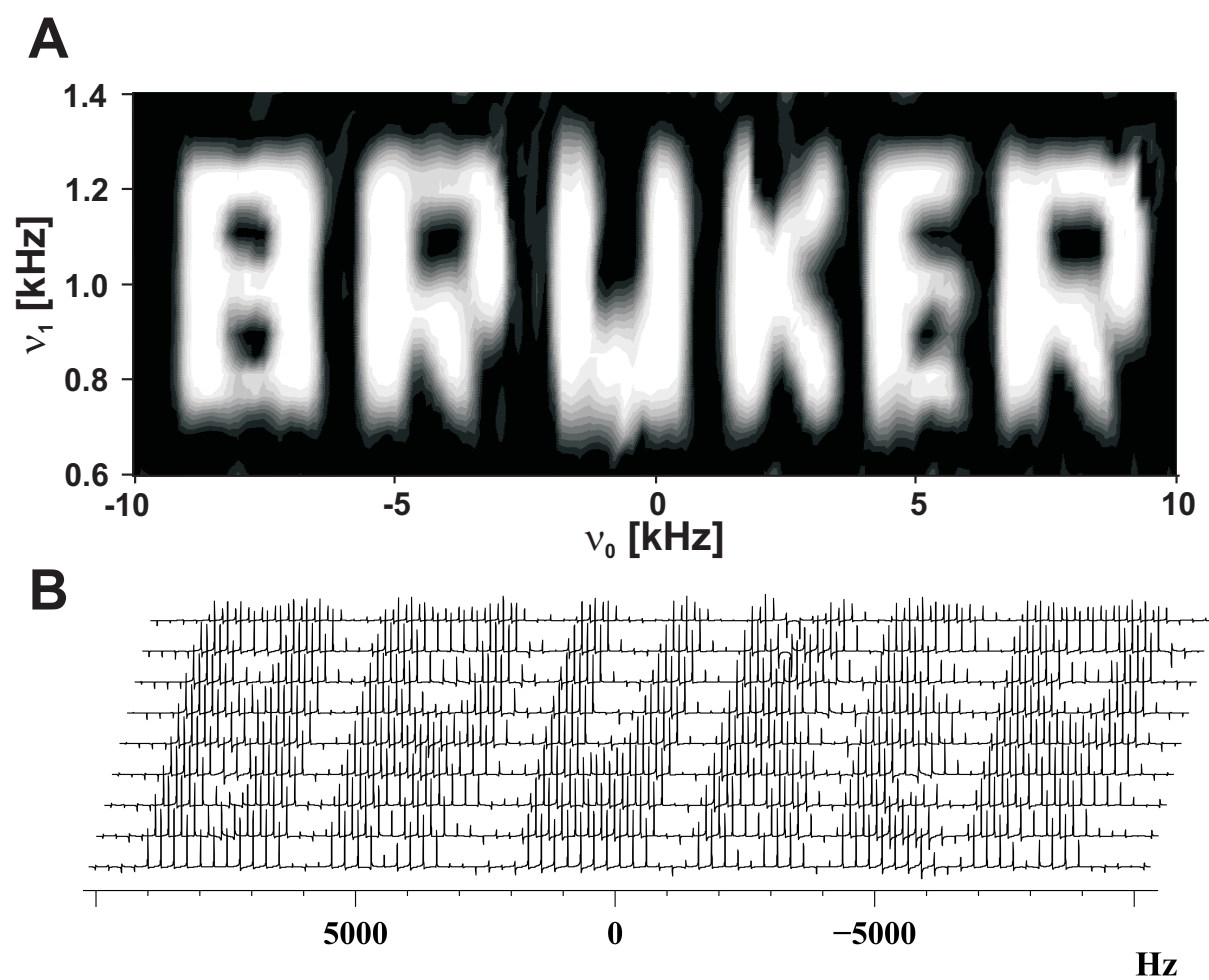
Figure 1.26: Simulated performance of another optimized pulse with complex excitation pattern (A) and the corresponding experimental (B) excitation profile, acquired in a traditional fashion, where each peak is a separetely acquired spectrum for a given combination of ν_0 and ν_1.
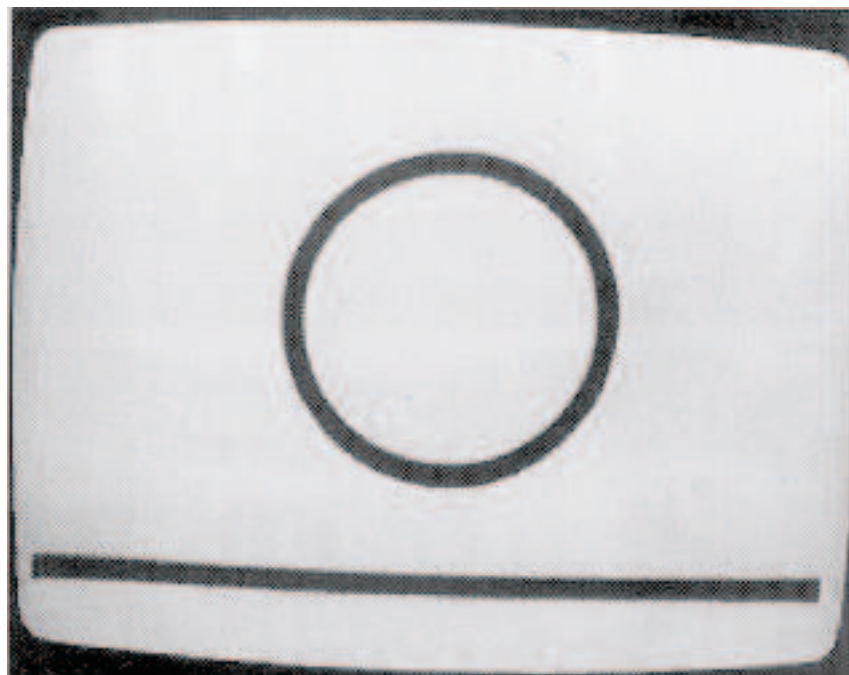
Figure 1.27: Possibly the first ever television test chart, this very simple pattern was broadcast by the BBC in 1934 using Baird's 30 line TV system. Figure taken from *http* : *//www.meldrum.co.uk/mhp/testcard/bbc_tune.html*

gradient and B_1 inhomogeneity are spatially correlated. Conversely, this effect may be useful to measure such correlations.

Figs. 1.22 A″-D″ and 1.23 C show experimental excitation patterns acquired using the first approach for N_0=41 different offsets ν_1 and N_1=17 different rf amplitudes (except for Fig. 1.22 A″, where N_1=20). In all cases, an excellent match is found between simulated and experimental excitation patterns.

1.5.3   Calibration pulses

The simple patterns created in this exploratory study are reminiscent of early test patterns used to calibrate TV sets. For example, in 1934, the BBC used a simple test card which showed a circle over a horizontal line (Fig. 1.27). In the following decades, more sophisticated test patterns were designed and are still being used by engineers to calibrate monitors. Similarly, specifically designed pattern pulses could also become a useful tool for setting up experiments and testing spectrometer hardware.

As an illustrative example, consider the calibration of rf amplitudes. Conventionally, this is done by iteratively changing rf amplitude of a rectangular pulse with fixed duration, determining the zero crossing of the signal where the flip angle is 180° (or an integer multiple of 180°). In contrast to this approach, it might be of advantage, to be able
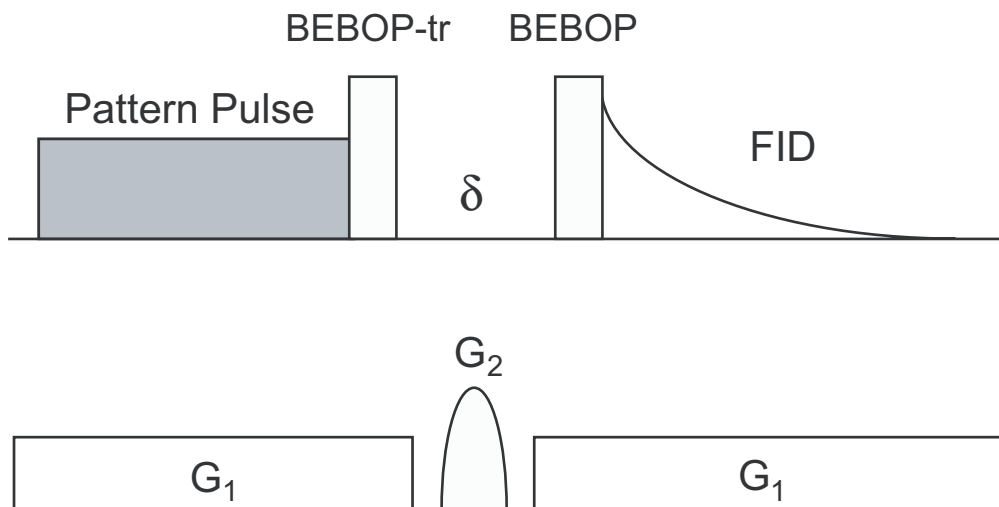
Figure 1.28: Schematic representation of an experiment for the acquisition of the excitation profile as a function of offset ν_0 in a single shot. The investigated excitation pulse of duration T (grey rectangle) is applied in the presence of the gradient G_1. Immediately after the excitation pulse, x magnetization is brought back to the z axis by a time reversed broadband excitation pulse (BEBOP-tr) [34,36,56,57], and during the delay δ any remaining transverse magnetization is dephased by applying a gradient G_2. Finally, in the presence of G_1, the stored z magnetization is rotated to the x axis by a BEBOP pulse and the FID is recorded.

to measure the current attenuation missetting of the amplifier in a single shot and to simply adjust the attenuator setting accordingly. The simple pattern shown in Fig. 1.22 C directly translates rf amplitude into excitation frequency and hence, the rf amplitude ν_1 can be directly infered from the excitation frequency in a single shot experiment. The flexibility of pattern pulses makes it possible to design more sophisticated calibration pulses which provide internal "tick marks" to directly quantify a given rf misadjustment. To illustrate this approach, we designed the test pattern shown in Fig. 1.29 A for the calibration of a rf pulse with an amplitude ν_1 of 10 kHz. The desired excitation pattern consists of five separate frequency bands at the offsets 0 kHz, $\pm$ 1.5 kHz, and $\pm$ 3.5 kHz, which were designed to have different bandwidths in order to be easily distinguishable. For the desired rf amplitude of 10 kHz, the central band at an offset of 0 kHz is not excited, whereas the bands at -1.5 kHz and -3.5 kHz are negative (corresponding to $-x$ magnetization) and the bands at $+1.5$ kHz and $+3.5$ kHz are positive (corresponding to $+x$ magnetization). If the actual rf amplitude is only 6 kHz, all five bands in the excitation profile are positive, whereas for an rf amplitude of 14 kHz, all five bands are negative. For any intermediate rf amplitude, the resulting excitation profile as a function of ν_0 allows to determine the actual misadjustment of the rf amplitude. A corresponding pulse with a duration of 6 ms was optimized to create this pattern and the simulated excitation profile is shown in Fig. 1.29 B.
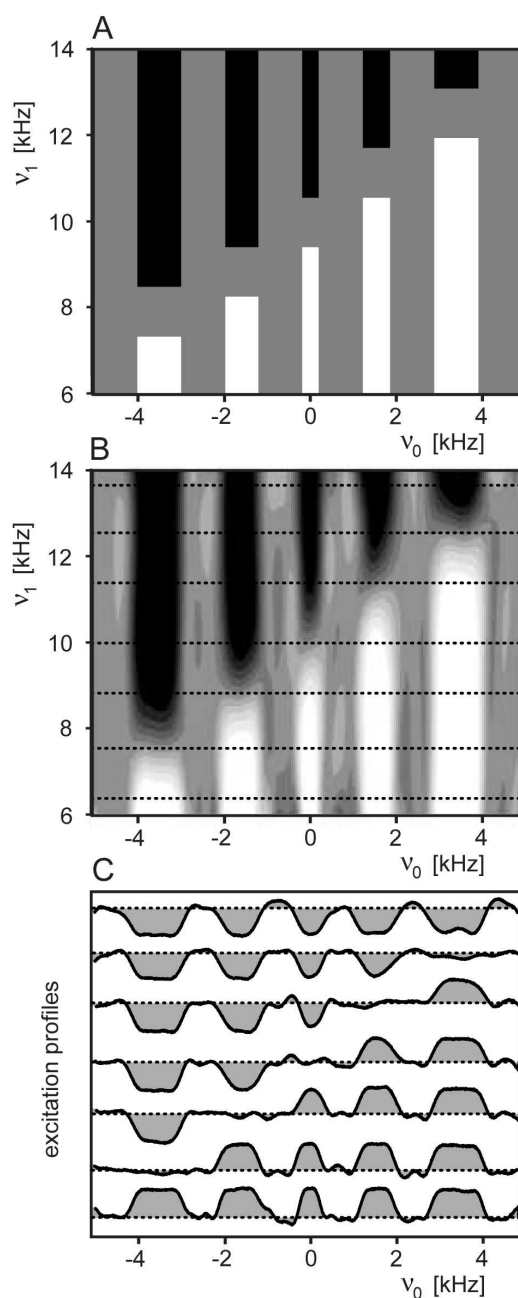
Figure 1.29: Example of a specifically designed test pattern for the experimental calibration of rf amplitudes in a single shot, (A) target excitation pattern (white: $M_x = 1$, grey: $M_x = 0$, black: $M_x = -1$). In (B), the simulated excitation pattern of an optimized pulse is shown. At the rf amplitudes indicated by dashed horizontal lines (6.3 kHz, 7.4 kHz , 8.7 kHz, 10.0 kHz, 11.2 kHz, 12.6 kHz, and 14.1 kHz, corresponding to attenuations of 4 dB, 2.6 dB, 1.2 dB, 0dB, -1 dB, -2 dB, and -3dB, respectively), the experimental single shot spectra shown in (C) were acquired.

The characteristic excitation profile of a single shot experiment provides a direct check if the rf power is set correctly or by what amount the rf attenuation needs to be corrected. Fig. 5 C shows seven experimental single shot spectra for rf amplitudes between 6.3 and 14.1 kHz, corresponding to rf amplitude missettings between $+4$ and -3 dB. Each of these spectra would allow to determine the necessary attenuator correction to achieve the desired pulse amplitude. In practice, several such calibration pulses with different grid resolution could be used for rough and subsequent fine adjustment of the rf power level.

Here we demonstrated the ability to design complex excitation patterns as a function of offset and rf amplitude, using efficient optimization algorithms based on ideas from optimal control theory. Clearly, the achievable resolution in ν_0 and ν_1 of a desired excitation pattern depends on the pulse duration, the pulse digitization and the number of optimization parameters. We expect that the ability to create virtually arbitrary excitation patterns as a function of ν_0 and ν_1 will find numerous applications in NMR spectroscopy and imaging. For example, the flexibility of pattern pulses makes it possible to excite a predefined region of interest in localized NMR experiments in the presence of both B_0 and B_1 gradients. The presented pattern pulses are point-to-point transformations that rotate a given initial magnetization vector to a desired final vector, however the methodology is also applicable to the development of potentially useful general rotation pulses (*vide infra*).

1.6   Creating universal rotations from point-to-point transformations

All the pulses described in previous sections are point-to-point rotations, therefore for every offset they are defined for they rotate the initial state z to some defined target state. The rotation *axis*, however, is generally undefined. It means, that, while for every single value of chemical shift offset the performed rotation *is* a unitary one, the rotation axes for different chemical shift offsets are different and do not correlate with each other.

However, here we found a surprisingly simple recipe for constructing a desired UR pulse from a PP pulse with half the flip angle. This allows one to draw from the vast literature on PP pulses [18–20, 50–53] and to exploit efficient PP pulse optimization algorithms [2, 13, 34, 36, 56, 57, 69] for the design of UR pulses with unprecedented flexibility.

And of course, the algorithm described in previous sections can also be modified in a way to allow one to optimize directly the universal rotations pulses. In cases, where no suited half-angle pulse is available to produce the universal rotation, such direct optimization is an alternative to the optimization of the half-angle pulse.

1.6.1   Construction procedure

In order to demonstrate the basic construction principle, we first consider the special case of UR rotations around the x axis before turning to general UR pulses with arbitrary rotation axes.

The unitary transformation $U_k(\alpha)$ corresponding to a rotation by angle α around axis k (equal to x, y, or z) is given by

$$U_k(\alpha) = \exp\{-\mathrm{i}\ \alpha\ I_k\}. \tag{1.58}$$

We can decompose the rotation operator $U_x(\alpha)$ into two consecutive rotations of angle $\alpha/2$ around the x axis as

$$
\begin{aligned}
U_x(\alpha) &=\ U_x(\alpha/2)\, U_x(\alpha/2) \\
&=\ U_x(\alpha/2)\left[U_y(\pi)\, U_x(-\alpha/2)\, U_y^{-1}(\pi)\right] \\
&=\ \left[U_x(\alpha/2)\, U_y(\pi)\, U_x^{-1}(\alpha/2)\right] U_y^{-1}(\pi),
\end{aligned}
\tag{1.59}
$$

where in the second line we have used the well-known relation $U \exp\{A\}\, U^{-1} = \exp\{U A U^{-1}\}$ for $A = -\mathrm{i}\,(\alpha/2)I_x$ and $U = U_y(\pi)$ which yields $U_x(\alpha/2) = U_y(\pi)\, U_x(-\alpha/2)\, U_y^{-1}(\pi)$. In the last line we have simply regrouped the operators and written $U_x(-\alpha/2) = U_x^{-1}(\alpha/2)$. But this grouping now represents a rotation by $\alpha/2$ about the x axis, which is applied to the operator I_y in the exponent of $U_y(\pi)$. However, this result can be achieved by *any* PP rotation which has the same net effect, rotating I_y to an angle $\alpha/2$ above the y axis in the y, z plane (ie., $I_y \rightarrow I_y \cos\frac{\alpha}{2} + I_z \sin\frac{\alpha}{2}$). Hence, letting $V(\nu)$ represent the propagator of such a composite (or shaped) PP pulse $\mathbf{V}$, which

is applied to a spin with a given offset ν, we can also express $U_x(\alpha)$ as

$$
\begin{aligned}
U_x(\alpha) &= \left[V(\nu)\, U_y(\pi)\, V^{-1}(\nu) \right] U_y^{-1}(\pi) \\
&= V(\nu) \left[U_y(\pi)\, V^{-1}(\nu)\, U_y^{-1}(\pi) \right].
\end{aligned}
\tag{1.60}
$$

We thus consider how $V^{-1}(\nu)$ transforms under a π rotation about the y axis. The following relations hold for *any* unitary transformation $W(\nu)$ effected by a composite pulse $\mathbf{W}$ at offset ν. For the *time-reversed* pulse $\mathbf{W}^{\mathrm{tr}}$, the propagator $W^{\mathrm{tr}}(-\nu)$ at offset $-\nu$ is [18]

$$
W^{\mathrm{tr}}(-\nu) = U_z(\pi)\, W^{-1}(\nu)\, U_z^{-1}(\pi).
\tag{1.61}
$$

For the *phase-inverted* pulse $\overline{\mathbf{W}}$, with the algebraic signs of all phases (expressed in rad or degrees) inverted, the resulting propagator at offset ν is [18]

$$
\overline{W}(\nu) = U_x(\pi)\, W(-\nu)\, U_x^{-1}(\pi).
\tag{1.62}
$$

Note that the symmetry relations [18] for phase-reversed pulses as defined above are different from the symmetry relations derived for 180° phase shifted pulses [70], which have been denoted phase inverted pulses. As a direct consequence of Eqs. 1.61 and 1.62, the propagator $\overline{W}^{\mathrm{tr}}(\nu)$ for the time-reversed *and* phase-inverted pulse $\overline{\mathbf{W}}^{\mathrm{tr}}$ is given by

$$
\begin{aligned}
\overline{W}^{\mathrm{tr}}(\nu) &= U_x(\pi)\, W^{\mathrm{tr}}(-\nu)\, U_x^{-1}(\pi) \\
&= U_x(\pi) \left[U_z(\pi)\, W^{-1}(\nu)\, U_z^{-1}(\pi) \right] U_x^{-1}(\pi) \\
&= U_y(\pi)\, W^{-1}(\nu)\, U_y^{-1}(\pi),
\end{aligned}
\tag{1.63}
$$

where we have inserted Eq. 1.61 in the second line and used $U_x(\pi)\, U_z(\pi) = U_y(\pi)$. As this general relation also holds for the special case $W(\nu) = V(\nu)$, we can finally express Eq. 1.60 in the form

$$
U_x(\alpha) = V(\nu)\, \overline{V}^{\mathrm{tr}}(\nu).
\tag{1.64}
$$

Hence, in a desired range of offsets ν, a UR pulse corresponding to a rotation around the x axis by an angle α can be constructed based on a composite or shaped pulse $\mathbf{V}$ which simply effects a PP rotation from I_y to $(I_y\cos\frac{\alpha}{2} + I_z\sin\frac{\alpha}{2})$ in the desired range of offsets. First, the time-reversed and phase-inverted PP pulse is applied, followed by $\mathbf{V}$. The phase inverted version of a 90_y° pulse is a 90_{-y}° pulse, where the sign of the pulse phase $\phi = \pi/2$ (corresponding to "y" in the usual short-hand notation) is changed to $\phi = -\pi/2$ (corresponding to "$-y$"). However, the phase inverted version of a 90_x° pulse is also a 90_x° pulse (not a 90_{-x}° pulse), because here $\phi = 0$ (corresponding to "x") remains $\phi = 0$ if the sign of ϕ is inverted. An explicit construction example is provided in Fig. 1.30.

As shown in section 1.6.2 A (*vide infra*, it is straightforward to generalize the result of Eq. 1.64 for UR pulses with rotation angle α and any rotation axis, i.e. with arbitrary azimuthal angle θ and phase φ. The construction of such a general UR pulse $U(\alpha, \theta, \varphi)$ can be summarized as follows:
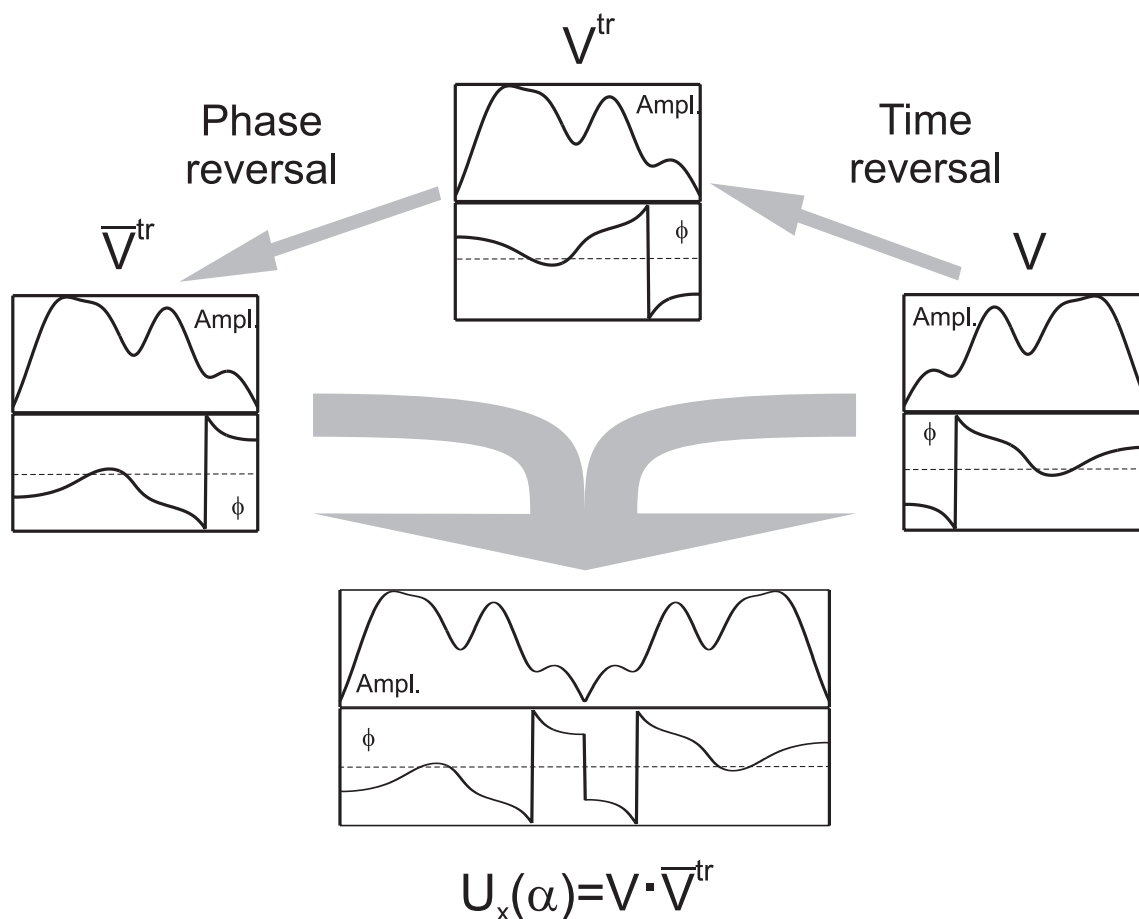
Figure 1.30: Demonstration of the construction principle for universal rotation pulses. Starting from a point-to-point transformation pulse $\mathbf{V}$ that transforms I_y magnetization into $I_y \cos(\alpha/2) + I_z \sin(\alpha/2)$, the time reversed and phase inverted pulse $\overline{\mathbf{V}}^{tr}$ is produced. The combined UR pulse consists of $\overline{\mathbf{V}}^{tr}$ followed by $\mathbf{V}$, effecting the rotation $U_x(\alpha) = V \, \overline{V}^{tr}$. The same procedure can be applied to produce UR pulses around an arbitrary rotation axis (see text for details).

1. Pick (or design [13, 34, 36]) a (composite or shaped) PP pulse **V** which effects the rotation

$$\begin{pmatrix} 0 \\ 1 \\ 0 \end{pmatrix} \rightarrow \begin{pmatrix} -\sin\frac{\alpha}{2}\cos\theta \\ \cos\frac{\alpha}{2} \\ \sin\frac{\alpha}{2}\sin\theta \end{pmatrix} \qquad (1.65)$$

for a desired range of offsets ν, where the initial vector corresponds to I_y and the final vector corresponds to $(I_y \cos\frac{\alpha}{2} + I_\gamma \sin\frac{\alpha}{2}) = (I_y \cos\frac{\alpha}{2} + I_z \sin\frac{\alpha}{2}\sin\theta - I_x \sin\frac{\alpha}{2}\cos\theta)$, c.f. section 1.6.2 A.

2. Construct a combined pulse $\mathbf{U}(\alpha, \theta, 0)$ consisting of the *time-reversed* and *phase-inverted* PP pulse $\overline{\mathbf{V}}^{\mathrm{tr}}$ followed by the PP pulse **V**.

3. Create the desired UR pulse $\mathbf{U}(\alpha, \theta, \varphi)$ by shifting all phases of the individual pulse elements of $\mathbf{U}(\alpha, \theta, 0)$ by φ.

As a simple example, consider the construction of a refocussing pulse effecting a universal 180°_x rotation (i.e. a UR pulse with $\alpha = \pi$, $\theta = \pi/2$, and $\varphi = 0$) in the offset range $\nu_{\min} \leq \nu \leq \nu_{\max}$. According to Eq. 1.65 in step 1, we first need to find a pulse **V** which effects the PP rotation

$$\begin{pmatrix} 0 \\ 1 \\ 0 \end{pmatrix} \rightarrow \begin{pmatrix} 0 \\ 0 \\ 1 \end{pmatrix}, \qquad (1.66)$$

i.e. which flips I_y to I_z for the desired range of offsets. Suppose we are given a PP excitation pulse **W** which rotates I_z to $-I_y$ in the offset range $-\nu_{\max} \leq \nu \leq -\nu_{\min}$. From Eq. 1.61, it follows that the time-reversed pulse $\mathbf{W}^{\mathrm{tr}}$ corresponds to a pulse V which effects the required PP transformation from I_y to I_z (c.f. relation 1.66) in the desired range $\nu_{min} \leq \nu \leq \nu_{max}$. In step 2, a UR pulse $\mathbf{U}(\pi, \pi/2, 0)$ can be constructed by first applying the pulse $\overline{\mathbf{V}}^{\mathrm{tr}} = \overline{\mathbf{W}}$, (the phase-inverted version of the excitation pulse **W**), followed by $\mathbf{V} = \mathbf{W}^{\mathrm{tr}}$ (the time-reversed version of the excitation pulse **W**). As in the given example $\varphi = 0$, step 3 has no effect. This procedure is illustrated in Fig. 1.31 for the case of a broadband PP excitation pulse **W** of 500 μs duration as previously optimized using optimal control theory [36] with $\nu_{\max} = -\nu_{\min} = 20$ kHz. Figure 1.31 A shows amplitude and phase of the pulse. Note that the pulse phase was shifted by $-\pi/2$ compared to Fig. 1 of [36] in order to effect a z to $-y$ rather than a z to x PP rotation. The combined UR 180°_x pulse consisting of $\overline{\mathbf{V}}^{\mathrm{tr}} = \overline{\mathbf{W}}$ followed by $\mathbf{V} = \mathbf{W}^{\mathrm{tr}}$ is shown in Fig. 1.31 A'. Figs. 1.31 B,C and 1.31 B',C' show the effective rotations as a function of offset for the PP pulse **W** and for the combined UR 180°_x pulse. As expected, the effected rotations of the constructed UR pulses closely approach the desired rotation in the active range of offsets, where the PP pulse is functional.

Note that the presented approach would yield an exact 180°_x UR pulse if the excitation pulse **W** would be perfect. This is in sharp contrast to a previously suggested approach [71] for the design of refocussing pulses, which attempts to construct 180°_x UR pulses by
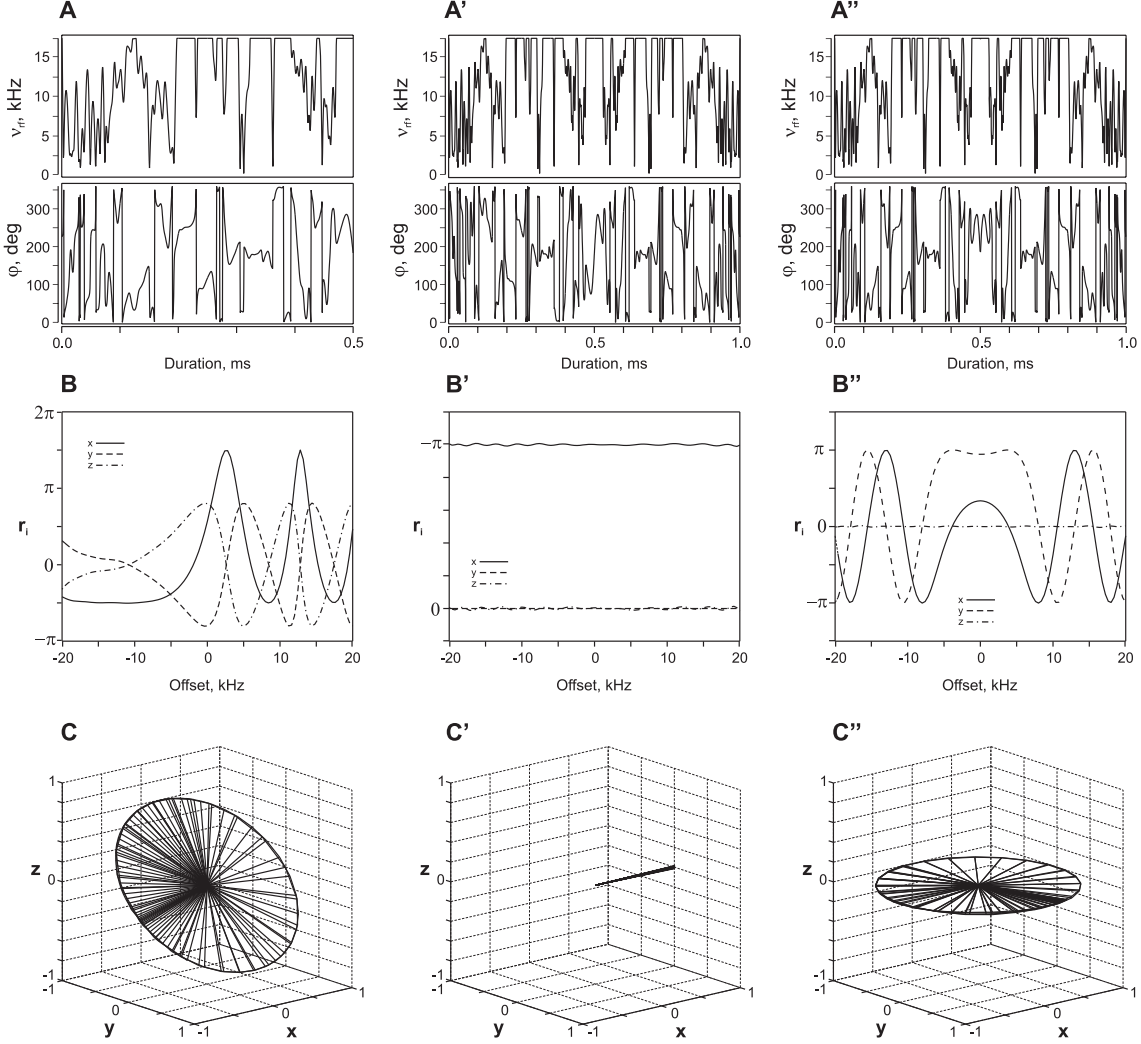
Figure 1.31: Example for the construction of a refocussing pulse out of a previously published PP excitation pulse [36]. (A) Amplitude and phase of the original excitation pulse, (A′) the constructed refocussing pulse using the procedure described in Fig. 1.30, and (A″) a pulse constructed for refocussing using the procedure described in [71]. The corresponding offset profiles of the effective rotations are displayed in B,B′, and B″: x, y, and z components of the rotation vector $\vec{r} = \beta\vec{e}$, where β is the effective rotation angle and $\vec{e}$ is the unit vector pointing along the rotation axis, are given in radians. In C, C′, and C″ the rotation axes $\vec{e}$ are visualized in a 3D-plot for 100 offsets ν equally spaced in the range between $\pm$ 20 kHz. A universal 180°_x rotation is achieved in the entire offset range only for the refocussing pulse shown in A′. For excitation pulses the vectors lie in a tilted plane (c.f. section 1.6.2 B), while the pulse shown in A″ is a PP inversion pulse with rotation axes in the $x - y$ plane (c.f. section 1.6.2 C).

simply applying an excitation pulse $\mathbf{W}$ (rather than $\overline{\mathbf{W}}$) followed by the time-reversed excitation pulse $\mathbf{W}^{\mathrm{tr}}$. For comparison, the resulting effective rotations are shown as a function of offset in Fig. 1.31 B″,C″. While the original excitation pulse has rotation axes distributed in a tilted plane as derived in section 1.6.2 B, the composite pulse consisting of the pulse $\mathbf{W}$ followed by $\mathbf{W}^{\mathrm{tr}}$ still shows a variety of rotation axes with respect to offset in the x, y plane, resulting in an inversion pulse (for a detailed derivation see sectioon 1.6.2 C). Hence, the approach of Ref. [71] in general does not provide a functional refocussing pulse, in contrast to the procedure presented here. The two approaches are of course equivalent for the special case of purely amplitude-modulated pulses with phase x or $-x$, where $\mathbf{W} = \overline{\mathbf{W}}$, i.e. if the excitation pulse is invariant under phase inversion. Hence, time-symmetric phase-alternating composite 180_x° UR pulses result from phase-alternating $90°$ PP pulses. Conversely, $90°$ PP pulses can be obtained from the first half of symmetric phase-alternating composite 180_x° UR pulses, as previously shown in [41].

The general construction principle presented here, based on PP pulses of duration T, always results in UR pulses of duration $2T$ with symmetric rf amplitude, i.e. $\nu^{\mathrm{rf}}(t) = \nu^{\mathrm{rf}}(2T - t)$ where $\nu^{\mathrm{rf}}(t) = \sqrt{(\nu_x^{\mathrm{rf}}(t))^2 + (\nu_y^{\mathrm{rf}}(t))^2}$. For rotations with $\varphi = 0$, the x component of the rf amplitude ν_x^{rf} is symmetric, i.e. $\nu_x^{\mathrm{rf}}(t) = \nu_x^{\mathrm{rf}}(2T - t)$, whereas the y component is antisymmetric with $\nu_y^{\mathrm{rf}}(t) = -\nu_y^{\mathrm{rf}}(2T - t)$. Note that pulses of this symmetry class are known to give net rotation axes in the xz plane [72].

Experimental results for the pulses from Fig. 1.31 A′ and A″ are shown in Fig. 1.32. All experiments were acquired on a Bruker Avance 250 spectrometer with linearized amplifiers and SGU400 boards for pulse control using a copper sulfate doped 99.9 % D_2O sample. For validation of the refocussing pulse an echo experiment as shown in Fig. 1.32A was performed with offsets of the shaped pulse varied from -22 kHz to 22 kHz to cover and exceed its 40 kHz refocussing bandwidth. Over the whole bandwidth the theoretical performance is achieved. For comparison, Fig. 1.32C shows the effect of the pulse constructed according to [71].

The presented procedure describes a surprisingly simple method for the construction of universal rotation (UR) pulses from point-to-point (PP) pulses. For a general rotation with an arbitrary flip angle α, a specific PP pulse with flip angle $\alpha/2$ is required. For example, refocussing pulses can be constructed from known excitation pulses in a straightforward way. However, since excitation pulses are usually optimized starting from I_z, they have to be time reversed first for constructing the UR pulse. The resulting refocussing pulses are only twice as long as the initial excitation pulses used for construction. With recent improvements in short broadband excitation pulses [34, 36, 56, 57, 69] relatively short and robust refocussing pulses can be constructed using the presented approach. The proposed construction principle is very general and can be used for obtaining broadband as well as selective, or pattern-type UR pulses. Potential applications of robust pattern-type UR pulses include NMR imaging techniques and NMR-spectroscopy in inhomogeneous B_0-fields [73] and robust local operations in quantum information processing.
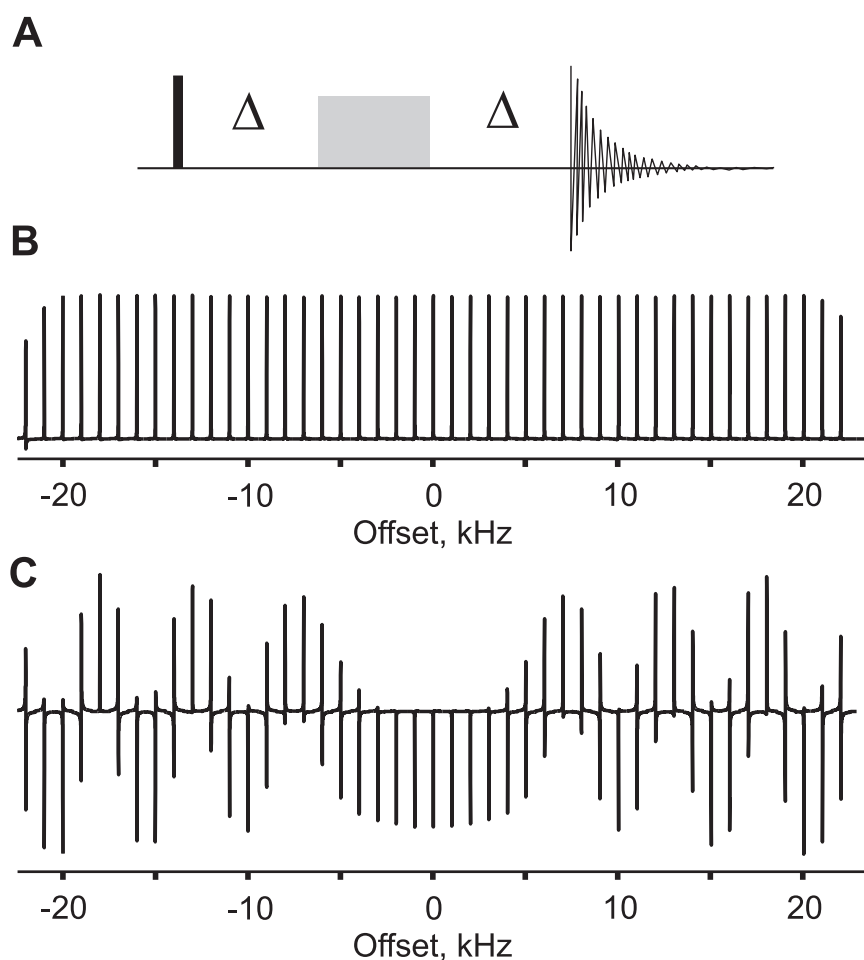
Figure 1.32: Experimental validation of the refocusing pulses shown in Fig. 1.31 A$'$. The pulse sequence uses an echo with delay $\Delta = 100$ ms after excitation (A). The offset of the shaped refocusing pulse was varied in increments of 1 kHz for the range of -22 kHz to 22 kHz with results shown in B. Excellent refocusing properties are obtained for a ± 20 kHz offset range, for which the original excitation pulse (Fig. 1.31 A) was optimized. The pulse constructed using the procedure described in [71] (c.f. Figs. 1.31 A$''$ - C$''$) produces the offset profile shown in C.

1.6.2 Some helpful formulas

A: Decomposition of arbitrary rotations into PP pulses

Here we derive the decomposition of a general universal rotation (UR) into two point-to-point (PP) pulses of half the flip angle. A general UR can be characterized by the orientation of the rotation axis and by the rotation angle α around this axis. The orientation of the rotation axis is uniquely defined by the azimuthal angle θ (with $0 \leq \theta \leq \pi$) and the phase φ (with $0 \leq \varphi \leq 2\pi$). For the special case, where the rotation axis points along the x axis (i.e. $\theta = \pi/2$ and $\varphi = 0$), the decomposition was derived in the main text (Eqs. 1.58-1.64). We first generalize this derivation for arbitrary θ (but still assuming $\varphi = 0$), which corresponds to a rotation axis in the x-z plane. The corresponding unitary operator is

$$U(\alpha, \theta) = \exp\{-i\ \alpha\ I_\theta\} \tag{1.67}$$

with

$$I_\theta = I_z \cos\theta + I_x \sin\theta. \tag{1.68}$$

Using the identities

$$\exp\{-i\frac{\alpha}{2}\ I_\theta\} = \exp\{-i\ \pi\ I_y\}\ \exp\{i\ \frac{\alpha}{2}\ I_\theta\}\ \exp\{i\ \pi\ I_y\} \tag{1.69}$$

and

$$\exp\{-i\ \frac{\alpha}{2}\ I_\theta\}\ I_y\ \exp\{i\ \frac{\alpha}{2}\ I_\theta\} = I_y \cos\frac{\alpha}{2} + I_\gamma \sin\frac{\alpha}{2} \tag{1.70}$$

with

$$I_\gamma\ =\ i[I_y, I_\theta] = I_z \sin\theta - I_x \cos\theta, \tag{1.71}$$

$U(\alpha, \theta)$ can be rewritten as

$$
\begin{aligned}
U(\alpha, \theta)\ =&\ \exp\{-i\ \frac{\alpha}{2}\ I_\theta\}\ \exp\{-i\ \frac{\alpha}{2}\ I_\theta\} \\
=&\ \exp\{-i\ \frac{\alpha}{2}\ I_\theta\}\ \exp\{-i\ \pi\ I_y\}\ \exp\{i\ \frac{\alpha}{2}\ I_\theta\}\ \exp\{i\ \pi\ I_y\} \\
=&\ \exp\{-i\ \pi\ (\exp\{-i\ \frac{\alpha}{2}\ I_\theta\}\ I_y\ \exp\{i\ \frac{\alpha}{2}\ I_\theta\})\}\ \exp\{i\ \pi\ I_y\} \\
=&\ \exp\{-i\ \pi\ (I_y \cos\frac{\alpha}{2} + I_\gamma \sin\frac{\alpha}{2})\}\ \exp\{i\ \pi\ I_y\}. \tag{1.72}
\end{aligned}
$$

Given any composite (or shaped) pulse effecting PP rotations $V_\theta(\nu)$ which transform I_y to $(I_y \cos\frac{\alpha}{2} + I_\gamma \sin\frac{\alpha}{2}) = (I_y \cos\frac{\alpha}{2} + I_z \sin\frac{\alpha}{2} \sin\theta - I_x \sin\frac{\alpha}{2} \cos\theta)$ for a range of offsets ν, i.e.

$$V_\theta(\nu)\ I_y\ V_\theta^{-1}(\nu) = I_y \cos\frac{\alpha}{2} + I_\gamma \sin\frac{\alpha}{2}, \tag{1.73}$$

Eq.1.72 can be written in the form

$$
\begin{aligned}
U(\alpha, \theta)\ =&\ \exp\{-i\ \pi\ (V_\theta(\nu)\ I_y\ V_\theta^{-1}(\nu))\}\ \exp\{i\ \pi\ I_y\} \\
=&\ V_\theta(\nu)\ \exp\{-i\ \pi\ I_y\ \}\ V_\theta^{-1}(\nu)\ \exp\{i\ \pi\ I_y\} \\
=&\ V_\theta(\nu)\ \overline{V}_\theta^{\text{tr}}(\nu), \tag{1.74}
\end{aligned}
$$

where in the final step we used Eq. 1.63 with $W(\nu) = V_\theta(\nu)$.

This decomposition of a UR pulse with a rotation axis in the x-z plane (i.e. $\varphi = 0$) can readily be generalized for arbitrary UR pulses with a unitary operator

$$
\begin{aligned}
U(\alpha, \theta, \varphi) &= \exp\{-\mathrm{i}\,\varphi\,I_z\}\,U(\alpha, \theta)\,\exp\{\mathrm{i}\,\varphi\,I_z\} \\
&= \exp\{-\mathrm{i}\,\varphi\,I_z\}\,V_\theta(\nu)\,\overline{V}_\theta^{\mathrm{tr}}(\nu)\,\exp\{\mathrm{i}\,\varphi\,I_z\} \\
&= \exp\{-\mathrm{i}\varphi I_z\}\,V_\theta(\nu)\,\exp\{\mathrm{i}\varphi I_z\} \\
&\quad \times\,\exp\{-\mathrm{i}\varphi I_z\}\,\overline{V}_\theta^{\mathrm{tr}}(\nu)\,\exp\{\mathrm{i}\varphi I_z\}.
\end{aligned}
\tag{1.75}
$$

Hence, given a composite pulse corresponding to $U(\alpha, \theta) = V_\theta(\nu)\,\overline{V}_\theta^{\mathrm{tr}}(\nu)$ for $\varphi = 0$, the general UR pulse with $U(\alpha, \theta, \varphi)$ can be constructed simply by adding φ to the phase of each individual element of the composite pulse.

B: Rotation vectors for PP pulses

Consider any pair of initial and final vectors $\vec{v}_i$ and $\vec{v}_f$. The angle η between the two vectors is defined by $\cos\eta = \vec{v}_i \cdot \vec{v}_f$ with $0 \le \eta \le \pi$. For a PP rotation from $\vec{v}_i$ to $\vec{v}_f$, the rotation axis must be located in the plane through the origin which is orthogonal to $\vec{v}_i - \vec{v}_f$. The actual rotation angle β (i.e. the length of the rotation vector) depends on the orientation of the unit rotation vector $\vec{e}$ in this plane:

$$
\cos\beta = -\frac{1 - (1 + \cos 2\gamma)\cos 2\frac{\eta}{2}}{1 - \sin 2\gamma \cos 2\frac{\eta}{2}},
$$

where γ is the angle between the unit vector $\vec{e}$ and the vector $\vec{v}_i \times \vec{v}_f$, with $\cos\gamma = \vec{e} \cdot (\vec{v}_i \times \vec{v}_f)$. The rotation angle β is positive for $|\gamma| \le \pi/2$ and negative for $|\gamma| > \pi/2$. For example, if $\vec{e}$ is parallel or antiparallel to $\vec{v}_i \times \vec{v}_f$ (i.e. $\gamma = 0$ or $\gamma = \pi$), the rotation angle β is η or $-\eta$, respectively. If $\vec{e}$ is colinear to $\vec{v}_i + \vec{v}_f$ (i.e. $\gamma = \pm\pi/2$), the rotation angle β is π.

C: Rotation vectors for symmetrized pulses according to reference [71]

Here we analyze the effect of an excitation pulse $\mathbf{W}$ followed by the time-reversed excitation pulse $\mathbf{W}^{\mathrm{tr}}$ as suggested in [71]. We assume that the PP pulse $\mathbf{W}$ transforms I_z to I_γ for a given range of offsets ν, i.e.

$$
W(\nu)\,I_z\,W^{-1}(\nu) = I_\gamma,
\tag{1.76}
$$

where I_γ is in the transverse plane (e.g. $I_\gamma = I_y$). Subsequent application of $\mathbf{W}^{\mathrm{tr}}$ to I_γ yields

$$
\begin{aligned}
W^{\mathrm{tr}}(\nu)I_\gamma\{W^{\mathrm{tr}}(\nu)\}^{-1} &= \exp\{-\mathrm{i}\pi I_z\}W^{-1}(-\nu)\exp\{\mathrm{i}\pi I_z\}I_\gamma \\
&\quad \times \exp\{-\mathrm{i}\pi I_z\}W(-\nu)\exp\{\mathrm{i}\pi I_z\} \\
&= -\exp\{-\mathrm{i}\pi I_z\}W^{-1}(-\nu)\,I_\gamma\,W(-\nu)\exp\{\mathrm{i}\pi I_z\},
\end{aligned}
\tag{1.77}
$$

where we used Eq.1.61 and $\exp\{i\pi I_z\}I_\gamma \exp\{-i\pi I_z\} = -I_\gamma$. Eq. 1.77 can be further simplified, provided the excitation profile of the PP pulse $\mathbf{W}$ is symmetric with respect to offset. In this case, I_z is transformed to I_γ not only for offset ν but also for offset $-\nu$, i.e.

$$W(-\nu)\ I_z\ W^{-1}(-\nu) = I_\gamma. \tag{1.78}$$

Multiplying Eq. 1.78 from the left by $W^{-1}(-\nu)$ and from the right by $W(-\nu)$, we find

$$W^{-1}(-\nu)\ I_\gamma\ W(-\nu) = I_z \tag{1.79}$$

and Eq. 1.77 can be written as

$$\begin{aligned} W^{\text{tr}}(\nu)I_\gamma\{W^{\text{tr}}(\nu)\}^{-1} &= -\exp\{-i\pi I_z\}\ I_z\ \exp\{i\pi I_z\} \\ &= -I_z. \end{aligned} \tag{1.80}$$

Hence, for an excitation pulse $\mathbf{W}$ which transforms I_z to I_γ for offset ν and $-\nu$, the application of $\mathbf{W}$ followed by $\mathbf{W}^{\text{tr}}$ results in a PP inversion pulse which transforms I_z to $-I_z$. However, in general this combined pulse is not a refocussing pulse because the effective axis of the π rotation can be located anywhere in the transverse plane, c.f. Fig. 1.31 C″. Only for the special case of a purely amplitude-modulated pulses $\mathbf{W}$ with phase x or $-x$, the resulting symmetric PP pulse is also a UR pulse with a unique rotation axis [74].

1.7   Direct optimizations of universal rotations

Though in a previous section we described the procedure to create universal rotations from point-to-point transformation, this doesn't answer all the questions about universal rotations. First, we cannot say anything about generality of this approach - it is well possible, that the proposed procedure is not optimal and the same universal rotations could be implemented more efficiently with other pulses. Second, not every rotation can be realized with this construction procedure - since the inherent symmetry of constructed pulses implies that rotation axes for all offsets lie in one plane, no rotation with offset dependent rotation axes with some of the axes lying off that plane can be produced this way. Therefore we have at least two reasons to apply the GRAPE algorithm to explicitly optimize universal rotations: we need a tool to create rotations we cannot create by construction from point-to-point transformations, and we want to test the performance limits of universal rotation pulses, similarly as we did in section 1.3.3, and compare them to the performance of constructed pulses.

1.7.1   Choice of the optimization function

An important step in the application of the GRAPE algorithm is the choice of the performance function, since it defines the whole optimization flow. In a simplest analogy to a point-to-point transformation on ensemble of non-interacting spins one can choose a scalar product between target propagator and propagator at the end of the optimized pulse as the performance function, as this product is defined in Eqn. 1.34. However, the propagator U optimized this way will be only one particular case of a more general family of propagators $e^{i\phi}U$ with phase factor $e^{i\phi}$ equal to 1. So, for the sake of generality a quality factor has to be used, that is insensitive to the phase factor, *e.g.* the squared scalar product, defined in Eqn. 1.37.

Though the aforementioned concerns about phase factors are generally correct, for a considered case the phase factor can take only certain values. Since the propagators of interest are all generated by the traceless spin Hamiltonians, (and are though elements of the special unitary group, $U \in SU(2)$), the well known property $\det\{e^A\} = e^{\text{tr}\{A\}}$ implies for all our propagators U that $\det\{U\} = +1$. The same should of course remain true for a propagator $e^{i\phi}U$. Thus using the property $\det\{rA\} = \det\{rE_n \cdot A\} = r^n\det\{A\}$, which holds for any $n \times n$ matrix A and all scalars r, for our 2×2 propagators U we can write

$$\det\{e^{i\phi}U\} = (e^{i\phi})^2\det\{U\} = +1. \tag{1.81}$$

Therefore $(e^{i\phi})^2$ should also be equal to $+1$ and the equation

$$(e^{i\phi})^2 = \cos2\phi + i\sin2\phi = +1, \tag{1.82}$$

has the solution $\phi = n\pi$, which implies, that $e^{i\phi} = \pm1$ or in other words, the phase factor can only have two values, $+1$ and -1. Thus, as a result of optimisations with performance function Φ_1 as defined in Eqn. 1.37 one can expect pulses, approaching

Table 1.3: Constraints used for optimizations of universal rotations

$\Delta\nu^a$ (kHz)	n_{off}	t_p, (μs)	rotation type	performance function
10	200	10 - 170	90°	$\|\langle U_F\|U(T)\rangle\|^2$
20	500	10 - 310	90°	$\|\langle U_F\|U(T)\rangle\|^2$
30	500	10 - 430	90°	$\|\langle U_F\|U(T)\rangle\|^2$
10	100	10 - 180	180°	$\|\langle U_F\|U(T)\rangle\|^2$
20	100	10 - 330	180°	$\|\langle U_F\|U(T)\rangle\|^2$
30	100	10 - 490	180°	$\|\langle U_F\|U(T)\rangle\|^2$
10	100	10 - 140	90°	$+\langle U_F\|U(T)\rangle$
20	100	10 - 250	90°	$+\langle U_F\|U(T)\rangle$
30	100	10 - 380	90°	$+\langle U_F\|U(T)\rangle$
40	100	10 - 490	90°	$+\langle U_F\|U(T)\rangle$
50	100	10 - 630	90°	$+\langle U_F\|U(T)\rangle$
10	100	10 - 150	180°	$+\langle U_F\|U(T)\rangle$
20	100	10 - 290	180°	$+\langle U_F\|U(T)\rangle$
30	100	10 - 360	180°	$+\langle U_F\|U(T)\rangle$
10	100	10 - 190	90°	$-\langle U_F\|U(T)\rangle$
20	100	10 - 290	90°	$-\langle U_F\|U(T)\rangle$
30	100	10 - 350	90°	$-\langle U_F\|U(T)\rangle$
40	100	10 - 520	90°	$-\langle U_F\|U(T)\rangle$
50	100	10 - 650	90°	$-\langle U_F\|U(T)\rangle$

^{a}) $\Delta\nu$ is defined as offset range used in the optimization.

either the target propagator U_F or the propagator $-U_F$. Intuitively the latter can be understood as rotation in the opposite direction with rotation angle $2\pi - \alpha$, with α being the target rotation angle. Two such rotations are fully equivalent in their effect and virtually undistinguishable. It is also clear, that all the cases should become equivalent for 180° rotation.

A systematic study of the pulse performance, similar to the one performed in section 1.3.3, was performed on universal rotation pulses with tools of optimal control theory. Sets of 90° and 180° rotations were calculated for different bandwidths. Moreover, for every parameter set we performed the otimization series with various choices of performance functions: the square of the scalar product Φ_1 (Eqn. 1.37) and the simple scalar product Φ_1 (Eqn. 1.34), once with unchanged target propagator U_F, and once with target propagator $-U_F = e^{i\pi}U_F$. In all cases, the nominal (unscaled) rf-amplitude was limited to 10 kHz. For each set, pulse lengths t_p were varied in ranges as listed in Table 1.3. Generally, pulse durations were incremented until the corresponding quality factor exceeded 0.995. Each chosen bandwidth was divided into equal increments, with $n_{off} = 100$. The time digitization for the optimized shapes was 0.5 μs in all cases.
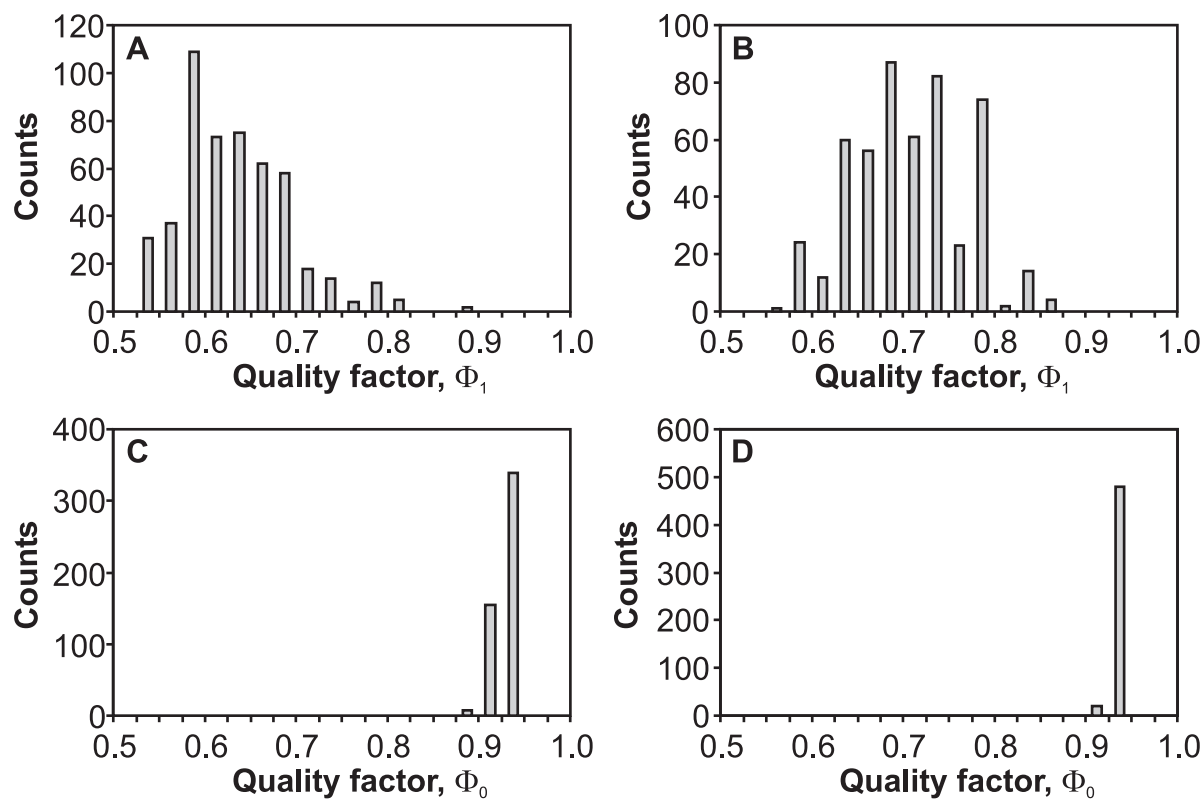
Figure 1.33: Histogram distribution of quality factors Φ obtained for 500 optimizations of 90° (A, C) and 180° (B, D) rotations with 40 kHz bandwidth, 230 μs duration and no rf-variation. The performance function was chosen as $\Phi_1 = |\langle U_F | U(T) \rangle|^2$ in (A) and (B) and as $\Phi_0 = \text{Re}\langle U_F | U(T) \rangle$ in (C) and (D). Whereas in cases (C) and (D) very narrow distribution of quality factors is achieved around the optimal one, in cases (A) and (B) the distribution is very broad and only a small part of initial random pulses leads to an optimal quality factor.

As in section 1.3.3, initially one hundred randomized starting pulses were generated to start 100 optimizations for each data point in Figs. 1.34 and 1.35. However, it turned out that distributions of quality factors obtained for every starting random pulse, appeared to be quite different for the two different choices of performance functions. The distribution for the performance function Φ_0 (scalar product) resembles that of the quality factors for point-to-point transformations (see Fig. 1.33 C and D and compare to Fig. 1.7), whereas the distribution for the performance function Φ_1 (square of the scalar product) was much broader and only very little part of initial pulses converged to the optimal values (see Fig. 1.33 A and B). Apparently, the possible ambiguity in the final phase factor makes the search space larger and the search procedure less efficient. However, for the case of 180°-rotation (Fig. 1.33 B), where all possible phase factors are equivalent, the search efficiency is only slightly better than for 90°-rotation (Fig. 1.33 A). Therefore, the number of randomized starting pulses was increased for optimizations of 90°-rotations with larger offset ranges and performance function Φ_1.

The results of the optimizations of 90° and 180° rotations are shown in Figs. 1.34 and 1.35, respectively: the performance of the optimized pulses described by the quality factors Φ_0 or Φ_1, respectively, is given as a function of the pulse length. Similarily to the curves in section 1.3.3, these curves show a step-like behaviour, but if former ones generally had the property, that for longer pulses the best reached quality factor is at least as good as the best quality factor for any of the shorter pulses, actual curves for 90° rotations have systematic oscillations of the best reached quality factor, so that for certain pulse lengths much shorter pulses can provide significantly better performance. This can be explained by the presence of the offset term in the effective Hamiltonian and the necessity to cancel its effect. So, for point-to-point transformations with initial magnetization $M(t_0) = M_z$ this initial state is not affected by the offset term and therefore any extention of the applied pulse with points with zero amplitude should not modify the effect of the pulse and hence provides the lower limit for best possible performance of the optimized pulse with such elongated duration. In contrast, universal rotations do not imply any particular initial or target magnetization state, but rather should perform equally when applied to any magnetization. The offset term is explicitly included in every optimization step, therefore any additional digits to the pulse shape have to be compensated, which is apparently not always effectively possible. However, as Fig. 1.35 shows, for 180° rotations this compensation is possible, and the curves do not show oscillations anymore, but rather a stepwise increase in pulse performance with increased pulse duration. Obviously, in the case of 180° rotation with rotation axes in the xy-plane the offset terms are refocused, and the pulse can also be elongated by adding equal periods with zero amplitude at the beginning and at the end of the pulse shape (so that the offset evolution during this added period could be refocused) wthout losses in performance.

1.7.2 Role of the phase factor

As was mentioned in section 1.2.4, for practical applications it is sufficient to approach the target propagator U_F only up to an arbitrary phase factor $e^{i\phi}$, and the performance
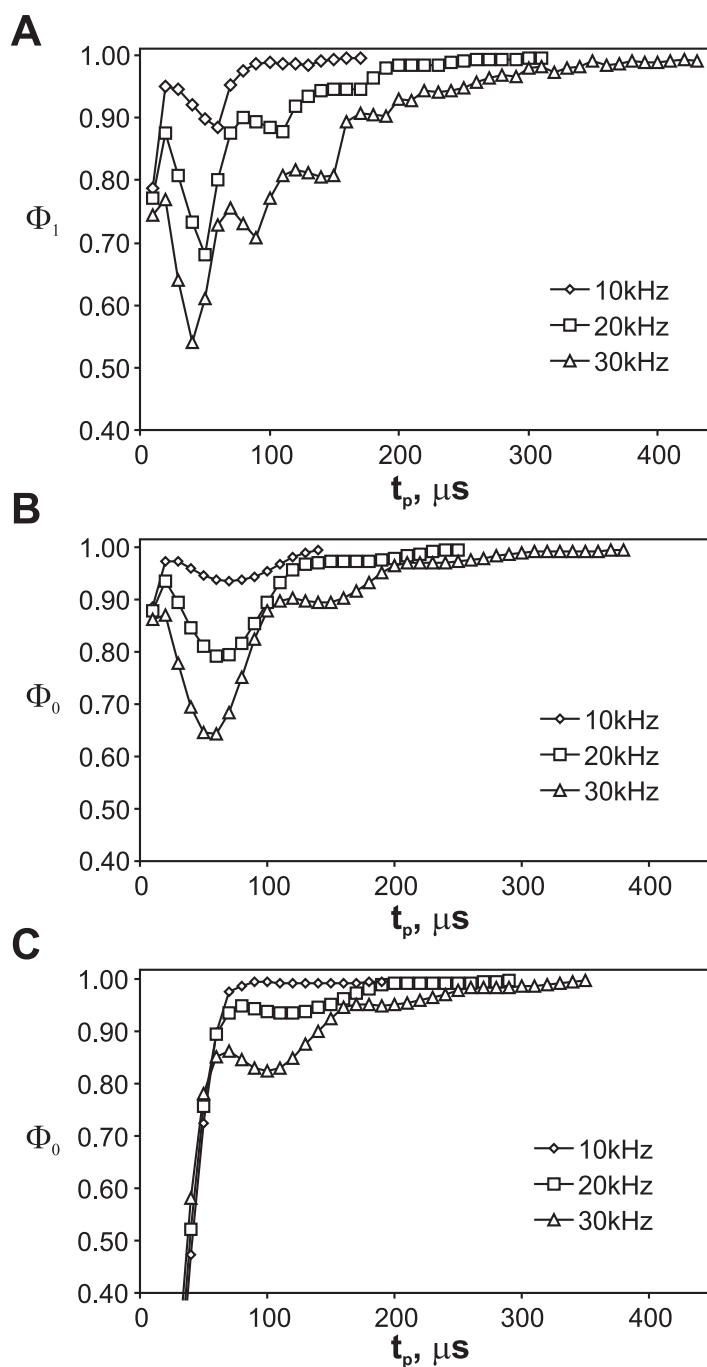
Figure 1.34: Maximum quality factors reached with different performance functions for broadband universal 90° rotations with rf-amplitudes limited to 10 kHz and various chemical shift offset ranges with respect to pulse duration. Optimization function $\Phi_1 = |\langle U_F | U(T) \rangle|^2$, allowing all values for the phase factor $e^{i\phi}$ was used in (A), while function $\Phi_0 = \langle U_F | U(T) \rangle$ was used in (B) and (C) with predefined values $e^{i\phi} = +1$ in (B) and $e^{i\phi} = -1$ in (C). The maximum quality factors with respect to pulse duration are given for the three different bandwidths $\Delta\nu$ equal to 10 kHz, 20 kHz and 30 kHz.

A

B
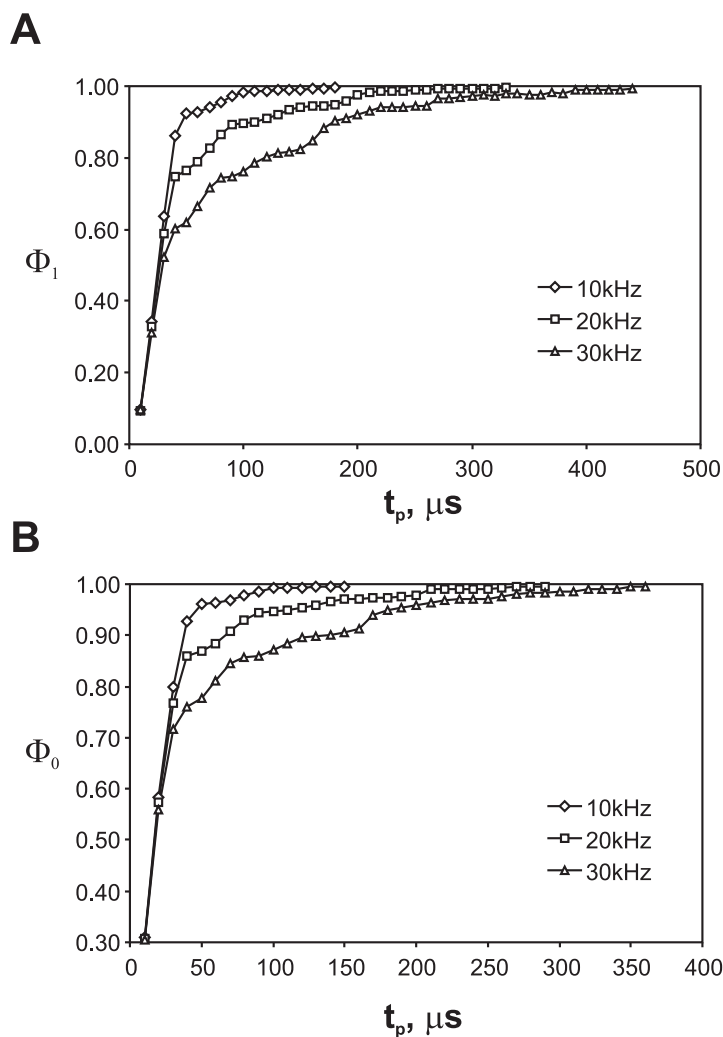
Figure 1.35: Maximum quality factors reached with different optimization functions for broadband universal 180° rotations with rf-amplitudes limited to 10 kHz and various chemical shift offset ranges with respect to pulse duration. The performance function $\Phi_1 = |\langle U_F | U(T) \rangle|^2$, allowing all values for the phase factor $e^{i\phi}$, was used in (A), while the function $\Phi_0 = \langle U_F | U(T) \rangle$ was used in (B) with predefined value $e^{i\phi} = +1$. The maximum quality factors with respect to pulse duration are given for the three different bandwidths $\Delta\nu$ equal to 10 kHz, 20 kHz and 30 kHz.

function Φ_1 defined in equation 1.37 assures that the search for an optimum is performed within the full space of all possible transformations, or in other words, all values of the phase factor $e^{i\phi}$ are allowed. Whereas the choice of the performance function Φ_0 as defined in Eqn. 1.34 limits the space of allowed transformations to the phase factor $e^{i\phi} = +1$ only.

However, as was already pointed out in the previous section, for a given class of transformations the phase factor in question can only have two values, $+1$ and -1. This mirrors the fact, that in a given system the rotation around the axis γ with rotation angle ψ is fully equivalent to a rotation around the axis $-\gamma$ with rotation angle $2\pi - \psi$. In other words, the target propagator U_F is up to the direction of the rotation equivalent to propagator $-U_F$. It can happen that, depending on the chosen constraints for the rotation to be optimized, one target propagator, U_F or $-U_F$, could easier be reached then the other. Thus every optimization with performance function Φ_1 results in pulses performing either transformation U_F or transformation $-U_F$, and therefore every curve in Fig. 1.34 A should be a combination of corresponding curves from Figs. 1.34 B and C. A closer look to these curves and their juxtaposition is provided in Fig. 1.36. The value of the function Φ_0 is evaluated for every optimized pulse obtained in the optimization with performance function Φ_1 and its absolute value is plotted as a function of pulse length in Fig. 1.36 C and F, while its sign is marked on the plots. As expected, a part of the pulses has negative values of the function Φ_0 and the other part has positive values. Moreover, they are not randomly distributed, but arranged in periods, and these periods with different signs of the performance function alternate periodically, with period length of about 55 μs, which at the chosen power level of 10 kHz is slightly longer then a π-rotation. The periods where the optimized pulses have positive value of the performance function Φ_0, the performance of the best pulse optimized with predefined positive value of the phase factor $e^{i\phi}$ gets better then the performance of the best pulse optimized with predefined negative value of the phase factor; while periods with negative value of the performance function Φ_0 correspond to the periods where pulses with predefined negative value of the phase factor become best performing. This can be seen in Figs. 1.36 A and D, where the crossover periods of performances for $e^{i\phi} = \pm 1$ are indicated. Not only signs and period lengths are identical, so are the values on the curves, as can be seen when comparing the plots B with C and E with F in Fig. 1.36. Thus, the optimization which does not limit the value of the phase factor of the propagator, depending on the pulse length, results in same pulses as the best of either optimization with positive or negative performance function Φ_0 only. The situation is somewhat easier for 180°-rotation with rotation axis in the xy-plane since the two possible values of the phase factor describe identical rotations. Therefore, the 180° pulses optimized with the performance function Φ_1 are practically identical to pulses optimized with Φ_0 (c.f. Fig. 1.35).

1.7.3 Comparison to constructed rotations

As was shown in section 1.6, it is possible to construct a universal rotation pulse from pulse performing point-to-point transformation with half the desired flip-angle. The same
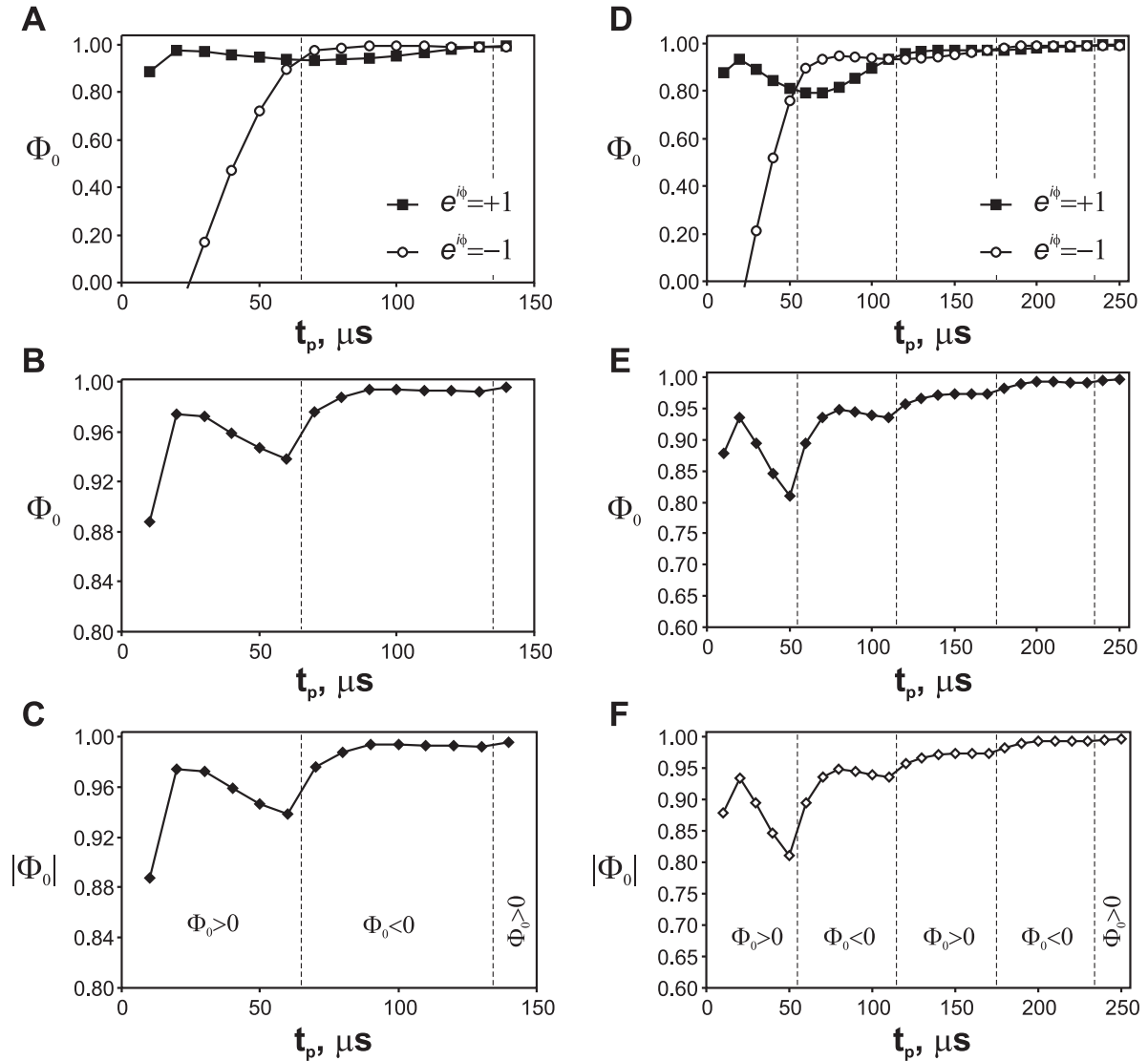
Figure 1.36: Comparison of maximum quality factors reached for optimizations of 90° rotations with performance function Φ_0 with different predefined phase factors for 10 kHz (left column) and 20 kHz (right column) offset ranges. Curves from Fig. 1.34 showing maximum quality factor vs. the pulse length for two possible phase factors are juxtaposed in (A) and (D), with corresponding combined best performances shown in (B) and (E). Performance curves obtained with performance function Φ_1 for the same offset ranges are shown in (C) and (F) with quality factors of final optimized pulses reevaluated according to the formula of performance function Φ_0 for which the absolute value is shown. Regions where rotations with different signs of the phase factor provide best performances are separated by dashed lines.

Table 1.4: Constraints used for optimizations of PP-pulses to be compared with UR-pulses

$\Delta\nu^a$ (kHz)	n_{off}	t_p, (μs)	flip angle
10	100	5 - 70	$\pi/4$
20	100	5 - 125	$\pi/4$
30	100	5 - 195	$\pi/4$
40	100	5 - 245	$\pi/4$
50	100	5 - 295	$\pi/4$
10	100	5 - 105	$3\pi/4$
20	100	5 - 150	$3\pi/4$
30	100	5 - 190	$3\pi/4$
40	100	5 - 225	$3\pi/4$
50	100	5 - 320	$3\pi/4$

^{a}) $\Delta\nu$ is defined as offset range used in the optimization.

rotations can also be optimized directly with procedures described in this chapter. It is therefore interesting to assess how the two procedures correlate, if at all, and to figure out whether the rotations constructed from point-to-point transformations can approach the optimal performance and under which circumstances.

As we just figured out, the optimizations of universal rotations result generally in two families of transformations differing in the sense of effective rotation, one or the other being preferred for the chosen parameter set. The effective rotation angle of one familie of transformations being the actual target angle ψ, and $2\pi - \psi$ being the effective rotation angle of the other family. This underlines the fact, that any universal rotation can be constructed from point-to-point transformations in two ways: either from PP-pulse with flip angle $\psi/2$ or from PP pulse with flip angle $(2\pi - \psi)/2$ (for the special case of 180°-rotation these two situations are obviously identical). Therefore we have to compare two different families of optimized pulses with two different families of constructed pulses.

For that purpose we optimized sets of PP-pulses for the same optimization parameters as for UR-pulse sets described in Table 1.3. Naturally, since now the pulses have to perform only point-to-point transformations with half the flip angle, the ranges of optimized pulse lengths differ now from lengths of the UR-pulse. According to aforementioned considerations we had to optimize sets of PP-pulses with flip angle of $\pi/4$ and with flip angle of $3\pi/4$ to compare with universal rotations with flip angle $\pi/2$, as well as sets of PP-pulses with flip angle $\pi/2$ to compare with universal rotations with flip angle π. The latter however did not require extra optimization runs, since one can use pulses optimized in section 1.3.3. To be relevant for the comparison to the construction procedure all optimizations of these point-to-point pulses have to consider $M_0 = M_y$ as initial magnetization. Full parameter sets of optimized pulses are listed in Table 1.4.
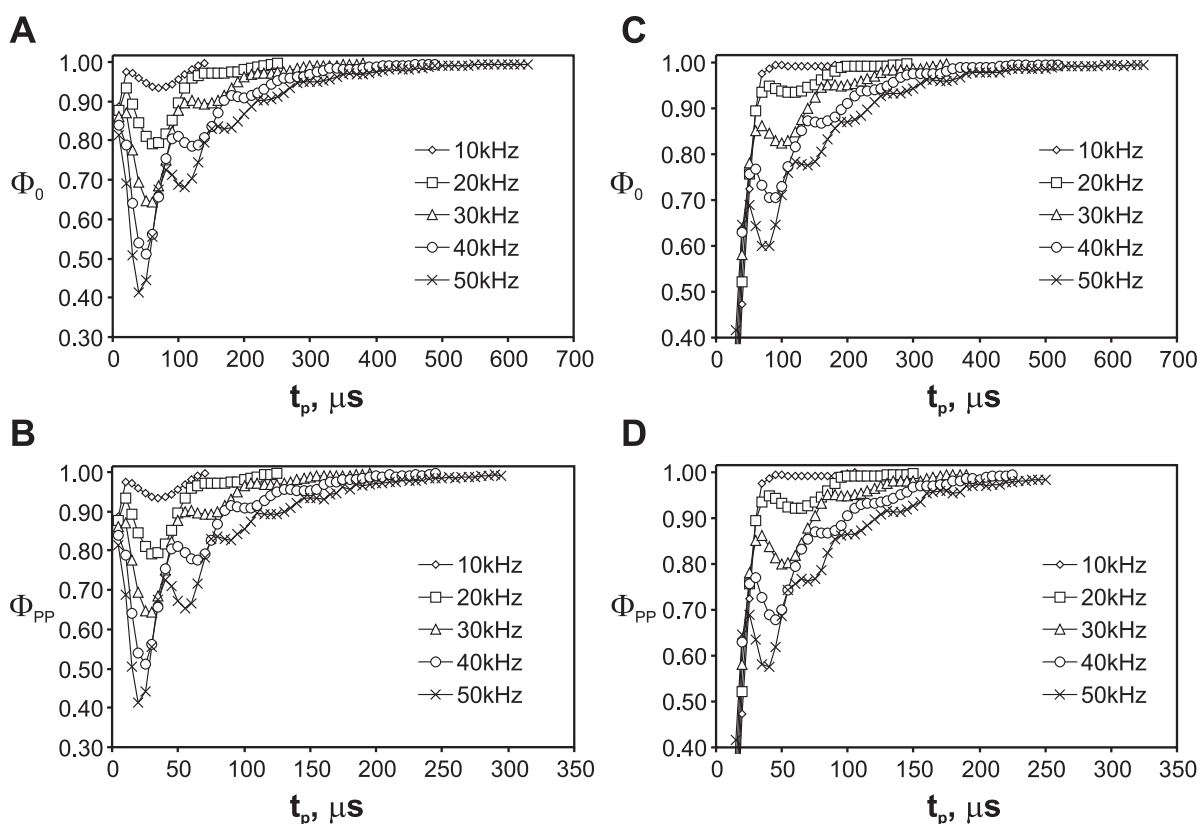
Figure 1.37: Comparison of constructed and directly optimized universal rotations. Maximal quality factors reached for optimizations of 90° rotations with performance function Φ_0 and phase factors preset to +1 (A) and -1 (C) in comparison with maximal quality factors reached for optimizations of point-to-point pulses with flip angle $\pi/4$ (B) and $3\pi/4$ (D) and same optimizations parameters as for the plots (A) and (C) respectively.

The results of the calculations are shown in Fig. 1.37. One can see that the curves for 90° universal rotation propagators with phase factor +1 (plot A) are identical to the curves for point-to-point pulses with flip angle 45° (plot B) with the only difference that the latter is exactly two times shorter. Analogously, the curves for 90° universal rotation propagators with phase factor -1 (plot C) have identical appearance as the curves for point-to-point pulses with flip angle 135° (plot D) with latter curves being again two times shorter, then the former ones. Remarkably, the point-to-point pulses show strongly oscillating curves, unlike the curves for excitation pulses from section 1.3.3. The reason for this was discussed in the previous section: since both initial and target magnetization states have transverse components, for shorter pulses the additional chemical shift evolution cannot be refocused with increased pulse length.

The quality factors of point-to-point pulses cannot be directly compared with the ones of universal rotations, because they are defined differently. But the direct comparison of quality factors of UR-pulses constructed from these optimised half flip-angle PP-pulses

with quality factors of directly optimized pulses of the same length (twice the length of th PP pulse) shows that they are basically identical with differences up to only $\pm 0.01\%$ for the 10 kHz offset range and $\pm 4\%$ for the 50 kHz offset range. This shows that these two ways of obtaining universal rotations are largely equivalent, and the construction of universal rotations from point-to-point transformations produces pulses that are already optimal for a chosen parameter set. However, the direct optimization procedure is by no means redundant: one can easily imagine a situation where the construction procedure simply is not able to create a desired universal rotation which otherwise can be created by direct optimization. Since the construction procedure implies that the rotation axes are symmetric with respect to the offset (see section 1.6), it is generally impossible to create UR-pulses with rotation axes varying with offset or rf-amplitude (a "pattern rotation" similar to "pattern pulses" described in section 1.5) by simple construction out of PP-pulses.

1.7.4 Symmetry properties of universal rotations

The comparison of performance efficiencies of directly optimized universal rotation pulses has shown that they are equivalent to the efficiencies of pulses constructed out of point-to-point transformations. It is therefore interesting to figure out, how do the pulse shapes correspond to each other. The construction procedure generates pulses with symmetric pulse shape: if presented in cartesian coordinates they have one component symmetric with respect to the center of the shape, the other component is antisymmetric. The optimization procedure does not impose any symmetry constraints whatsoever. The question therefore is, whether the directly optimized pulses also have the same kind of symmetry, or if there are also some other pulse families with equal performance.

Some typical representative pulse shapes from direct optimization of 90°-rotation over 30 kHz offset range are shown in Fig. 1.38. As for other optimizations in previous sections, for very short pulse lengths the usual hard pulse with constant amplitude and phase has the best performance. With increasing pulse length the hard pulse first gets slightly more complicated, this time by two symmetrically placed 180° phase jumps. With pulses getting longer, the pulse shapes also get more complicated. Fig. 1.38 shows that most of the optimized pulses do possess in fact a certain symmetry. As expected, we encounter pulses with the same symmetry as in the construction procedure (Fig. 1.38 D) with one component being symmetric and the other antisymmetric, but also pulses with both components symmetric, as well as pulses where one component has zero intensity, which can also be considered as a special case of one of the previous symmetries. A fourth class of pulses (though relatively small percentage of all optimized pulses) has shapes which are neither symmetric nor antisymmetric in any of its components.

Since no symmetry constraints were imposed on the pulse shapes during the optimizations, it is of no surprise that some of the produced pulses have nonsymmetrical pulse shape. It is more surprising that such nonsymmetrical pulses constitute only a small minority among pulses with symmetrical pulse shapes. Among symmetric pulses we could figure out two distinct kinds of symmetry: pulses with both symmetric components (called
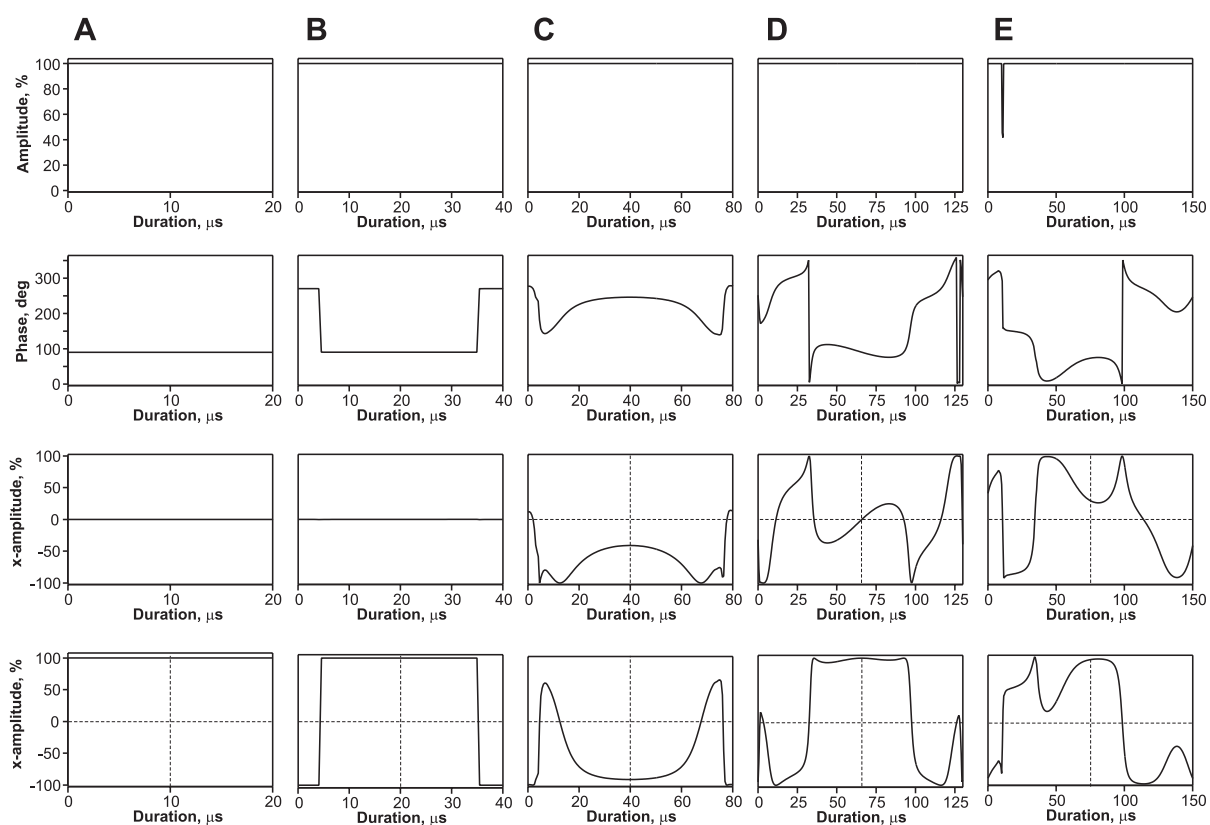
Figure 1.38: Pulse shapes of some universal $\pi/2$-rotation pulses optimized for 30 kHz offset range. Amplitudes and phases are shown (upper two rows) as well as representations in Cartesian Coordinates (lower two rows). To underline the symmetries of the pulses reference dashed lines are drawn at the middle of time and amplitude scales in the lower two rows.

Table 1.5: Constraints used for optimizations of PP-pulses with imposed symmetry constraints

$\Delta\nu^a$ (kHz)	n_{off}	t_p, (μs)	rotation angle	phase factor	symmetry type
30	100	10 - 380	$\pi/2$	+1	I
30	100	10 - 380	$\pi/2$	+1	II
30	100	10 - 380	$\pi/2$	+1	III
30	100	10 - 380	$\pi/2$	+1	IV
30	100	10 - 350	$\pi/2$	-1	I
30	100	10 - 350	$\pi/2$	-1	II
30	100	10 - 350	$\pi/2$	-1	III
30	100	10 - 350	$\pi/2$	-1	IV
30	100	10 - 360	π	+1	I
30	100	10 - 410	π	+1	II
30	100	10 - 230	π	+1	III
30	100	10 - 230	π	+1	IV

^{a}) $\Delta\nu$ is defined as offset range used in the optimization.

type I) and pulses with one symmetric component and other antisymmetric (called type II). However one can imagine two more similar kinds of symmetry: the one with one symmetric component and the other antisymmetric (like type II, but with exchanged components, called type III), and the type with both components being antisymmetric (called type IV). The question is whether the universal rotations with symmetries of types III and IV really cannot be as good as those with symmetries of types I and II, or if it is just a coincidence, that only universal rotation with symmetries I and II were produced in optimizations. To figure that out we performed a series of optimizations where we intentionally imposed the discussed symmetry constraints onto the pulse shapes. For each set of parameters, pulse lengths were varied in ranges as listed in Table 1.5.

The results of the optimizations are shown in Fig. 1.39. The performance of the optimized pulses described by the quality factor Φ_0 is given as a function of pulse length for 90°-rotations (A) with propagator phase factor +1, 90°-rotations with phase factor -1 (or equivalent to 270°-rotations)(B) and for 180°-rotations (C). For every rotation type four different symmetry constraints were imposed. For comparison, results of optimizations with same optimization parameters and without symmetry constraints are shown in Fig. 1.39 A'-C'. As can be seen, the two symmetry classes which we have observed amongst shapes optimized without symmetry constraints have almost identical performance curves on the whole optimization interval, with pulses of class II being slightly better performing over the short interval between 150 and 200 μs for 90°-rotations (Fig. 1.39 A), and pulses of class I being slightly better performing over the short interval between 80 and 160 μs for 270°-rotations (Fig. 1.39 B). The pulses with symmetry of the type III and
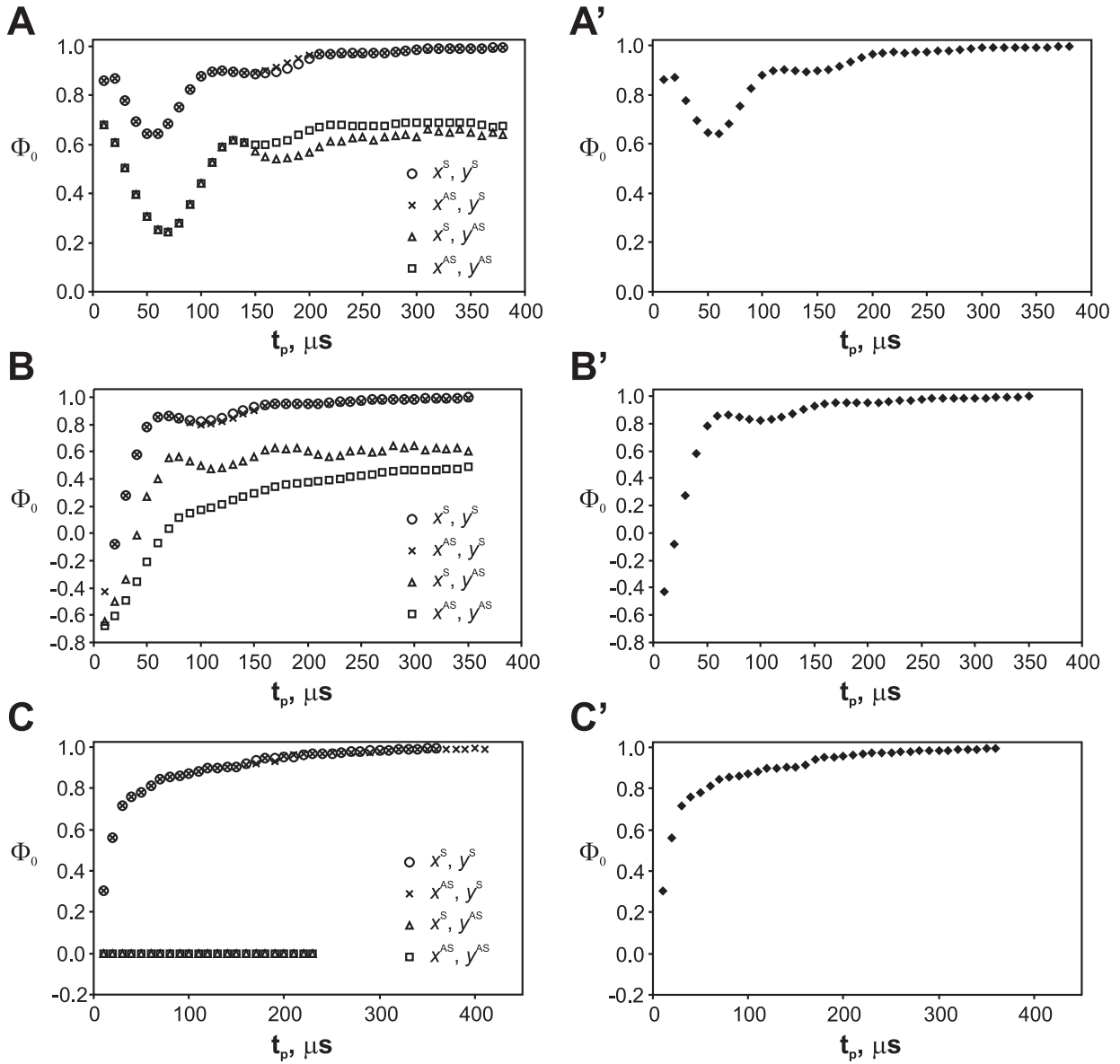
Figure 1.39: Comparison of universal rotation pulses optimized with symmetry constraints imposed (A-B) with pulses optimized with no symmetry constraints (A'-C'). $\pi/2$-rotations (A, B) and π-rotations (C) were optimized for a 30 kHz offset range with performance function Φ_0 and phase factors preset to +1 (A) or -1 (B), respectively (see text). Pulses without symmetry constraints were optimized under identical conditions. Four symmetry types were used (see text for details).

IV have clearly worse performance, and therefore it is clear why they did not show out in optimizations with unrestricted symmetries. In the case of 180°-rotations (Fig. 1.39 C) the figure is similar: the curves for the pulses with symmetry types I and II are almost identical, while those for symmetry types III and IV not only indicate worse performance of corresponding pulses, but they have quality factor value of exactly zero for pulses of any duration. Moreover, in every plot the best performing symmetric pulses have the same performance as best optimized pulse from the right column of Fig. 1.39. One can thus conclude, that for a given set of parameters the subspace of symmetric pulses of types I and II is already optimal. Though few unsymmetric pulses emerged during unconstrained optimization, they could in fact be suboptimal pulses with uncompletely converged optimizations (with the optimal symmetric pulse being only slightly better and of virtually undistinguishable performance), and the subspace of symmetric pulses would indeed be the subspace of optimal solutions.

As was pointed out in [72], the symmetries of the total rotation R_{tot} applied to a magnetization lead without further manipulation to symmetries of the magnetization response. Also the fact that for 180°-rotations the two out of four possible symmetries produce pulses with quality factor of exactly zero clearly indicates that in that case the symmetry alone leads to a rotation fully orthogonal to the target rotation. It is therefore interesting to figure out which symmetries in the magnetization responses are introduced by the four symmetry types we are dealing with. Therefore to gain first insight to these symmetries we investigated the effective rotation produced by such symmetric pulses. Fig. 1.40 shows the x, y and z components of the rotation vectors $\vec{r} = \beta \vec{e}$, where β is the effective rotation angle and $\vec{e}$ is the unit vector pointing along the rotation axis, for four optimized pulses with four different symmetry types and 60 kHz offset range, whereas the pulses were optimized for the offset range of only 30 kHz. At a first glance one can see that in cases of rotations with one symmetric component and one antisymmetric one rotation component cancels completely, while rotations with both symmetric components or both antisymmetric components have rotation components symmetric or antisymmetric with respect to the rf-offset. In the following we consider this properties in more detail for all four cases.

Fully symmetric case

To show the offset properties of rotations introduced by the symmetry of the rotation we use the notations introduced in [72] and some formulas derived there.

A composite rotation can be represented as a series of piecewise constant rotations, which for a rotation at an offset ω can be represented as

$$\mathbf{R}_{\text{tot}}(\omega) = \mathbf{R}_n \cdots \mathbf{R}_2 \mathbf{R}_1, \tag{1.83}$$

and the effective rotation caused by the same pulse train at the offset $-\omega$ can therefore be represented as

$$\mathbf{R}_{\text{tot}}(-\omega) = \mathbf{R}_n^Z \cdots \mathbf{R}_2^Z \mathbf{R}_1^Z, \tag{1.84}$$
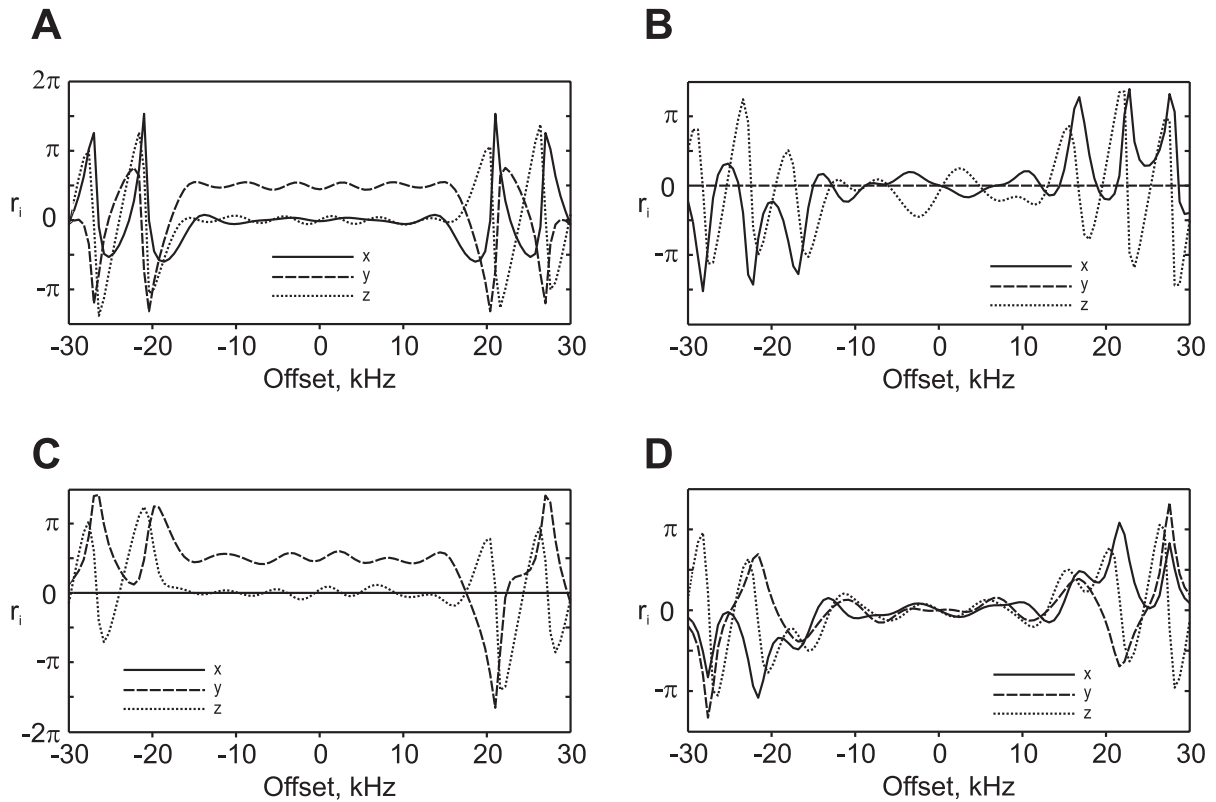
Figure 1.40: The offset profiles of four pulses optimized to perform $\pi/2$-rotation around y-axes with symmetry constraints imposed: (A) both x- and y-components of the pulse shape are symmetric, (B) x-components is symmetric, y antisymmetric, (C) x-components is antisymmetric, y symmetric, (D) both x- and y-components are antisymmetric. x, y and z components of the rotation vector $\vec{r} = \beta\vec{e}$, where β is the effective rotation angle and $\vec{e}$ is the unit vector pointing along the rotation axis, are given in radians.

where the superscript Z represents the reflection of a rotation axis across the plane $z = 0$ (then, as shown in [72], $[\mathbf{R}(V_x, V_y, V_z)]^Z = \mathbf{R}(V_x, V_y, -V_z)$). While our rotation is fully time symmetric, one can rewrite Eqn. 1.84 as

$$
\begin{aligned}
\mathbf{R}_{\text{tot}}(-\omega) &= \mathbf{R}_1^Z \mathbf{R}_2^Z \cdots \mathbf{R}_n^Z \\
&= \mathbf{R}_{\text{tot}}^Z(\omega).
\end{aligned}
\tag{1.85}
$$

Hence, for the fully time symmetric rotation the rotation components x and y are symmetric with respect to the rf-offset, while the z-component is antisymmetric, which can also be observed in Fig. 1.40 A.

Fully antisymmetric case

Consider now the case of a rotation with x and y components of the pulse shape being antisymmetric, for which therefore holds

$$
\mathbf{R}_m = \mathbf{R}_{n+1-m}^{XY}.
\tag{1.86}
$$

Thus for a negative offset $-\omega$ we can write

$$
\begin{aligned}
\mathbf{R}_{\text{tot}}(-\omega) &= \mathbf{R}_n^Z \cdots \mathbf{R}_2^Z \mathbf{R}_1^Z \\
&= \mathbf{R}_1^{ZXY} \mathbf{R}_2^{ZXY} \cdots \mathbf{R}_n^{ZXY} \\
&= \mathbf{R}_1^{-1} \mathbf{R}_2^{-1} \cdots \mathbf{R}_n^{-1},
\end{aligned}
\tag{1.87}
$$

where in the second line we have used the property 1.86 and then Eqn.(4) from [72], $\mathbf{R}^{XYZ} = \mathbf{R}^{-1}$. Using Eqn.(6) from [72] we can rewrite the last equation as

$$
\begin{aligned}
\mathbf{R}_{\text{tot}}(-\omega) &= \mathbf{R}_1^{-1} \mathbf{R}_2^{-1} \cdots \mathbf{R}_n^{-1} \\
&= (\mathbf{R}_n \cdots \mathbf{R}_2 \mathbf{R}_1)^{-1} \\
&= \mathbf{R}_{\text{tot}}^{-1}(\omega) = \mathbf{R}_{\text{tot}}^{ZXY}(\omega).
\end{aligned}
\tag{1.88}
$$

Hence, all rotation components of such pulse shape are antisymmetric with respect to the rf-offset, which is also observed in Fig. 1.40 D.

Symmetric/antisymmetric case

For the case where the x component of a pulse shape is symmetric and the y component antisymmetric we can write

$$
\begin{aligned}
\mathbf{R}_{\text{tot}} &= \mathbf{R}_n \cdots \mathbf{R}_2 \mathbf{R}_1 \\
&= \mathbf{R}_1^Y \mathbf{R}_2^Y \cdots \mathbf{R}_n^Y \\
&= (\mathbf{R}_n \cdots \mathbf{R}_2 \cdots \mathbf{R}_1)^Y \\
&= \mathbf{R}_{\text{tot}}^Y,
\end{aligned}
\tag{1.89}
$$

which means that this rotation is invariant with respect to reflection in the xz-plane, or in other words, that this rotation has all its components lying in the xz-plane, with the y-component of the rotation being strictly zero. This can also be seen in Fig. 1.40 B.

Analogously, for a case of a rotation with the y component of a pulse shape being symmetric and the x component being antisymmetric we will get

$$\mathbf{R}_{\text{tot}} = \mathbf{R}_{\text{tot}}^{X}, \tag{1.90}$$

which would mean that this rotation has all its components lying in the yz-plane, with x-component of the rotation being strictly zero. This can also be seen in Fig. 1.40 C.

No surprise therefore, that in the case of 180° rotations around the y axis, as has been optimized for the plots of Fig. 1.39, the rotations with symmetry types III and IV generated rotations fully orthogonal to the desired ones: in the first case the rotation components are all zero for the defined rotation axis, and in the second case the desired propagator can only be achieved one half of the offsets, while the other half will then experience the rotation in opposite direction.

1.8   Experimental applications of optimized pulses

Although dual compensation for RF inhomogeneity/miscalibration and chemical shift offset effects in excitation has been difficult to achieve [18, 35, 41, 48, 50, 75–82], broadband excitation by optimized pulses (BEBOP) has been shown (*vide supra*) to be an effective solution for RF tolerance of 10–15%, which is typical of calibrated pulses output by high-quality RF probes. Broadband in this context refers to a pulse capable of uniformly exciting the entire ^{13}C chemical shift range at field strengths of 800–900 MHz, requiring a bandwidth of 40–50 kHz.

Broadband pulses which tolerate an even higher degree of RF inhomogeneity could also be useful. NMR-spectroscopy on natural products is one potential application. For example, calibration of ^{13}C-pulses is extremely difficult for natural abundance samples at very low concentration. Moreover, significant variations in pulse length can be caused by varying salt concentrations. Sufficient RF tolerance would remove the need for painstakingly accurate pulse calibrations, which are also important for optimal sensitivity of many complex multidimensional experiments or the automated acquisition of a large number of strongly differing samples. To accommodate the majority of ^{13}C probes in use, the pulse should operate equally well for a peak RF output anywhere in the range 10–20 kHz (25–12.5 ls pulse width). The constant-amplitude pulse satisfying all this conditions was optimized by means of optimal control theory and described above in section 1.3.4. The assessment of the performance of this pulse in comparison with other existing pulses and its applications in HSQC and HMBC-type experiments are discussed in a following section.

1.8.1   Pulse performance and comparison to existing pulses

Although adiabatic pulses accomodate a wide range of peak power levels, the exceptional bandwidth of adiabatic inversion for a given peak RF amplitude does not translate to excitation. The orientation of the effective RF field at the end of an adiabatic excitation pulse, which, ideally gives the location of the magnetization, is not in the transverse plane for nonzero chemical shift offset. Other existing excitation pulses [18, 35, 41, 48, 50, 75–82] provide only limited dual compensation for RF variability and resonance offset. Moreover, they have not demonstrated a performance advantage over phase-compensated hard pulses, so hard 90° pulses could be considered the benchmark for broadband performance in sequences that are readily phase-corrrected.

The theoretical performance of the optimized pulse of Fig. 1.14 and of a conventional hard pulse are illustrated in Fig. 1.41. Contours of resulting x magnetization, M_x, are plotted as functions of resonance offset and RF amplitude of the pulses (Fig. 1.41 A,C). Similarly, the contours of magnetization in the transverse plane, $\sqrt{M_x^2 + M_y^2}$, are shown for the hard pulse in comparison (Fig. 1.41 B). The M_x magnetization excited by a hard pulse is strongly dependent on offset, with a narrow bandwidth of approximately ±2.5 kHz for greater than 99% excitation, using a calibrated RF amplitude of 15 kHz (Fig. 1.41 A). In most applications, however, excitation pulses are used around evolution periods, in
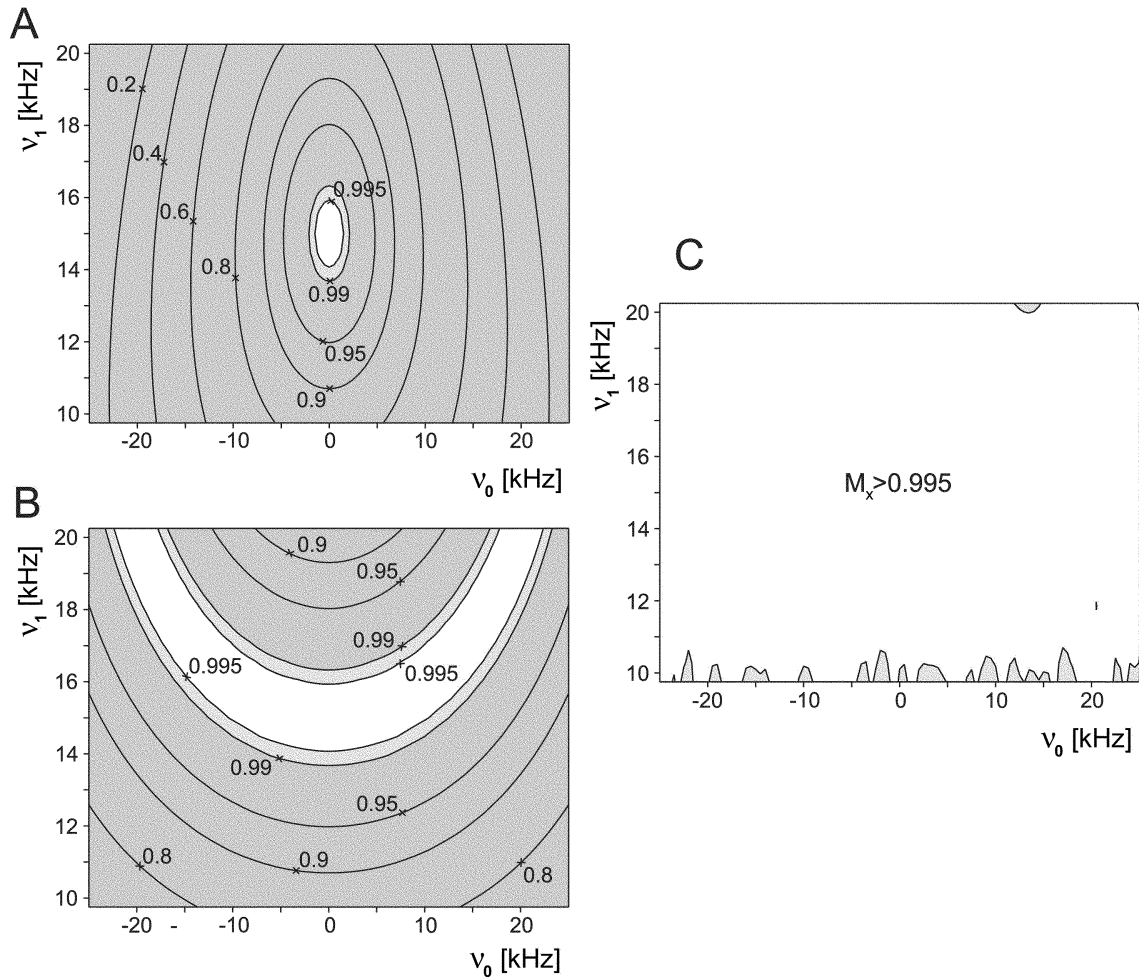
Figure 1.41: Simulated performance of a hard excitation pulse (A,B) and the optimized PM-BEBOP pulse of Fig. 1.14 (C) with nominal RF amplitude of 15 kHz each. Theoretical transfer from initial z magnetization M_0 to M_x (A,C) and M_0 to the transverse plane $\sqrt{M_x^2 + M_y^2}$ (B) is shown. White areas correspond to transfers larger than 99.5 %, light gray to transfer between 99.0 and 99.5 % and darker gray to transfer below 99.0 %. While transfer to M_x for the hard pulse has very limited bandwidth and tolerance to RF variation (A), the phase modulated BEBOP pulse shows almost perfect excitation over the whole offset and RF amplitude range shown. In readily phase- compensated pulse sequences the transfer of initial magnetization to the transverse plane is important, as shown in (B) for the hard pulse. The performance of the hard pulse in this case is strongly improved compared to its transfer properties to M_x, but there is significant loss per applied pulse for amplitudes lower than the nominal 15 kHz.
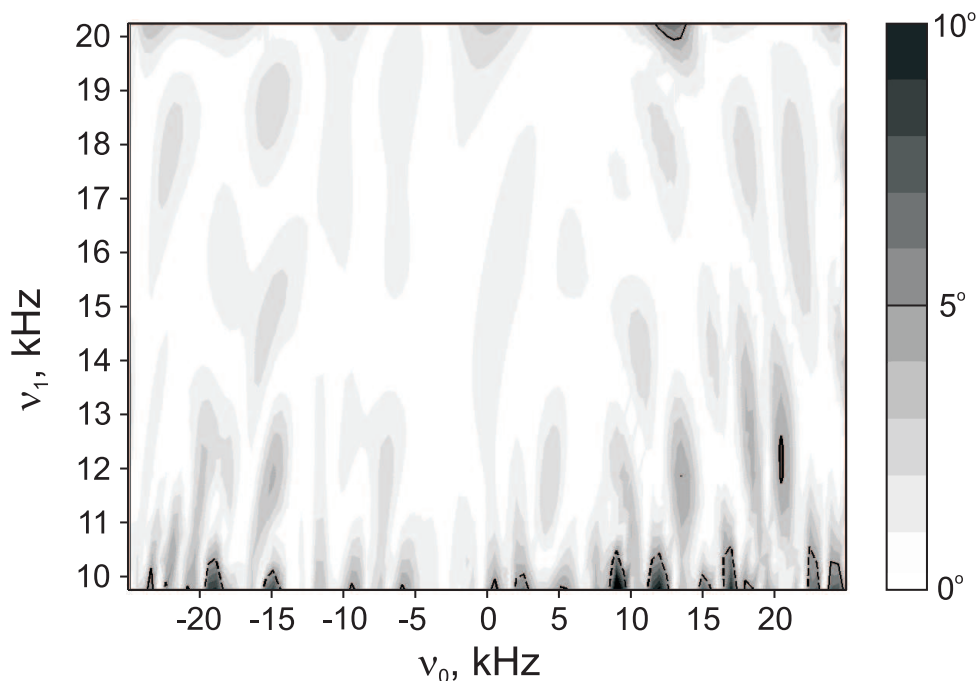
Figure 1.42: The phase behavior of the optimized PM-BEBOP pulse of Fig. 1.14 is plotted as a function of RF amplitude ν_1 and resonance offset ν_0. Phase deviations from an ideal excitation pulse are shown in 1° steps in different shades of gray (see scale to the right). For almost the entire range of offsets and RF amplitudes, the phase is less than $2-3$ °, with minor distortion in the $6-9$ ° range at the lowest RF (10 kHz) in the optimized range.

which case phase deviations can be compensated by a first order phase correction. Hence, the excitation profile of transverse magnetization, $\sqrt{M_x^2 + M_y^2}$, is more appropriate for a comparison, resulting in a bandwidth of ± 12.5 kHz with larger than 99% excitation for a calibrated 15 kHz hard pulse (Fig. 1.41 B).

Regardless of the application, hard excitation pulses are significantly affected by RF miscalibrations. On-resonance, where the performance is best, only 90 % of magnetization is brought into the transverse plane if the pulse amplitude deviates by 25 % from its nominal value. For the optimized phase- modulated BEBOP (PM-BEBOP) pulse of 1 ms duration the excited magnetization M_x is better than 99% of the initial z magnetization, M_0, over the targetted factor of 2 variation in the nominal RF delivered by the coil and resonance offsets of ± 25 kHz, as shown in Fig. 1.41 C. Phase deviations over the optimization window are typically less than $2-3$ ° (cf. Fig. 1.42), which is sufficient for the majority of NMR experiments. In applications with a high dynamic range, as for example in ^{1}H-NOESY experiments, this phase behavior might not be adequate. In such cases, pulses with more stringently optimized phase behavior (and shorter pulse length) can be used [36, 57], with the proviso that they also require more accurate calibration.

The experimentally acquired excitation profiles of this pulse, showing an excellent match with theory, are presented in Fig. 1.15.

1.8.2 2D – applications

The benefits of using PM-BEBOP in practical NMR applications are well- illustrated by ^{13}C-^{1}H correlated experiments, as e.g. HSQC or HMBC. An important element of these types of experiment is the sub-sequence $90°–t_1–90°$ applied to the ^{13}C spins to encode the frequencies for the first dimension of the 2D spectrum. The linear phase roll of a hard $90°$ pulse is commonly eliminated from the first spectral dimension by subtracting a constant time (equal to $4\,t_{90}/\pi$) from t_1. Details of the mechanism responsible for this "rephasing" are straightforward, but it suffices to note merely that one can expect approximately phase-corrected performance from hard $90°$ pulses in HSQC-type sequences, at least in the absence of RF inhomogeneity.

Two-dimensional spectra were recorded on a Bruker Avance 500 spectrometer using a $\approx$500 mM menthol sample dissolved in CDCl$_3$. Standard HSQC [83, 84] and HMBC experiments [85, 86] were acquired with variations in offset, RF amplitude, and the kind of pulses applied on ^{13}C nuclei. The maximum RF amplitude of the Bruker TXI probehead used corresponds to 14.3 kHz (equivalent to a $90°$ pulse of 17.5 μs). To avoid maximum power for the shaped pulses, we used slightly lower RF amplitudes of 12 kHz for the nominal power. This scales to a 1.2 ms PM-BEBOP pulse covering $\pm$20 kHz bandwidth (rather than the 15 kHz nominal amplitude corresponding to the 1 ms pulse, which has a bandwidth of $\pm$25 kHz). The total sweep width needed for covering the ^{13}C-spectra of menthol on a 500 MHz spectrometer is $\approx$8 kHz. We therefore decided to record three spectra with 0, 8, and 16 kHz offset relative to the center of the ^{13}C- spectral width, leading to a coverage of offsets corresponding to $-$4-4 kHz, 4- 12 kHz, and 12-20 kHz, respectively. Since spectral width and offsets are matched, no folding artefacts were observed.

Based on the procedure described in section 1.5.1 we also constructed a 2.4 ms universal rotation $180°$ pulse (consisting of both the phase and time- reversed and the original PM-BEBOP pulse of 1.2 ms duration each) with identical active bandwidth. The performance of the resulting refocussing pulse with respect to offset and RF amplitude in comparison to a hard $180°$ pulse is shown in Fig. 1.43. In order to test the robustness of the pulse sequences with respect to variation in RF amplitude, hard and shaped pulses were set to 8, 10, and 12 kHz RF amplitude.

For each combination of offset and RF amplitude three HSQC and three HMBC experiments were acquired using only hard pulses, hard excitation but shaped PM- BEBOP-based $180°$ pulses, and only shaped PM-BEBOP excitation and PM- BEBOP-based refocussing pulses, respectively, on ^{13}C nuclei (Fig. 1.44, 1.45). In the series of experiments with shaped excitation pulses, the $90°$ flip back pulse after the ^{13}C evolution period was replaced by the time reversed PM-BEBOP pulse for optimal transfer $M_x \rightarrow M_z$. In Figs. 1.46 and 1.47 representative slices of all 2D-spectra acquired through the signals corresponding to C$_6$H$_6^{eq}$ and C$_1$H$_7$, respectively, are shown. The slices taken from HMBC spectra are shown in magnitude mode.
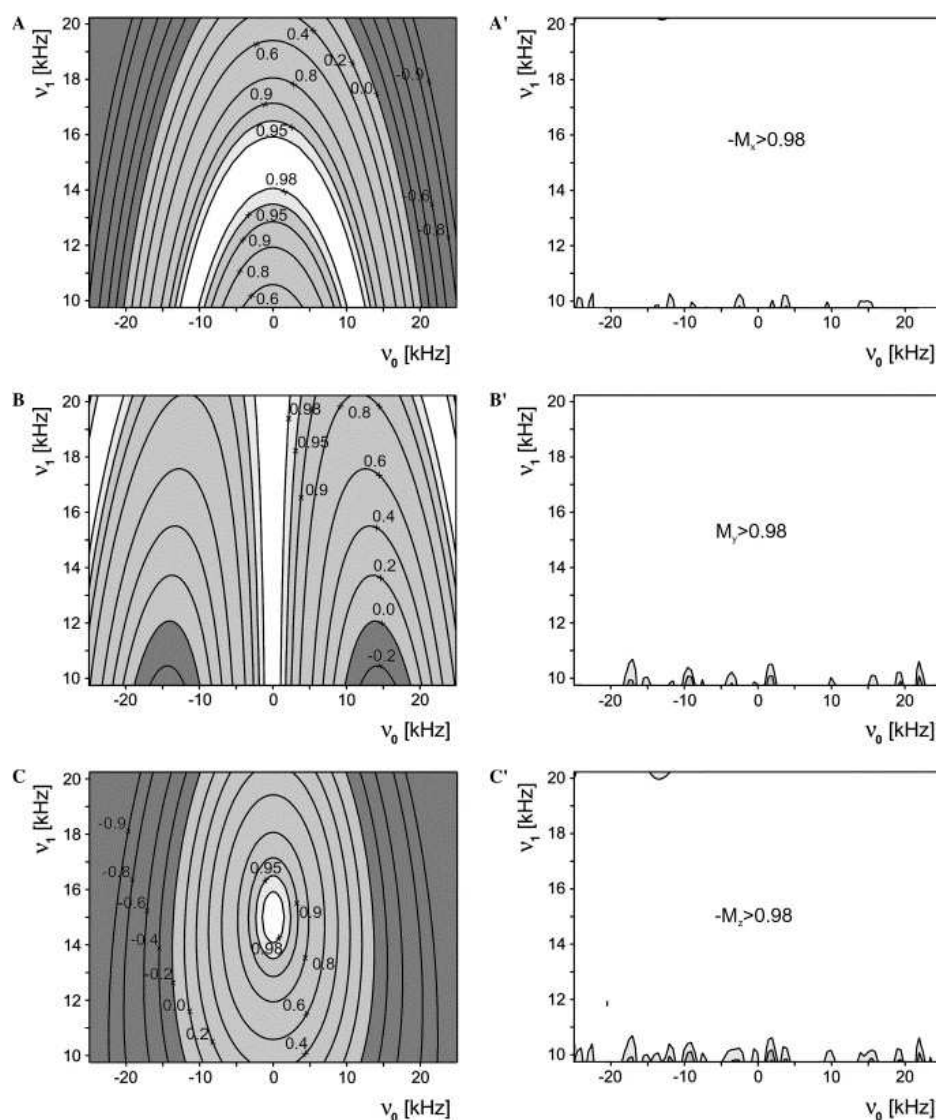
Figure 1.43: Simulated refocusing performance is shown as a function of RF amplitude ν_1 and resonance offset ν_0 for a hard 180° pulse generating the transformations (A) $-M_x \to M_x$, (B) $M_y \to M_y$, and (C) $M_z \to -M_z$. The corresponding performance of a shaped 180° pulse constructed from the optimized PM-BEBOP pulse of Fig. 1.14 using the procedure described in section 1.5.1 is shown in the second column of figures. The nominal RF amplitude is 15 kHz in all cases. White areas correspond to transfers larger than 98.0 %, light gray to transfer between 95.0 % and 98.0 %, gray to lower positive transfer, and dark gray to transfer where the resulting magnetization is still negative. While refocusing for the hard pulse has very limited bandwidth and tolerance to RF variation, the pulse constructed from the PM-BEBOP pulse shows very good refocusing properties over the whole offset and RF amplitude range shown.

On resonance and with correctly calibrated hard pulses, the performance of all three HSQC experiments is more or less identical (c.f. Fig. 1.46 A). However, as soon as either RF amplitude or resonance offsets are changed, the signal intensity of the hard pulse HSQC decreases substantially and at offsets larger than 15 kHz the signal falls to ≈0 (c.f. Fig. 1.46 C-C″). In addition, large phase rolls are observed in the indirect dimension.

Most of the signal loss is due to the bad performance of the uncompensated hard 180° pulses. As expected from previous reports [78,79,87,88], exchanging the hard pulses with the PM-BEBOP-based refocussing pulse recovers most of the signal, so that for RF amplitudes 3.5 dB lower than the nominal value and an 8 kHz offset the signal intensity is practically identical to the on resonance case with calibrated RF amplitude.

In comparison, it is difficult to find broadband adiabatic refocusing pulses that achieve the performance of the new pulse shown in Fig. 1.43. To work properly, they must be sufficiently adiabatic, which is determined by pulse length, peak RF, and the frequency sweep range of the pulse (related to bandwidth). Typical adiabatic pulse shapes require pulse lengths of 34 ms to refocus over a 20 % smaller bandwidth and smaller range of RF tolerance. The best adiabatic refocusing we could find (matching the 98 % refocusing of Fig. 1.43) was achieved with WURST-20 [89]. Using a 0.5 ms pulse with a 94 kHz frequency sweep as the constituent inversion pulse of the 3π procedure described in [79] resulted in a 2 ms refocusing pulse which covered the full 50 kHz bandwidth for peak RF in the range 11.5–22 kHz

Nevertheless, for larger offsets and lower RF amplitudes the overall intensity of experiments is also affected by the decreased performance of hard excitation pulses. At an offset of 16 kHz and a 3.5 dB miscalibrated RF amplitude, for example, the signal intensity is reduced by about one third (Fig. 1.46C″). When all carbon pulses are replaced by PM-BEBOP excitation and refocussing pulses, the signal intensity is restored also in these cases and virtually identical performance for the HSQC experiment is observed for the whole range of offsets and RF amplitude settings shown in Fig. 1.46.

The set of experiments recorded for the state of the art HMBC basically lead to identical results with respect to signal intensities (cf. Fig. 1.47). PM-BEBOP pulses appear to have a utility for excitation and refocussing pulses similar to adiabatic pulses for RF-compensated inversion, with no variation in pulse performance over the targetted offset and RF amplitude ranges.

We see, that a 1 ms pulse is capable of uniformly exciting the entire 200 ppm ^{13}C chemical shift range of a potential 1 GHz spectrometer for a peak RF amplitude anywhere in the range 10–20 kHz. This provides an unprecedented combination of bandwidth and tolerance to RF inhomogeneity. HSQC and HMBC experiments show the practical benefits of the new pulse. To the best of our knowledge, this is the first time that any shaped or composite RF pulse has proven to be significantly better than hard 90° pulses in applications where the linear phase roll of the hard 90° pulse is compensated (HSQC) or irrelevant (HMBC single-bond filter). For probes which have a peak RF in this range, which should cover the vast majority of probes, one needs only to set the RF slightly lower then maximum power to ensure complete and distortionless excitation. This removes one
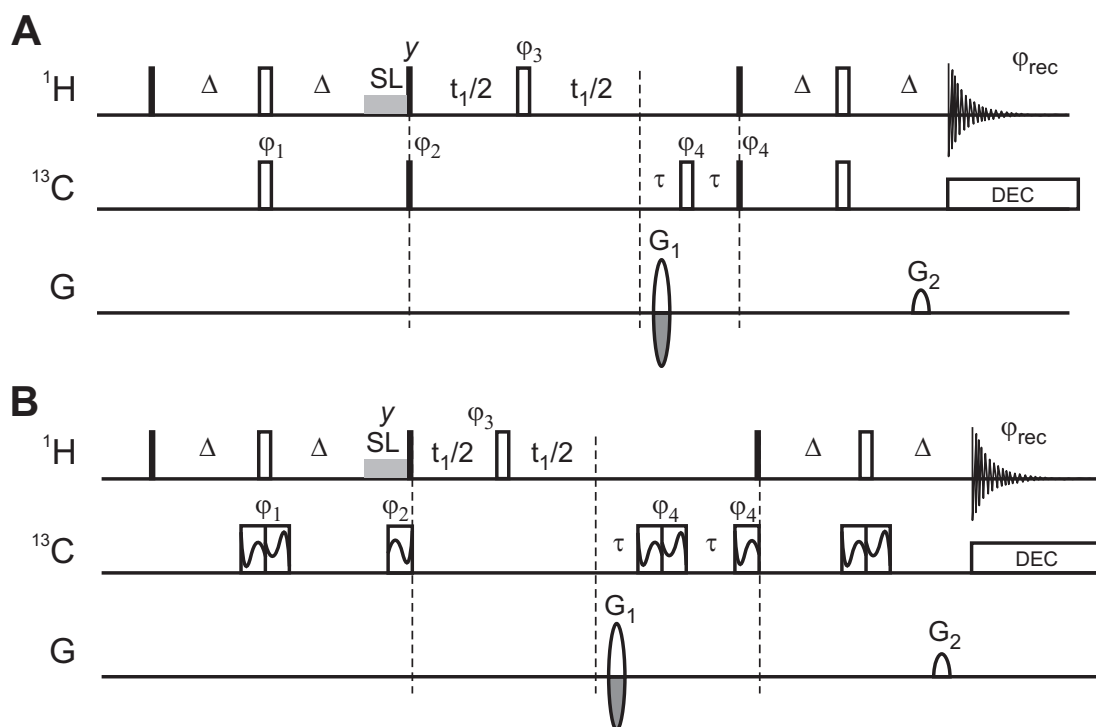
Figure 1.44: HSQC pulse sequences used for the comparison of signal intensities shown in Fig. 1.46. The reference HSQC based on hard pulses is shown in (A). In the sequence shown in (B) all ^{13}C-pulses are replaced by PM-BEBOP-based excitation and refocussing pulses. PM-BEBOP pulses are schematically shown as rectangular pulses (representing constant RF amplitude) containing a wavy line (representing phase-modulation). Phase and/or time reversals are illustrated by vertical and/or horizontal mirroring of the wavy lines in the boxes, respectively. Phases are $\varphi_1 = x$, $\varphi_2 = x, -x$, $\varphi_3 = x, x, -x, -x$, $\varphi_4 = 4(x), 4(-x)$, $\varphi_{rec} = x, -x, x, -x, -x, x, -x, x$. G1, φ_1, φ_2, and φ_{rec} are cycled $\pm$ according to echo/antiecho acquisition scheme. If not stated otherwise, all pulses have x phase.
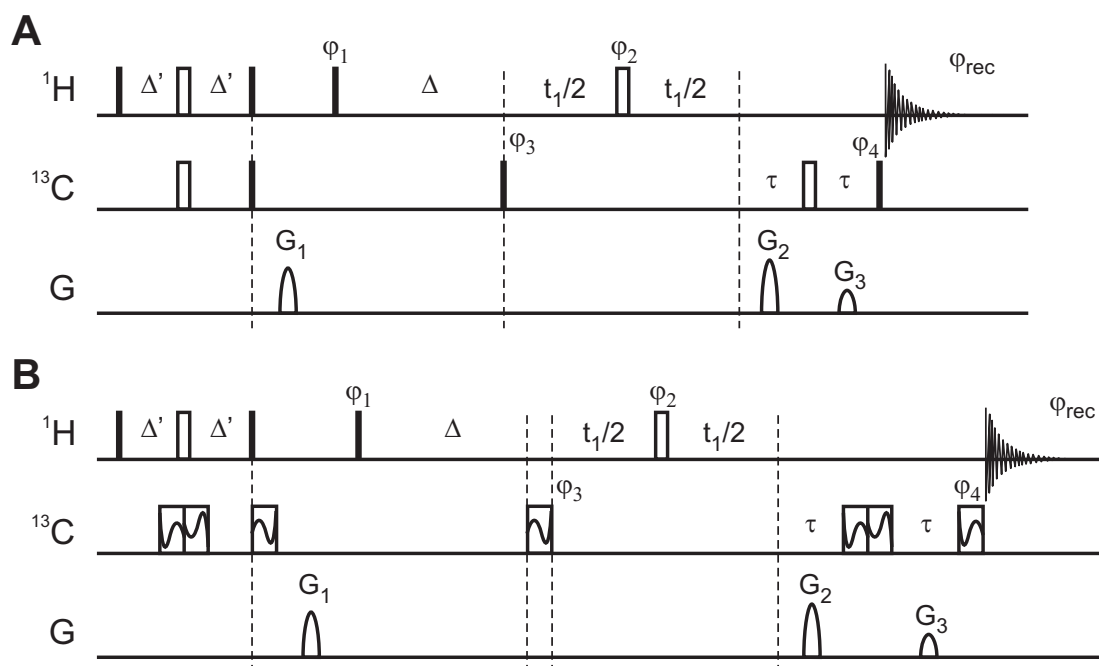
Figure 1.45: HMBC pulse sequences used for the comparison of signal intensities shown in Fig. 1.47. The reference HMBC based on hard pulses is shown in (A). In the sequence shown in (B) all ^{13}C-pulses are replaced by PM-BEBOP-based excitation and refocussing pulses. PM-BEBOP pulses are schematically shown as rectangular pulses (representing constant RF amplitude) containing a wavy line (representing phase-modulation). Phase and/or time reversals are illustrated by vertical and/or horizontal mirroring of the wavy lines in the boxes, respectively. Phases are $\varphi_1 = 4(x), 4(-x)$, $\varphi_2 = 8(x), 8(-x)$, $\varphi_3 = -x, x$, $\varphi_4 = x, x, -x, -x$, $\varphi_{rec} = x, -x, -x, x, -x, x, x, -x, -x, x, x, -x, x, -x, -x, x$. If not stated otherwise, all pulses have x phase. Echo and antiecho selections were achieved using gradients. The gradient pulses were 1ms long. The applied gradient strength ratios are: $G_1 : G_2 : G_3 = 33 : 50 : -30$ for echo and $G_1 : G_2 : G_3 = 33 : 30 : -50$ for antiecho. The carbon pulse phase φ_3 and φ_{rec} were incremented by π for every second t_1 increment to obtain States-TPPI-like data.

of the major obstacles to automated NMR, which has been the need to accurately calibrate the constituent RF pulses in complex 2D pulse sequences. As noted, adiabatic pulses are tolerant to a wide range of RF miscalibration only as an inversion pulse.
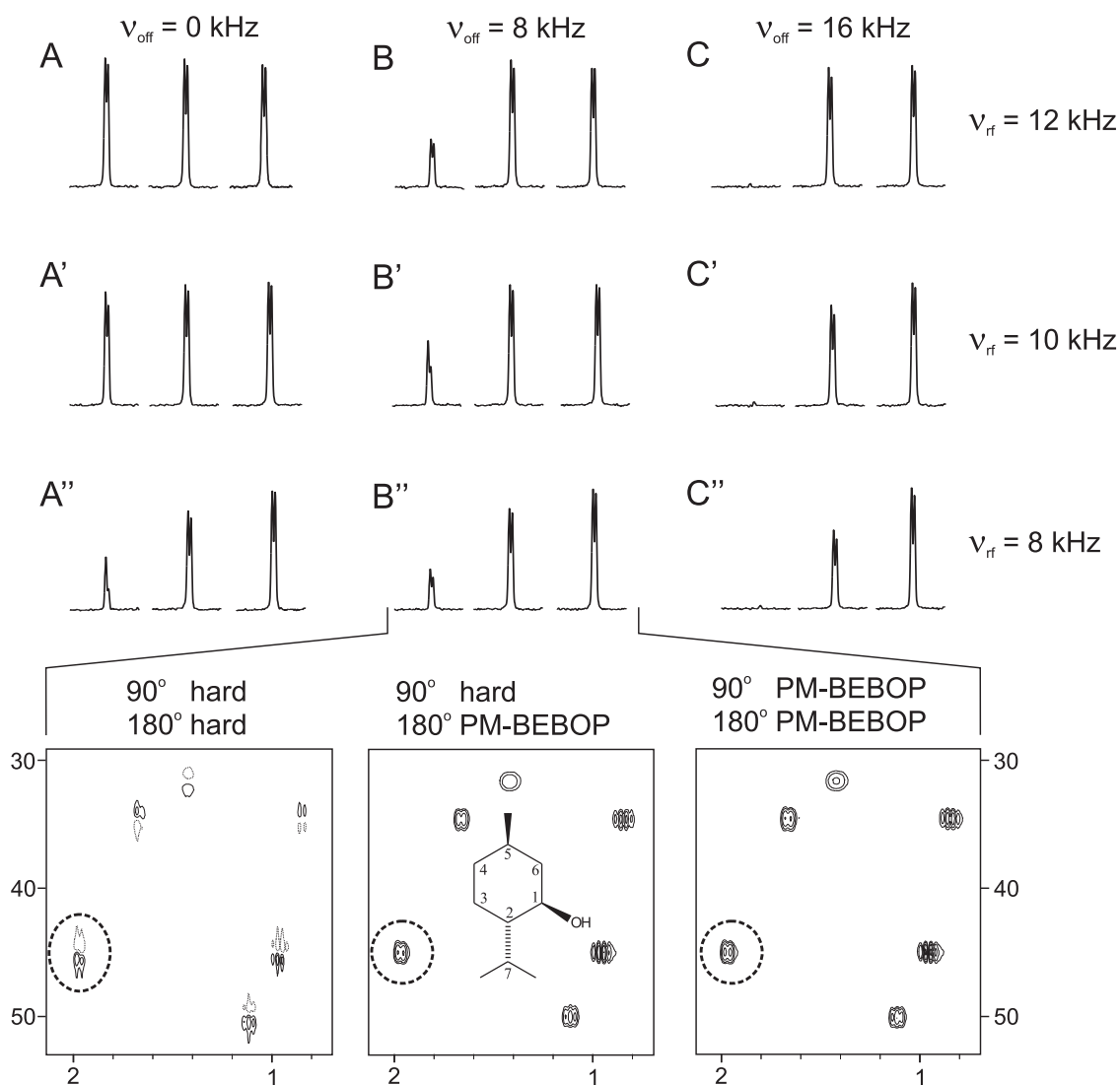
Figure 1.46: Traces through the C_6-H_6^{eq} signal of several HSQC spectra of menthol in CDCl$_3$ recorded with varying offsets, RF amplitudes, and ^{13}C pulses used. RF amplitudes were 12 kHz (A,B,C), 10 kHz (A′, B′, C′), and 8 kHz (A″, B″, C″) and on-resonant offsets were set to 0 kHz (A-A″), 8 kHz (B-B″), and 16 kHz (C-C″) (see main text for details). For each of the offset and RF amplitude combination the traces for three different HSQC experiments using different ^{13}C-pulses (see Fig. 1.44) are shown: only hard pulses (left), hard excitation and PM-BEBOP-based shaped 180° pulses (middle), and only PM-BEBOP excitation, and PM-BEBOP-based refocussing pulses (right). For B″ 2D-regions are also shown for the three different experiments for a better demonstration of the spectral quality. The circled signals correspond to the above traces. In the 2D-regions of hard pulse acquired spectra phase distortions can clearly be seen. These phase distortions have been corrected for all traces shown above in order to have a fair comparison of the intensities present in the various spectra.
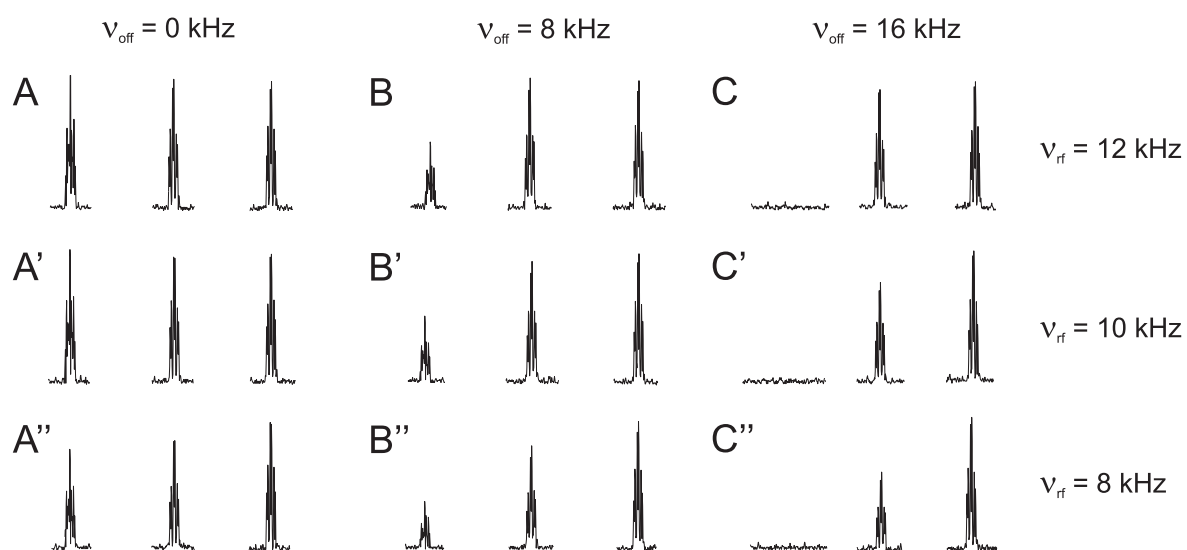
Figure 1.47: Traces through the C_1-H_7 signal in HMBC spectra analogous to the traces of HSQC spectra shown in Fig. 1.46. The replacement of hard 180° pulses by the BEBOP-constructed 180° pulse expectedly results in a strong improvement of the signal intensity (see also [78,79,87–89]). Further improvements can be seen if both PM-BEBOP excitation and PM-BEBOP-based refocussing pulses are used for ^{13}C: signal intensities basically stay constant for all RF amplitudes and offsets recorded.

Chapter 2

Partial alignment

It is the stretched soul that makes music.

Eric Hoffer, *"Reflections on the Human Condition"*

2.1 Introduction

Since all NMR active nuclei have non-zero magnetic moments and are therefore magnetic dipoles, they magnetically interact with each other through space, as all magnets do. These couplings, which depend on the relative orientation of the dipoles and their distance from each other, are the dominant interactions among other observable interactions in solid state NMR. It's still the largest interaction between nuclear spins of a liquid sample, though many of the ordinary users are not aware of this. Under isotropic solution conditions large internuclear dipolar couplings and other orientation-dependent magnetic interactions average to exactly zero as a result of Brownian rotational diffusion, which is many orders of magnitude faster than the time it takes to record an NMR signal. This averaging makes it possible to achieve high-resolution spectra with relative ease in liquid state NMR. However, solid state NMR allows spectroscopists to extract a wealth of structural information by measuring these interaction, which is of course lost in liquid state, where dipolar couplings vanish. However, back in 1963 a possibility was discovered to regain structural information contained in dipolar couplings, without losing the advantages of high-resolution NMR, — the *partial* orientation of solute molecules [90].

2.1.1 The Alignment Tensor

The key concept crucial for understanding residual dipolar couplings is the so-called *alignment tensor*. The alignment tensor characterizes the partial alignment acquired by the

molecule in the alignment medium and once known, allows to calculate the expected residual dipolar coupling constant for any spin pair. Almost every application of residual dipolar couplings necessarily includes the determination of the alignment tensor and its analysis.

The Hamiltonian of the dipolar interaction between two heteronuclear spins I and S with gyromagnetic ratios γ_I and γ_S and internuclear distance r_{IS} is given [17] by:

$$\mathcal{H}_D(t) = -\frac{\mu_0 \hbar}{8\pi r_{IS}^3} \gamma_I \gamma_S (3\cos^2 \vartheta(t) - 1) \cdot 2I_z S_z, \tag{2.1}$$

where $\vartheta(t)$ is a time dependent (due to molecular tumbling) angle between internuclear vector and direction of the external magnetic field. This can be written shorter as

$$\mathcal{H}_D(t) = \pi D \cdot 2I_\mathbf{z} S_\mathbf{z}, \tag{2.2}$$

where the *dipolar coupling constant* D is given by:

$$D = -\frac{\kappa}{r_{IS}^3} \left(\cos^2 \vartheta(t) - \frac{1}{3} \right) \tag{2.3}$$

and

$$\kappa = -\frac{3}{8\pi^2} \gamma_I \gamma_S \mu_0 \hbar \tag{2.4}$$

This dipolar coupling constant is scaled by fast motions originating from Brownian motion and dynamics within the molecule. In isotropic solutions it is averaged to zero. In the oriented medium the averaging is not complete and one can observe the *residual* dipolar coupling with constant $\overline{D}$:

$$\overline{D} = -\frac{\kappa}{r_{IS}^3} \left(\overline{\cos^2 \vartheta(t)} - \frac{1}{3} \right), \tag{2.5}$$

which depends on the average alignment of the molecule.

If the "alignment properties" of the molecule are known, then it is possible to calculate $\overline{D}$ for any pair of spins in that molecule, and full and comprehensive theory on that behalf was provided by Saupe already in 1964 [91]. As was shown in a nice review [92], main points of which are used here, this calculations can be surprizingly simple.

In the frame of reference, which is fixed to the molecule , the term $\overline{\cos^2 \vartheta(t)}$ can be conveniently expressed with the help of a probability tensor $\mathbf{P}$, which is a second order approximation of the orientational probability distribution of the direction of the external magnetic field in the molecular fixed frame of reference [93, 94]. This probability tensor $\mathbf{P}$ can be represented by an ellipsoid with a fixed orientation in the chosen molecular frame (x, y, z). The principal values $P_{\tilde{x}}$, $P_{\tilde{y}}$, and $P_{\tilde{z}}$ of the probability tensor are the probabilities to find the magnetic field along the corresponding principal axes of the probability ellipsoid, and hence $P_{\tilde{x}} + P_{\tilde{y}} + P_{\tilde{z}} = 1$.

The principal axes of the probability ellipsoid define a special molecular fixed axis system $(\tilde{x}, \tilde{y}, \tilde{z})$, in which the calculation of residual dipolar coupling constant is especially simple: if we know the three Cartesian components $r_{\tilde{x}}$, $r_{\tilde{y}}$, and $r_{\tilde{z}}$ of any given internuclear

unit vector $\vec{r}$ in this principal axis system, the term $\overline{\cos^2 \vartheta(t)}$ in Eq. 2.5 is simply given by

$$\overline{\cos^2 \vartheta(t)} = P_{\tilde{x}} r_{\tilde{x}}^2 + P_{\tilde{y}} r_{\tilde{y}}^2 + P_{\tilde{z}} r_{\tilde{z}}^2. \tag{2.6}$$

By inserting this equation into Eq. 2.5 the residual dipolar coupling constant can be predicted for any arbitrary spin pair in a molecule, as long as the orientation and principal values of the probability tensor are known.

More often, instead of describing the orientation of a molecule in terms of the probability tensor **P** (which corresponds in general to a real symmetric 3×3 matrix with trace 1), it is described in terms of its traceless part **P** - 1/3 **1**, which is called the *alignment tensor* **A** [95]:

$$\mathbf{A} = \mathbf{P} - \frac{1}{3}\mathbf{1}. \tag{2.7}$$

The three principal axes of **A** and **P** are identical and the three principal components of the alignment tensor **A** are simply given by

$$A_{\tilde{x}} = P_{\tilde{x}} - \frac{1}{3}, \quad A_{\tilde{y}} = P_{\tilde{y}} - \frac{1}{3}, \quad A_{\tilde{z}} = P_{\tilde{z}} - \frac{1}{3}. \tag{2.8}$$

The probability tensor **A** is traceless, hence $A_{\tilde{x}} + A_{\tilde{y}} + A_{\tilde{z}} = 0$, and therefore one or two of its components are always negative, in contrast to the probability tensor, which is always positive.

In terms of the principal components of the alignment tensor **A**, the term $\left(\overline{\cos^2 \vartheta(t)} - 1/3 \right)$ in Eq. 2.5 can be expressed as

$$\left(\overline{\cos^2 \vartheta(t)} - \frac{1}{3} \right) = A_{\tilde{x}} r_{\tilde{x}}^2 + A_{\tilde{y}} r_{\tilde{y}}^2 + A_{\tilde{z}} r_{\tilde{z}}^2. \tag{2.9}$$

This equation is also very often represented in spherical coordinates. Then, instead of having $r_{\tilde{x}}$, $r_{\tilde{y}}$, and $r_{\tilde{z}}$ components of the bond vector in the tensor frame of reference, one deals with azimuthal and axial angles θ and ϕ. Equation 2.9 takes the following form:

$$\left(\overline{\cos^2 \vartheta(t)} - \frac{1}{3} \right) = \frac{A_{\tilde{z}}}{2}(3\cos^2\theta - 1) + \frac{A_{\tilde{x}} - A_{\tilde{y}}}{2} \sin^2\theta \cos 2\phi. \tag{2.10}$$

Often, the *axial component* A_a and the *rhombic component* A_r of the alignment tensor are defined as [95]

$$A_a = \frac{3}{2}A_{\tilde{z}}, \qquad A_r = A_{\tilde{x}} - A_{\tilde{y}}. \tag{2.11}$$

With these definitions, Eqs. 2.9 and 2.10 can be expressed as

$$\left(\overline{\cos^2 \vartheta(t)} - \frac{1}{3} \right) = \frac{1}{3}\left\{ A_a(3\cos^2\theta - 1) + \frac{3}{2}A_r \sin^2\theta \cos 2\phi \right\}. \tag{2.12}$$

If one of these equations is inserted into Eq. 2.5, it is again possible to predict the residual dipolar coupling constant for any arbitrary spin pair in a molecule, provided that the orientation and principal values of the alignment tensor are known.

Conversely, the alignment tensor $\mathbf{A}$ (or the probability tensor $\mathbf{P}$) can be determined if a sufficient number of experimental dipolar coupling constants are measured for a given molecule [96]. It can be shown [92] that the alignment tensor $\mathbf{A}$ (and the probability tensor $\mathbf{P}$) is characterized by five independent parameters. Therefore, at least five dipolar coupling constants need to be measured in order to determine the five unknown parameters [96].

2.1.2   Alignment media

Three different ways of introducing partial alignment are known today: orientation via paramagnetic ions, alignment in a liquid crystalline phase, typically a lyotropic mesophase, alignment in a stretched gel. When a molecule has considerable magnetic susceptibility anisotropy, the molecule orients partially under the strong magnetic field. In the other two cases orientation is induced by an oriented molecular lattice, which then partially aligns the molecules of interest via steric or electrostatic interactions.

Paramagnetically induced alignment

Placing a molecule with an anisotropic magnetic susceptibility in a strong magnetic field causes a partial cancellation of the random Brownian motion, and a net alignment results, though very small, but measurable by NMR in some cases, as was shown back in 1980s [97, 98]. Paramagnetic alignment can be induced in molecules containing a paramagnetic ion, or such an ion can be bound to a specific ionic binding site, which either is present naturally or in some cases can be engineered by a paramagnetic tag. However, the self-aligning paramagnetic ion not only introduces RDCs but also an effect known as pseudo contact shift, which itself can be used for structure elucidation, but significantly complicate the evaluation of the spectra.

And though the paramagnetic alignment effect is very small, in 1995, James H. Prestegard and coworkers demonstrated that paramagnetic alignment of certain proteins (in this case cyanometmyoglobin, which has a very highly anisotropic paramagnetic susceptibility), taken at very high field, could be used complementary to NOEs to determine a tertiary fold [99]. Later this method was also used for exploring domain dynamics of protein calmodulin chelated to Tb^{3+} or Tm^{3+} [100].

Liquid Crystalline Phases

Liquid crystals have been the first alignment media, introduced in 1963, as the first spectrum of benzene partially oriented in the nematic mesophase of 4,4′-di-*n*-hexyloxyazoxybenzene was reported, a spectrum with at least 30 resonances and a width of a multiplet pattern of approximately 2500Hz [90]. Following this result, a flood of NMR spectra in various liquid crystalline phases was reported (see e.g. refs [94, 101–104]) using mainly nematic mesophases but also smectic [105–107], destroyed cholesteric [103, 108], and lyotropic nematic mesophases [109, 110]. Liquid crystals orient spontaneously in a

magnetic field and the weak interaction with the solute produces the desired partial orientation. Liquid crystalline phases, however, have a first order phase transition and therefore a limitation to a minimum alignment. It turned out that the orientation introduced by liquid crystalline phases generally is very strong, yielding numerous large splittings by RDCs that can hardly be interpreted for more complex organic molecules. Additionally, the strength of the introduced alignment is proportional to the strength of the inducing external magnetic field.

Poly-γ-benzyl-L-glutamate, dissolved in solvents like dichloromethane, chloroform, or dimethylformamide, was introduced by Panar and Phillips [108]. It was one of the least orienting liquid crystals known at that time and was used for the first successful measurement of RDCs in an organic solvent to obtain structural information of a small molecule [86, 111, 112]. Currently, new liquid crystalline phases for organic solvents have been developped that can achieve lower degrees of anisotropies. 4-n-Penthyl-4'-cyanobiphenyl [113] and Poly-γ-ethyl-L-glutamate [114] seem to be two promising candidates for the measurement of RDCs in small molecules. The existence of liquid crystalline phases with very low induced anisotropies was proven in last years in the field of biomolecular NMR. Several lipid/detergent mixtures [95, 115], filamentous phage [116], and other liquid crystalline phases [117, 118] were used to successfully measure RDCs for strucrure refinement of proteins and nucleic acids. These alignment media are, of course, also applicable to small molecules in aqueous solutions [119–124].

Stretched Polymer Gels

It was shown already in 1981 by Deloche and Samulski [125], that partial alignment can also be achieved by mechanical stretching of polymer gels. In polymer NMR this technique has since become standard to obtain information about polymer properties, but remained largely unnoticed by the rest of NMR community, occupied with chemical and biochemical applications. Only in the year 2000 the use of these stretched polymer gels was reinvented for aligning molecules dissolved inside the gel to obtain RDCs for structural investigation. The approach was called "strain induced alignment in a gel" and was demonstrated on stretched polyacrylamide [126–129], and polyacrylamide/acrylate [130] copolymers. Several ways of aligning by using a shigemi plunger [126], teflon funnels [131], or glass capillaries [130] have been developed and successfully applied to proteins as well as small molecules. An advantage of this method over liquid crystalline alignment media is independence of alignment with respect to the external magnetic field and wide scalability of the alignment.

2.1.3 Applications of RDCs

Since their re-introduction in the NMR community [95, 99], residual dipolar couplings have soon found broad appreciation, primarily in biomolecular NMR spectroscopy. While NOEs are local distance restraints, RDCs provide complementary long-range orientational information. And this information is now being widely used alongside of NOEs for the
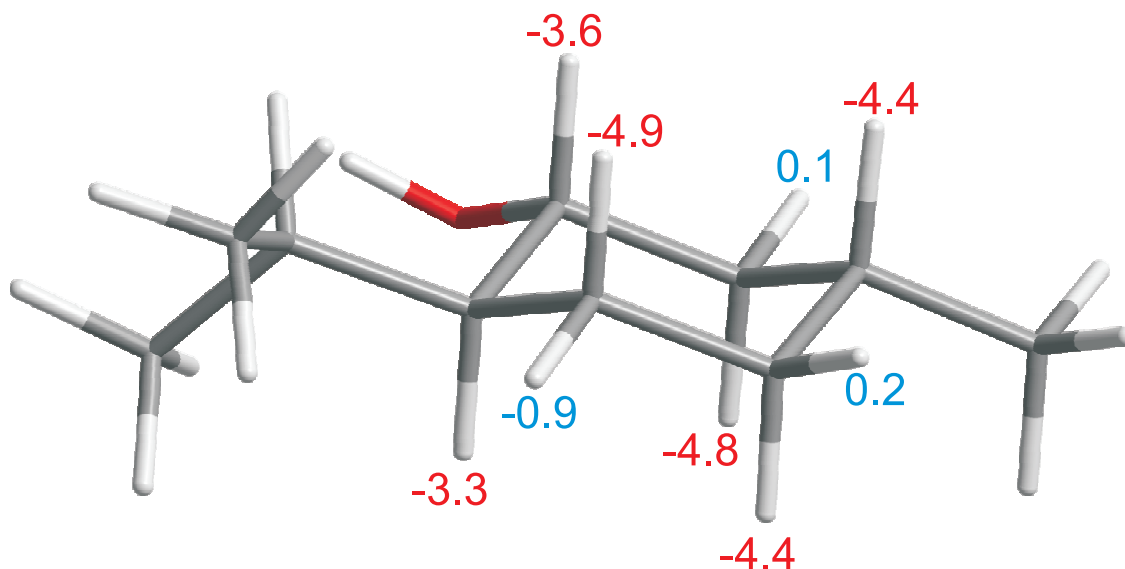
Figure 2.1: Measured D_{CH} RDCs for menthol in a PS/CDCl$_3$ gel (data taken from the Table 2.3). Axial and equatorial protons of can easily be distinguished by RDCs even without knowing the alignment tensor.

refinement of macromolecular structures (see e.g. review [132]). For small molecules, however, the potential of RDCs remained largely undiscovered until some very promising applications were reported recently.

Maybe the most elegant application of RDCs is found in six-membered chair-like rings, where RDCs can be used directly to distinguish axial and equatorial protons without having the need to derive an alignment tensor [123]. The method uses the fact that all axial C-H vectors are oriented in the same direction and therefore must have virtually identical D_{CH} couplings (this can also be seen on the data in the Table 2.3). The assignment then can simply be achieved by looking at the occurence of identical RDCs: all protons with very similar D_{CH} RDCs are axial while all others are equatorial (cf. Fig. 2.1).

The use of RDCs can also facilitate the assignment of prochiral protons of methylene groups in NMR spectra. Normally such assignment is acheved based on NOE information, but in many cases this is not possible, whether while the CH$_2$ group is isolated and there are no neighbouring protons or while the difference in distances to those are very small and undistinguishable by NOEs. If the alignment tensor is known then such assignment can be done even in those cases [86, 111], as also an example in section 2.3 illustrates.

Another important application can also be found in the determination of Z/E configurations [112] and the determination of the relative chirality of stereochemical centers [124, 133] even in different parts of the molecule that might be spatially distant. For this technique, structural models of all possible configurations have to be built first. The measured RDCs are then compared with RDCs backcalculated from the different structures. The best structural model provides the best fit.

A challenging application is the determination of the sugar pucker with RDCs. Freedberg [122] has shown that the RDCs measured for sucrose cannot be explained by a single conformation. On the other hand, a large number of potential sugar puckers can be ruled out, giving more insight into the population of structures and the dynamic behavior of sugars.

One should keep in mind that the alignment tensor is a value associated with a certain *rigid* structure and therefore it is difficult to handle dynamic regions in molecules. RDCs in dynamic regions are averaged over all populated states and might lead to misinterpretations if the populated structures differ significantly. However, the use of several different alignment media should make it possible to unambiguously identify flexible regions in a molecule and together with the improved prediction of alignment tensors [134], determined RDCs might be fitted to a small ensemble of structures in the future.

2.2   Stretched polystyrene gels for partial alignment of small organic molecules

In today's high resolution NMR of biomacromolecules the measurement of residual dipolar couplings (RDCs) can be viewed as a standard method for obtaining structural information and a large abundance of aqueous alignment media such as lipid bicelles [95, 115], stretched polyacrylamide gels [126, 128], filamentous phage [116] and other liquid crystalline phases [117, 118] are used. The field of small molecule NMR, however, started only recently to realize the potential of this new structural parameter and few, nevertheless impressive, demonstrations have been published so far [86, 111, 112, 114, 119–124, 129].

A limiting step for the application of RDCs to small molecules is still the availability of alignment media for organic solvents. Liquid crystalline phases such as poly-γ-benzyl-L-glutamate (PBLG) [86, 108, 111, 135] are known to align organic molecules in $CDCl_3$ and similar apolar organic solvents. Liquid crystals, however, have the disadvantage that for the phase transition a minimum concentration is needed and therefore only anisotropy larger than a certain minimum is induced in the sample. The strength of alignment depends also on the magnetic field of the spectrometer, while latter is the force, which forces molecules to orient. The development of specially designed crystalline phases with lower minimum alignment, as shown in the case of 4-n-pentyl-4'-cyanobiphenyl (PCBP) [113] and poly-γ-ethyl-L-glutamate (PELG) [114], will improve the applicability of such systems.

An alternative is given by strain induced alignment in a gel (SAG), which is independent of the magnetic field and scalable over a wide range. In aqueous solutions mechanically stretched polyacrylamide [126–128, 131] and an acrylamide/acrylate copolymer [130] were applied. But polymeric gels are also generally suited for partial alignment in organic solvents as was shown by the pioneering work of DeLoche and Samulski [125] and many follow up applications in polymer NMR spectroscopy (e.g. see [136–139]).

We developed an easy to apply and scalable method for the alignment of organic molecules and measurement of residual dipolar couplings in cross-linked polystyrene in different organic solvents, which can be extended to a large number of polymer/solvent combinations.

2.2.1   Gel preparation

Crosslinked polystyrene sticks were prepared in glass tubes with inner diameters of 3.4 mm and 4.0 mm. The glass tubes were carefully dried and treated with a 1:1 mixture of chlorotrimethylsilane and dichlorodimethylsilane for 18 hours to ensure apolar surfaces. After washing with dichloromethane (5 times) the tubes were dried at 50°C and one end was sealed by melting. Styrene (99%, Fluka) and divinylbenzene (80%, Fluka) were filtered (basic aluminum oxids, pH 10, Fluka) and distilled under reduced pressure. Immediately before polymerization the monomers were degassed for 15 minutes by ultrasound in vacuo and ventilated in an argon atmosphere. After carefully mixing styrene, divinylbenzene and 2,2'-azobis(2-methylpropionitrile) (AIBN) to desired concentrations
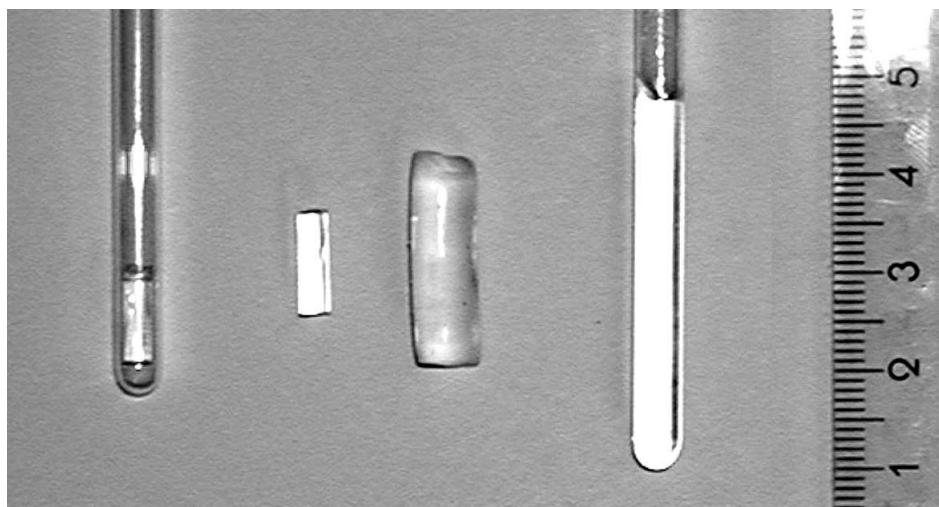
Figure 2.2: Photography of the cross-linked PS stick in different states of swelling. From left to right: unswollen polymer stick in standard 5 mm NMR-tube, polymer stick directly after polymerization, free polymer stick completely swollen, polymer stick swollen in the NMR-tube.

the mixture was filled into the prepared glass tubes and their tops sealed. Polymerization was performed for 5 days at 45°C and 2 days at 60°C. After breaking the glass tubes, bubble-free parts of the polymer sticks were cut into pieces of 1.0 cm to 1.5 cm length. All samples used for measurements were prepared by putting polystyrene sticks of defined diameters directly into NMR tubes and letting them swell in the chosen solvent for one to fourteen days (see Fig. 2.2). The swelling processes were monitored by acquiring ^{2}H NMR spectra of the deuterated solvents: with progressing swelling and stretching of a polymer the initially sharp single signal broadens irregularly, then turns into two broad lines and finally ends up with two relatively sharp lines for well equilibrated samples. Swelling times, necessary to obtain equilibrated sample differ significantly for different solvents used and different diameters of the polymer stick taken. Shortest swelling times were observed for samples swollen in dichloromethane; in this case, most of the polystyrene sticks of 3.4 mm diameter reached equilibrium state within 24 hours. Similar sticks swollen in chloroform were ready to use in about 2-3 days, while slowest swelling was observed for dioxane and benzene in which PS-sticks required up to two weeks to reach equilibrium. Within limits, the speed of the swelling process could be increased by increasing the sample temperature. In the end, all PS-sticks dissolved in one of the solvents discussed in the text resulted in nicely equilibrated samples with uniform splittings in the ^{2}H NMR spectra.

2.2.2 Physical properties of polystyrene gels

Of course, the method of measuring RDCs in stretched polystyrene gels has its limitations and we tried to find out the range of conditions under which stretched PS gels still show
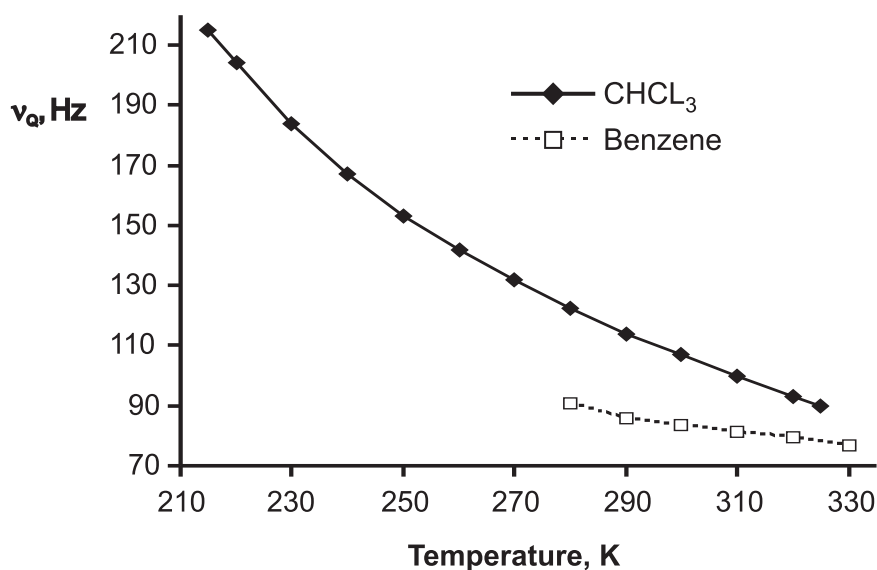
Figure 2.3: Temperature dependence of the quadrupolar deuterium splitting ν_Q of $CDCl_3$ added to the stretched PS-gel sample swollen in chloroform (solid line) and benzene (dashed line).

alignment properties that allow RDC measurement. A physical parameter of central importance is the sample temperature. Most liquid crystals show a phase transition with a specific transition temperature below or above which no partial alignment can be achieved [95, 101]. We therefore studied the anisotropy change of stretched PS-gels, monitored by the quadrupolar deuterium splitting, over the full temperature range of liquid $CDCl_3$ and C_6D_6. The result is shown in Fig. 2.3: no abrupt changes could be observed, only a steady increase of the observed splitting of 1.1 and 0.35 percent on average per degree towards lower temperatures. Therefore no general limitation of the method can be seen in the temperature range of $CDCl_3$ and C_6D_6 as solvents, but for practical applications it should be noticed that a defined temperature must be chosen to guarantee identical alignment conditions if RDCs measured in different experiments shall be compared.

An important parameter for the mechanism of alignment is the static magnetic field dependence of the induced anisotropy. While gel-alignment due to mechanical stretching should be independent of the magnetic field, auto-alignment of polymer chains as previously observed for macromolecules [98, 99] and liquid crystalline phases [111] should be field dependent. After careful calibration of the temperature, a series of quadrupolar splittings of a PS/$CDCl_3$ gel sample was measured for four different magnetic field strengths with the results shown in Table 2.1. The measured splittings are all within the error due to temperature variations and spectral noise, which we conservatively estimate to be about ±0.2 Hz. From this result we can deduce that the anisotropy of the gel originates from mechanical stretching only and no auto-alignment of the polymer chains

Table 2.1: Magnetic field strength dependence of quadrupolar coupling

	B_0 field, MHz			
	250	600	750	900
splitting, Hz	58.8	59.0	59.0	58.9

occurs, which is consistent with the finding that non-crosslinked PS dissolved in CDCl$_3$ does not cause any measurable quadrupolar deuterium splitting. This also implies that no lower anisotropy limit is imposed by the PS-gel alignment method since the mechanical stretching of the polymer can be varied continuously.

Of course, the alignment properties of a stretched PS-gel also depend on the consistency of the gel itself. Apperently, the anisotropy induced by the gel should dependent on the amount of cross linking agent used for polymerization. We performed the polymerization at 45°C with 2,2'-Azobis(2-methylpropionitrile) (AIBN) as a radical starter and different amounts of divinylbenzene (DVB) as crosslinker ranging from 0.05% to 5% (v/v). Five samples per concentration were swollen in CDCl$_3$ and quadrupolar deuterium splittings were recorded. The resulting graph is shown in Fig. 2.4 B: Anisotropies corresponding to quadrupolar deuterium splittings in the range of 0-540 Hz for PS-sticks with initial diameter of 4.0 mm could be achieved, which should basically cover all needs for partial alignment. Under these polymerization conditions we could not find any significant dependence of induced anisotropy on the amount of radical starter. However, if the polymerization is performed under higher temperatures (80 - 120 °C) and using dibenzoylperoxide (DBP) as a radical starter, such dependence is present and is shown in Fig. 2.4 A. Though, such polymerizations resulted in polymers of much lesser homogeneity, very often with such large amount of air bubbles inside, that no NMR study could be thinkable. Therefore, we came to a procedure described above, with moderate polymerization temperatures and AIBN as a radical starter.

A point of major interest in the applicability of PS-gels is the range of solvents in which molecules can be aligned. We therefore did a series of experiments where we tried to swell PS-sticks in a number of organic solvents. In line with the very low solubility of non-crosslinked PS [140], no swelling could be observed for very apolar solvents like octane and relatively polar solvents like acetone or acetonitrile. However, dichloromethane (DCM), tetrahydrofuran (THF), benzene, and dioxane showed significant swelling and were used for further experiments. The DVB-dependence of the induced anisotropy was measured by adding 5-10 % of CDCl$_3$ to the otherwise undeuterated solvents (Fig. 2.4 C). Quadrupolar deuterium splittings in the range of 0-400 Hz could be obtained for DCM and THF as solvents, showing overall similar behavior to chloroform. Benzene and dioxane both showed a relatively slow swelling with a different behaviour concerning quadrupolar splitting. Samples of 3.4 mm initial polymer diameter swollen in benzene result in similar
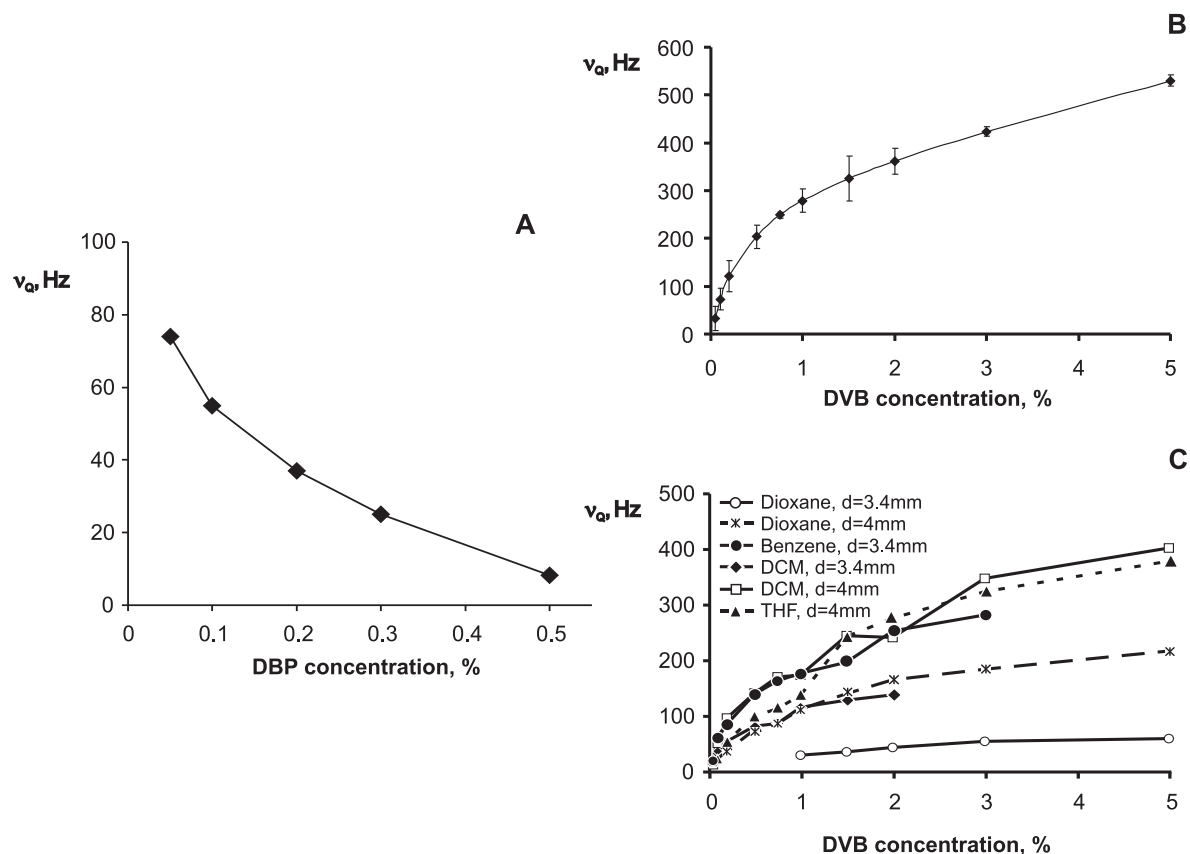
Figure 2.4: deuterium quadrupolar splitting ν_Q of $CDCl_3$ as a measure of induced anisotropy with respect to amount of radical starter and cross-linked agent DVB used for PS polymerization. (A) ν_Q values of $CDCl_3$ for different amounts of DBP used for polymerization at high (80 - 120°C) temperatures with 0.16% DVB. (B) ν_Q values of $CDCl_3$ are averaged ofer 4 - 5 different samples for each data point with standard deviations as error bars. Samples were prepared with PS sticks of 4 mm diameters. (C) ν_Q values are shown for 5 - 10% $CDCl_3$ added to the solvents dichloromethane, tatrahydrofurane, dioxane, and benzene. Samples were prepared with PS sticks of 3.4 and 4 mm diameters for the four solvents as indicated in the graph. Only one sample/data point was prepared. Deviations from a smooth curve as in (B) are probably due to variations in inner diameters of NMR tubes and glass tubes used for polymerization and slight distortions from a perfect cylindrical shape of some PS sticks used.
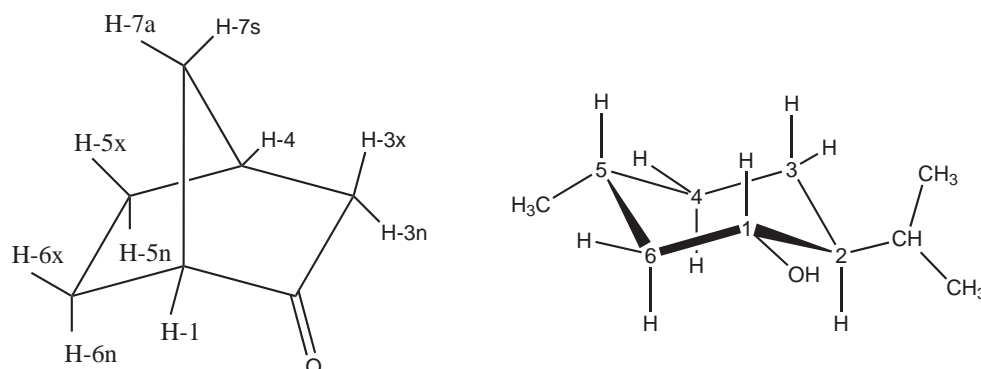
Figure 2.5: Structures of norcamphor (left) and menthol (right)

quadrupolar splitting as chloroform samples with 4 mm initial PS-stick diameter. Samples swollen in dioxane, on the other hand, show smaller quadrupolar splittings, than observed for the other solvents.

2.2.3 Alignment in polystyrene gels

Though the initial NMR studies on swollen and stretched polymers were performed to study the state of polymer itself [125], it is the state of a dissolved small molecule which we are concerned with, while it is the longing for structural information about this molecule, which brings one to dissolve it in the orienting medium.

Sample preparation, measurements and evaluation

The preparation involved several steps. First, norcamphor was added on top of already prepared PS-gel samples which were kept at room temperature for 2-3 days to allow for diffusion of the small molecule into the gel. The samples were then used to acquire standard coupled ^{1}H-^{13}C HSQC spectra with sensitivity enhancement and phase sensitive echo/antiecho gradient selection [141–143]. All 2D spectra were measured on Bruker DMX 600 spectrometers with 3.5 ppm spectral width in the ^{1}H-dimension (4096 complex points) and 70 ppm (256 increments) in the indirect ^{13}C-dimension. With 2 transients acquired per increment the total experiment time for each HSQC spectrum was about 16 minutes. Spectra were processed with exponential multiplication (with an additional linebroadening of 1 Hz) in the directly recorded dimension and a 90°-shifted sine-bell window function in the indirect dimension. Coupling constants were measured with the aid of the program SPARKY [144] using automated peak picking and by individually phasing the doublet components at slices along the direct detected dimension in cases of slight phase twists (c.f. procedure described in [123]). It turned out that the latter procedure gave more reliable results with deviations relative to the automated peak picking of up to 2 Hz. The errors of the coupling constants determined by the more elaborate procedure were generally
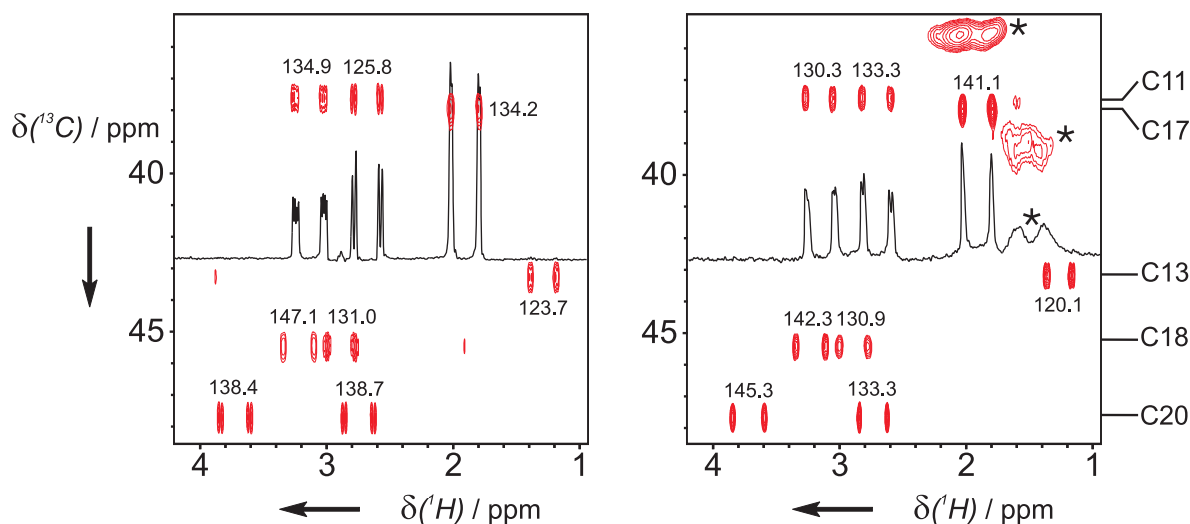
Figure 2.6: Region of the ^{1}H,^{13}C-correlation spectra (HSQC) acquired on 50 mg strychnine in CDCl$_3$ (left) and in a PS-gel swollen in CDCl$_3$ (right) at 300° K. $^1J_{CH}$ and $^1J_{CH} + D_{CH}$ couplings, respectively, are given next to the corresponding cross peaks. As can be seen from the 1D-slice at 37.8 ppm the couplings are easily measured. The broad signals of the PS-polymer are indicated with an asterisk.

below ±0.5 Hz, which was used as a conservative estimate for subsequent calculations. The alignment tensors were finally derived using only RDCs from signals without second order effects with the program PALES [134] using the *bestFit* option. Relative orientations in 5D-space and errors estimations of the alignment tensor calculations were calculated with the corresponding options in the PALES program. Samples for various solvents containing menthol were prepared and measured in the same way as norcamphor samples but no attempt to derive alignment tensors was pursued since only four C,H-vectors point in different directions.

For the initial proof of principle, that a small organic molecule diffuses inside the PS gel and gets oriented in there, we used strychnine, a standard sample in NMR spectroscopy [145]. A polymer stick with 0.16% DVB and 0.3% DBP and a resulting quadrupolar splitting in the deuterium spectrum of 25 Hz was used. Two HSQC-spectra without heteronuclear decoupling during acquisition were recorded for strychnine in CDCl$_3$ alone as reference and dissolved in the aligned polymer stick. The parts of these spectra are shown in Fig. 2.6. The PS-signals could easily be distinguished from strychnine signals because by their broad lines and practically no overlap between the resonances was observed. The difference of the coupling constants in aligned and non-aligned spectra directly results in the residual dipolar couplings D$_{CH}$. All dipolar couplings are in the range of -11 to 13 Hz, so that the sign of the couplings is unambiguously given by the larger $^1J_{CH}$-coupling (>120 Hz).

This shows, that polystyrene, swollen into a gel and stretched in organic solvents,

represents a system, allowing alignment of small organic molecules, easily scalable by modifications in polymer compositions or in size of used polymer stick, and in which the measurement of residual dipolar couplings can be performed relatively easy.

Orientations in different solvents

To further characterize the influence of organic solvent on the swelling of a gel and on the resulting orientation of dissolved molecules, we derived the alignment tensors for norcamphor (for structure see Fig. 2.5) as a test sample which is soluble in all solvents of interest and allows an accurate determination of alignment tensors with only few measured RDCs. A total of four out of ten signals in the HSQC-spectra of norcamphor showed strong coupling artefacts and were not used for the alignment tensor determination. The remaining six dipolar D_{CH}-couplings are summarized in Table 2.2 together with the parameters of the alignment tensors as derived by the program PALES [134]. A first inspection of RDCs obtained already reveals that alignment for the five different solvents is very similar but not identical: All derived alignment tensors have a strong negative A_{zz} component, but its orientation and the rhombic components differ slightly. The relative angles of the resulting alignment tensors relative to each other are summarized in Table 2.4, varying from $10°$ to $21°$ for the different solvent combinations. The alignment tensors for DCM and chloroform are very similar, but for THF, dioxane, and benzene as solvents the three eigenvector components A_{xx}, A_{yy} and A_{zz} are tilted considerably with respect to each other. In Fig. 2.7 the tensors for the five different solvents are shown in an orientation that pronounces the differences in alignment

We also measured sets of ^{1}H,^{13}C-RDCs for menthol in PS-gels swollen in the five different solvents. ^{1}H,^{13}C-RDCs are summarized in Table 2.3. Although the limited number of differently oriented C-H vectors in menthol does not allow the reliable determination of alignment tensors, the comparison of RDCs leads again to the conclusion that alignment in PS-gels is solvent dependent. So, for example, most RDCs measured in THF show sign inversion compared to RDCs from other solvents, which is unambiguous evidence that the alignment tensors differ in this case.

The difference in alignment of norcamphor and menthol in the five different solvents can be explained in many ways: Most likely there are specific interactions of the solvent with either the organic molecule of interest and/or the PS-polymer. Also, the structure of the polymer or the solute itself might change in the different solvents. Maybe the different alignments can also be explained by variations in the dielectric constants for the solvents used (on this subject see e. g. [146]). Solvent dependent alignment was also observed for Polyvinylacetate as a polymer (*vide infra*) and it will be very interesting to study these effects with additional solutes and polymer gels.

2.2.4 NMR properties of polystyrene gels

Spectra of partially aligned samples are different from conventional isotropic liquid samples. In general, more complex multiplet patterns because of additional dipolar couplings

Table 2.2: Measured ^{1}H, ^{13}C-RDCs of directly bound atoms at ^{13}C natural abundance and resulting alignment tensor parameters (axial and rhombic components (D_a, D_r), correlation factor R, and principal axes A_{xx}, A_{yy}, and A_{zz} with their corresponding eigenvectors) for norcamphor in organic solvents as calculated with the program PALES

Assignment	CDCL$_3$	DCM	Dioxane	THF	Benzene
D_{C1-H1} (Hz)	5.9	3.5	3.3	12.9	2.5
D_{C3-H3n} (Hz)	1.1	0.2	-2.9	-3.1	-2.5
D_{C3-H3x} (Hz)	14.0	7.9	8.2	20.1	6.1
D_{C4-H4} (Hz)	-3.9	-1.0	0.2	-1.0	1.0
D_{C7-H7a} (Hz)	-13.3	-10.3	-11.2	-23.9	-8.8
D_{C7-H7s} (Hz)	15.7	8.4	7.6	19.1	5.2
D_a (av)	-2.37×10^{-4}	-1.40×10^{-4}	-1.48×10^{-4}	-3.75×10^{-4}	-1.01×10^{-4}
D_a (std dev)	3.89×10^{-6}	5.00×10^{-6}	1.19×10^{-5}	4.98×10^{-6}	7.52×10^{-6}
D_r (av)	-7.68×10^{-5}	-4.72×10^{-5}	-5.45×10^{-5}	-6.18×10^{-5}	-3.12×10^{-5}
D_r (std dev)	4.37×10^{-6}	6.91×10^{-6}	1.57×10^{-5}	6.18×10^{-6}	9.62×10^{-6}
R	1.000	0.999	0.992	0.998	0.995
A_{xx}	1.22×10^{-4}	7.07×10^{-5}	7.21×10^{-5}	2.83×10^{-4}	5.76×10^{-5}
A_{yy}	3.51×10^{-4}	2.08×10^{-4}	2.20×10^{-4}	4.66×10^{-4}	1.42×10^{-4}
A_{zz}	-4.74×10^{-4}	-2.79×10^{-4}	-2.92×10^{-4}	-7.49×10^{-4}	-2.00×10^{-4}
EV A_{xx}	-0.27, -0.51, 0.82	-0.24, -0.41, 0.88	-0.21, -0.28, 0.94	0.10, -0.67, 0.74	0.21, -0.64, 0.74
EV A_{yy}	-0.74, 0.65, 0.16	-0.70, 0.70, 0.13	0.77, -0.64, -0.23	0.76, -0.43, -0.49	0.75, -0.38, -0.54
EV A_{zz}	0.61, 0.57, 0.55	0.67, 0.59, 0.45	0.61, 0.71, 0.35	0.64, 0.61, 0.47	0.63, 0.67, 0.40
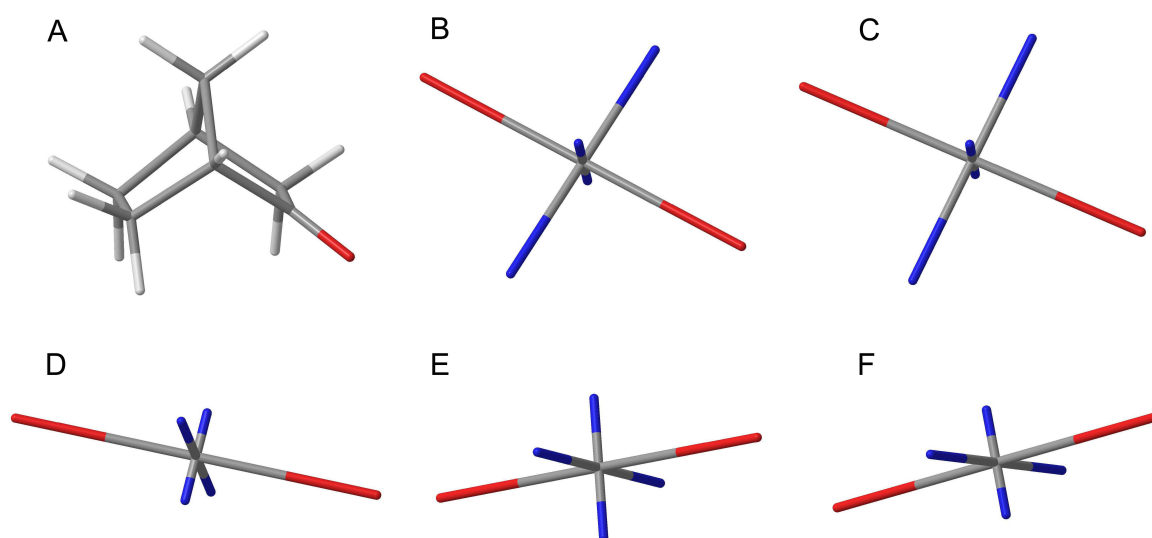
Figure 2.7: Illustration of the alignment tensors of norcamphor in stretched PS gels prepared in different organic solvents: (A) orientation of norcamphor as reference frame for the alignment tensors (axes A_{xx}, A_{yy}, and A_{zz} drawn with their length proportional to the magnitude of the Eigenvalues and with the orientation according to the Eigenvectors of the alignment tensors) in (B)-(F). Alignment tensors were derived with the program PALES for samples swollen in chloroform (B), dichloromethane (C), dioxane (D), tetrahydrofurane (E), and benzene (F) (cf. Table 2.2). Positive components of the alignment tensors are shown in red, and negative tensor components, in blue. The view angle relative to the molecule was chosen to pronounce the differences in alignment tensors.

Table 2.3: Measured ^{1}H,^{13}C-RDCs for menthol in stretched PS gels swollen in organic solvents

coupling	CDCl$_3$	DCM	dioxane	THF	benzene
D_{C1-H1}	-3.6	-8.7	-7.2	2.7	-3.0
D_{C2-H2}	-3.3	-9.7	-2.4	6.3	-2.0
D_{C3-H3a}	-4.9	-12.7	-17.7	16.5	1.2
D_{C3-H3e}	-0.9	-2.9	-13.6	-3.1	4.2
D_{C4-H4a}	-4.4	-20.2	-7.1	-0.9	-5.6
D_{C4-H4e}	6.2	-5.0	-10.3	-14.0	6.2
D_{C5-H5}	-4.4	-10.7	-5.9	-0.4	-5.0
D_{C6-H6a}	-4.8	-16.9	-11.4	1.2	-2.8
D_{C6-H6e}	0.1	-3.1	-8.4	-5.3	-0.2

Table 2.4: Relative angles (deg) of the alignment tensors of norcamphor in solvents (see Table 2.2) in five-dimensional (5D) space as calculated with the program PALES

	5D-angles				
	CDCl$_3$	DCM	dioxane	THF	benzene
CDCl$_3$		10.5	21.2	14.6	20.9
DCM	10.5		16.9	13.4	18.2
dioxane	21.2	16.9		20.1	17.6
THF	14.6	13.4	20.1		10.4
benzene	20.9	18.2	17.6	10.4	

through space must be expected that mostly lead to what looks like a single broad line (cf. Fig. 2.9). On the other hand, narrowed signals can be observed in few cases when RDCs of opposite sign reduce the splitting due to already existing J-couplings (e.g. left signal 23 in Fig. 2.9 B and C). The appearance of a spectrum depends on many parameters like the density of NMR-active nuclei, the strength and orientation of alignment and the J-coupling network.

But what is the line width that can be principally achieved in a stretched PS-gel? The consistency of the polymer can be considered quite heterogeneous with a wide distribution of shorter and longer polymer chains and varying concentrations of cross-links between chains which might affect the line shape of a sample. We therefore tried to get a good shim for a swollen PS-gel with an intermediate induced anisotropy (ν_Q (CDCl$_3$) $\approx$ 110 Hz): A line width below 1 Hz for the CHCl$_3$ proton signal was easily obtained as shown in Fig. 2.8 A. Line shape distortions due to gel micro- heterogeneity therefore must be of minor importance and can be neglected.

Besides the multiplet pattern also resonance frequencies are affected by the stretched PS-gel (Fig. 2.9 B and C). Two effects are expected: first, PS works as a co-solvent that shifts all resonances upfield compared to the conventional liquid CDCl$_3$ sample; second, a change in chemical shifts is directly induced by the anisotropy of the stretched gel, leading to so-called residual chemical shift anisotropy (RCSA) [147–151]. Chemical shift changes in aliphatic regions as shown in Fig. 2.9 B and C are practically solely due to the co-solvent effect since CSA is negligibly small in this case (for sizes of measured RCSA, see e.g. [101]). Aromatic ^{13}C-chemical shifts, however, might be significantly shifted due to relatively strong RCSA. The main disadvantage resulting from the chemical shift changes is that in certain cases it might be necessary to repeat parts of the assignment process.

Finally, the main drawback of PS-gels as alignment media are the undesired NMR signals originating from the polymer itself. In Fig. 2.8 C the proton spectrum of a strychnine PS-gel sample is shown with broad PS signals in the aromatic and aliphatic region. The difference in line width of strychnine and PS signals allows their clear distinction and the measurement of coupling constants out of one-dimensional experiments is possible but
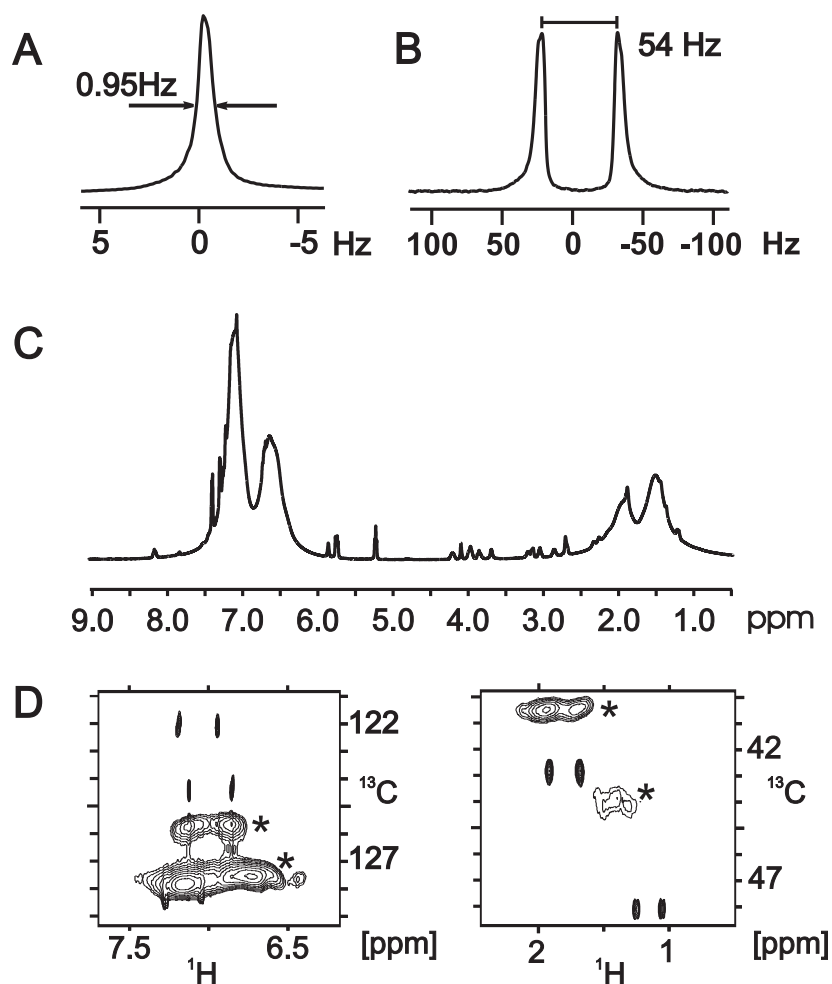
Figure 2.8: Achievable line width and polymer signals in a stretched PS gel. (A) Signal of residual CDCl$_3$ in the gel: Although most signals are broadened due to residual dipolar couplings, the experimentally achievable line width in a PS gel is not significantly larger than in conventional liquid samples. (B) Typical quadrupolar splitting of CDCl$_3$ as observed in equilibrated PS-gel samples. (C) A 1D-spectrum of a 50 mg strychnine sample in a stretched PS gel is shown. The strong broad signals in the aliphatic and aromatic regions originate from PS. (D) The polymer signals do not interfere with the signals of strychnine in heteronuclear 2D-experiments. In the case of strychnine the full set of ^{1}H-^{13}C heteronuclear RDCs can be measured. 2D-contours resulting from PS-gel signals are marked with asterisk.
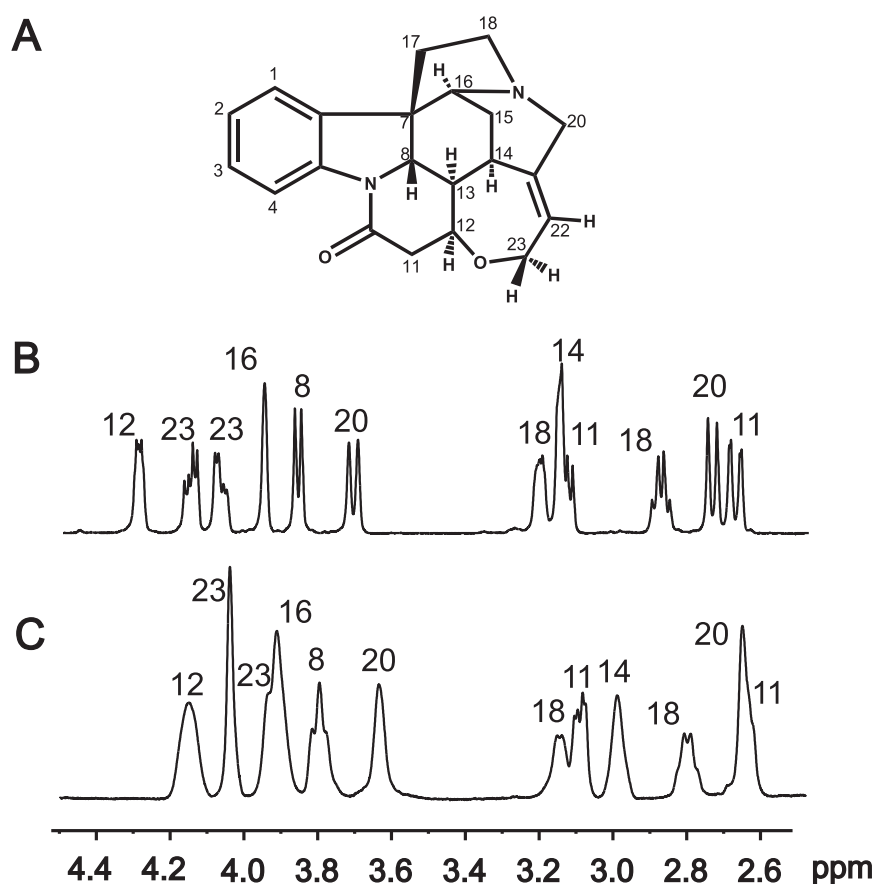
Figure 2.9: Chemical shift changes of strychnine (A) due to PS gel and section of 1D-spectra of strychnine acquired in CDCl$_3$ (B) and in a stretched PS gel swollen in CDCl$_3$ (C). PS as a cosolvent causes upfield changes in chemical shifts, and small additional changes due to RCSA might be present. Chemical shifts in both spectra were referenced to internal TMS.

difficult. In two-dimensional spectra the situation is strongly improved, since the probability of signal overlap is reduced and data analysis can be accomplished in a conventional way. Strychnine e.g. allows the measurement of a complete set of ^{1}H-^{13}C dipolar coupling constants from an uncoupled HSQC spectrum because only one aromatic signal partially overlaps with PS, for which the reliable measurement of RDCs is still possible (Fig. 2.8 D). However, suppression of PS-signals would increase the overall quality of the spectra and allow the measurement of less concentrated samples. We therefore tested two relaxation filtering approaches for PS-signal reductions: The first filter uses the difference in T$_2$ relaxation rates of the small molecule of interest compared to the large polymer and is accomplished by a spin lock period in which the magnetization is kept in the xy-plane (Fig 2.10 A). A second method uses a z-filter period to suppress spin pairs with efficient relaxation pathways for the operator $2I_zS_z$. The relaxation in this case is mainly deter-

mined by ^{1}H-^{1}H NOE which is quite efficient for the PS-polymer network (Fig. 2.10 B). The separation in this case is therefore best if the molecule of interest has a correlation time with vanishing nuclear Overhauser enhancement. The quality of suppression for both approaches can be seen in Fig. 2.11 for various filter periods: Both methods work well for the backbone aliphatic PS-signals which are already strongly reduced in the conventional HSQC (Fig. 2.11 A) and can be suppressed completely with relaxation filter delays of 100 ms (Fig. 2.11 B and D). The aromatic PS-signals instead appear to have relatively short correlation times, probably due to the increased flexibility in the side chain. Long relaxation filter periods are necessary for partial suppression of these signals and even after 500 ms relaxation filter periods, aromatic PS-signals remain visible (Fig. 2.11 C and E).

In comparison of the two methods introduced in Fig. 2.10, spin locking provides the slightly better PS-signal suppression for identical filter periods. However, the approach can lead to offset dependent suppression and even inversion of desired signals (Fig. 2.11C) if the spin lock field used cannot cover the bandwidth of the spectrum. In addition, irradiation of medium to high power rf for longer periods will lead to significant sample heating. Here, an extended z-filtering delay appears to be a very attractive alternative.
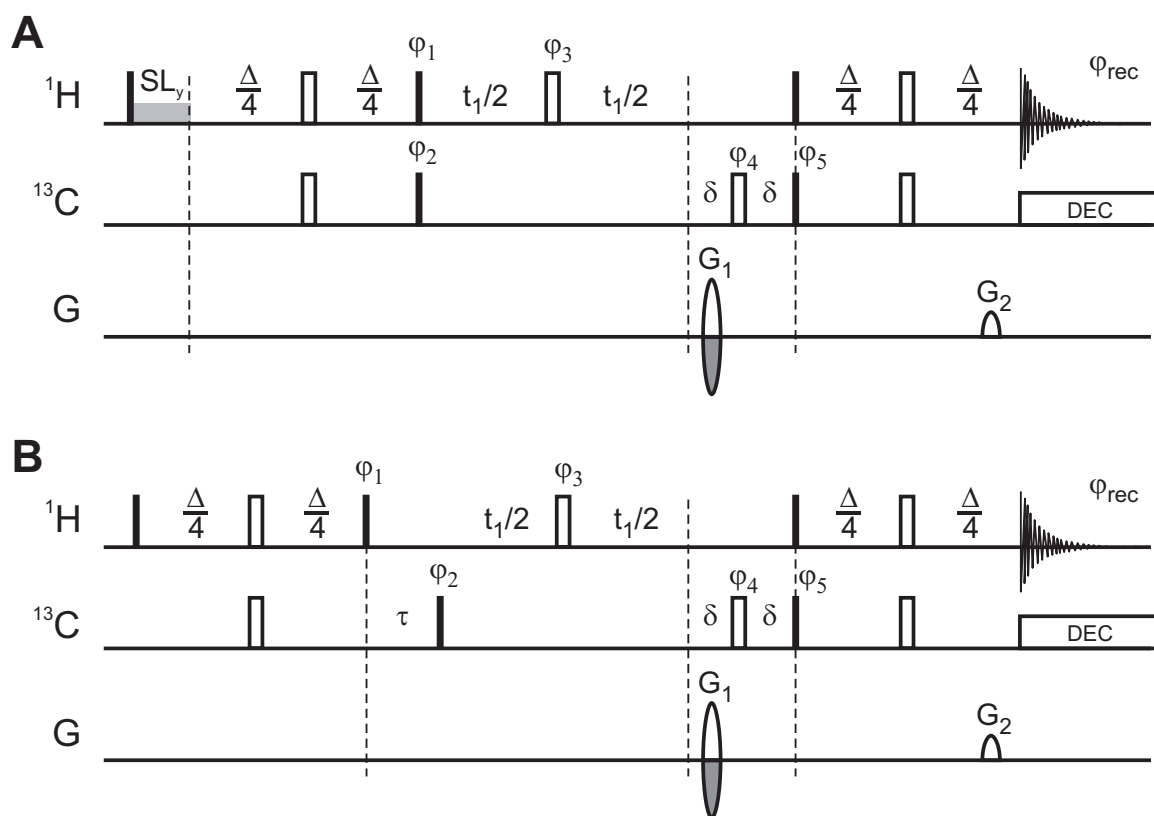
Figure 2.10: HSQC-pulse sequences with building blocks used to suppress signals originating from PS. (A) Standard HSQC experiment with additional spin lock period (SL) as a T_2 relaxation filter. (B) Standard HSQC experiment with extended z-filter delay τ which uses the difference of ^{1}H-^{1}H NOE relaxation rates of the polymer network relative to the small molecule observed. Phase cycles are: $\Phi_1 = y$; $\Phi_2 = x, -x$; $\Phi_3 = x, x, -x, -x$; $\Phi_4 = \Phi_5 = x, x, x, x, -x, -x, -x, -x$; $\Phi_{rec} = x, -x, x, -x, -x, x, -x, x$. Filled and open bars correspond to 90° and 180° pulses, respectively, with x-phase unless indicated otherwise. $\Delta = 1/^1J_{CH}$, δ compensates for G1 gradient duration. Gradients are of equal length (1ms) with ratio G1:G2 = 80:20.1 for ^{1}H,^{13}C-correlation. Phase sensitive detection in the indirect dimension is achieved by cycling G1, Φ_2 and Φ_{rec} according to echo-antiecho mode.
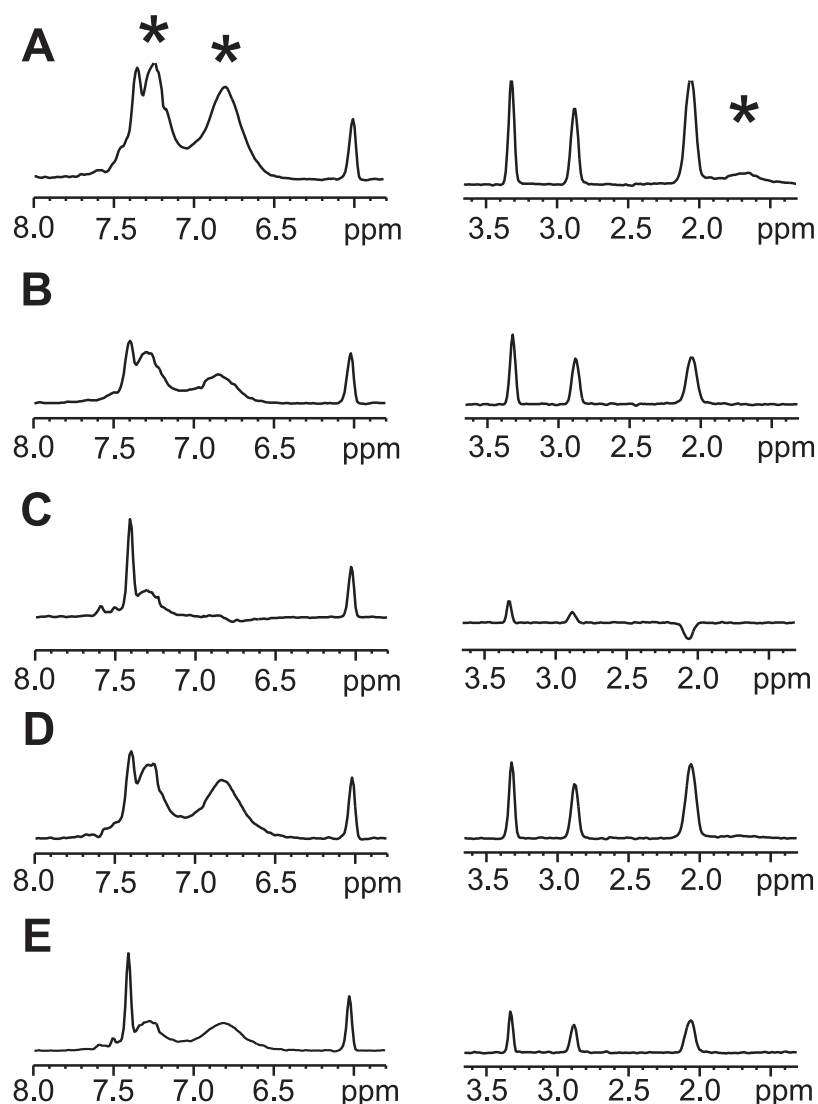
Figure 2.11: (A-E) Traces of aromatic and aliphatic regions from HSQC spectra with relaxation filters implemented as described in Fig. 2.10. No filtering (A), spin lock filtering with 100 ms (B) and 400 ms (C) spin lock times, and z- filtering with 100 ms (D) and 400 ms (E) z-filter delays. Broad polymer signals are indicated with asteriks, all other relatively sharp signals originate from strychnine dissolved into the gel. While aliphatic signals can easily be suppressed by both methods (their intensities are already strongly reduced in the HSQC experiments without relaxation filter (A)), suppression of the more flexible aromatic PS-signals can only be achieved with significant loss of desired strychnine signals. Spin locking (with 3000 Hz rf-amplitude used) can lead to inversion or even suppression of strychnine signals (C), an effect not observed for the z-filtering method (E).

2.3   Stretched poly(vinyl acetate) gels

As was already mentioned above, a number of alignment media are known for aqueous solutions, such as bicelles [115], filamentous phage [116], liquid crystalline phases [117], or stretched polyacrylamide based gels [126, 128]. For relatively apolar organic solvents, liquid crystals like poly-γ- benzyl-L-glutamate (PBLG) [86, 111, 112, 135] or deuterated 4-n-pentyl-4-cyanobiphenyl (PCBP) [113] as well as stretched polystyrene (PS, *vide supra*) and polydimethylsiloxane (PDMS) [133] gels were used to obtain structural information from RDCs. For polar organic solvents like methanol or DMSO, however, no alignment medium was available for a long time. Here the use of stretched polyvinylacetate (PVAC) gels for partial orientation of molecules dissolved in polar organic solvents is described. Lately, some new promising alignment media compatible with polar organic solvents were also reported, like the copolimer of 2-(acrylamido)-2-methylpropanesulfonic acid and N,N-dimethylacrylamide linked with N,N'-methylenebisacrylamide [152] or poly-acrylonitrile [153].

2.3.1   Gel preparation

Crosslinked PVAC-polymer sticks were produced in a similar way as described previously for PS. Glass tubes with inner diameters of 2.4 mm, 3.4 mm and 4.0 mm were sealed by melting on one end and dried carefully, followed by a treatment with a 1:1 mixture of chlorotrimethylsilane and dichloromethylsilane for 18 h to ensure hydrophobic glass surfaces. After washing with dichloromethane tubes were dried at 50°C. Vinyl acetate (Fluka) and adipic acid divinyl ester (ABCR) were filtered with basic aluminum oxide (pH 10) and distilled under reduced pressure. The monomers then were degassed for 15 minutes under vacuum in an ultrasonic bath and ventilated with argon. Immediately afterwards vinyl acetate, adipic acid divinyl ester and azoisobutyronitrile were mixed in the desired concentrations and filled into the glass tubes. The open end was sealed by melting and polymerization performed for 5 days at 45°C and another two days at 60°C.

2.3.2   Alignment properties of PVAC gels

As a first test we put crosslinked PVAC-sticks in various organic solvents and watched the swelling behavior. The sticks were swelling in basically all tested solvents, such as chloroform, tetrahydrofurane (THF), dioxane, benzene, ethylacetate (EtAc), acetone, acetonitrile (MeCN), methanol (MeOH) and DMSO. We repeated the swelling inside NMR-tubes and added 5 % (v/v) CDCl$_3$ to the non- deuterated solvents to be able to monitor any induced anisotropy by the deuterium quadrupolar splitting ν_Q. In all cases significant splittings with sharp lines could be observed (Table 2.5) after letting the gels equilibrate for 13 days. In addition, we recorded the dependence of the quadrupolar splitting on the amount of crosslinker used for polymerization for four solvents (DMSO, MeOH, THF, and dioxane; c.f. Fig. 2.12). The resulting curves are similar to the one observed for PS-gels (see Fig. 2.4), corroborating the general trend that higher crosslinking concentrations

Table 2.5: Quadrupolar deuterium splittings (Hz) of $CDCl_3$ (5 % v/v) added to PVAC sticks (0.1 % v/v cross linker, 3.4 mm and 4.0 mm inner diameter) swollen in various non-deuterated solvents.

	MeCN	Acetone	EtOAc	Benzene	$CDCl_3$
3.4 mm	36.6	33.8	49.4	83.1	72.8
4.0 mm	47.5	54.7	67.7	$-^{a)}$	106.1
	DMSO		MeOH	THF	Dioxane
4.0 mm	10.0		35.2	54.6	39.5

$^{a)}$ Gel disrupted during swelling

lead to stronger induced anisotropies [133].

In a next step we tested the alignment properties of norcamphor in PVAC-gels swollen in the four deuterated solvents available in our laboratory. Norcamphor (cf. Fig. 2.5) was chosen as a sample for two reasons: it is highly soluble in almost every organic solvent and its protons all point in different directions. In DMSO-d_6, methanol-d_4, acetonitrile-d_3, and $CDCl_3$ we were able to measure at least six D_{CH} RDCs and derive the alignment tensors using the program PALES with the bestFit option [134] (see Table 2.6). Interestingly, the four alignment tensors differ significantly: D_a/D_r ratios differ for the four solvents and the axial component for methanol even has the opposite sign compared to the others. We can only speculate about this different behavior, but most probably specific interactions of the solvents with the polymer and/or the solute lead to this phenomenon. However, the most important result for the use of stretched PVAC- gels as alignment media is that RDCs in the desired range of ±20 Hz can be measured in all cases.

2.3.3   Application to a natural product

A large field of potential applications is the structure determination of natural products. We therefore applied the method also to the well-characterized antibiotic sphaeropsidin A as a more realistic test sample [154, 155]. After diffusion of 6 mg of sphaeropsidin A into an already swollen PVAC/DMSO gel with a quadrupolar $CDCl_3$ splitting of 10.1 Hz, two coupled HSQC-spectra, optimized for aliphatic and olefinic nuclei, respectively, were acquired on a Bruker DMX900 spectrometer (Fig. 2.13). Compared to sphaeropsidin A cross peaks, relatively strong PVAC and DMSO signals are present in both spectra, but D_{CH} RDCs can still be measured in most cases since sphaeropsidin A and PVAC signals do not overlap. Only the methylene protons attached to C_{11} show significant overlap and second order effects so that a reliable RDC measurement was not possible. All couplings were carefully measured by extracting slices out of the 2D-spectra and applying the phase correction approach described in detail in [123]. As a starting point we looked at the eight C-H-vectors containing the atoms C_1, C_2, C_3, C_5, and C_{14}. The diastereotopic protons of the methylene groups of C_2 and C_3 were easily derived by using the simple method to
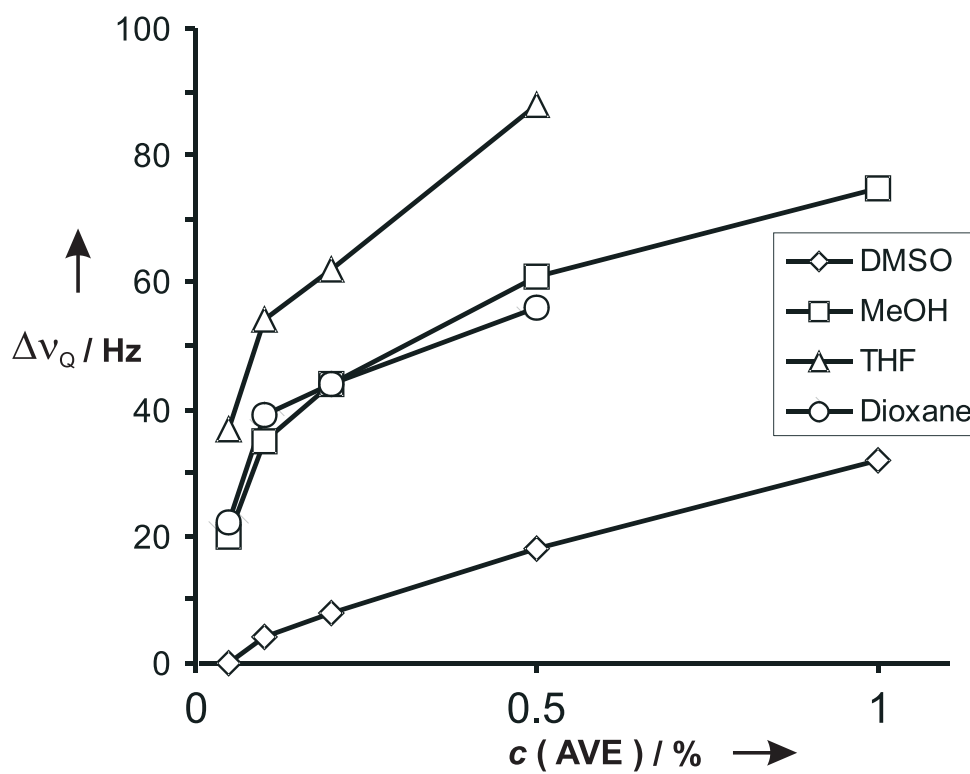
Figure 2.12: Dependence of the quadrupolar deuterium splitting ν_Q of $CDCl_3$ on the amount of cross linker adipic acid divinyl ester (AVE). To obtain the splittings 5 % (v/v) of $CDCl_3$ has been added to the PVAC-sticks swollen in the otherwise non-deuterated solvents

Table 2.6: RDCs and alignment tensor parameters of norcamphor[a] dissolved in PVAC gels that are swollen in different deuterated solvents.

	[D$_6$]DMSO	CD$_3$OD	CD$_3$CN	CDCl$_3$
$\Delta\nu_Q(CDCl_3)$	18.5 Hz[b]	70.4 Hz[b]	85.2Hz[c]	21.7 Hz[d]
RDCs				
$C_1 - H_1$	-2.37	-0.86	1.24	0.31
$C_3 - H_{3x}$	-3.61	-12.61	-1.04	-0.44
$C_3 - H_{3n}$	-15.51	-7.24	-8.51	-2.07
$C_4 - H_4$	10.31	18.22	6.21	1.29
$C_7 - H_{7a}$	15.71	-7.79	0.61	-3.70
$C_7 - H_{7s}$	-10.83	8.22	-6.18	-3.97
A_{xx}	-1.6180×10^{-4}	4.1254×10^{-5}	-3.1161×10^{-5}	-8.9383×10^{-6}
A_{yy}	-3.6670×10^{-4}	9.2611×10^{-4}	-2.1580×10^{-4}	-7.5429×10^{-5}
A_{zz}	5.2850×10^{-4}	-9.6736×10^{-4}	2.4696×10^{-4}	8.4368×10^{-5}
D_a	2.6425×10^{-4}	-4.8368×10^{-4}	1.2348×10^{-4}	4.2184×10^{-5}
D_r	6.8302×10^{-5}	-2.9495×10^{-4}	6.1546×10^{-5}	2.2164×10^{-5}
R	0.992	0.990	1.000	0.854

[a] Norcamphor $\approx$ 130 mg/sample. [b] PVAC: 0.5 % crosslinker, stick diameter 4.0 mm. [c] PVAC: 0.2 % crosslinker, stick diameter 4.0 mm. [d] PVAC: 0.1 % crosslinker, stick diameter 2.4 mm.

distinguish between axial and equatorial C-H-vectors [123]. The initial alignment tensor derived from the six unambiguous D_{CH} couplings then allowed us to do the prochiral assignment of the methylene groups containing C_1 and C_{12} (for methodology used see e.g. [86, 111]). This is remarkable, because in both cases the difference in distance of axial/equatorial or *syn/anti* protons, respectively, to unambiguously identified neighbouring protons like H_5 or the methyl group containing C_{17} is only ≈ 0.1 Å, too little to reliably be identified by NOEs. By deriving D_{CC} RDCs out of the measured D_{CH} couplings with the formula 2.13 finally also the methyl groups at C_4 could be assigned. RDCs of spin pairs containing C_{15}, C_{16}, and C_{17} could not be fitted to any reasonable structural model. This most probably is indicative for intrinsic dynamics that lead to averaged RDCs at this part of the molecule. Taking into account the significant changes in chemical shifts of C_{14} - C_{16}, and H_{14} - H_{16} it might even be concluded that the gel introduces a difference in population of the exchanging conformations in this region. However, this effect is not yet understood and we can only speculate. The 12 remaining assigned RDCs were used to refine the alignment tensor that is shown together with the correspondence of experimentally determined and backcalculated RDCs in Fig. 2.14 B-D. The correlation factor R of 0.966 in this case is a clear indication that the structural model is consistent with the experimental data, which also can be seen easily in Fig. 2.14 E.

So, stretched PVAC-gels can be used as scalable alignment media for polar organic solvents. With this possibility the gap between relatively apolar solvents like dichloromethane or chloroform and aqueous solutions is closed and RDCs can now be measured in practically all common NMR-solvents. The applicability of the new alignment method is demonstrated on norcamphor and the antibiotic sphaeropsidin A. Although PVAC-signals did not pose a serious problem in heteronuclear correlation experiments, more sophisticated NMR-methods like relaxation filters (*vide supra*) can be included in experiments to obtain spectra of higher quality.
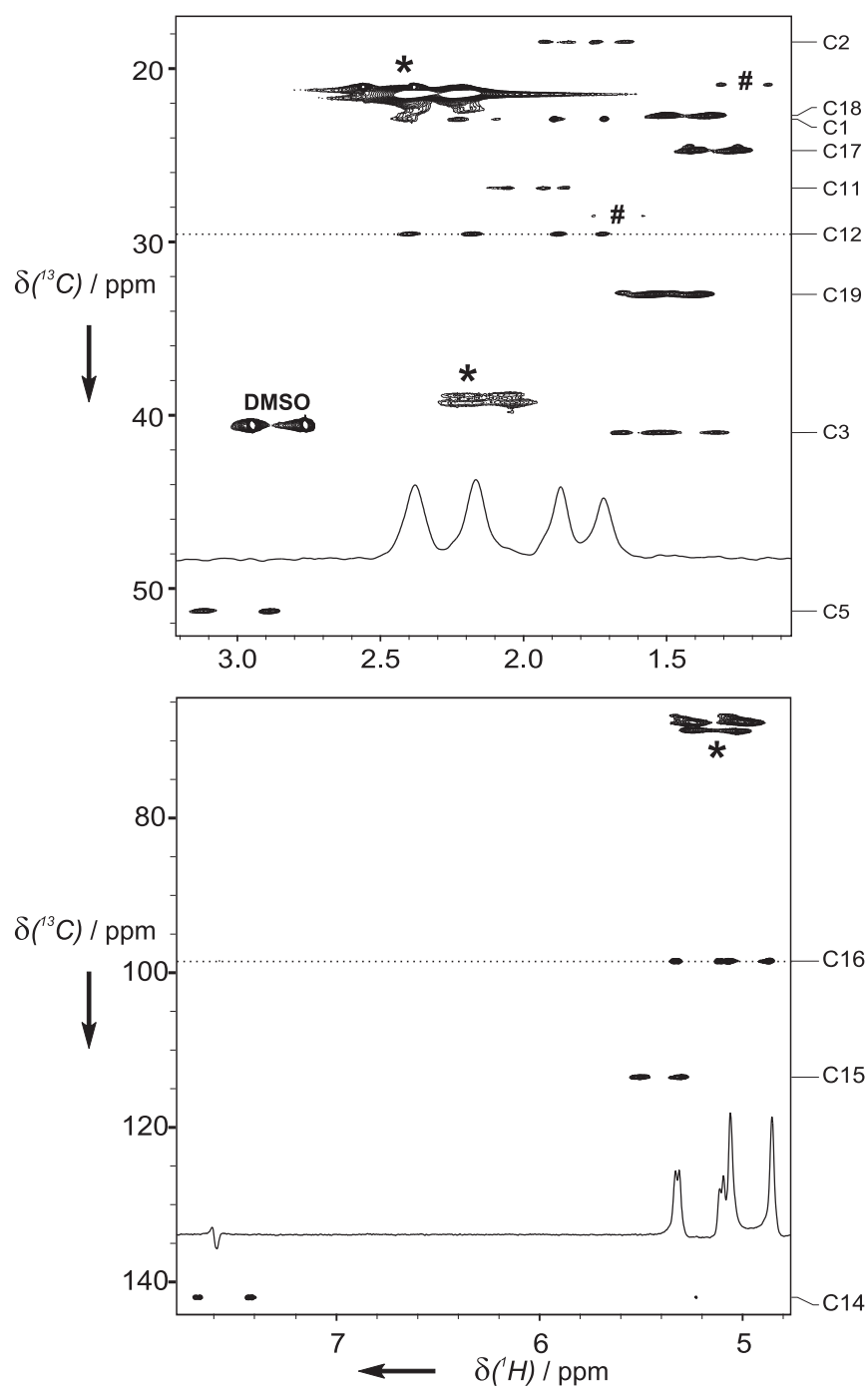
Figure 2.13: Aliphatic (top) and olefinic (bottom) coupled ^{13}C,^{1}H-HSQC spectra acquired on 6 mg sphaeropsidin A dissolved in a PVAC/DMSO-gel. DMSO signals (DMSO), PVAC signals (*) and signals originating from unpolymerized monomers (#) are indicated in the spectra. Slices at the dotted lines are shown to give an impression on the overall quality of the cross peaks.
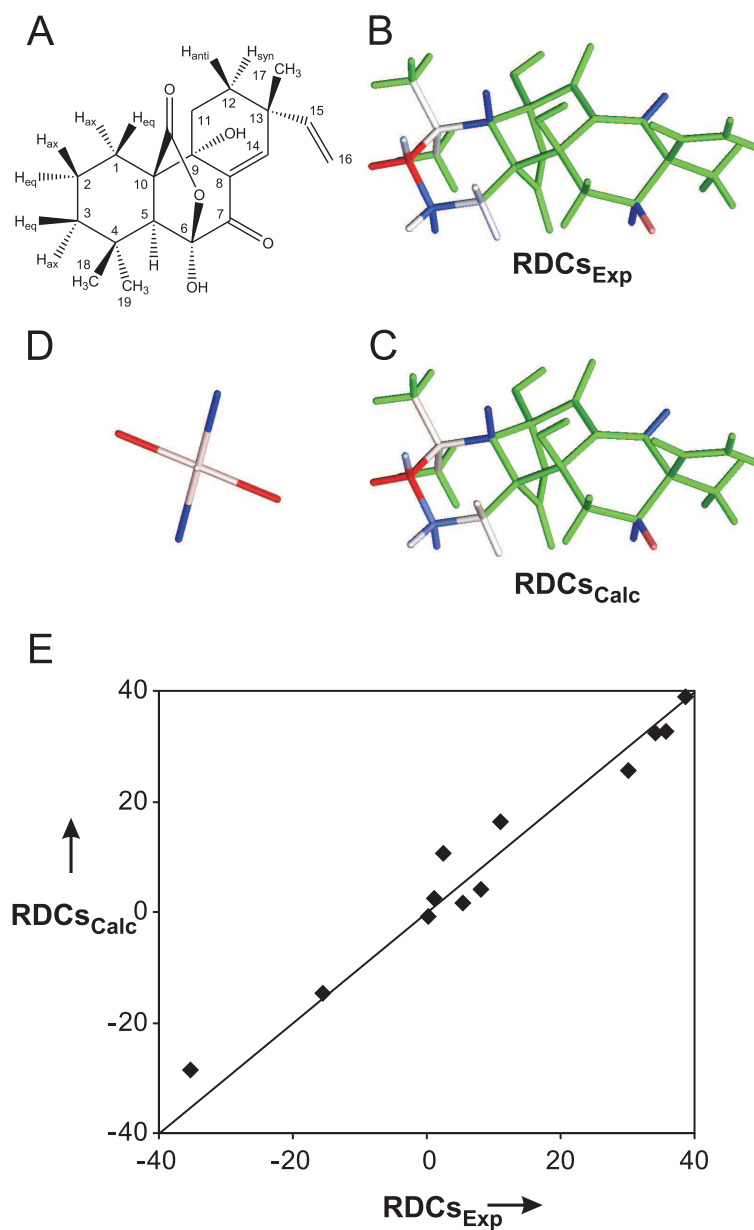
Figure 2.14: Correspondence between experimental and backcalculated RDCs of sphaeropsidin A dissolved in a PVAC/DMSO gel. (A) Structure and numbering of sphaeropsidin A. (B) and (C) color representation of the experimental and backcalculated RDCs, respectively, onto sphaeropsidin A. Red corresponds to negative, blue to positive, white to intermediate and green to no RDCs measured. (D) Representation of the alignment tensor in the coordinate frame of sphaeropsidin as shown in (B,C) with red being negative and blue positive tensor axes. (E) The plot of experimental vs. backcalculated RDCs shows a good correlation.

2.4 Stretched gelatin gels as chiral alignment medium

It is well known, that orienting medias can be used not only to measure RDCs, but also as a chiral auxiliary to perform NMR experiments on mixtures of chiral substances, allowing enantiomeric discrimination (see e.g. ref [156]). In general, verification of the enantiomeric purity of a product and measurement of the enantiomeric excess is becoming more and more an everyday problem in modern organic chemistry, requiring thus a development of convenient methods for this purpose. Classical NMR-methods used to differentiate enantiomers with an aid of some chiral auxiliaries like chiral derivatising agents, lanthanide chiral shift reagents or chiral solvating agents [156, 157] only work for functionalized chiral molecules of interest which can interact with these auxiliaries to build a detectable diastereomeric compound or adduct. In contrast, chiral orienting media provide an enantiomer discrimination due to the differential ordering effect of enantiomers inside the chiral oriented phase [158, 159]. So, even compounds possessing no polar groups and are thus bad candidates for the common means used in laboratories, like saturated chiral hydrocarbons [160], and even prochiral elements in symmetrical molecules [161, 162] can be distinguished by NMR spectroscopy in such media.

So far only surfactant bilayers [163–165] and various other chiral liquid crystalline media [166–170] or non-chiral liquid crystals combined with chiral cages [171] were reported to be suited for the task of enantiomeric discrimination. Such media are usually not easy to prepare, operate as a rule only within certain temperature intervals and their orientation depends on the strength of the magnetic field. In contrast, covalently crosslinked stretched polymer gels, as was shown above (also see refs. [126, 128]), are relatively easy to handle and provide field-independent orientation. We tried therefore to realize a partial alignment using chiral gels. Gelatin in the form of "Gummibärchen" (famous German sweets) was used for the initial proof that alignment can be achieved with this kind of polymer. In further experiments we were able to show that stretched gelatin gels as chiral alignment media not only provide an approach with which it is possible to obtain structural information via residual dipolar couplings [95, 99], but also to discriminate between enantiomers and to measure enantiomeric excess. Hereby it is interesting to note that gelatin represents a new subfamily of gels used for alignment media: polymer gels with the spatial structure almost solely stabilized by hydrogen bonds.

2.4.1 Sample preparation

Gummibärchen of a well-known German brand were swollen in deionized water to about twice their original dimensions (Fig. 2.15). After cutting the swollen bodies to a roughly cylindrical shape, they were dried on a glass capillary and inserted into NMR tubes together with D_2O. After two days of equilibration, deuterium NMR-spectra with a clearly visible quadrupolar splitting in the range of $\approx$20 Hz (Fig. 2.17 a) were acquired. After this successful proof that partial alignment can be achieved with gelatin-based gels, a more elaborate strategy was pursued: Gelatin gels were prepared from standard household gelatin (Dr. Oetker) by following the procedure prescribed by the manufacturer. Heated
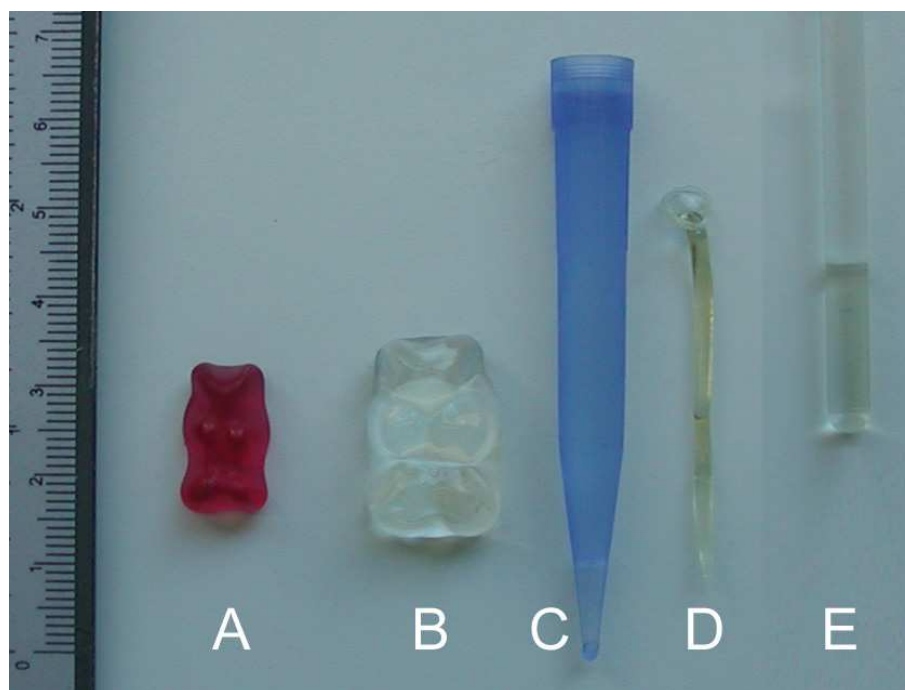
Figure 2.15: Various stages of the preparation of stretched gelatin samples. (A) Gummibärchen, (B) Gummibärchen swollen in water, (C) 10% gelatin gel prepared in pipette tip , (D) gel after drying in pipette tip, (E) equilibrated gelatin sample with a D_2O deuterium splitting of 117 Hz (Fig. 2.17 B).

gelatin solution ($\approx$10% (w/v)) was poured for the gelation in a standard pipette tip with a sealed tip end and left for drying (Fig. 2.15). After several weeks, solid sticks of $\approx$1.9 mm diameter and uniform appearance were obtained and directly put into NMR tubes for constrained swelling upon addition of D_2O (similar to the procedure described above for polystyrene sticks). After a couple of days of swelling and a single solvent exchange to wash out unwanted substances, the gel showed a D_2O quadrupolar splitting of 117 Hz at 25°C (Fig. 2.17 B). A mixture of 30 mg L-alanine and 25 mg D-alanine (9% ee) was added to the sample and allowed for diffusing into the gel. Despite the polar nature of the solutes added and the hydrogen-bond stabilized 3D-structure of the gel, no gel deterioration and hence no change in the deuterium quadrupolar splitting of the solvent was observed over a period of two months. A specially designed J-experiment (Fig. 2.16) was acquired that allowed separation of the two enantiomers.

2.4.2   Measurement of enantiomeric excess

In principle, any order-dependent NMR interaction can be used for the distinction of enantiomers. So far mostly 1D- [158, 159, 163, 167, 168, 170–178] and 2D- [159, 160, 179–181] ^{2}H spectra at natural abundance are reported which use the difference in residual quadrupo-
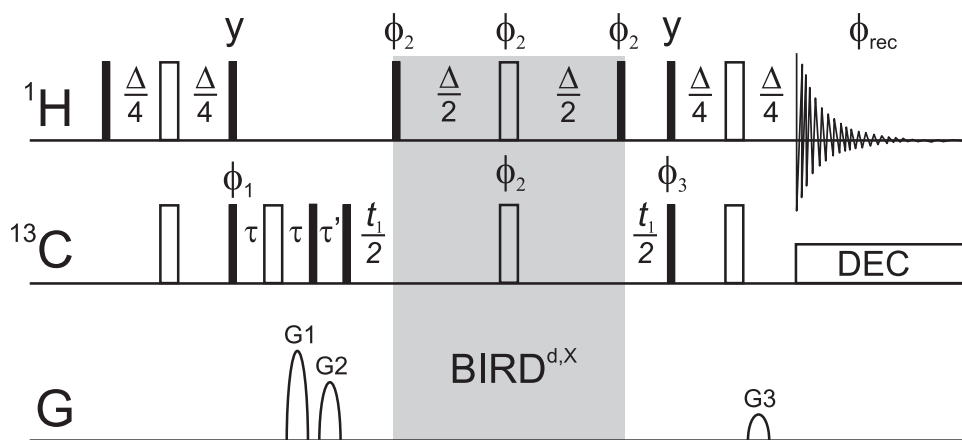
Figure 2.16: ^{1}H,^{13}C-BIRD^{d,X}-J-experiment for the phase sensitive, high resolution detection of one bond $(D_{CH} +^1 J_{CH})$-couplings. $90°$ and $180°$ pulses are indicated by solid and open bars, respectively, with phase along x unless indicated otherwise. Phase cycles are $\phi_1 = y, y, y, y, -y, -y, -y, -y$; $\phi_2 = x, x, -x, -x$; $\phi_3 = x, -x$; $\phi_{rec} = x, -x, x, -x, -x, x, -x, x$. The delay $\Delta = 1/(^1J_{CH} + D_{CH})$, τ and τ' are delays for gradient application. Typically, gradients of 1 ms duration with 200 μs recovery delay were used with gradient strength ratios G1:G2:G3 = 80:30:20.1. The BIRD^{d,X}-element for suppression of long-range ^{1}H,^{13}C - couplings is shaded gray. Phase sensitive States-TPPI can be achieved by cycling ϕ_1. Alternatively, simple t_1-incrementation can be applied using the processing procedure described in [184, 185].

lar couplings for this purpose. However, low natural abundance of deuterium nuclei makes experimental times long or requires the use of deuterated compounds. Recently, J-spectroscopy on ^{1}H [179] and ^{13}C [182] nuclei was proposed as an alternative technique in which case different alignment tensors of the enantiomers lead to distinguishable NMR signals. However, the relatively strong minimum alignment of known chiral liquid crystalline alignment media results in RDCs that easily can reach the size of $^1J_{CH}$ coupling constants (see for example [111]) and one is therefore limited to very basic NMR-experiments with known disadvantages: ^{1}H-J-spectra are not phase sensitive and broadened linewidths due to ^{1}H, ^{1}H-RDCs lead to hardly interpretable spectra in many cases. Directly detected ^{13}C-J-spectra, on the other hand, have the disadvantage of a low signal to noise ratio. In contrast, compressed gels with relatively weak induced alignments make the use of conventional heteronuclear pulse sequence building blocks possible since the condition $D_{CH} \ll {}^1J_{CH}$ is fulfilled. We therefore were able to design a ^{1}H excited and detected ^{13}C, ^{1}H-correlated pulse sequence with an additional BIRD^{d,X}-element [183] for the suppression of long range ^{13}C, ^{1}H scalar and dipolar couplings during the J-evolution period (Figure 2.16). This experiment has reasonable signal intensity and due to phase sensitive detection and reduced multiplicity of the cross peaks, the signal width in the indirect dimension allows the distinction of very small differences in one-bond D$_{CH}$ coupling constants.
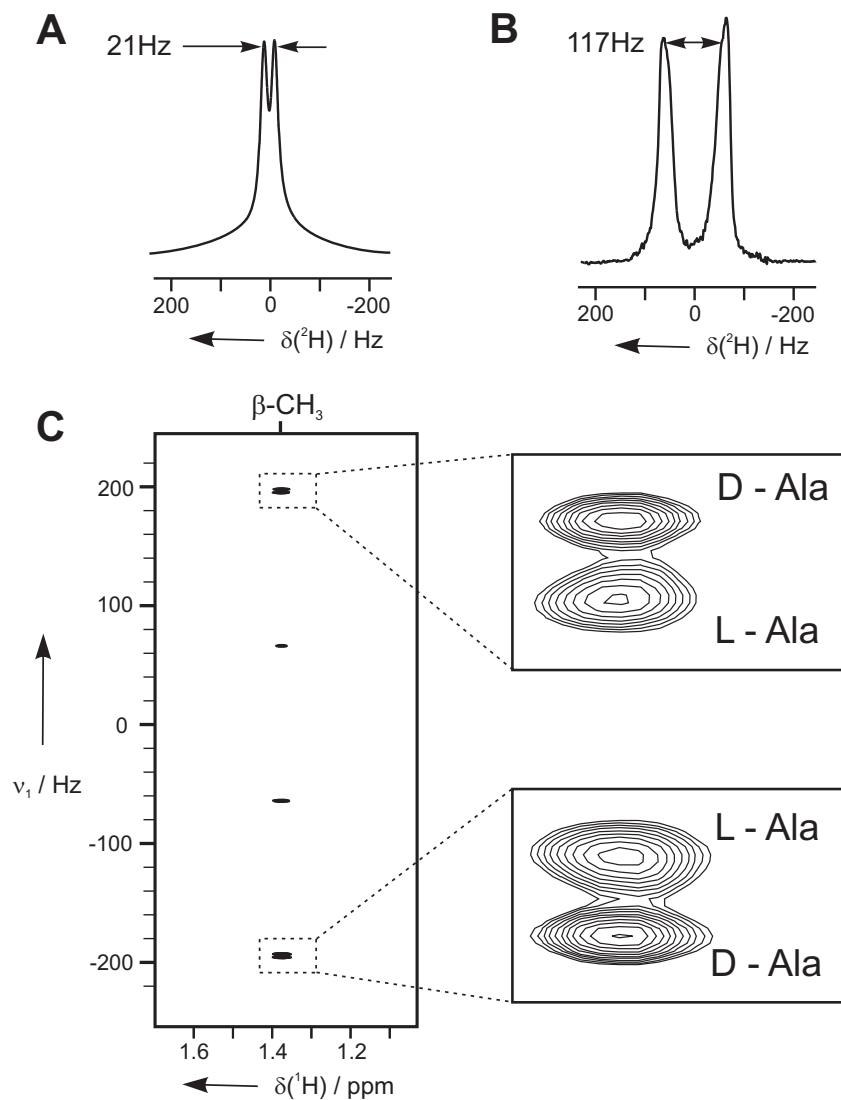
Figure 2.17: NMR-spectra acquired on stretched gelatin samples. (A) ^{2}H-spectrum of a stretched Gummibärchen-sample swollen in D_2O. The measured quadrupolar splitting is clear evidence for partial alignment. (B) ^{2}H-spectrum of the gelatin sample prepared as described in the text. So far, the alignment is stable for more than two months. (C) ^{1}H,^{13}C-BIRD^{d,X}-J-spectrum of L-Ala/D-Ala (1.2:1) diffused into the gelatin sample. The two enantiomers are clearly distinguished and integration leads to a measured ee of 7% with an estimated error of ±5%. The spectrum was acquired using the sequence described in Figure 2.16 with 2048 t_1-increments and processed in both dimensions in phase sensitive mode.

The pulse sequence was applied to the L-alanine/D-alanine (1.2:1) sample diffused in a stretched gelatin gel: Two β-CH$_3$-multiplets are observed with a well-resolved difference in outer J-multiplet components of 2.5 Hz (Figure 2.17 C). A control experiment with a sample prepared with L-alanine revealed only one signal at the same position as the stronger component of the mixed sample, providing clear evidence for the difference of D$_{CH}$ RDCs of the enantiomers in the chiral alignment medium being the origin of the split signal. Signal separation of the proposed experiment even allows integration of the cross peaks to determine enantiomeric excess. In the present case an ee of 7% $\pm$ 5% is obtained, very close to the expected value. Regarding signal integration, it should be noted that for the proposed experiment the coherence transfer and therefore also the cross peak intensities depend on the scalar and dipolar coupling constants according to $\sin^2(\pi[^1J_{CH} + D_{CH}]\Delta/2)\cos(\pi[^1J_{CH} + D_{CH}]\Delta)$. For the case shown in Figure 2.17 C this leads to a systematic error of less than 0.3% in ee.

So, this demonstrates the usefulness of gelatin gels for the partial alignment of molecules in aqueous solutions. They form three-dimensional networks of polypeptide chains due to the partial renaturing of native collagen [186], so no additional crosslinking agent is necessary to connect the polymer chains as in other gels used for the same purpose [126, 128, 133, 152, 187, 188]. Interestingly, such a polymer network, almost solely crosslinked by hydrogen bonds, is able to withstand the forces present in the constrained swollen gels. However, gelatin gels are generally not stable at temperatures above 35°C [186], and chemical stability of the stretched gels with respect to solutes needs to be studied in more detail. Surprisingly, even at large pH range and room temperature prepared samples did not change alignment properties for more than two months.

Chiral alignment media lead to differential orientation of enantiomers and therefore allow discrimination of enantiomeric mixtures by NMR-spectroscopy [159]. To our knowledge, gelatin is the first chiral alignment medium that combines the possibility of enantiomeric distinction with the advantages of partial alignment due to mechanical stretching. The easily scalable alignment in this case opens the possibility to use more sophisticated NMR-spectroscopical methods to enhance sensitivity and obtain sharper lines because of reduced multiplet patterns. The combination of chiral gel based alignment media, providing alignment independent of the magnetic field, and field-independent J-spectroscopy-based measurement techniques might eventually allow conducting these measurements even on low-field, low-cost NMR- spectrometers as long as chemical shift resolution is not necessarily needed. The approach is not limited to gelatin, but most probably other chiral gels or achiral gels with chiral cages can be found which then should allow enantiomer discrimination also in nonaqueous solutions.

2.5 Measurement of Residual Dipolar Couplings

NMR experiments on oriented samples have some specialities in the setup. In most of the cases they should be run unlocked, because the lock signal is usually split by the quadrupolar coupling of the deuterium nuclei. As a consequence, the spectrometer might lock on one or the other half of the doublet and the spectrometer frequency references that are based on the defined lock signal typically lead to wrongly referenced chemical shifts. In the worst case, the lock control system might eventually jump from one deuterium line to the other, correspondingly changing all the chemical shift references, which would be fatal to any 2D or long-running 1D experiment. Similarly, the lock signal cannot be used to shim the sample, since the usual shimming procedure maximizing the lock signal would in this case lead to a collapse of the naturally split signal into an artificial singulet, correspondingly distorting the natural lineshapes of all other lines in the spectrum. Instead, it is necessary to shim on the integral of the FID or directly on the spectrum. Otherwise the acquisition is straightforward.

Of course, depending on the chosen alignment medium, solvent and sample concentration, necessary measures should be taken to eventually suppress the signals of the solvent and of the alignment medium, as for example was described in section 2.2.4.

In some favorable cases RDCs are measurable even in usual 1D experiments (if the assignment is known). Though it is highly improbable to meet the conditions to be able to measure proton-proton RDCs in simple 1D experiments (the alignment will either be too small and unmeasurable or strong enough to broaden all the lines to a degree where multiplets collapse), proton-coupled ^{13}C spectra provide useful information in this regard. In fact, if the alignment is so strong that RDCs are on the order of $^1J_{CH}$ coupling constants, one-dimensional experiments provide the only viable way to measure RDCs [111]. However, if the largest RDCs are in the desired range of ± 30 Hz, more advanced NMR experiments with high sensitivity and better resolution can be applied. The most easily measurable RDCs are one bond D_{CH} couplings, which can be measured using standard coupled HSQC or HMQC experiments (*vide infra*). Some methods to measure one bond and long range D_{CH} couplings are discussed in detail in this section.

2.5.1 One-bond heteronuclear couplings

As was already mentioned above, the most easily measurable RDCs are one bond D_{CH} couplings, which can be measured using standard coupled HSQC or HMQC experiments [86, 111, 112, 123, 124, 129] (see for example Figs. 2.6 and 2.13). However, in many cases the resolution of standard HSQC/HMQC experiments is not sufficient, especially for large biomolecules with strongy overlapped spectra and lines broadened due to relaxation, and in alignment media with very large and non scalable alignment. For such cases a large number of specialized techniques was developed in the field of biomolecular NMR to accurately measure one bond D_{CH} and D_{NH} couplings. Some examples of these are spin-state selective excitation [189, 190] and coherence transfer [191], IPAP [192], J modulation [193], JE-TROSY [185], and quantitative J experiments [194]. For methylene groups, the

socalled SPITZE-HSQC provides a separation of multiplet components in four spectra that allow RDC determination in more crowded regions [195]. In most of the experiments the use of BIRD filtering techniques can further improve spectra by selectively decoupling long-range C-H couplings [183, 196, 197], as was used for this purpose also in section 2.4. Due to the fast averaging, D_{CH} RDCs of methyl groups cannot be used directly as structural information. However, they can be converted into D_{CC} RDCs to the attached carbon via the formula [86]:

$$D_{CC} = D_{CH_3} \left(-3 \frac{\gamma_C}{\gamma_H} \right) \cdot \frac{r_{CH}^3}{r_{CC}^3} \tag{2.13}$$

One of the advantages of stretched polymer gels as alignment media are their usually relatively low and scalable induced anisotropy and correspondingly relatively small sizes of residual dipolar couplings. Therefore the achievable spectral quality in this case is comparable to that of isotropic samples. The measurements of one bond heteronuclear couplings in such alignment media is relatively straightforward and in most cases can be performed with the same methods as in isotropic samples, as shown in Fig. 2.6. However, because of the variation in $(^1J_{CH} + D_{CH})$ couplings, which is significantly larger than usual variations in $^1J_{CH}$-couplings, the INEPT-delays in HSQC pulse sequences will be inevitably mismatched for a big part of present couplings, whatever average value one would chose for this delay. In this situation the incompletely refocused antiphase magnetisation will contribute to the phase distortions of corresponding spectral lines, as can be seen in Fig. 2.19 A. If this distortion is moderate and there is no overlap with other multiplets with significantly different coupling, one can simply phase each line separately and then measure the distance between correctly phased lines and hence the coupling [123]. However, this approach is not only time consuming, but simply will not work in a case, where two doublets with significantly different couplings overlap, while in this case the two overlapping doublets have different phase distortion and therefore might not be correctly phasable.

This situation can be significantly improved with a simple trick. First, to reduce losses associated with imperfect INEPT-transfer the simple version of the HSQC pulse sequence has to be used, the one without sensitivity enhancement and only one INEPT delay in the back-transfer step. Now the unwanted antiphase component at the end of the INEPT-transfer step can be converted into double-/zero-quantum terms by a simple 90° pulse and the phase distortions casued by dispersive antiphase components are removed. The corresponding pulse sequence can be seen in Figure 2.18 A. Applied to an oriented sample with large distribution of effective one-bond couplings, this pulse sequence results in a spectrum with pure phases of all present multiplets, as can be seen in Fig. 2.19 B. The deviation of the effective length of the INEPT delay from the ideal value is reflected now in the reduced signal intensity, since only part of the magnetization is transformed into observable magnetization.

With slight modifications, this pulse sequence can also be used to create pure antiphase spectra. It can be done simply by removing the carbon refocusing pulse in the final INEPT-transfer step. The final 90° pulse on carbon can be either removed, or com-
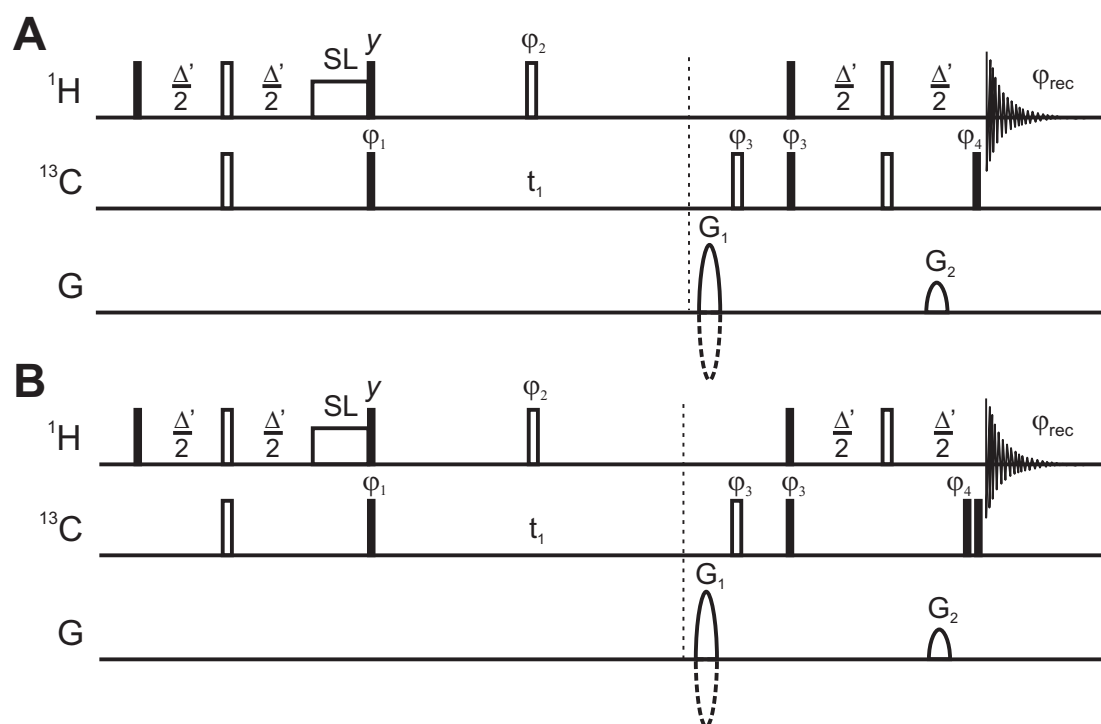
Figure 2.18: Pulse sequences for the Clean-HSQC, in-phase (A) and anti-phase (B) versions. Narrow and thick bars represent 90° and 180° RF-pulses, respectively. Unfilled rectangles represent 1 ms spin-lock pulses. Pulse phases are along x unless indicated otherwise. Phase cycles are: $\phi_1 = x, -x$; $\phi_2 = x, x, -x, -x$; $\phi_3 = 4(x)4(-x)$; $\phi_4 = x, -x$; $\phi_{rec} = x, -x, x, -x, -x, x, -x, x$. The INEPT-delay $\Delta = 1/(2\ ^1J_{CH})$ is typically set to 3.846 ms corresponding to $^1J_{CH} = 130$ Hz. Echo and antiecho sselections vere achieved using gradients. Applied gradient strength ratios are: $G_1 : G_2 = 80 : 20.1$. ϕ_1 was incremented according by π for each t_1 increment to obtain to States-TPPI-like data.
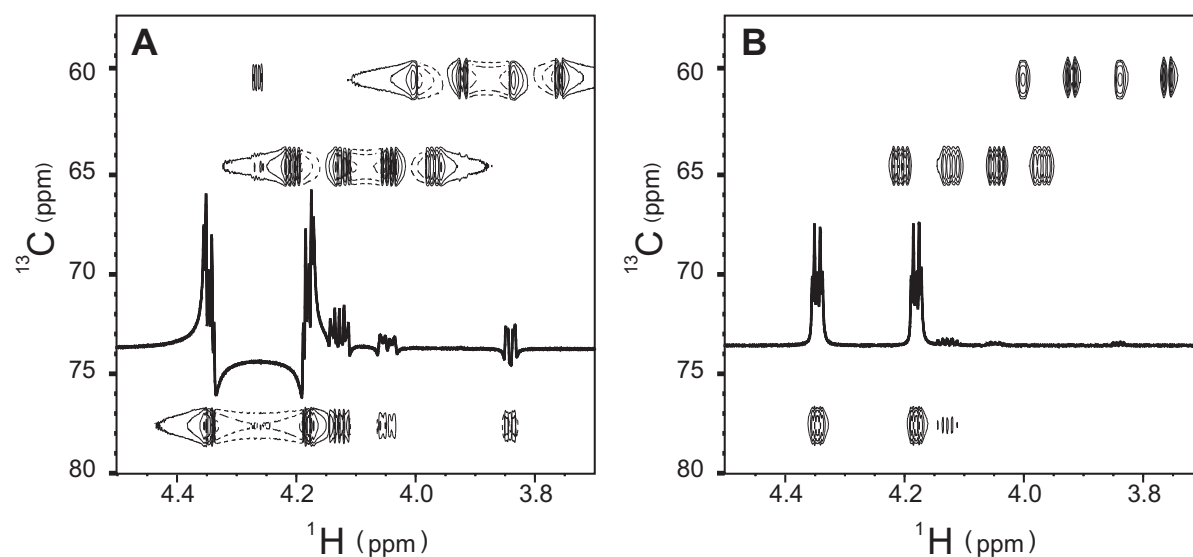
Figure 2.19: Region of HSQC spectra on strichnine with a peak with 150 Hz splitting and INEPT delays matched to a coupling value of 100 Hz. Conventional HSQC (A)and HSQC with cleansing pulse at the end of the final INEPT delay (B). (Figure courtesy of Andreas Enthart)

pensated with another 90° pulse with different phase, so that the simple phase cycle removes additional artifacts due to possible imperfections of proton pulses. This variant of a pulse sequence is shown in Fig. 2.18 B. The combination of the two sequences can now be used in an IPAP fashion to extract the subspectra with α- and β-components of a multiplet to eventually resolve overlapping signals, like e.g. in a case of a CH_2 group where the right component of the downfield proton signal overlaps with the left component of the upfield signal.

2.5.2 Long-range heteronuclear couplings

The other important source of structural information carried by the RDCs and widely used since the introduction of alignment media with sufficiently low induced anisotropy for conformational studies also for larger organic molecule, are long-range heteronuclear couplings [95, 113–117, 126, 128, 152, 187, 188, 198]. Therefore there exist a demand for accurate measurement of long range $^nJ_{CH}$ and the corresponding D_{CH} residual dipolar couplings (RDCs). In contrast to the $^3J_{CH}$ coupling determination in isotropic samples, the sign information of the long-range couplings is of equivalent importance in partially aligned samples.

Long range heteronuclear coupling constants have also always played an important role in NMR-spectroscopical studies of small to medium-sized molecules before the introduction of residual dipolar couplings. Especially $^3J_{CH}$ coupling constants follow the Karplus relation and build a more reliable tool for the determination of relative configurations as

e.g. NOE connectivities, which often do not allow unambiguous conclusions [199–210].

On our search for reliable experiments for detecting long-range heteronuclear RDCs, we examined a large number of pulse sequences. Out of the manifold of different techniques, the three experimental schemes discussed here are among the best available for measuring $^nJ_{CH}$ and the corresponding D_{CH} couplings. In this context, most selected pulse sequences were also subject to modifications that resulted in improved spectral quality in our hands. Since all presented methods have been derived during recent years, it can also be understood as a kind of extension to the excellent survey provided by Marquez *et al.* [211],in which most of the previously published methods are already compared.

Three experiment types are explored in the following: The intensity and multiplet pattern based coupling measurement out of an HMBC with a corresponding reference HSQC [86], the pattern-based coupling extraction from CPMG-type transfer experiments [212–214], and the displacement based coupling determination from IPAP-type HSQC-TOCSY experiments [215, 216].

HMBC and correlated reference HSQC

The idea of using a reference experiment for coupling extraction exists for quite some time now [217, 218]. For heteronuclear long-range couplings usually proton-based reference experiments are recorded with identical phase distortions as the corresponding HMBC-type spectrum. This approach was recently extended significantly in the way that a given multiplet pattern can be fitted to its shape *and intensity simultaneously* by acquiring the corresponding reference HSQC with identical phase distortions due to ^{1}H,^{1}H couplings [86]. Since signal intensities in HMBC experiments are proportional to $\sin \pi \, ^nJ_{CH}T$ (T being the effective long-range transfer period), they can equally be used for coupling determination so long as the lineshape and intensity of a reference signal of an already determined coupling are known [86].

The pulse sequences for an HMBC and its corresponding reference HSQC are shown in [86] and Figure 2.20, respectively. The originally published reference HSQC [86] involves two consecutive t_1-evolution periods and the resulting spectra in our hands contained considerable t$_1$-noise.It is also clear that intensities of the reference HSQC compared to the HMBC would vary significantly for molecules with non-negligible transverse relaxation.We therefore redesigned the reference experiment as shown in Figure 2.20B: after the initial filter for one-bond-coupled coherences, $2I_xS_z$ terms are converted in heteronuclear ZQ/DQ-terms to avoid further coupling evolution. In this way, the reference experiment duration could be reduced to be identical to the corresponding HMBC experiment in Figure 2.20A. As long as the relaxation of the ZQ/DQ-term does not significantly differ from the relaxation of the antiphase term $2I_xS_z$ present in the HMBC, the intensity and pattern based fitting procedure will be applicable.

A second modification to both experiments is the introduction of constant time (CT) evolution on carbon [219, 220] for improved cross peak appearance (see Figure 2.21). The main advantage is the elimination of the carbon chemical shift dependence of the measured multiplet lineshape, which helps to reduce errors in the subsequent fitting procedures.
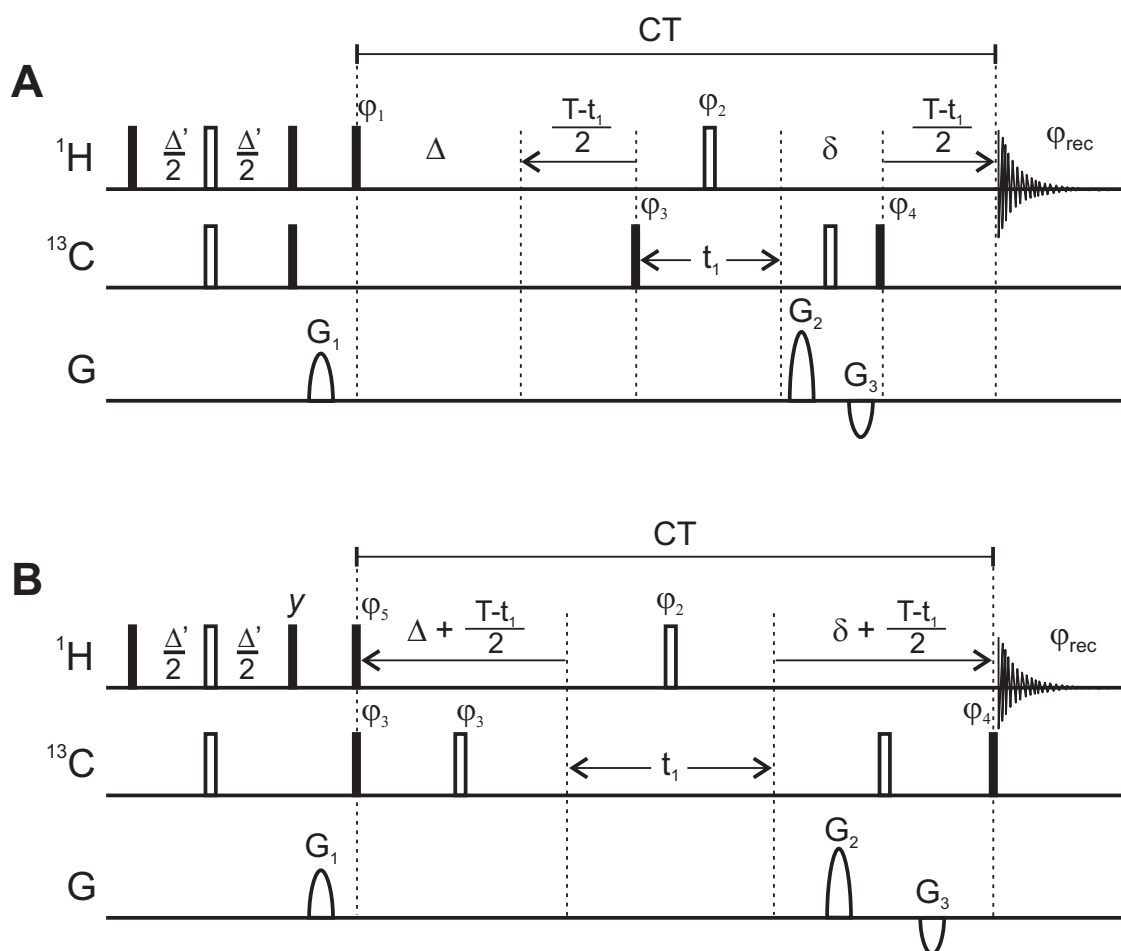
Figure 2.20: Pulse sequences for the constant-time HMBC (A) and reference constant-time HSQC experiment (B). Narrow and thick bars represent 90° and 180° RF-pulses, respectively. Pulse phases are along x unless indicated otherwise. Phase cycles are: $\phi_1 = 4(x), 4(-x)$; $\phi_2 = 8(x), 8(y)$; $\phi_3 = -x, x$; $\phi_4 = x, x, -x, -x$; $\phi_5 = 4(y), 4(-y)$; $\phi_{rec} = x, -x, -x, x, -x, x, x, -x, -x, x, x, -x, x, -x, -x, x$. The long-range polarization transfer delay Δ is typically set to 62.5 ms, which corresponds to optimal transfer for a long-range heteronuclear coupling value of $^n J_{CH} = 8 Hz$. The length of the constant time period T is set up according to the chosen spectral width in the indirect dimension and number of increments. Echo and antiecho selections were achieved using gradients. The gradient pulses were 1 ms long. The applied gradient strength ratios are: $G_1 : G_2 : G_3 = 33 : 50 : -30$ for echo and $33 : 30 : -50$ for antiecho. The carbon pulse phase ϕ_3 and ϕ_{rec} were incremented by π for every second t_1 increment to obtain States-TPPI-like data.
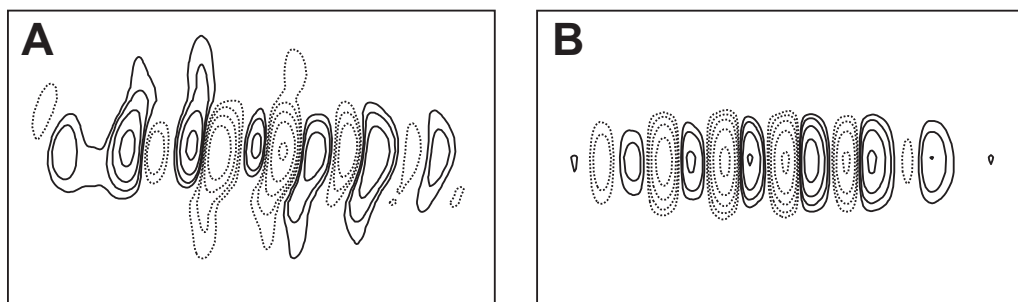
Figure 2.21: A typical cross-peak acquired using a conventional HMBC sequence (A) and a constant-time HMBC (B). Dashed lines represent negative contour levels.

We applied the pulse sequences to two widely used test samples, strychnine and menthol dissolved in $CDCl_3$. The overall quality of all spectra was good with no significant artefacts visible. The phase-sensitive processing of the data results in very complex multiplet patterns with significant dispersive contributions from homonuclear antiphase coherences. For the visualization of typical cross peaks and to give an impression of the accuracy of the fitting procedure, two characteristic signals from each CT-HMBC spectrum are shown in Figure 2.22 with the corresponding lineshape and intensity fits for the best determined couplings and for small deviations of ± 0.6 Hz. While the fit for large couplings is mainly determined by the lineshape, small couplings apparently profit significantly from the strong intensity dependence of their fit. This is, of course, due to the differences in transfer efficiency, which are proportional to $\sin \pi \, ^{n}J_{CH}T$ and are most sensitive for deviations of small $^{n}J_{CH}$ couplings, for which the sine changes approximately linearly. Larger $^{n}J_{CH}$ couplings close to ideal transfer conditions, instead, show very similar signal intensities since the transfer efficiency describes a plateau in this case.

We found that coupling constants for the two test molecules could be determined quite reliably. The complex multiplet patterns with mixed absorptive and dispersive contributions help with the applicability of the fitting procedure but also make the acquisition of large data sets necessary. The coupling extraction procedure is not yet implemented in any available software, so that we had to write a minimization script for the fitting ourselves. The coupling determination from HMBC-type spectra is generally not sign-sensitive, as can also be seen in the original paper for the described procedure [86]. This fact strongly limits its use for the determination of long-range RDCs, where the sign contains valuable structural information.

CPMG-based experiments

Two kinds of CPMG-based, purely absorptive pulse sequences for measuring $^{n}J_{CH}$ couplings can be found in the literature. The LR-CAHSQC [212] with a slight modification using composite pulses [213] and the socalled BIRD^{r,X}-CPMG-HSQMBC [214]. Sequences for both experiment types are shown in Figure 2.23 with small additional changes: in the
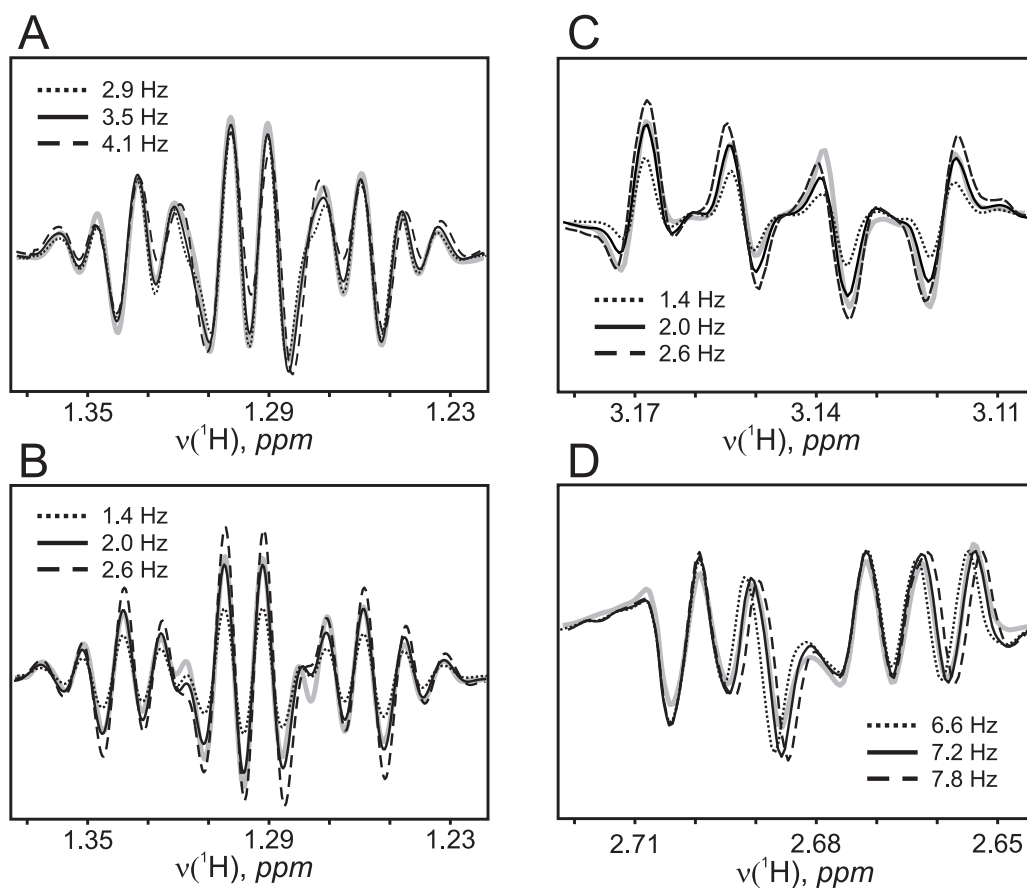
Figure 2.22: Some fitting results for cross-peaks between H_1 and C_2 (A), and H_1 and C_3 (B) of menthol and between C_{12} and $H_{11,ax}$ and C_{12} and $H_{11,eq}$ (C, D) of strychnine in chloroform. The rows extracted from HMBC spectra are plotted grey and best fits are shown with solid lines. To assess the precision of measurement, two more traces are shown for each case, with 0.6 Hz larger (dashed line) and 0.6 Hz smaller (dotted line) trial couplings.

LR-CAHSQC version no suppression of heteronuclear one-bond coherences is applied since homonuclear isotropic mixing conditions distribute magnetization into the spin system anyway and in the BIRD^{r,X}-CPMG-HSQMBC the conventional BIRD^{r,X} filter element is replaced by a CAGEBIRD^{r,X} filter [221] for a more consequent use of the CPMG properties. For convenience, we will refer to the CAGEBIRD^{r,X}-CPMG-HSQMBC as the CBC-HSQMBC in the rest of the work.

CPMG-type periods for the transfer via small heteronuclear couplings were first applied in ^{1}H,^{31}P-correlation experiments [222]. Due to the repeating inversion elements with typically an XY16 supercycle [223, 224], TOCSY conditions are fulfilled for scalar couplings [212, 222, 225, 226], leading to inphase transfer solely via undetectable ZQ-coherences. The absence of observable homonuclear antiphase coherences during the CPMG periods finally allows the phase sensitive detection of heteronuclear long-range correlations in pure absorption and with higher efficiency than previously published methods.

However, the approach comes with certain limitations. Every multiple pulse sequence has an offset dependence with respect to its Hartmann-Hahn matching conditions. The corresponding offset dependence of a typical XY16-expanded CPMG-sequence (rf$_{max}$ =20 kHz, $\Delta/2 = 100$ μs) for the homonuclear Hartmann-Hahn transfer $I_{1x} \rightarrow I_{2x}$ and the offset dependence describing the evolution of initial inphase coherences into unwanted antiphase terms $I_{1x} + I_{2x} \rightarrow 2I_{1y}I_{2z}$ are given in Figure 2.24A and B, respectively. Clearly visible is the correlation of efficient TOCSY inphase transfer (light area in Figure 2.24A) with the absence of antiphase coherences (black area in Figure 2.24B). The bandwidth for reasonable antiphase suppression can be estimated to be ≈3000 Hz along the antidiagonal, which covers most protons on small to medium-sized spectrometers but does not allow coverage of the full proton chemical shift range on high fields. A similar offset dependence exists for the inversion of carbon nuclei. For typical ^{13}C rf-amplitudes of rf$_{max} = 12.5$ kHz and a CPMG-delay $\Delta/2 = 100$ μs the inversion bandwidth covers ≈11.8 kHz, which, of course, might be compensated to some extend by using appropriate composite pulses [39, 56, 213, 227].

The main difference between the LR-CAHSQC and the CBC-HSQMBC is the transfer efficiency via long-range couplings to carbons directly attached to protons. For the LR-CAHSQC all nuclei of the corresponding spin system, i.e. the carbon and the coupled proton network, contribute to the coherence transfer. The most simple, non-trivial case is a three spin system consisting of a carbon, the directly bound proton and a remotely coupled proton, as shown in Figure 2.25A and B. The coherence transfer function of the resulting ILL coupling topology (homonuclear isotropic mixing and heteronuclear longitudinal mixing conditions [228]) is mainly modulated by the homonuclear isotropic transfer and additional modulations are due to the large heteronuclear one-bond coupling. Depending on the combination of sign and size of the participating coupling constants and the transfer time chosen for the LR-CAHSQC, corresponding cross peaks can be inverted or even vanish (see the two cases shown in Figure 2.25 for a typical $^3J_{CH}$ (A) and $^2J_{CH}$ coupling network (B)).

In the CBC-HSQMBC, instead, the effective coupling topology is reduced to 0L0, i.e.
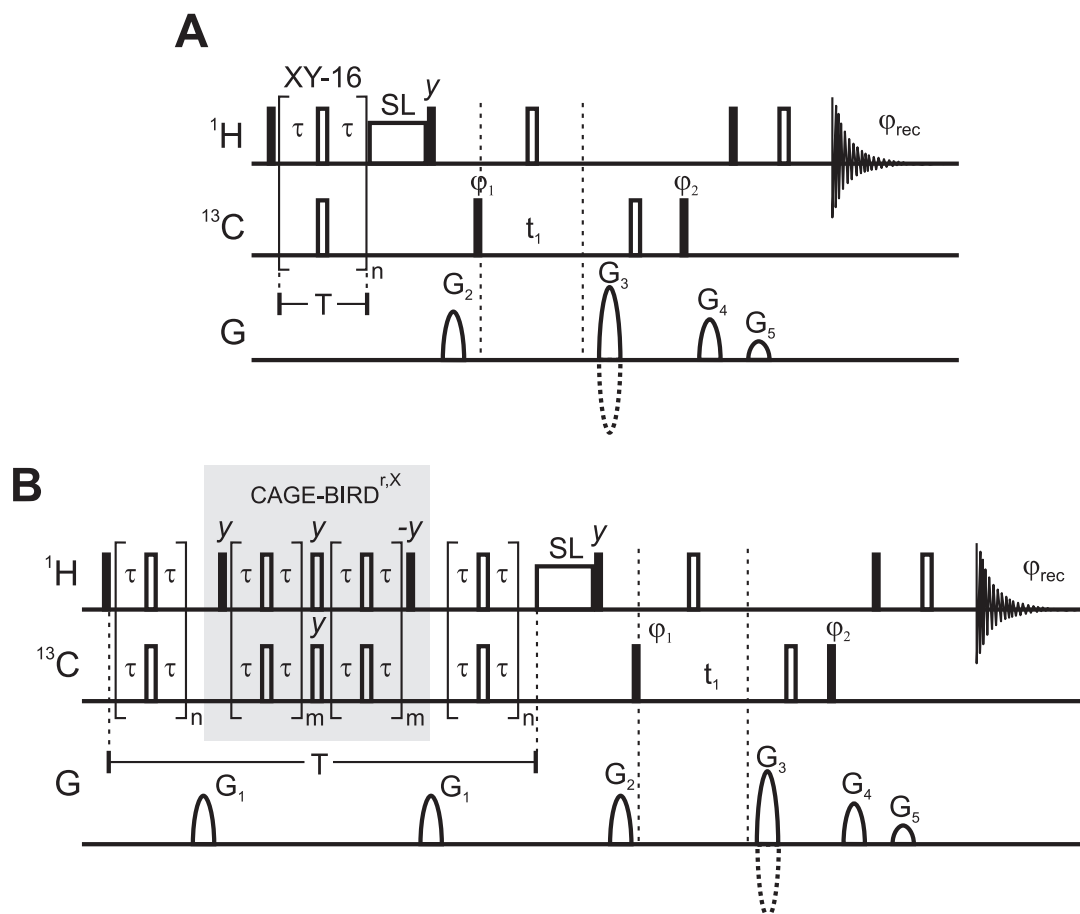
Figure 2.23: Pulse sequences for the LR-CAHSQC (A) and CBC-HSQMBC (CAGEBIRD^{r,X}-CPMG-HSQMBC) experiment (B). Narrow and thick bars represent 90° and 180° RF-pulses, respectively. The unfilled rectangle represents a spin-lock pulse (1ms). Pulse phases are along x unless indicated otherwise. Phase cycles are: $\phi_1 = x, -x$; $\phi_2 = x, x, -x, -x$; $\phi_{rec} = x, -x, -x, x$. The long-range polarization transfer delay T is typically set to 62.5 ms to roughly correspond to the usual transfer delay for the long-range coupling of ≈ 8 Hz. The CPMG-delay τ should be set equal or larger than 100 μs. The number of cycles in the CAGEBIRD element m corresponds to a single XY16 supercycle for the CPMG period. n is set to several XY16 supercycles in order to accomodate for the overall transfer duration T. Echo and antiecho selections were achieved using gradients G_3 and G_5. Gradient pulses have typical durations of $1ms$. Applied gradient strength ratios are: $G_1 : G_2 : G_3 : G_4 : G_5 = 33 : 50 : \pm 80 : 41.7 : 20.1$. The carbon pulse phase ϕ_1 and the receiver phase ϕ_{rec} were incremented by π for every second t_1 increment to obtain States-TPPI-like data.
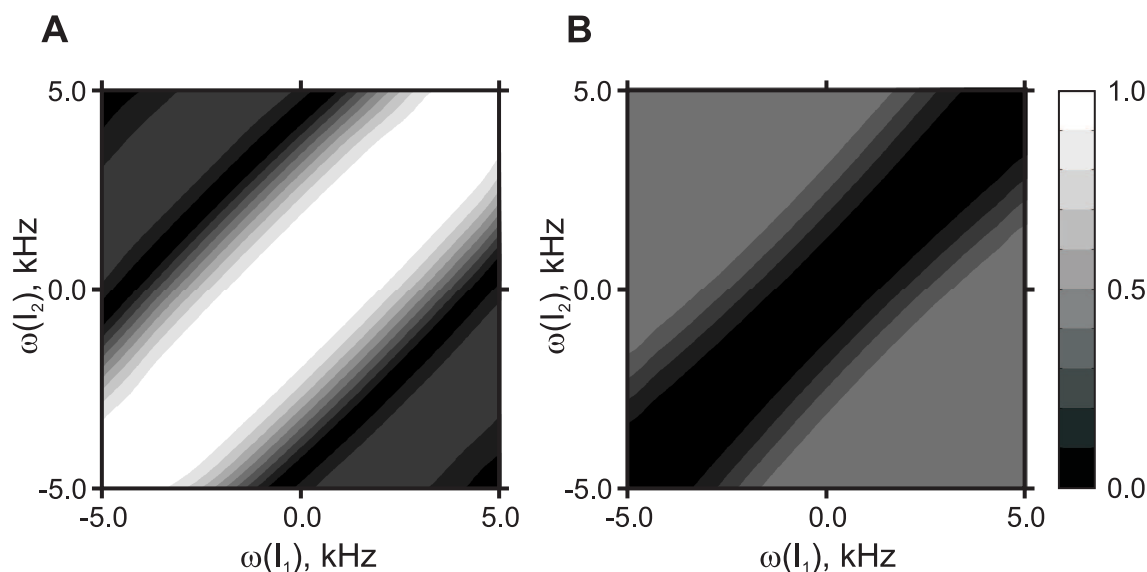
Figure 2.24: Transfer properties of a CPMG pulse train as used in a pulse sequence of Fig. 2.23 with delay $\tau = 100\mu s$ and a hard inversion pulse applied at 20 kHz RF-power. Transfer is simulated for a homonuclear two-spin system with a $J =12.63$ Hz isotropic coupling and optimal transfer length of $1/(2J)$ =39.6 ms. The offset dependence of the transfer efficiency are shown for typical TOCSY-transfer $I_{1x} \rightarrow I_{2x}$ (A) and the evolution of inphase into undesired antiphase terms $I_{1x} + I_{2x} \rightarrow 2I_{1y}I_{2z}$ (B). For the CPMG parameters chosen an active bandwidth for reasonable antiphase suppression can be derived to be approximately 3000 Hz along the antidiagonal.

an effective heteronuclear two spin system, because the directly bound proton is decoupled by the CAGEBIRD^{r,X} element (Figure 2.25 C,D). This reduction of the effective spin system in the CBC-HSQMBC experiment compared to the LR-CAHSQC clearly gives an advantage concerning its applicability to compounds of unknown spin systems, since the effective spin systems are reduced and also unnecessary one-bond correlations are effectively removed.

Examples cross peaks for coupling extraction from lineshape fitting using the LR-CAHSQC and CBC-HSQMBC are given in Figure 2.26 B-E. The corresponding reference lineshapes can either be obtained from a conventional proton 1D-experiment or from slices of an HSQC. In the LR-CAHSQC the reference might also be taken from the corresponding one-bond correlation, if present. This case is shown in 2.26 A.

For most signals the coupling measurement is straightforward and accuracy of the determined coupling is mainly limited by the signal-to-noise ratio of the corresponding cross peak. However, signals with broad multiplets and no characteristic, easily recognizeable pattern pose a problem. In such cases, as for example demonstrated in Figure 2.27 for the H$_1$-C$_6$ and H$_2$-C$_1$ cross peaks of menthol, lineshape fitting alone can result in a large uncertainty of up to several Hz.
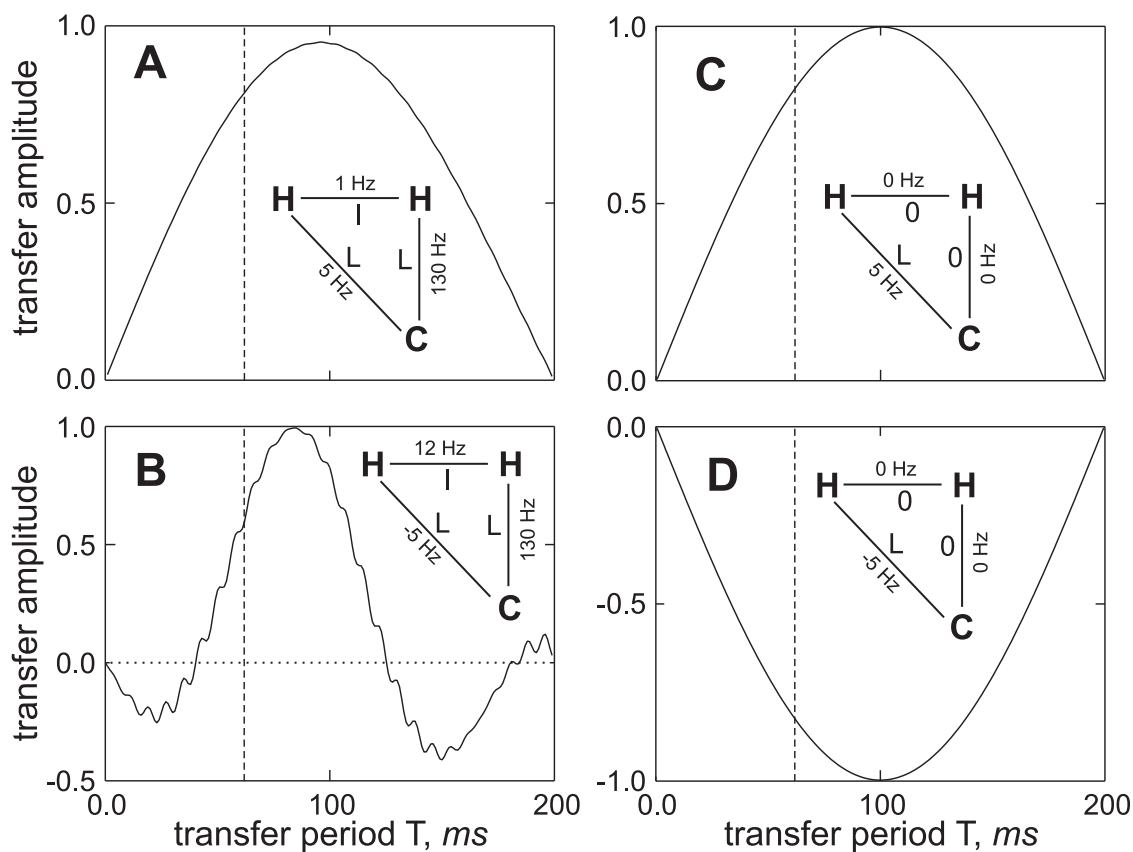
Figure 2.25: The calculated efficiency of the transfer of in-phase proton magnetization to anti-phase carbon magnetization by a CPMG train for two typical constellations corresponding to $^3J_{CH}$ (A,C) and $^2J_{CH}$ (B,D) cases. Transfer functions for both the LR-CAHSQC corresponding to an effective ILL spin topology (A,B) and the CBC-HSQMBC with its effective 0L0 topology (C,D) are calculated. Vertical lines correspond to the mixing times used in actual experiments.
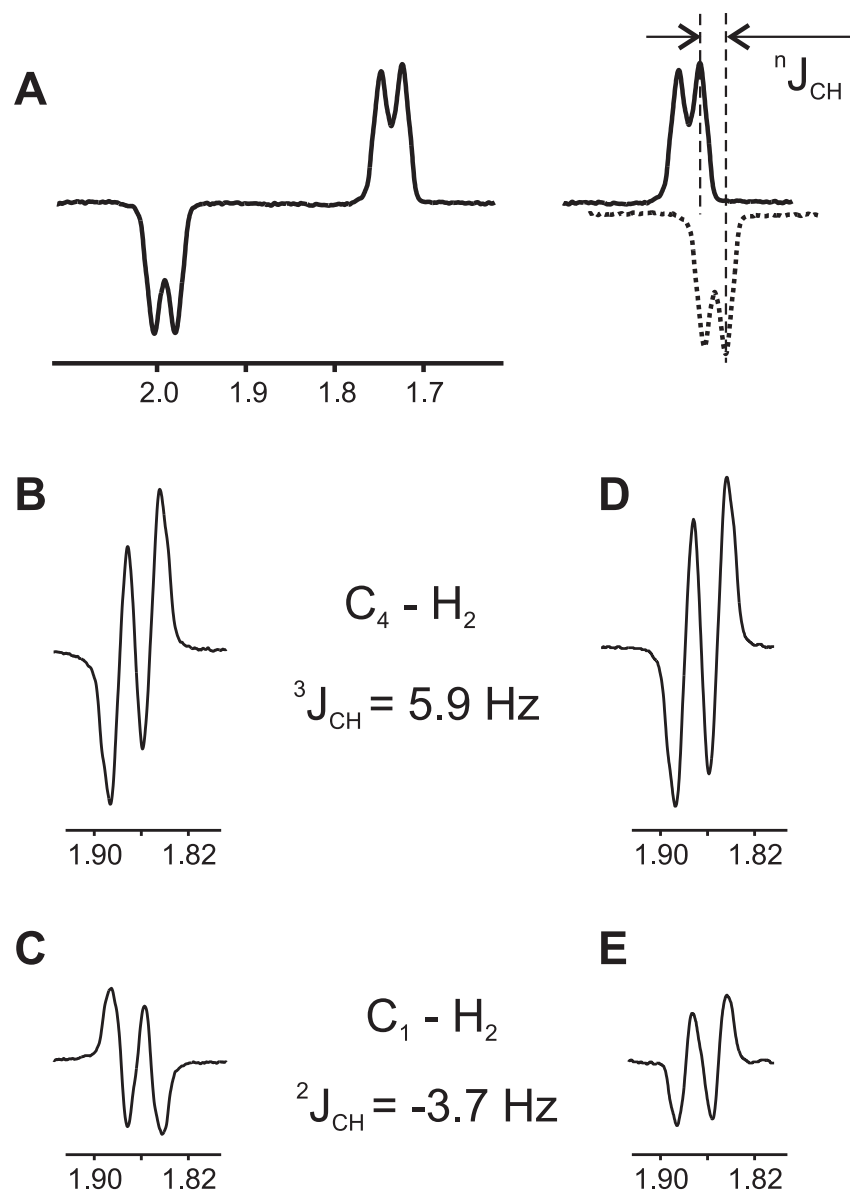
Figure 2.26: Pattern-fitting procedure for coupling extraction out of both CPMG-based methods presented.(A) Reference signal taken from the H_2-C_2 cross peak of the LR-CAHSQC with the construction of the resulting antiphase multiplet sketched next to it. (B,C) example cross peaks taken from the LR-CAHSQC to indicate the pseudo-sign-sensitive measurement discussed in the text. (D,E) Identical cross peaks in the CBC-HSQMBC with no inversion of the multiplet-tilt.
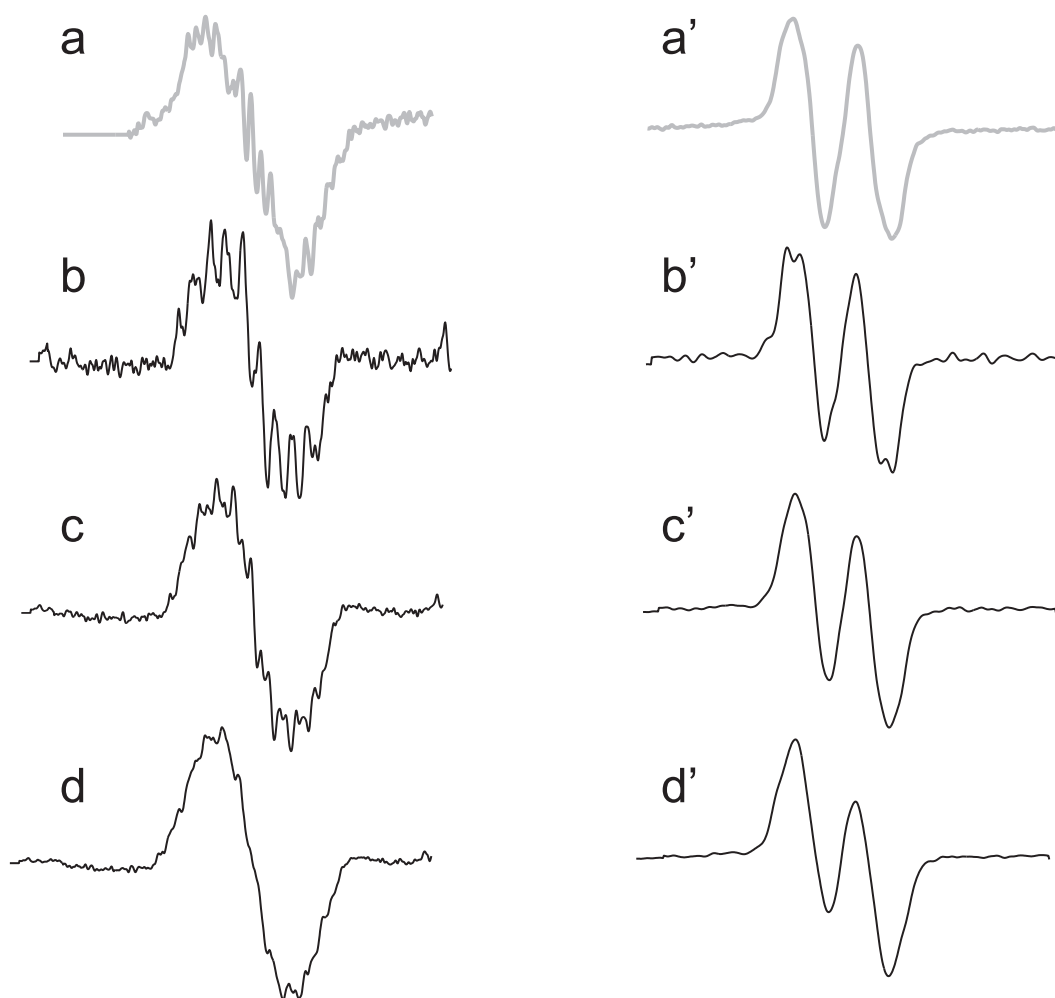
Figure 2.27: Two examples of insufficient accuracy in coupling constant determination using the pattern-fitting approach. Slices through cross-peaks between H_1-C_6 (left, a) and H_2-C_1 (right, a′) of the LR-CAHSQC acquired on menthol in $CDCl_3$ are shown together with several pattern-fits for various couplings.Couplings constants as determined by the HSQC-TOCSY-IPAP approach (Figure 2.28) are 3.4 Hz (a) and 1.8 Hz (a′). The trial peaks have been calculated for coupling constants of 3 Hz (b), 8 Hz (c), 15 Hz (d), and 2.0 Hz (b′), 4.2 Hz (c′), and 6.8 Hz (d′).

A noteworthy effect concerning the pseudo-sign-sensitive determination of coupling constants should be mentioned: For a transfer time $T =62.5$ ms the LR-CAHSQC provided all coupling constants of menthol with the correct relative sign (negative for $^2J_{CH}$, positive for $^3J_{CH}$ couplings) as demonstrated in Figure 2.26 for two example cross peaks. This somewhat surprising result can be rationalized using the ILL topology of Figure 2.25. Since the coherence transfer function is mainly influenced by the homonuclear coupling under isotropic mixing conditions, coherence transfer at $T =62.5$ ms is achieved with identical sign for both $^2J_{CH}$ and $^3J_{CH}$ situations (Figure 2.25A and B, respectively). The final evolution of the long-range antiphase coherence during acquisition is then sign-sensitive with $\sin \pi \, ^nJ_{CH}$ (as seen in Figure 2.26). Although the pseudo sign sensitivity in the coupling measurement might be present in many cases involving carbons with directly attached protons, coherence transfer properties are strongly influenced by the proton spin system and also depend strongly on the transfer time T used. It must be clearly stated that the LR-CAHSQC is generally *not* sign-sensitive. In the CBC-HSQMBC, multiplet patterns always have the same construction direction independent of the $^nJ_{CH}$ sign (cf. Figure 2.26). Exceptions only occur in the case of negative ^{1}H,^{1}H coherence transfer [229, 230].

Both CPMG-based pulse sequences allow transfer via dipolar couplings [226]. However, for the combination of dipolar and scalar couplings CPMG-type transfer does not result in homonuclear isotropic mixing conditions, but rather in cylindrical mixing conditions [231, 232] with inphase to antiphase evolution. Therefore spectra will contain dispersive elements and the advantage compared to conventional HMBC-type experiments is lost. In addition, ^{1}H,^{1}H-RDCs typically provide broad multiplet patterns without characteristic elements and lineshape fitting alone does not lead to conclusive results, as was demonstrated in Figure 2.27. Therefore the applicability of CPMG-based sequences seems to be limited to isotropic samples.

HSQC-TOCSY-IPAP

The first experiment published for sign-sensitive measurement of long-range $^nJ_{CH}$ couplings is the socalled HETLOC pulse sequence [216]. The E.COSY-type displacement in the resulting spectra contains information about the $^nJ_{CH}$ and $^1J_{CH}$ couplings of a specific carbon to its directly attached proton and the remote proton with the corresponding chemical shift of the cross peak in the directly acquired dimension. In addition to the size, the relative sign of long-range vs. one-bond couplings can be determined by the tilt of the E.COSY-pattern [233].

Many HSQC-TOCSY-type pulse sequences have been proposed based on the original principle with all kind of modifications (see for example [196, 216, 234–239]). A significant improvement in terms of resolution was accomplished by the introduction of spin state selectivity [215, 240], which separates multiplet components into two subspectra and therefore reduces the amount of signals in a single spectrum by a factor 2. The α and β-components in these experiments are selected via spin state selective coherence transfer [241]. This approach works well so long as INEPT transfer delays are matched with the

corresponding one-bond $^1J_{CH}$-couplings. Since one of our aims in the present study is the potential application of pulse sequences to partially aligned samples with a wide distribution of $(^1J_{CH} + D_{CH})$ couplings, we were looking for an improved version for a spin state selective HSQC-TOCSY with clean α and β component spectra in this case. The resulting pulse sequences based on the acquisition of an inphase (HSQC-TOCSY-IP) and antiphase (HSQC-TOCSY-AP) spectrum are shown in Figure 2.28: Pure absorptive heteronuclear inphase or antiphase coherences are achieved by removing all other heteronuclear terms by phase cycled carbon pulses applied directly before the TOCSY mixing period. In addition, recently derived ZQ-suppression schemes [242] are introduced around the isotropic mixing multiple pulse sequence which considerably clean up the spectrum (Fig. 2.29).

The construction of spin state selective subspectra out of the HSQC-TOCSY-IPAP experiments is illustrated in Figure 2.30 for simple cases. For typical isotropic samples with a narrow distribution of corresponding $^1J_{CH}$ coupling constants, INEPT transfer periods result in close to ideal performance and inphase and antiphase spectra are of equal intensity as long as aliphatic and aromatic regions are acquired separately. In such a case, spectra can be simply added or subtracted, respectively.

In cases where aliphatic and aromatic region shall be covered in a single experiment or where partial alignment causes a wide distribution of $^1J_{CH} + D_{CH}$ couplings, IP and AP spectra will be clean in the HSQC-TOCSY-IPAP experiments, but contain cross peaks of different intensities. This difference in intensities has to be corrected for each row by a simple procedure using standard functions for manipulation of 1D spectra as implemented in most processing programs like for example XWINNMR or TOPSPIN: First, identical rows have to be extracted from IP and AP spectra with corresponding diagonal cross peaks due to the direct $^1J_{CH}$ coupling. For the diagonal cross peaks with the large one-bond splitting, α and β components usually are well separated and clearly identifiable in the spectra and the intensity of IP and AP rows are easily adjusted until these diagonal components are of identical magnitude. Because the TOCSY transfer is identical for both the HSQC-TOCSY-IP and the HSQC-TOCSY-AP, it is sufficient to adjust the diagonal peak intensities (see also e.g. [243]). The intensity-adjusted rows can be saved and the corresponding sum and difference subspectra can directly be used for the $^nJ_{CH}$ coupling extraction by simply measuring the displacement of a certain cross peak in the two subspectra.

With the described procedure for coupling determination, the HSQC-TOCSY-IPAP approach can be applied identically to isotropic and partially aligned samples. The method is entirely sign-sensitive relative to the direct $^1J_{CH} + D_{CH}$ coupling which is usually of positive sign. In addition, spectra are very clean and far easier to interpret than other experiments examined. The major disadvantage of the approach is the limited number of couplings that can be extracted due to two limitations: Firstly, couplings can be measured only to carbons with directly attached protons, and secondly, not all remote protons might be reachable by the applied mixing scheme. Although TOCSY transfer provided excellent signal intensities for all potentially measurable long-range couplings for our two test molecules, transfer via DIPSI-2 and a single mixing time might not lead to sufficient signal intensities for all desired signals. In this case modifications to the mix-
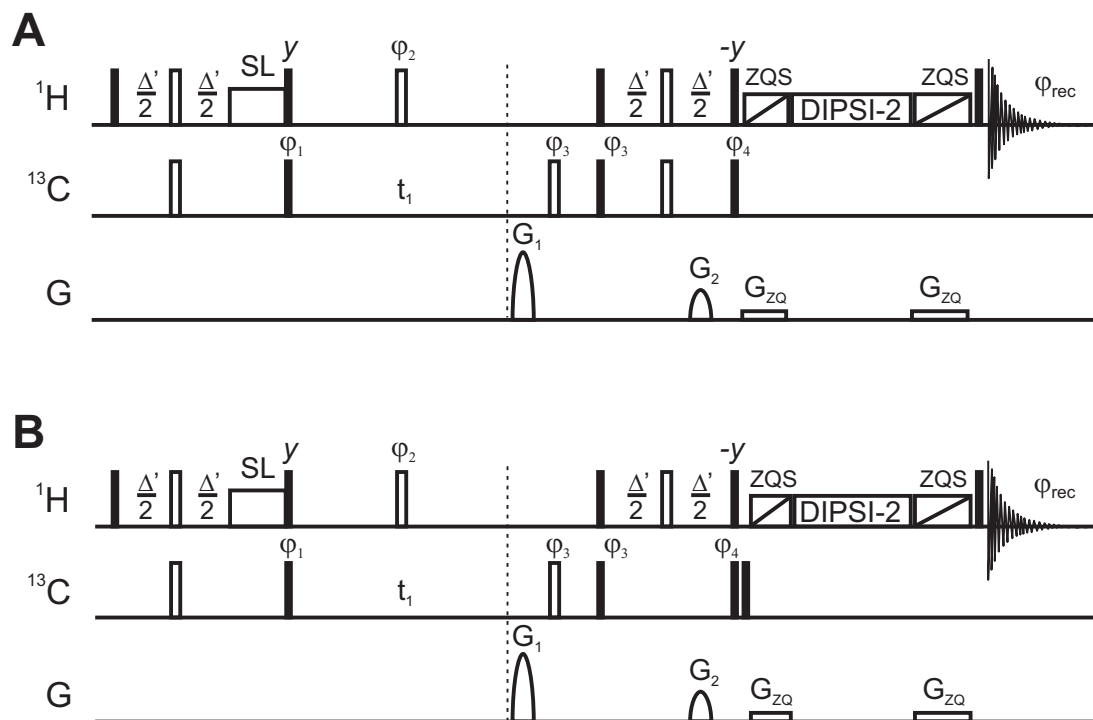
Figure 2.28: Pulse sequences for the HSQC-TOCSY-IPAP approach, involving the in-phase HSQC-TOCSY-IP (A) and anti-phase HSQC-TOCSY-AP (B) sequences. Narrow and thick bars represent 90° and 180° RF-pulses, respectively. Unfilled rectangles represent 1 ms spin-lock pulses. Pulse phases are along x unless indicated otherwise. Phase cycles are: $\phi_1 = x, -x$; $\phi_2 = x, x, -x, -x$; $\phi_3 = 4(x)4(-x)$; $\phi_4 = x, -x$; $\phi_{rec} = x, -x, x, -x, -x, x, -x, x$. The INEPT-delay $\Delta = 1/(2\ ^1J_{CH})$ is typically set to 3.846 ms corresponding to $^1J_{CH} = 130$ Hz. Open rectangles with oblique line represent adiabatic inversion pulses used in combination with gradient pulse G_{ZQ} as a filter to suppress unwanted zero-quantum coherences. The adiabatic pulses were chosen as smoothed Chirp pulses with 50 kHz sweep width over a duration of 30 ms and 50 ms, respectively. The G_{ZQ} gradient pulses are of corresponding durations and were calibrated using the detailed procedure provided online at http://www-keeler.ch.cam.ac.uk. Other gradient pulses are of 1 ms duration. Applied gradient strength ratios are: $G_1 : G_2 = 64 : 16.1$. ϕ_1 was incremented according to States-TPPI phase sensitive detection.
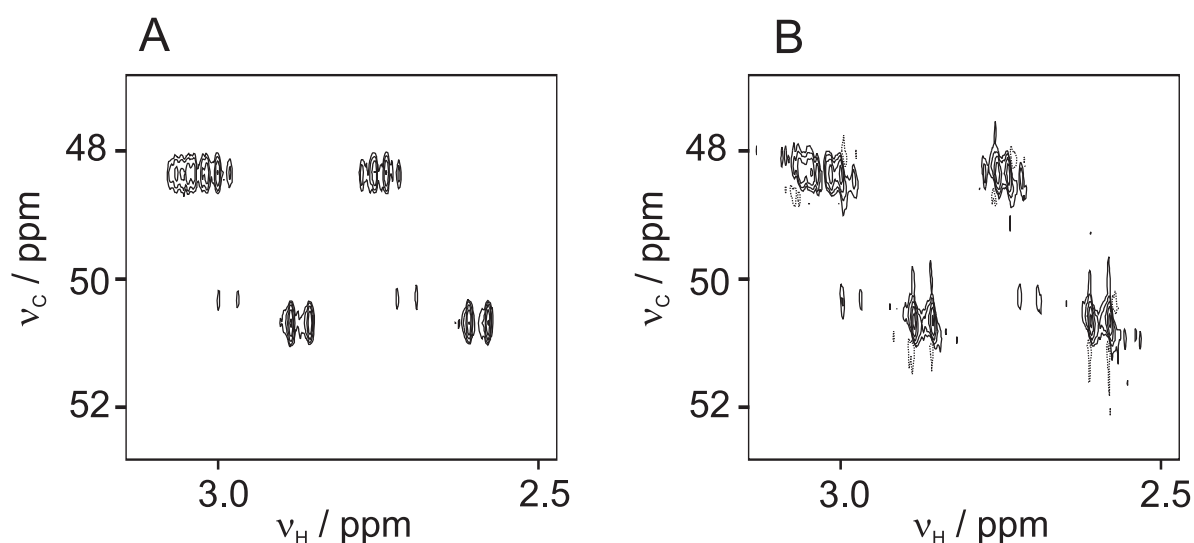
Figure 2.29: Arbitrarily chosen region of the HSQC-TOCSY-IP spectra of strychnine acquired with (A) and without (B) ZQ-suppression scheme. Clearly the reduction of small artefacts is visible throughout the spectra.

ing scheme can be tried like varying the mixing time, using tailored TOCSY sequences like for example the HNHA or COIN-TACSY [244, 245], or even applying a totally different homonuclear mixing scheme like a NOESY period. For partially aligned samples, also the use of MOCCA-XY16 multiple pulse sequence might be considered which simultaneously allows efficient transfer also via homonuclear J_{HH} and D_{HH} couplings [225, 226].

If resolution of the spectra is not sufficient, the pulse sequences of Figure 2.28 might easily be extended to 3D versions with an additional ^{1}H evolution period before the homonuclear mixing scheme.

Experimental

All spectra shown in this section were recorded on a Bruker Avance 500 spectrometer equipped with a TXI probehead using a $\approx$500 mM menthol and a $\approx$100 mM strychnine sample dissolved in CDCl$_3$. The CT-HMBC and reference CT-HSQC (c.f. Figure 2.20) were acquired using a transfer delay $\Delta = 62.5$ ms with 8192 data points in 16 scans (strychnine) and 4096 in 4 scans (menthol), respectively, for 640 increments. LR-CAHSQC and BIRD^{r,X}-HSQMBC spectra were acquired with overall 35.7 ms long CPMG transfer periods with 100 μs delay τ (see Fig. 2.23) and 180° pulses applied with rf-amplitudes of 12.76 kHz on the proton channel and 7.16 kHz rf-amplitude on the carbon channel. 8192 data points in 16 scans (for strychnine) and 4096 data points in 4 scans (for menthol), respectively, were collected for each of the 640 increments in the indirect dimension. HSQC-TOCSY-IP and HSQC-TOCSY-AP spectra were acquired with 50 ms mixing time using the DIPSI-2 mixing sequence [246] applied at 6.38 kHz RF-power and the MOCCA-
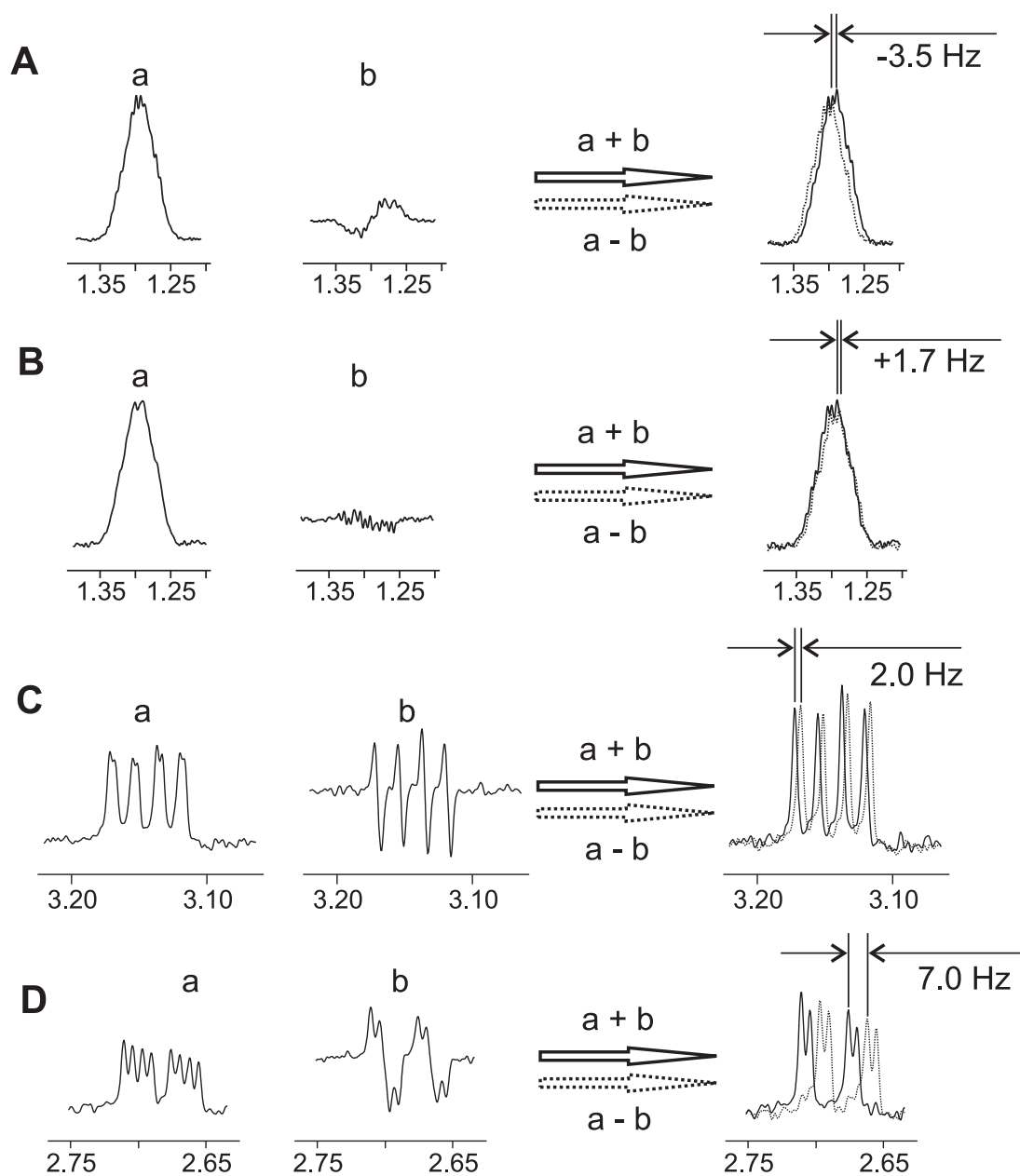
Figure 2.30: The coupling measurement procedure in its simpliest form. Coupling determination is illustrated on the same example cross peaks used in Figure 2.22: H_1 - C_2 (A) and H_1 - C_3 (B) of menthol and C_{12} to both H_{11} (C, D) of strychnine. This time the measurement is fully sign sensitive.

XY16 scheme as described in [225,226] with $\Delta/d = 2.2$, respectively. 8192 data points in 8 scans (strychnine) and 4096 data points in 2 scans (menthol), respectively, were collected for each of the 640 increments in the indirect dimension.

All spectra had an overall spectral width for strychnine of 10×120 ppm (folded signals did not overlap at the applied ^{13}C resolution) and 6×80 ppm for menthol and were processed by zero filling the data to 16384 points in the direct dimension and 1024 points in the indirect dimension. For apodization a 90°-shifted squared sine-bell weighting function was applied in both dimensions prior to Fourier-transformation.

Discussion

The precision of every coupling measurement strongly depends on the signal-to-noise ratio. All experiments discussed here provide very good sensitivity compared to other approaches for measuring long-range couplings. The CT-HMBC relies on the size of homonuclear *and* heteronuclear couplings evolving during acquisition of the corresponding antiphase terms. If these couplings are smaller than the linewidths, overlap of the multiplet components of opposite sign will significantly reduce the cross peak intensities. The same must be considered for heteronuclear couplings in the BIRD^{r,X}-HSQMBC and LR-CAHSQC, while homonuclear coherences (within limits) remain inphase during the CPMG transfer steps. The HSQC-TOCSY-IPAP results in inphase subspectra only so that reduction of signal intensities because of small involved couplings is not an issue in this case.

CPMG-based sequences and the HSQC-TOCSY-IPAP, on the other hand, depend on the homonuclear coherence transfer functions active in a particular spin system. Optimal sensitivity in this case can be achieved in principle by adjusting the TOCSY periods to the desired spin system, but in practice only empirically derived mixing times are applied once with more or less undefined intensities for the signals of interest. The sensitivity of the LR-CAHSQC in particular depends on the chosen mixing time (see Figure 2.25) due to the influence of the large heteronuclear one-bond coupling to the carbon of interest.

All experiments described here are designed for first order spectra. The presence of strong coupling or second order artefacts influences the extraction of coupling constants in several ways. For all intensity-based methods, ^{1}H,^{1}H homonuclear coherence transfer via strong coupling contributions will lead to an exchange of ^{1}H,^{13}C coherences and corresponding peak intensities are corrupted. Depending on the nature of the spin system this might lead to stronger or weaker signals. Since practically all homonuclear coupled spins have a slight second order contribution to their Hamiltonian, the measurement of couplings with a precision of less than $\approx$0.2 Hz in general is whishful thinking. For coupling extraction from pattern fitting like in the BIRD^{r,X}-HSQMBC or the CT-HMBC with the according reference-HSQC, the same caution has to be taken. Since the multiplet pattern is fit from a signal split by the corresponding heteronuclear one-bond coupling, second order effects on both multiplet components will be different. The effects will again be different for the signal of the $^nJ_{CH}$ cross peaks of interest, since the chemical shift for each multiplet component is again shifted by a few Hz with slightly changed strong coupling contributions. The situation in the HSQC-TOCSY-IPAP is only better in the

sense that second order effects are eventually easier recognizeable due to differences in the peak shape of the α and β components. A measurement with higher accuracy is still not possible.

Conclusion

For fast coupling measurement in isotropic samples and in cases where reliability and precision of couplings is not of utmost importance, as for example for configurational studies via $^3J_{\mathrm{CH}}$ coupling constants in isotropic samples, the CBC-HSQMBC is most likely the experiment of choice. A single measurement provides all information needed and couplings can be extracted with reasonable effort.

For accurate coupling measurement with high reliability, we found that the HSQC-TOCSY-IPAP gave best results. It is the only one of the presented experiments providing the sign of the couplings relative to the large heteronuclear one-bond coupling. However, coupling measurement is limited to ^{1}H-attached carbons only. Therefore all remaining couplings have to be measured with additional methods, preferrably e.g. the presented CT-HMBC with its corresponding reference HSQC. Since lineshape and intensity are fitted simultaneously, most reliable couplings are extracted. The missing sign-information must then be inferred from other data.

The signal-to-noise ratio is comparable for all examined pulse sequences with maybe the least average intensity for the LR-CAHSQC. For all other approaches signal intensities strongly depend on the couplings present in a particular spin system.

Chapter 3

Hadamard spectroscopy

And now for something completely different.

Monty Python

3.1 Spin state selective Hadamard encoding during transfer periods using multiple selective CW-HCP

In nuclear magnetic resonance, Hadamard encoding was first implemented in imaging applications [247–250] and has recently become a viable alternative to Fourier transform in multidimensional NMR spectroscopy [251–257]. If the resonance frequencies of desired signals are known, a set of multiple selective inversion pulses can be created and applied in a way that spectra are unambiguously reconstructed using the Hadamard transformation [258, 259]. As in conventional multidimensional NMR spectroscopy, single scans add up constructively without loss in sensitivity, but the number of incremented 1D-spectra is only determined by the number of selectively inverted frequency regions and not by the sweep width and desired resolution. This can lead to significant reductions in measurement time especially for samples with few cross peaks and might also be used to selectively correlate a subset of signals [259, 260] or the suppression of water [261].

Hadamard encoding is usually achieved with a multiple selective inversion pulse applied instead of a t_1-evolution period [259]. The selectivity of the inversion pulse dictates the pulse length and is of similar duration as a constant time period with identical resolution. For larger molecules, however, this can affect signal intensity and shorter overall experiment times are generally desireable. One possibility for reducing experiment duration is the use of highly selective transfer building blocks for direct Hadamard encoding without additional inversion pulses. Such selective transfer is achieved e.g. by double selective continuous wave heteronuclear cross polarization (CW-HCP) [262–264], for which a

151

number of interesting applications has been shown [265–269], including spin state selective spectroscopy [243, 270, 271].

In the following, general technical details for Hadamard encoding via multiple selective transfer building blocks will be examined on the example of CW-HCP. Offset effects, modifications of the building block for selective inversion during transfer, requirements for phase alignment and the application of spin state selectivity are discussed in detail. Results are verified experimentally on a ^{15}N,^{13}C-labelled pentapeptide and uniformly ^{15}N,^{13}C-labelled ubiquitin.

3.1.1 Theory

Transfer Characteristics of CW-HCP

Continuous wave heteronuclear cross polarization (CW-HCP) has been shown in a nice series of publications to provide doubly selective transfer with a very narrow transfer bandwidth on both irradiated nuclei [262, 264]. Best results are achieved for a radiofrequency amplitude of $\mathrm{rf}_{cw} = \sqrt{3}J/4$ with J being the active coupling between the two coupled spins. This low rf-amplitude results onresonant in a planar Hamiltonian [274]

$$\mathcal{H}_p^x = \pi J\{I_y S_y + I_z S_z\} \tag{3.1}$$

with full transfer after a transfer period of $\tau = 1/J$. In contrast to conventional high-power CW-HCP, the low relative ratio of rf_{cw} and J yields a good compensation of B$_1$-field inhomogeneity [264]. Several transfers can be achieved with CW-HCP. The conventional application would be the transfer of inphase to inphase magnetization $I_x \rightarrow S_x$ via planar mixing as a result of CW$_x$ irradiation. However, if initial magnetization is oriented along z perpendicular to the irradiation axis, i.e. I_z, only the one component of the Hamiltonian orthogonal to both the irradiation and magnetization axes contributes to the transfer and weak coupling evolution takes place resulting in transfer from inphase into ZQ/DQ terms $I_z \rightarrow -2I_x S_y$ after $\tau = 1/J$. Since the ZQ/DQ term $2I_x S_y$ can easily be converted into antiphase magnetization by a simple 90° pulse, we will refer to this transfer as inphase to antiphase in the following. These two transfer pathways have already been used for reducing multiplets [274] and for bandwidth and spin state selective transfer [243, 270, 271] and will be discussed here later in terms of their applicability to multiple selective transfer.

The offset dependence of both transfer types is shown in Figure 3.1 A and B. The bandwidth of inphase to inphase coherence transfer is restricted to ≈0.55 J with additional transition regions with undesired transfer up to approximately 2.4 J. The inphase to antiphase transfer has similar selectivity in the target dimension but a slightly more diffuse transition region in the initial dimension which, however, still provides sufficient selectivity for many applications.

CW-HCP transfer can be further manipulated by irradiating CW with a shifted phase on the second nucleus. The resulting onresonant transfers for an inverted, i.e. shifted by 180°, CW-irradiation on the S spin are $I_x \xrightarrow{CW_x(I)/CW_{-x}(S)} -S_x$ and $I_z \xrightarrow{CW_x(I)/CW_{-x}(S)} +2I_x S_y$ with the corresponding inverted offset profiles. Since the rotating frames of the
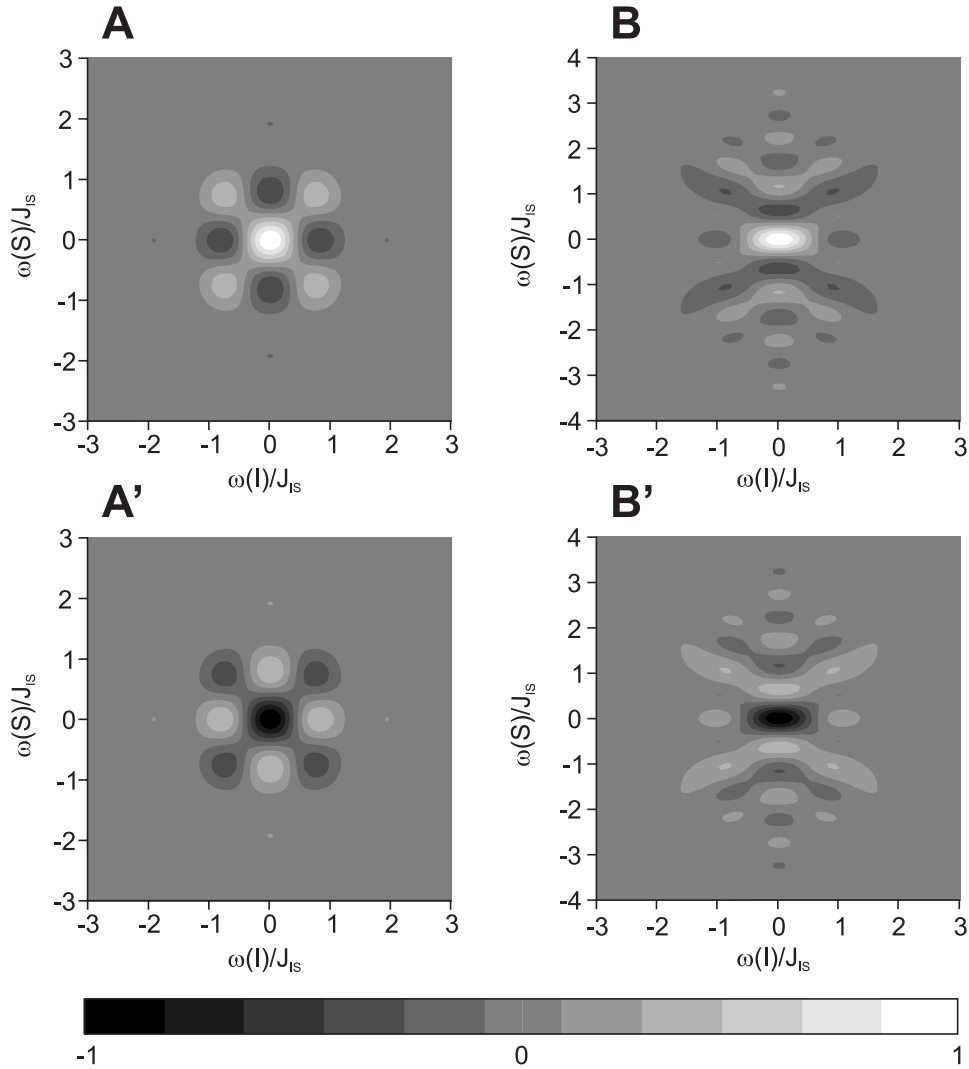
Figure 3.1: Offset dependence of inphase to inphase and inphase to antiphase transfers using CW-HCP of duration $1/J$ applied in the following ways: (A) $S_x \xrightarrow{CW_x(I,S)} I_x$; (B) $S_z \xrightarrow{CW_x(I,S)} -2I_yS_x$; inphase to inphase transfer by irradiating at two offset frequencies ($\pm\, 2J$ (C) and $\pm\, J$ (D)) on spin I with overall $\mathrm{rf}_{cw} = \sqrt{3}J/2$ while only one frequency is irradiated onresonant on spin S with $\mathrm{rf}_{cw} = \sqrt{3}J/4$; inphase to antiphase transfer by irradiating at two offset frequencies $\pm\, 2J$ with an amplitude $\mathrm{rf}_{cw} = \sqrt{3}J/2$ on the I (E) and S (F) spin, respectively, with the corresponding other spin irradiated onresonant with $\mathrm{rf}_{cw} = \sqrt{3}J/4$. The plots were simulated using self-written code based on the simulation program SIMONE [272, 273].

two heteronuclei are independently defined, the shift of the director of the CW-irradiation generally results in a phase shift of the evolving coherences.

Multiple Selective CW-HCP and Hadamard Encoding

Multiple selective CW-HCP can be achieved by the addition of several constant amplitude pulses with differing linear phase sweeps corresponding to the desired multiple frequencies. The creation of such a pulse shape is easily performed using standard procedures implemented for example in the Bruker pulse shape tool and is shown schematically for two frequencies in Figure 3.3. Generally, for n separated irradiation frequencies on one nucleus the rf-amplitude also increases to n times rf_{cw}.

The multiple selectivity can be chosen independently for the two nuclei. Figures 3.1C-E contain examples where two frequencies are chosen for spin I, while only one frequency is selected for the S spin for inphase to inphase and inphase to antiphase transfer, respectively. Inphase to antiphase transfer with one frequency on the I spin but two irradiated frequencies on the S spin is shown in Figure 3.1F. In the case of two selected frequencies as shown in Figure 3.2A, transfer can occur between all four frequency combinations. If a constant amplitude pulse at a single frequency is added with a 180° phase shift for the multiple selective CW pulse, the transfer at this specific frequency is also inverted (Figure 3.2B-D).

The obtained offset dependencies for multiple CW irradiation are the sum of the individual CW-HCP offset dependencies centered at the specified frequency combinations of I and S spins. Overlap of transfer regions between two neighboring CW-frequencies leads to incomplete or undesired transfer properties and should strictly be avoided. If the minimum distance of 1.8 J between two irradiation frequencies is maintained, clean multiple selective CW-HCP is achieved.

Hadamard spectra can be obtained with the S spin in the indirect dimension by encoding positive and negative transfers [247, 275]. This can be achieved by addition and subtraction of the corresponding frequency components in the pulse shapes for the I and S spin as described above. The most simple non-trivial case of two selected frequencies for both the I and S nuclei is shown with its offset dependency plots in Figure 3.2. With the combination of all positive transfers (Figure 3.2A), selective inversion of a single frequency on the I spin, S spin, and both spins (Figure 3.2B-D), the spectra at all four frequency-combinations can be reconstructed [275, 276]. The Hadamard encoding can be extended to $4n$ selected irradiation frequencies by adding and subtracting the phase-modulated CW-elements in the multiple selective CW-HCP according to the corresponding Hadamard matrices [259].

Phase Alignment

When setting up experiments, special care has to be taken with respect to the correct phase alignment when creating the multiple selective CW shaped pulses. Because CW of different frequencies is added for the CW-HCP, a defined phase is only provided at a single point of the resulting shapes, typically at the beginning or at the end of the shaped
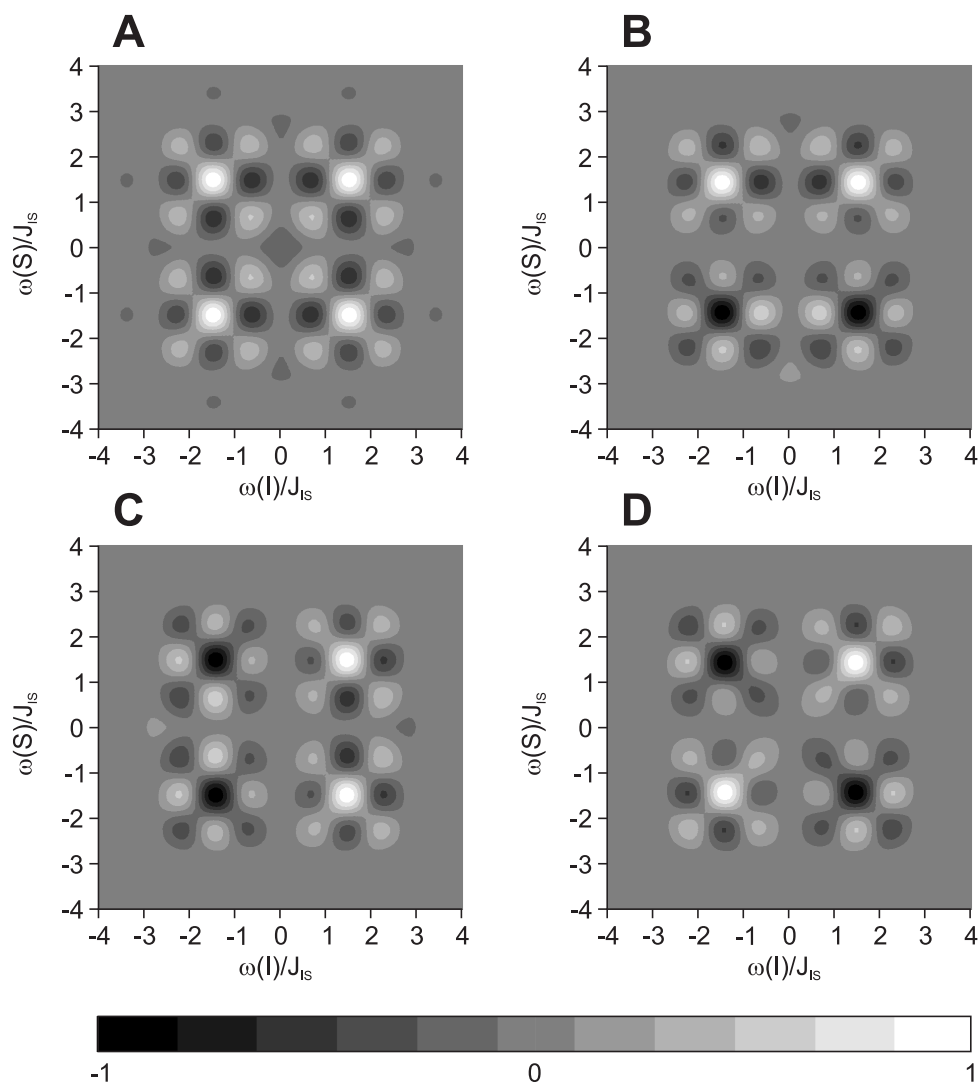
Figure 3.2: Hadamard matrix encoding for dual selective inphase to inphase transfer using CW-HCP with selectively inverted CW-elements. All offset dependency plots were simulated with CW irradiated on I and S spins at frequencies of $\pm 1.5\ J$ with an overall amplitude of $rf_{cw} = \sqrt{3}J/2$. While in (A) the phases of all CW-components have identical phases, the CW-component at frequency -1.5 J is inverted on the S spin (B), I spin (C), and both spins (D) to obtain the desired Hadamard-encoding during the multiple selective transfer period.

pulse (see Figure 3.3 for a simple vector addition of two CW frequencies). Magnetization oriented along z obviously is not sensitive with respect to phase alignment. Transverse coherences, instead, only result in defined transfers for the specified frequencies if the corresponding pulse phases are identical. For the transfer $I_x \rightarrow S_x$, for example, the phases of the individual constant amplitude CW-pulses have to be aligned at the beginning of transfer step for the I spin, while they have to be aligned at the end of the pulse shape for the S spin. The inphase to antiphase transfer $I_z \rightarrow 2I_xS_y$ requires phase alignment at the end of the shaped pulse for both spins. Two pulse sequences for Hadamard encoded multiple selective CW-HCP based correlation experiments with inphase and antiphase detection, respectively, are presented in Figure 3.4, with phase alignment of the multiple selective CW indicated by open arrows.

Spin State Selectivity

For spin state selectivity with respect to the α and β states of the heteronucleus, the resulting antiphase spectrum is added or subtracted from the inphase spectrum. As shown previously [190, 191, 243, 277, 278], the combination of spin state selective heteronuclear transfer with an homonuclear mixing step like TOCSY provides the possibility to measure size and sign of long-range heteronuclear couplings.

3.1.2   Experimental

The applicability of the method is demonstrated on 2 mM uniformly ^{15}N,^{13}C-labelled cyclic pentapeptide cyclo(-D-Pro-Ala-Ala-Ala-Ala-) (PA$_4$) in DMSO-d$_6$ (Figure 3.5), as well as on 0.5 mM uniformly ^{15}N,^{13}C -labelled ubiquitin dissolved in 90% D$_2$O / 10% H$_2$O (Figure 3.6).

The alanines of the pentapeptide PA$_4$ result in four ^{15}N-split doublets for the amide protons in the ^{1}H-1D. The inner two amide signals, however, are too close at a spectrometer frequency of 600 MHz to be separated by multiple selective CW-HCP regarding the heteronuclear coupling of $^1J_{\mathrm{NH}} \approx 90$ Hz. While their separation of approximately 70 Hz in ^{1}H and 65 Hz in ^{15}N results in significantly reduced transfer if all four amide groups are irradiated simultaneously in the multiple selective transfer steps, full transfer can be achieved for three amide groups, if only one of the central signals is irradiated (Figure 3.5B).

For the experimental verification of the multiple selective CW-HCP Hadamard encoding, we initially chose the most simple example corresponding to a 2×2 Hadamard matrix. The two outer amide groups separated by 584 Hz in ^{1}H and 530 Hz in ^{15}N at a 600 MHz spectrometer have been irradiated according to the pulse sequences shown in Figure 3.4 and the multiple selective CW-HCP building blocks of 11.1 ms duration constructed according to Figure 3.3 and Figures 3.2A,B. Hadamard-encoded inphase to inphase and inphase to antiphase transfer could be achieved with the transfer elements as described in the theory section. The subsequent addition/subtraction of the corresponding spectra leads to individual inphase/antiphase signals and even to spin state selective
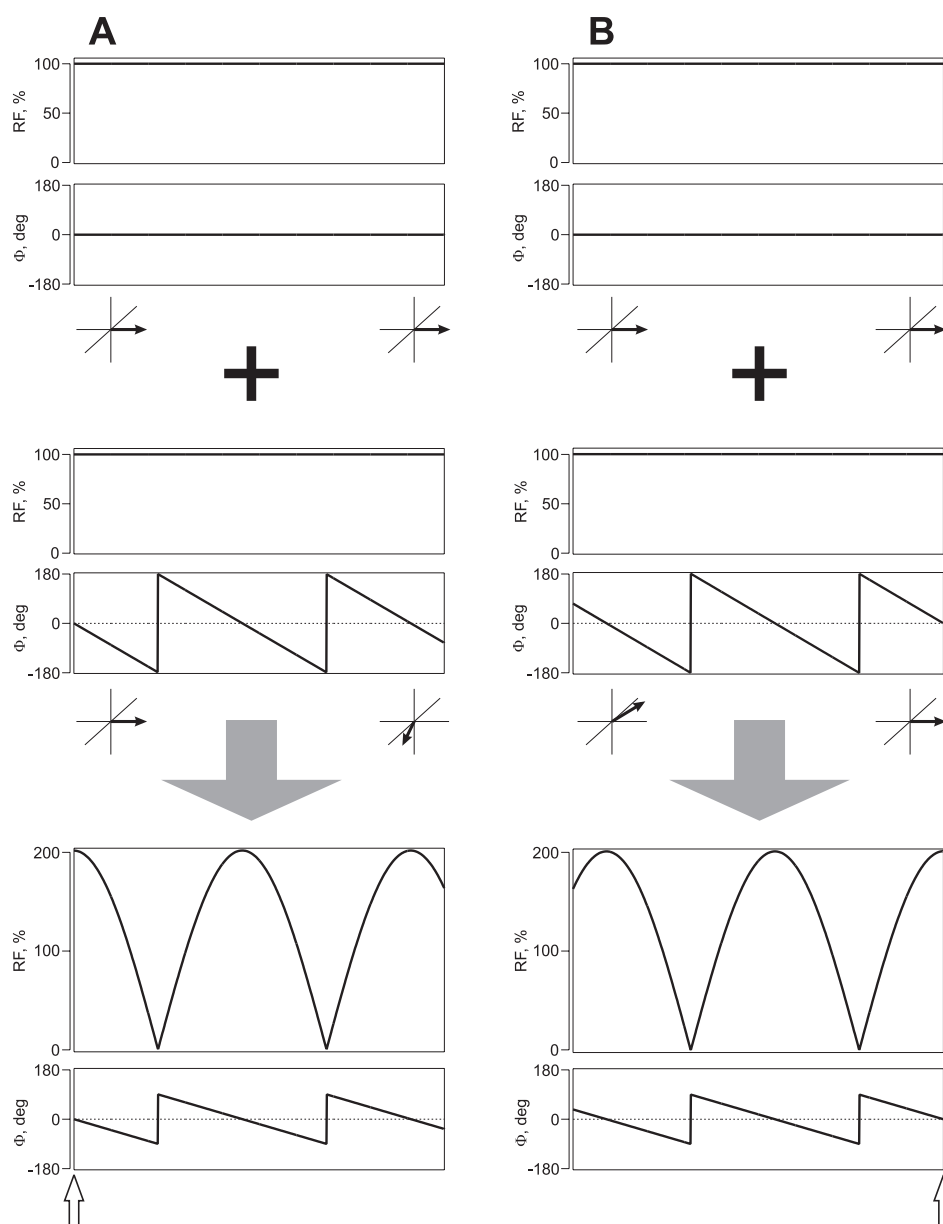
Figure 3.3: Vector addition and phase alignment for multiple selective CW-HCP demonstrated by the addition of two constant amplitude CW pulses. Onresonant CW with constant amplitude and phase (top) is added vectorially with CW of constant amplitude at a specific offset (middle) with phases of the individual pulses aligned along x ($0°$) at the beginning (A) and at the end (as also indicated by the open arrows at the very bottom). The resulting pulse shapes are cosine-modulated pulses with a constant phase sweep of twice the original maximum rf-amplitude (bottom). Coordinate systems with a vector indicating the position of the CW-rotating frame have been introduced to visualize the relative phases at the beginning and at the end of the individual pulses.
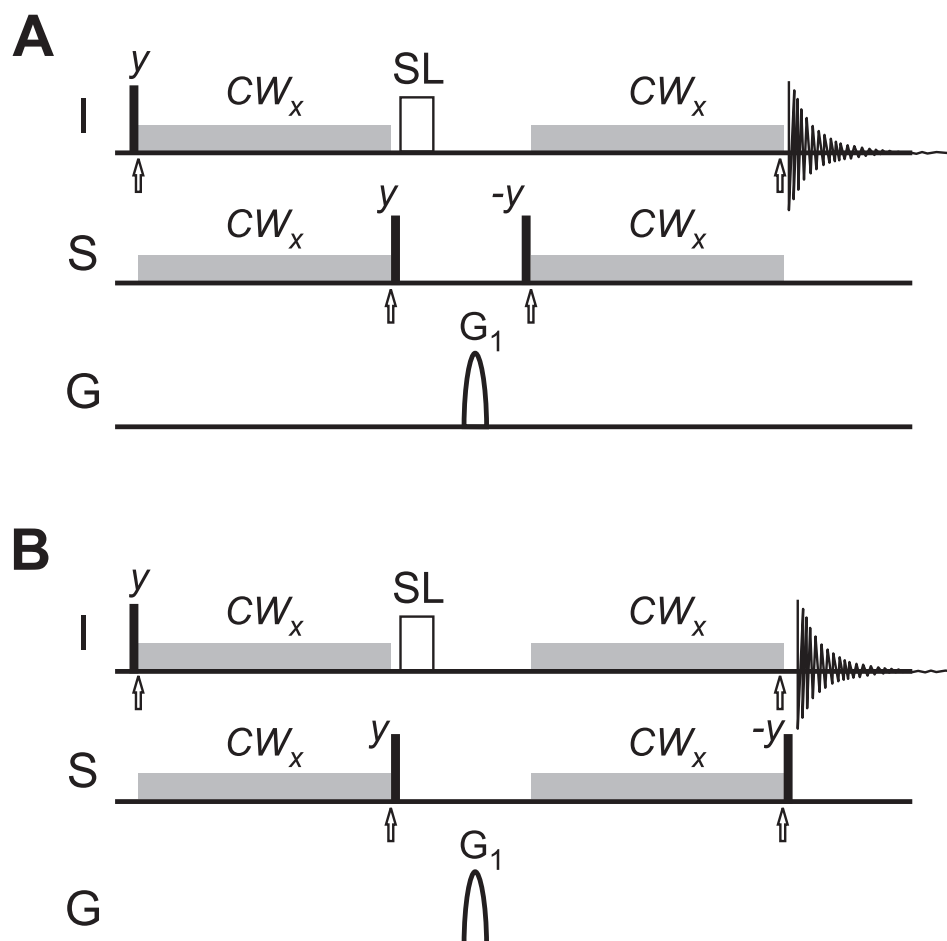
Figure 3.4: Pulse sequences for Hadamard encoded multiple selective CW-HCP correlations. (A) Sequence for the detection of inphase magnetization and (B) the corresponding sequence for antiphase detection. Open arrows indicate points of phase alignment of the multiple selective CW-HCP shaped pulses as demonstrated in Figure 3.3. Black bars represent 90° pulses, gray bars annotated with CW_x mark mutliple selective CW-irradiation with phase aligned along x at the open arrows and the open box with SL stands for a spinlock period of typically 1-2 ms duration. The CW_x-irradiation used for experiments in all presented cases has a duration of $1/J$. The purging gradient G_1 is of medium strength and typically 1-5 ms duration. With the magnetization of interest stored on spin S along z, the combination of spinlock and purging gradient is known to provide excellent suppression of unwanted signals [184, 243]. Hadamard encoding is achieved within the CW-HCP pulse shapes as described in the text.

spectra (Figure 3.5C).

A more elaborate example was recorded on ubiquitin, where four cross peaks were arbitrarily chosen for selective transfer with relative frequencies of 0 Hz, 315 Hz, 527 Hz, 770 Hz on ^{1}H and 0 Hz, 628 Hz, 895 Hz, 1075 Hz on ^{15}N (Figure 3.6). In order to obtain maximum selectivity, Hadamard encoding was performed on both channels simultaneously [275], resulting in altogether 16 separate experiments for inphase spectra and another 16 experiments for antiphase spectra. These data have been combined by applying the Hadamard transformation using a 4×4 Hadamard matrix for each channel separately [260, 275]. The encoded spectra are shown in Figure 3.6 B and C for the inphase and antiphase case, respectively. Again, these subspectra can be added/subtracted to achieve additional spin state selectivity (Figure 3.6D). Clearly visible are also the selectivity limitations of the method for one of the obtained signals where the strong cross peak marked with an asterisk resonates at an offset combination in the transition region of CW-HCP (Figure 3.1A). This leads to relatively efficient inphase transfer and the observed undesired signal. Because the offset dependence of inphase to antiphase transfer is different (Figure 3.1B), the resulting antiphase spectra contain other undesired artefacts resulting from transfer of signals in the CW-HCP transition region.

All experiments were performed on a Bruker DMX 600 spectrometer. The multiple selective pulses for CW-HCP transfers were created using the Bruker "shape tool" software incorporated in XWINNMR version 3.5 by vector addition of square pulses with phase slopes corresponding to the desired irradiation offsets. As part of the shape tool also the phase alignment of the pulse shapes could be chosen as described in the theory section. The Hadamard encoding was achieved by adding additional 180° phase shifts to the corresponding individual frequency components. The pulse amplitudes were first set to theoretical values of $(\sqrt{3}/4)J_{\mathrm{NH}}$ per irradiation frequency, and then corrected by systematically varying the amplitudes on both channels close to this value until reaching maximum signal intensity.

For PA$_4$, 4 scans per FID with 2048 points were recorded in all cases. The ^{1}H,^{15}N-HSQC of ubiquitin was recorded with 2048 × 512 points and 4 scans per FID. The corresponding multiple selective CW-HCP Hadamard-encoded spectra were acquired with 8192 data points, 64 transients per individual experiment and CW-irradiation periods of 11.1 ms duration. Additional low-power presaturation was applied for water suppression in the case of ubiquitin. All spectra were zero-filled to twice the original number of acquired points and apodized exponentially before Fourier transform.

3.1.3 Discussion

Highly selective CW-HCP has been shown to be a powerful tool for multiple selective Hadamard encoding. However, several limitations to the technique apply. The main disadvantage is probably the selectivity of transfer, which is limited by the heteronuclear coupling. Significantly narrower transfer bandwidths are only feasible using CW-HCP-based techniques with significantly longer transfer periods as for example described in [262,264,279,280]. These longer transfer periods will result in reduced transfer efficiencies
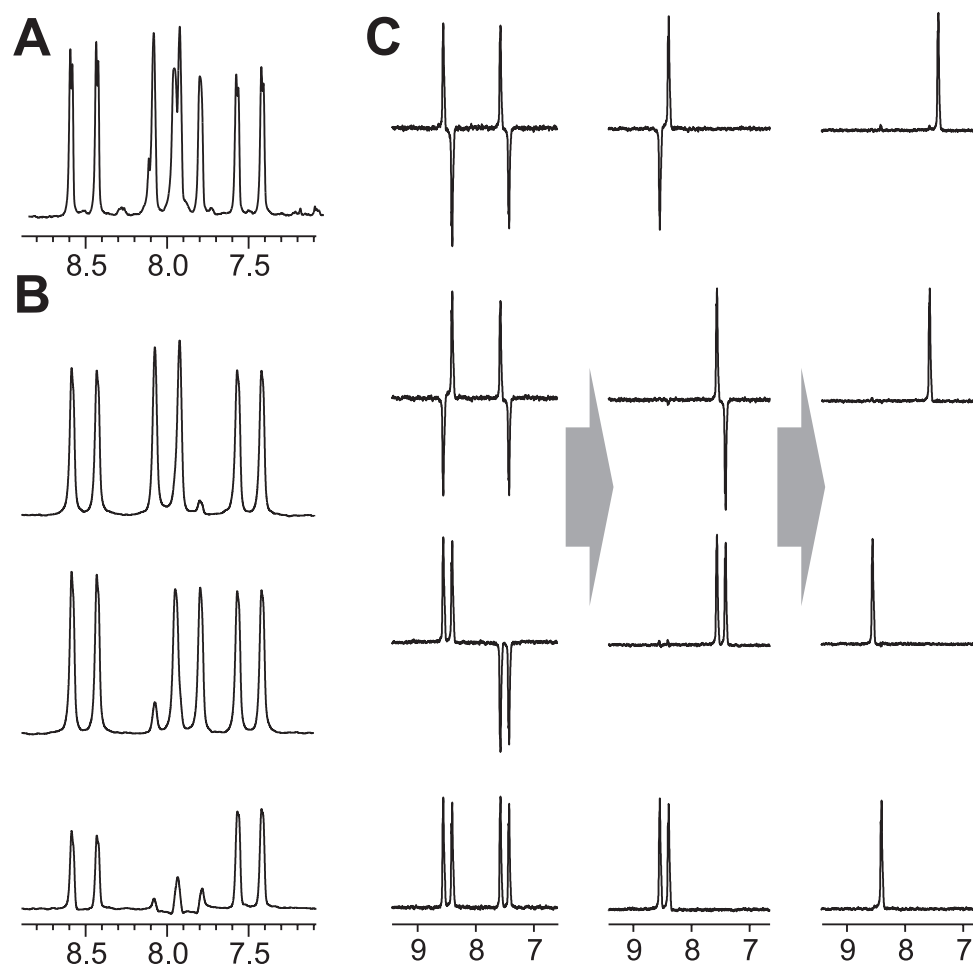
Figure 3.5: Demonstration of achievable multiple selective CW-HCP transfer and a simple example for Hadamard-encoding including spin state selectivity using the $^{15}N,^{13}C$-labelled pentapeptide PA$_4$. (A) ^{1}H-1D of the amide region of PA$_4$. (B) While multiple selective ^{1}H,^{15}N CW-HCP cannot be achieved for all four alanine amide groups due to the insufficient separation of only ≈ 0.8 $^1J_{\mathrm{NH}}$ of the inner signals (bottom), it is well possible for three selected signals (top and middle). (C) Hadamard-encoding is demonstrated on the two outer amide signals for which inphase and antiphase detected experiments (Figure 3.4) have been detected using twice-selective CW-HCP with all individual constant amplitude pulses added with the same phase (see Figure 3.2A) and with one phase on spin S inverted before vector addition (see Figure 3.2B). By applying the 2×2 Hadamard-matrix, which is equivalent to addition/subtraction the two antiphase and inphase spectra, respectively, subspectra with individual antiphase/inphase signals are obtained. By combining these antiphase and inphase signals a second time in the IPAP manner, the four resulting subspectra represent the muliplet components of the individual spin states.
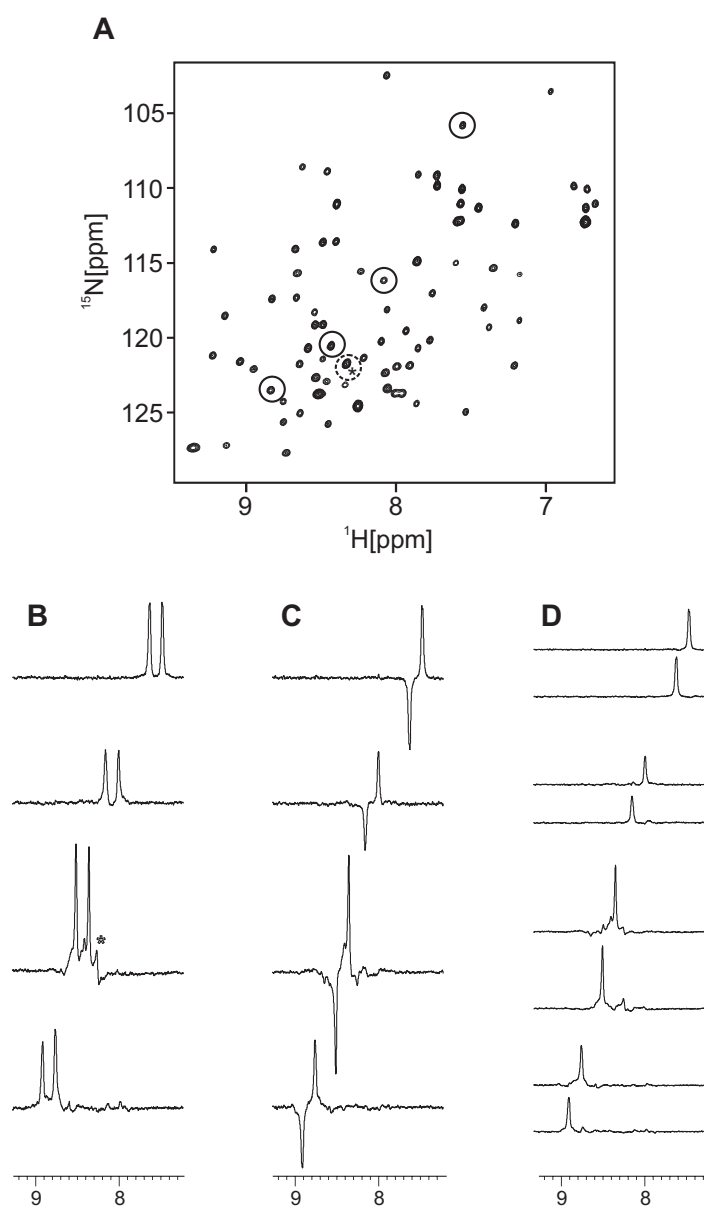
Figure 3.6: Application of the multiple selective CW-HCP Hadamard encoding on ubiquitin by choosing four arbitrarily selected amide groups. (A) ^{1}H,^{15}N-HSQC of ubiquitin with the four arbitrarily selected resonances indicated by circles. (B) The four resulting spectra out of 16 individually recorded inphase spectra using the pulse sequence of Figure 3.4A after sequentially applying 4×4 Hadamard transformations on spins I (^{1}H) and S (^{15}N). (C) The corresponding spectra resulting from the 16 antiphase spectra recorded using the pulse sequence of Figure 3.4B and corresponding Hadamard encoded CW-HCP. (D) By adding/subtracting inphase and antiphase spectra, individual multiplet components can be obtained. Limitations due to undesired transfer in the transition region of CW-HCP (see Figure 3.1) are marked in one case with an asterisk.

due to relaxation.

Generally, it must be noticed that CW-HCP has quite large transition regions concerning its coherence transfer offset dependence (see Figure 3.1). Other planar mixing schemes [228] optimized for selective coherence transfer, as e.g. the Gaussian pulse shape based PLUSH-TACSY [281] or the computer optimized kin-HEHAHA sequences [282], might well reduce resulting offset dependent artefacts. One could also think of optimizing selective heteronuclear or even homonuclear transfer building blocks by e.g. optimal control theory [13, 282, 283], which has shown its potential in many applications like the design of specific pulse shapes [34, 56, 69, 284] or specifically optimized transfers in solid and liquid state applications [285–289]

A comparison of selectivity of CW-encoding vs. conventional Hadamard-encoding using selective inversion pulses of identical duration is shown in Figure 3.7. The selectivity of CW-HCP is comparable to the selective inversion by a low-power CW pulse. Although the CW-transfer is not optimal with respect to the transition region, the actual transfer bandwidth is narrower as for example the bandwidth of a Gaussian inversion pulse with a truncation level of 15 %. It can be assumed that the use of shaped pulses as e.g. applied in the PLUSH-TACSY [281] will lead to a reduced transition region also in the case of selective coherence transfer. Since physically the selectivity of a pulse sequence element is mainly determined by the time spent in the transverse plane, this result is not surprising. Potentially, the selectivity performance of a coherence transfer step might also be improved if the sequences irradiated on the two nuclei are treated separately in an optimization of band-selective transfer as has been previously demonstrated in [282].

In all multidimensional experiments coherence transfer steps are inevitable. The time for coherence transfer is not fully used in conventional Hadamard encoding procedures involving selective inversion pulses. In HSQC-type experiments, as shown here, a period of at least $1/J$ with the magnetization in the transverse plane can be gained by including the frequency selection into the transfer steps. This will generally result in higher sensitivity because of reduced relaxation losses. Most likely the two Hadamard encoding approaches can even be combined for obtaining spectra with higher selectivity and cleaner appearance.

Hadamard encoding with multiple selective CW-HCP requires several pulse shapes to be created for each 1D-experiment due to the various phase alignment conditions that must be fulfilled. The effort in this case is higher than in conventional Hadamard encoding schemes and is very time consuming if pulses are created individually. Nevertheless, pulse shape creation could easily be automated by a suitable computer program.

The original Hadamard encoding is restricted to frequency matrices that are multiples of $4n$. As has nicely been shown by Kupče and Freeman [290], the approach can be extended to an arbitrary number of frequencies, if not only sign inversion but encoding with $360°/n$ phase shifts is used. This extension can be directly transferred to multiple selective CW-HCP if the phases of the individual CW components are chosen accordingly.

In contrast to conventional Hadamard encoding using selective inversion pulses, multiple selective CW-HCP in principle offers the possibility to encode the frequencies of both participating nuclei without increase in experiment time for each scan. In the simple 2D-like correlation experiments discussed in Figure 3.4, Hadamard encoding on both
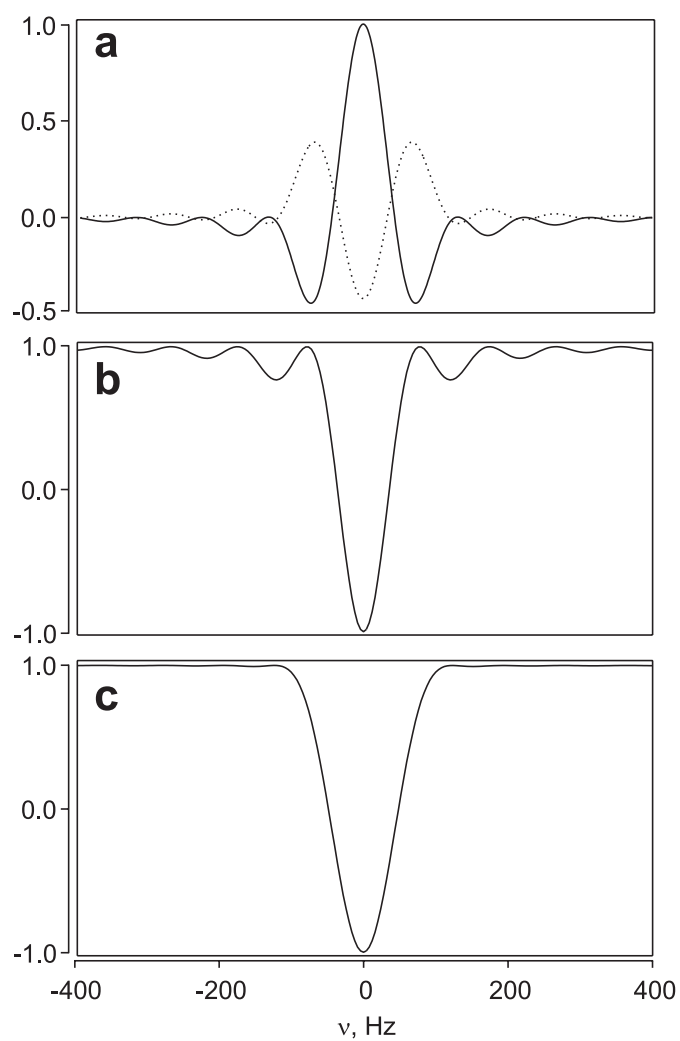
Figure 3.7: Comparison of offset dependencies of CW-HCP (a), selective inversion using CW (b) and a Gaussian shaped pulse truncated at 15 % (c). The duration of CW-HCP and the pulses in all cases is 11.111 ms. For CW-HCP the transfer profile of the S spin is shown onresonant for the I spin (solid line) and for the I spin at an offset of ≈ 0.8 J (dotted line).

nuclei simultaneously is not necessary, since the proton dimension is directly detected anyway. In 3D-experiments the situation is different and the possibility of simultaneously encoding two frequency distributions in a single transfer element seems especially attractive in situations where fast relaxation processes limit the applicability of conventional frequency-discrimination techniques.

As mentioned above, the presented approach seems promising whenever relaxation prevents conventional Hadamard encoding using relatively long selective inversion pulses. The decrease in experiment time due to the inherent selectivity of the doubly selective CW-HCP will directly translate into gains in signal intensity. Possibly, the situation might be improved even further by the introduction of relaxation optimized transfer elements like the ROPE [8] and CROP [7] sequences, which both show an inherently bandwidth-selective transfer comparable to CW-HCP.

The pulse sequences discussed in this chapter can be found in the Appendix 4.3.

Chapter 4

Appendix

4.1 Optimization program OCTOPUS

OCTOPUS is the main optimization program used throughout this work to perform optimizations of all kinds of point-to-point transformations described in the previous chapters. The program is written in the Fortran programming language and was compiled by the INTEL$^{\circledR}$ Fortran Compiler 8.0 for Linux. The optimizations are performed according to the formulas derived in chapter 1.2.3. The user has to list all optimization parameters in a file with fixed format (*vide infra*) and run the optimization by the command

$$octopus \ -[\text{options}] \ optname,$$

where *optname* being the name of the parameter file. The parameter file has the following form:

```
#****************************************************************
#                   Optimization parameters
#****************************************************************
Range, Hz = 100
Checks = 2
MaxB1 deviation, % = 10
nB1 = 1
Pulse length, us = 50
Timestep, us = 0.5
RF limit, Hz = 10000
Start RF, Hz = 10000
N_optimizations = 5
Seed = 216
Tolerance = 1.0d-6
#*****************************████
#     Initial state
#*****████████████████████████
```

```
initial_x = 0
initial_y = 0
initial_z = 1
#*****************************
#    Target state
#*****************************
target_x = 0
target_y = 0
target_z = -1
#*********************************************************************
```

The user has to define the offst range in Hz which the pulse has to cover (*Range* in the file above), the number of different offsets that are used in the calculation (*Checks*), the size of included rf-amplitude variations in $\pm\%$ of the nominal rf value (*MaxB1 deviation*) and the number of different rf-amplitudes in the calculation (*nB1*, if it is equal to 1 then no rf-inhomogeneity will be considered), the length of the optimized pulse and the length of the single pulse digit (*Timestep*, should be smaller, then the pulse length), the maximum allowed rf-amplitude or rf-power, respectively, (*RF limit*), and the maximum amplitude in the intial generated random pulses (*Start RF*, can be also larger then the RF limit, will be clipped later in the optimization; larger amplitudes of random pulses generally guarantee the larger distribution of final quality factors, increasing thus the chances to get better pulse), the overall number of optimized pulses (*N_optimizations*), the seed for the random numbers generator (*Seed*) and the convergency criterion *Tolerance*. The initial and target magnetization states are defined by their x, y and z components, which do not neccesary have to be normalized - the normalization is performed automatically. One can further modify the optimization setup by chosing one of the following options:

- **-c**: to optimize pulses with constant rf-ampitude;

- **-p**: to optimize pulses with limited rf-power deposition, with parameter *RF limit* limiting now the **average** rf-power;

- **-u**: to optimize a universal rotation; the program optimizes the point-to-point transformation with half flip-angle and constructs the universal rotation according to the procedure described in chapter 1.6;

- **-s** *pattern_file*: to optimize a pattern pulse (see chapter 1.5; the optimization pattern to be defined in the file *pattern_file*, which should have the following format:

$$0123\cdots333$$
$$32123\cdots88$$
$$\vdots$$
$$0123\cdots333$$
$$32123\cdots88$$

with individual numbers defining the target magnetization state for a combination of the offset and the rf-field strength, which is defined by the position of the corresponding number. The overall number of rf-miscalibrations calculated is then defined by the amount of numbers in the row, and the number of offsets calculated is defined by the amount of rows. The corresponding entries in the parameter file are then ignored. The initial states for every cell of a pattern is the one defined in the parameter file, and the target states are encoded by the numbers, with 0 standing for z, 1 or any other symbol for x, 2 for y, 3 for $-x$, 4 for $-y$ and 5 for $-z$.

More than one option can be specified at the same time. Nonsense combination generate a warning message (like *-c* and *-p* at the same time). Running the program without giving the name of the optimization file generates a warning message and opens the help file. The program first generates random pulses (number of which is defined by the parameter *N_optimizations*) and saves them in the temporary directory *optname_temporary*, which is removed at the end of the run. The quality factor is evaluated for every random pulse and they are sorted accordingly. Then the optimization is started on every of the random pulses. Resulted pulses are stored in the newly created directory *optname_results* under the names *pulse1, pulse2* and so on. When all optimizations are performed, the optimized pulses are reassorted according to their quality and converted to the format compatible with Bruker software and saved under the names *pulse1.bruker, pulse2.bruker* and so on (whereas initially they had x-y-amplitude representation). After the sorting the pulse with the lowest number is the best performing pulse. The program generates the following output protocol:

```
-------------------------------------------
Generating starting pulses...
 Done.
 Calculating transfer efficiencies...
 Done.
 te1(       1 )= -0.904332250071345
 te1(       2 )= -0.956595183712871
 te1(       3 )= -0.970209075730468
 te1(       4 )= -0.979908039553965
 te1(       5 )= -0.983564797426899


 Starting 1st level OCT
 te(         1 )=  0.999949999929785
 te(         2 )=  0.999949999204033
 te(         3 )=  0.999949973071452
 te(         4 )=  0.999950000023467
 te(         5 )=  0.999950000103240


 Ranked efficiecies:
 New te(           1 )=  0.999950000103240
```

```
New te(                2 )=  0.999950000023467
New te(                3 )=  0.99949999929785
New te(                4 )=  0.999949999204033
New te(                5 )=  0.999949973071452
 -------------------------------------------
```

In the same form this protocol is saved in a file under the name *optname.log*

In the case of pulses optimized with limited rf-power deposition the important parameter crucial for its practical application is the peak rf-power of the pulse. This is stored in the header of the pulse shape in bruker format:

```
##$SHAPE_PARAMETERS= Power Limited pulse, Nominal RF=   10251.382
```

The resulting pulses are stored in two different representations. In the first one the file has three columns: the first contains absolute values of the x-component of the rf-amplitude, the second column the y component and the third the length of the corresponding digit in seconds:

```
   ......
 -8804.89926869434        3776.42019499668        5.000000000000000E-007
 -8823.93621481248        3785.10026868566        5.000000000000000E-007
 -8842.18282915578        3793.81545495536        5.000000000000000E-007
 -8861.14966898076        3802.16648120918        5.000000000000000E-007
   .......
```

The files in this representation are saved under names without extension: *pulse1, pulse2* and so on. The second format the pulses are saved in is the format compatible with XWIN-NMR and TOPSPIN software from Bruker. They have the header of corresponding format containing additional information about the pulse, and the pulse shape is represented in two columns: relative rf-amplitude in % and phase in degrees. The nominal rf-amplitude corresponding to 100% is given in the header:

```
##TITLE= /akbl1/kk/simone_1/OCTOPUS/temp_results/pulse1.bruker
##JCAMP-DX=
##DATA TYPE= Shape Data
##ORIGIN= OCTOPUS optimization software
##OWNER= <kk>
##DATE= 11-Jun-07
##TIME= 11:00:38
##$SHAPE_PARAMETERS= Nominal RF (Hz):    10000.000
##MINX=   99.9999999999999
##MAXX=   100.000000000000
##MINY=   155.844761905960
##MAXY=   157.301385290965
##$SHAPE_EXMODE= Excitation
```

```
##$SHAPE_TOTROT=    180.000000000000
##$SHAPE_TYPE= Inversion
##$SHAPE_USER_DEF=
##$SHAPE_REPHFAC=
##$SHAPE_BWFAC=  5.000000000000000E-003
##$SHAPE_BWFAC50=
##$SHAPE_INTEGFAC=  0.999999999999999
##$SHAPE_MODE= 0
##NPOINTS=          100
##XYPOINTS= (XY..XY)
 100.0000000000, 156.8233825233
 100.0000000000, 156.7169389969

⋮

100.0000000000, 155.8447619060
##END=
```

4.2   Simulation programs

4.2.1   Simulation of pulse performance: program OCTOSIM

The program OCTOSIM simulates the performance of rf pulses over the defined range of chemical shift offsets and rf-field amplitudes. It assumes an ensemble of uncoupled spins and uses three dimensional rotations of magnetization vectors as they are also implemented in the program OCTOPUS. Since the program is intended to simulate the performance of pulses optimized with the program OCTOPUS it can directly be used with input files of the latter.

Running the program

To run the program one has to deliver it with the pulse shape to be simulated and the parameter file, containing all parameters relevant for a simulation. Simulation starts with the command:

octosim *par file name   pulsename*

The parameter file can be either the same as used for the optimization of the corresponding pulse shape, or its shortened form, containing only the data relevant for the optimization:

```
#*****************************************************************
#                   Optimization parameters
#*****************************************************************
Range, Hz = 20000
Checks = 120
MaxB1 deviation, % = 40
nB1 = 20
Pulse length, us = 25
RF limit, Hz = 10000
#*****************************
#    Initial state
#*****************************
initial_x = 0
initial_y = 0
initial_z = 1
#*****************************
#    Target state
#*****************************
target_x = 1
target_y = 0
target_z = 0
#*****************************************************************
```

The pulse has to be in Bruker format, hence in two columns with relative rf-amplitudes in % and phases in degree separated by commata. The header of the file is ignored and can therefore be omitted. The program generates the following messages:

```
Number of digits in a pulse:          1
Pulse length (us):    25.0000000000000
Digit length (us)=    25.0000000000000
te=  0.779056163677190
```

With *te* being the average quality factor of the pulse over the specified range of chemical shift offsets and rf-amplitudes. The quality factor is calculated as the scalar product of the magnetization at the end of the pulse with the target magnetization as it's defined in the input file. If the input values for the components of target or initial magnetization define the vectors with amplitudes other then 1, they will automatically be normalized before running the optimization.

Results and visualizations

As a result of the simulation the program generates four output files: the file *Sim-DataAxX.dat* contains the values of all single chemical shift offsets used in the simulation, the file *SimDataAxY.dat* contains the value of all single rf-amplitudes used in the simulation. The files *SimDataX.dat*, *SimDataY.dat*, *SimDataZ.dat* contain correspondingly the x, y and z components of the magnetization at the end of the pulse, with every data row in the file corresponding to a single offset value and columns corresponding to the values of rf-amplitudes, so for 3 rf-amplitudes and 12 offsets the files will have the form:

```
 ...
 0.666974505012919       0.197150066460594      -0.261510194376641
 0.664546402781363       0.191116890358538      -0.271462545615974
 0.662145841995019       0.185151341624442      -0.281305538313521
 0.659773461896480       0.179255044048590      -0.291036397275915
 0.657429895576712       0.173429606004882      -0.300652373079853
 0.655115769745181       0.167676619857728      -0.310150743111036
 0.652831704501977       0.161997661374033      -0.319528812594351
 0.650578313112047       0.156394289140539      -0.328783915614864
 0.648356201781603       0.150868043986760      -0.337913416129152
 0.646165969436836       0.145420448413765      -0.346914708966564
 0.644008207505000       0.140053006029068      -0.355785220819931
 0.641883499697983       0.134767200987841      -0.364522411225325
 ...
```

To visualize the simulation results we have written a script for the Matlab package, which has the following form:

```
%------------------------------------------------------------
```

```
f1=figure;
u=-1.0:0.05:1.0;
clear;
fname='/akbl1/kk/SIMULATION_PROGRAMS/OCTosim/SimDataAxX.dat';
fid=fopen(fname,'r');
axx=fscanf(fid,'%e',[inf]);
status=fclose(fid);
fname='/akbl1/kk/SIMULATION_PROGRAMS/OCTosim/SimDataAxY.dat';
fid=fopen(fname,'r');
axy=fscanf(fid,'%e',[inf]);
status=fclose(fid);
fname='/akbl1/kk/SIMULATION_PROGRAMS/OCTosim/SimDataX.dat';
fid=fopen(fname,'r');
gr=max(size(axy));
x=fscanf(fid,'%e',[gr inf]);
status=fclose(fid);
fname='/akbl1/kk/SIMULATION_PROGRAMS/OCTosim/SimDataY.dat';
fid=fopen(fname,'r');
y=fscanf(fid,'%e',[gr inf]);
status=fclose(fid);
fname='/akbl1/kk/SIMULATION_PROGRAMS/OCTosim/SimDataZ.dat';
fid=fopen(fname,'r');
z=fscanf(fid,'%e',[gr,inf]);
status=fclose(fid);
subplot(3,2,1);
v=contour(axx,axy,x);
clabel(v);
title('Mx');
subplot(3,2,3);
v=contour(axx,axy,y);
clabel(v);
title('My');
subplot(3,2,5);
v=contour(axx,axy,z);
clabel(v);
title('Mz');
xy=sqrt(x.*x+y.*y);
subplot(3,2,2);
v=contour(axx,axy,xy);
title('Mxy');
clabel(v);
phase=360.0*atan(y./x)/2/pi;
subplot(3,2,4);
```

```
v=contour(axx,axy,phase);
title('Phase');
clabel(v);
%------------------------------------------------------------
```

To run the script one has to specify the correct full paths to the data files. The script produces a figure with 5 subplots showing all three magnetization components as well as the amount of magnetization in the xy-plane and its phase as a function of chemical shift offset and rf-amplitude, as shown in Fig. 4.1.

4.2.2   Simulation of decoupling sequences

To investigate the performance of decoupling sequences composed of optimized pulses a specialized program was written. The program calculates the evolution of a heteronuclear two-spin system with one spin being decoupled by the train of shaped pulses. The program uses the subroutines from the SIMONE package [272,273] and calculates the evolution of initial I_x magnetization in the system of two coupled spins with weak coupling Hamiltonian. In contrast to the optimization and simulation programs described above, this program (and the one described in the next chapter) uses quantum mechanical description and calculates the evolution of 4×4 matrixes in the Hilbert space corresponding to an effective two-spin system.

Running the program

The program produces a series of FIDs for a series of different values of the chemical shift offset of the decoupled nucleus. To run the program one has to deliver the pulse shape to be simulated and the parameter file, containing all parameters relevant for the simulation. Simulation starts with the command:

$$\textbf{DecSim} \ \ par\ filename$$

The simulation results are saved in the file *parfilename.out*. The input file has the following format:

```
#***************************************************************
#                   Simulation parameters
#***************************************************************
#------ Observe channel ---------------------
Spectral width, Hz = 10000
T2,s = 0.05
Time domain, points = 4096
#------Hamiltonian--------------------
Het. coupling constant, Hz = 150.0
#------ Decoupler channel ---------------------
Central frequency, Hz = 0.0
```
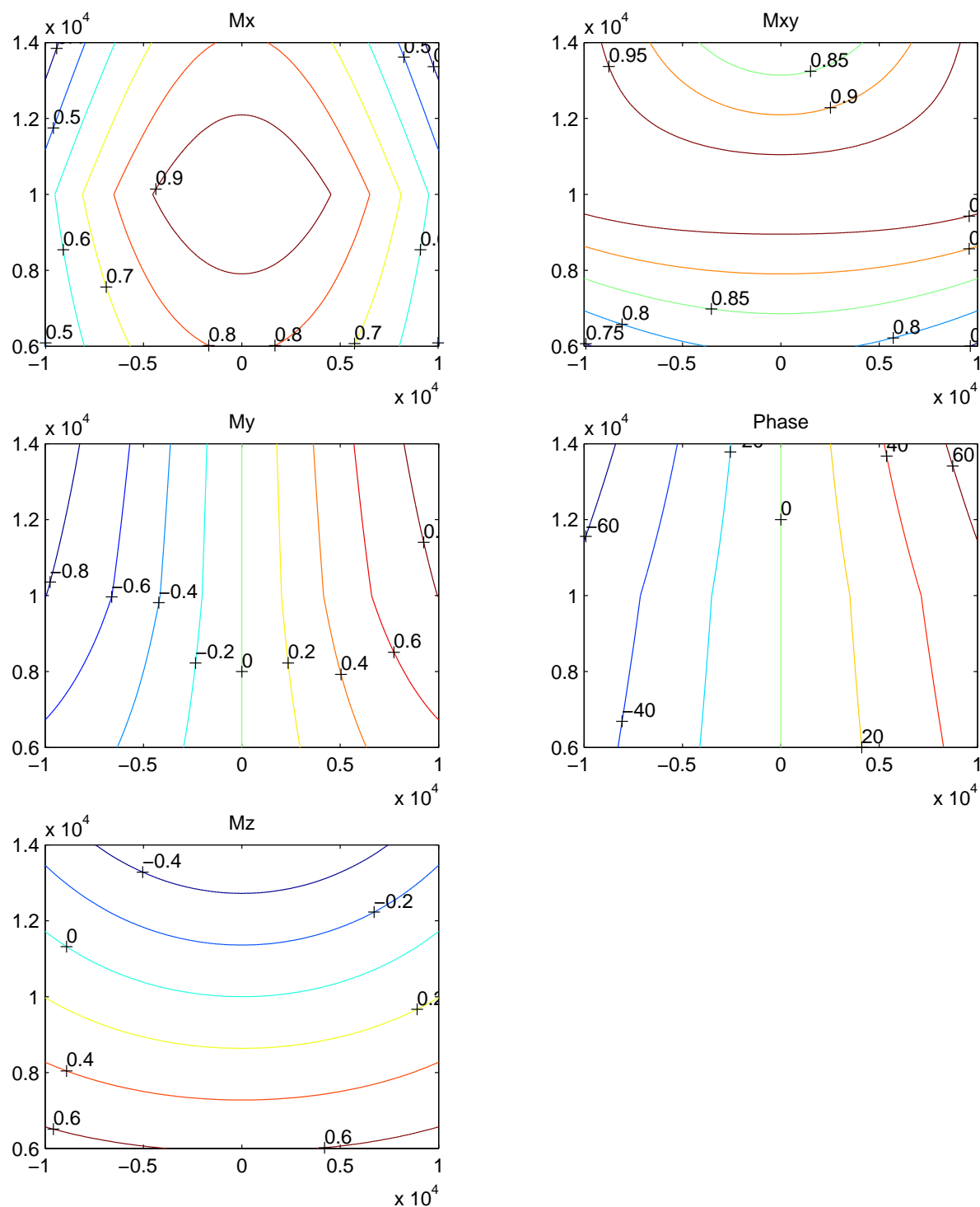
Figure 4.1: Visualization in Matlab of the simulation of the performance of an optimized pulse. The amounts of x, y and z magnetizations are shown in the left column, as well as the phase and the amount of magnetization in the xy-plane in the right column as a function of the chemical shift offset and rf-amplitude.

```
Offset range, Hz = 30000
Checks = 20
Shape file = square10
Pulse power, Hz = 2500.0
Pulse length, us = 200
Phase cycle = 3
#----Here choose one of the followings:
#**********************************************************
#    1 - no cycle
#                    __
#    2 - MLEV-4   (RRRR)
#                    __
#    3 - MLEV-4(2)(RRRR)
#                    __    __
#    4 - MLEV-8   (RRRR RRRR)
#                    __ _  _ __    __
#    5 - MLEV-16 (RRRR RRRR RRRR RRRR)
#                    __ _  _ __    __      _ __   ___    __
#    6 - MLEV-32 (RRRR RRRR RRRR RRRR RRRR RRRR RRRR RRRR)
#                        ____ ____
#    7 - XY-16    (XYXY YXYX XYXY YXYX)
#                         _
#    8 - WALTZ-4   (123 in MLEV expansion)
#**********************************************************
```

The fields have the following meanings:

- `Spectral width, Hz`

  The spectral width of the observable nucleus, defines the sampling rate of the FID;

- `T2,s`

  The rate of the exponential decay of the FID, defines the linewidth in the resulting spectrum;

- `Time domain, points`

  Number of points calculated for every single FID;

- `Het. coupling constant, Hz`

  Heteronuclear coupling constant; the Hamiltonian is then defined as weak coupling Hamiltonian;

- `Central frequency, Hz`

  Chemical shift offset of the decoupled nucleus;

- `Offset range, Hz`

  Range of chemical shift offsets of the decoupled nucleus for which the FIDs are calculated;

- `Checks`

  Number of offsets of the decoupled nucleus, number of calculated FIDs

- `Shape file`

  The name of a file defining the shape of the pulse, for which the performance for decoupling is tested; the pulse should be situated in the same directory where the program is started;

- `Pulse power, Hz`

  The peak amplitude of the shaped rf-pulse in the decoupling sequence;

- `Pulse length, us = 200`

  Length of the individual pulses in the decoupling sequence;

- `Phase cycle`

  Chose one of the supercycles listed.

Results and visualization

While running the program generates the following message with all simulation parameters listed:

```
*****************************************
 --------- Observe Channel ----------------------
 Spectral width:  10000.00 Hz
 Dwell time:       0.10 ms
 Transverse relaxation time:      0.05 s
 Time domain:          4096
 --------- Decoupler Channel ----------------------
 Elementary pulse:  square10
 Central frequency:  1000.00 Hz
 Offset range: 30000.00 Hz
 Calculated points:           20
 Pulse power:  2500.00 Hz
 Elementary pulse length:     200.00 us
 Phase cycle:  MLEV-4(2)
 *****************************************
```

And as a result of the simulation the file *parfilename.out* is created which has the following appearance:

```
 #    10000.0000000000                        4096
 #    30000.0000000000
 1.000000000000      0.000000000000
 0.996926709256      0.000000000000
 ...
```

The header contains the information to help decipher the following rows of numbers: in the first line the spectral width and number of points in the single FID, in the second line the offset range of the decoupled nucleus. Then the calculated FIDs are recorded one after each other with real part in the left column and imaginary part in the right. To visualize the simulation results we have used the Matlab package for wich the following script was written:

```
%------------------------------------------------------------
clear;
f1=figure;
fname='/akbl1/kk/SIMULATION_PROGRAMS/DecSim/input2.out';
[sw, td]=textread(fname,'#%f%f',1);
range=textread(fname,'# %f',1,'headerlines',1);
[a b]=textread(fname,'%f%f','headerlines',2);
c=length(a);
N=c/td;
for k=1:N,
 for j=1:td,
    data(j,k)=a((k-1)*td+j)+b((k-1)*td+j)*i;
 end;
end;
x=-range/2:range/(N-1):range/2;
y=-sw/2:sw/(td-1):sw/2;
spec=fft(data);
spec=fftshift(spec,1);
a=real(spec);
clear spec;
a=a/max(max(a));
v=[0:0.1:1];
contour(x,y,a,v);
axis([min(x) max(x) -100 100]);
xlabel('Offset on S, Hz');
ylabel('Offset on I, Hz');
colorbar;
%------------------------------------------------------------
```

The script performs Fourier transformation of the FIDs and creates the contour plot of stacked spectra, as shown in Fig. 4.2.
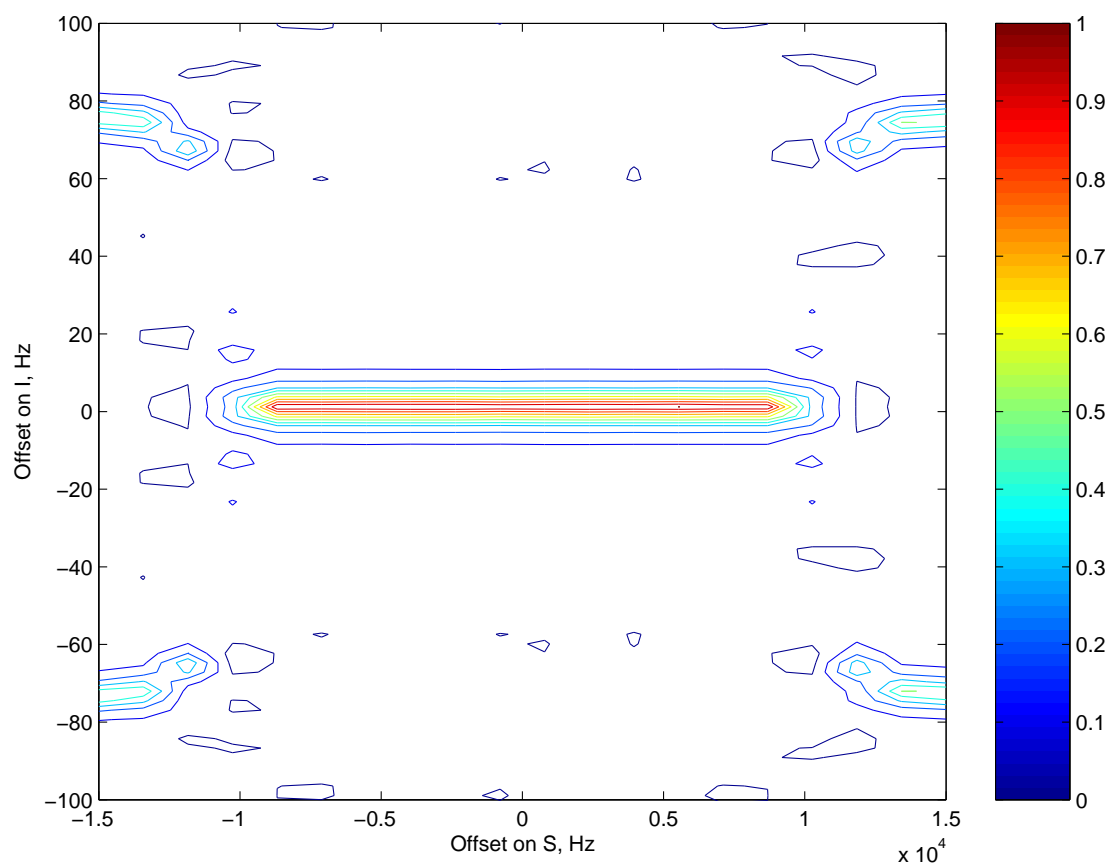
Figure 4.2: Visualization in Matlab of the simulation of decoupling efficiency of a certain decoupling scheme including optimized pulses. The 2D representation of a stack of spectra is shown.

4.2.3 Simulation of transfer efficiencies of homo- and heteronuclear mixing sequences

The program HAHASIM was written to simulate the performance of different mixing sequences in homonuclear or heteronuclear two-spin systems. It is written in the FORTRAN programming language and is compiled by INTEL$^{®}$ Fortran Compiler 8.0 for Linux.

The program systematically changes two simulation parameters and calculates for every pair the efficiency of the transfer from the defined initial state to the defined target state. The user should define, which parameters have to be varied, and which should be kept constant. Those available for variation are: offsets of both spins, RF powers on both channels, and the scalar and dipolar coupling constants.

The user has to define the Hamiltonian, which can be either simple weak coupling Hamiltonian $2\pi J_{het}I_zS_z$, or full isotropic coupling Hamiltonian $2\pi J_{iso}(I_xS_x + I_yS_y + I_zS_z)$, and can also include an extra term for dipolar coupling: $2\pi J_{dip}(2I_zS_z - I_xS_x - I_yS_y)$. Setting one of the constants J_{iso}, J_{het}, J_{dip} to zero eliminates the corresponding term from the active Hamiltonian.

One can compose the mixing sequence out of arbitrary shaped pulses by defining an elementary pulse of a sequence as a standard shape file in BRUKER format, which can further be expanded into a cycle.

Transfer from any initial state can be performed and the amount of any state at the end of the transfer can be checked by selecting corresponding terms in the input file.

Running the program

Simulation starts with the command

$$\textbf{hahasim} \;\; par\,filename,$$

where *parfilename* is a name of an input file, where the user defines all simulation parameters. This file has the following format (Imortant: Do not change anything in this file besides numbers on the right side of the "=" signs!):

```
#******************************************************************
#                    Simulation parameters
#******************************************************************
Heteronuclear (y/n): y
#------Spin I---------------------
Central frequency on spin I, Hz = 1000.0
Shape file for spin I = square1
Pulse power on I, Hz = 39
#------Spin S---------------------
Central frequency on spin S, Hz = 0.0
Shape file for spin S = square1
Pulse power on S, Hz = 39
```

```
#------Hamiltonian--------------------
Isotropic coupling constant, Hz = 0.0
Het. coupling constant, Hz = 200.0
Dipolar coupling constant, Hz = 50.0
#-----------------------------------------------------------------
#  Parameters to modify
#  (set 1 and 2 for those to be modified
#   or 0 for parameters kept constant)
#-----------------------------------------------------------------
Spin I offset = 1
Spin S offset = 2
Pulse power on I = 0
Pulse power on S = 0
Isotropic coupling constant = 0
Het. coupling constant = 0
Dipolar coupling constant = 0
#----Parameter 1-------------
First parameter range = 10000
First parameter number of points = 50
#----Parameter 2------------
Second parameter range = 10000
Second parameter number of points = 50
#------General--------------------
Pulse length, us = 11111.11
Mixing time, ms = 11.11111
Phase cycle = 1
#----Here choose one of the followings:
#    1 - no cycle
#              --
#    2 - MLEV-4  (RRRR)
#                -- -  - --      --
#    3 - MLEV-16 (RRRR RRRR RRRR RRRR)
#               --      --
#    4 - MLEV-8  (RRRR RRRR)
#      -- -  - --      --      - --    ---      --
#    5 - MLEV-32 (RRRR RRRR RRRR RRRR RRRR RRRR RRRR RRRR)
#       ---- ----
#    6 - XY-16   (XYXY YXYX XYXY YXYX)
#****************************************************************
Initial state
#****************************************************************
Ix = 1
Iy = 0
```

```
Iz = 0
I+ = 0
I- = 0
Sx = 0
Sy = 0
Sz = 0
S+ = 0
S- = 0

#  (Don't forget 2!)
IxSx = 0
IxSy = 0
IxSz = 0
IxS+ = 0
...


#*****************************
Target state
#*****************************
Ix = 0
Iy = 0
...


#***************************************************************
```

The fields, that might not be self-explanatory, have the following meanings:

- `Heteronuclear (y/n): y`

  Here we define, whether we want to simulate homonuclear (HEHAHA) or heteronuclear transfer (HOHAHA or TOCSY).

- `Central frequency on spin I, Hz = 1000.0`

  Here we define the central or the only offset of spin I (the same later for spin S).

- `Shape file for spin I = square1`

  Define the name of the file with the rf-shape to be applied on spin I. In the case of a homonuclear simulation the similar entry for the spin S will simply be ignored. In the case of a heteronuclear simulation take care that the size (number of digits) of the shapes is the same on both channels.

- `Pulse power on I, Hz = 39`

  Define the rf-power in Hz to be applied on the corresponding channel

- `Hamiltonian`

  In this section define the active Hamiltonian. By setting one of the constants to zero the corresponding part of the Hamiltonian is set to zero and is ignored in the calculation.

- `Parameters to modify`

  In this section chose two parameters that will be varied in the smulation, e.g. if you want to get a plot with the offset of spin 2 plotted vs. the offset of spin 1, then set 1 in the line "Spin I offset = 1" and 2 in the line "Spin S offset = 2." All other parameters in this section should be marked with 0

- `First parameter range = 10000`

  Here the parameter variation range should be set. For example, if you chose to vary offset of spin I, then it will be varied around the value, defined before as "Central frequency on spin I" within this range, so in the example shown from -4 kHz to 6 kHz.

- `Initial state`

  and

  `Target state`

  Define, transfer between which state you want to simulate. Take care about correct normalization coefficient (e.g. 2 for bilinear terms like $I_z S_x$) and its sign.

Results and visualization

When running the program produces the following output:

```
****************************************
 Performing homonuclear simulation
****************************************
--------- Spin I ----------------------
Elementary pulse:  testshape
Offset range:  VARIABLE from  -5000.00 Hz to   5000.00 Hz
              with 101 points calculated
Central frequency:     0.00 Hz
Pulse power: 10000.00 Hz
--------- Spin S ----------------------
Elementary pulse:  testshape
Offset range:  VARIABLE from  -5000.00 Hz to   5000.00 Hz
              with 101 points calculated
Central frequency:     0.00 Hz
```

```
Pulse power: 10000.00 Hz
--------- Hamiltonian ------------------
Isotropic coupling constant:     0.00 Hz
Heteronuclear coupling constant:     0.00 Hz
Dipolar coupling constant:    10.00 Hz
----------------------------------------
Elementary pulse length:     90.00 us
Mixing time:  48.9600 ms
Phase cycle:  XY-16
Overall number of building blocks:        34
Overall number of elementary pulses:       544
****************************************
Initial state=
   1 Z :          1.000
Target state=
   1  Z:          1.000
----------------------------------------
Calculating Spin I offset vs. Spin S offset
----------------------------------------
 ...Done...
```

And the results of the simulation are stored in a file *parfilename.out*, which has the following format:

```
Size         101         101
 Data:   w_I(Hz)       w_S(Hz)        te
       -5000.00      -5000.00    0.0391543759472
       -5000.00      -4900.00    0.0361719147664
       -5000.00      -4800.00    0.0237784462478
       -5000.00      -4700.00    0.0101656835866
...
```

where the header first indicates the number of data points in every simulation dimension and in the second line the modified variables are indicated with actual simulation data afterwards in three columns: value of both variables and the transfer efficiency. To visualize the simulation results we used the following Matlab script:

```
%--------------------------------------------------------------
clear;
fname='/akbl1/kk/SIMULATION_PROGRAMS/HAHAsim/dipsi2.inp.out';
limit=1000;
[size1,size2]=textread(fname,'Size%f%f',1);
[name1,name2]=textread(fname,'Data:%s%s',1,'headerlines',1);
[param1,param2,data]=textread(fname,'%f%f%f','headerlines',2,'delimiter',' ');
if param1(1) == param1(2)
```

```
for i=1:size1,
    for j=1:size2,
        k(j,i)=data((size2*(i-1))+j);
    end
    x(i)=param1(size2*(i-1)+1);
end
for i=1:size2,
    y(i)=param2(i);
end
end
if param2(1) == param2(2)
for i=1:size2,
    for j=1:size1,
        k(i,j)=data((size1*(i-1))+j);
    end
    y(i)=param2(size1*(i-1)+1);
end
for i=1:size1,
    x(i)=param1(i);
end
end
v=[0:1/10:1];
map=[v' v' v'];
f1=figure;
f2=pcolor(x,y,k);
shading interp;
set(f1,'colormap',map);
lighting phong;
axis square;
caxis([-1 1]);
xlabel(name1);
ylabel(name2);
colorbar;
%-------------------------------------------------------------
```

The script reads in the data into the data matrix the size of which is defined in the header (in this case 101×101) and creates a contour plot, as shown in Fig. 4.3.
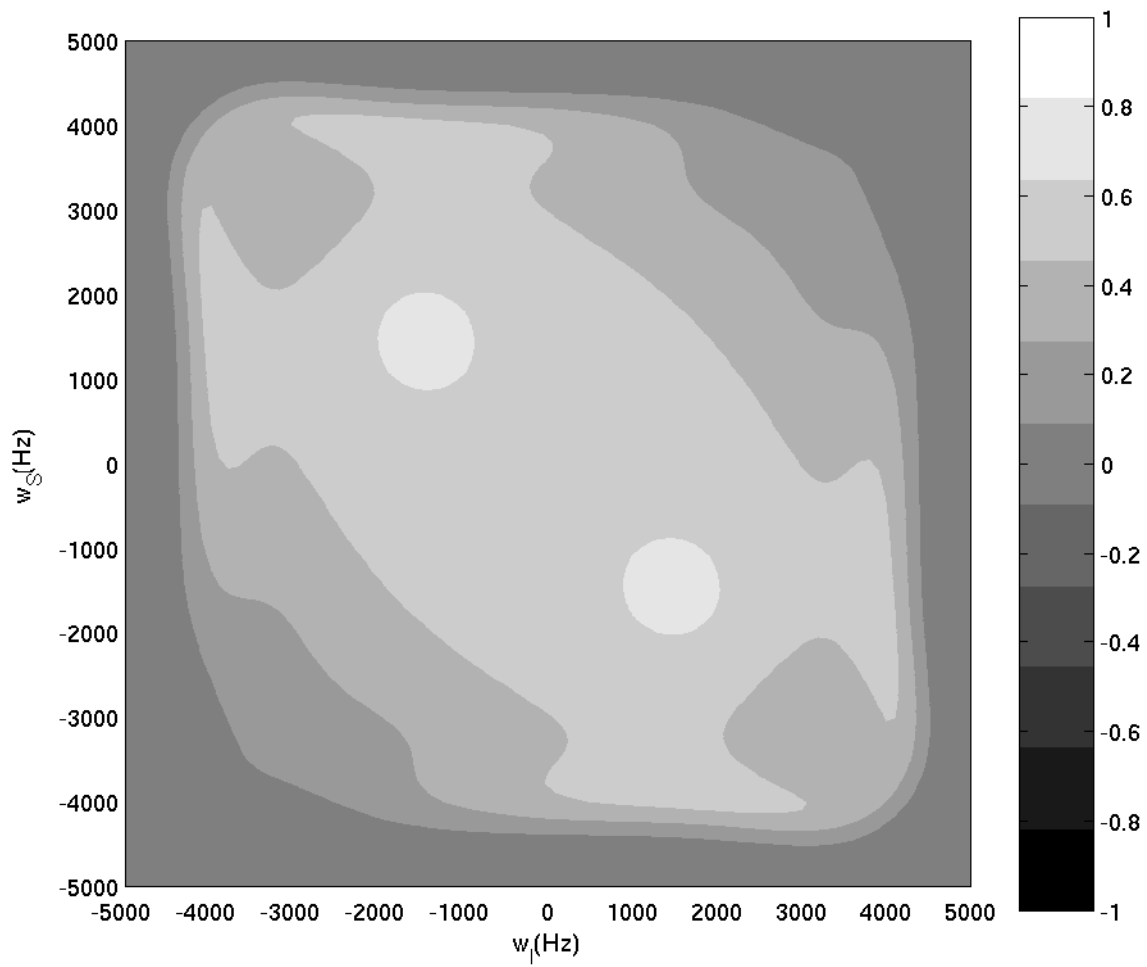
Figure 4.3: Visualization in Matlab of the simulation of some exemplary Hartmann-Hahn transfer.

4.3   Pulse programs

4.3.1   Constant-time HMBC

```
;CT-HMBC
;Constant-time HMBC for the measurement of long-range heteronuclear couplings,
;should be applied together with reference experiment of pulse sequence CT-HSQC.ref
;avance-version
;K. Kobzar, B. Luy, J. Magn. Reson. 186, 131-141 (2007)

#include <Avance.incl>
#include <Grad.incl>

define list<gradient> EA1 = { cnst22 cnst23 }
define list<gradient> EA2 = { -cnst23 -cnst22 }


"p2=p1*2"
"p4=p3*2"
"d4=1/4*cnst4"
"d5=1/2*cnst5"
"l0=td1/2"
"d0=3u"
"d10=(in0*td1)/2"
"in10=in0"
"d11=30m"
"d6=d0*2+p2"

1 ze
  100u UNBLKGRAD
2 d1 BLKGRAD
3 d11
4 p1 ph0
  d4
  (p2 ph0):f1 (p4 ph0):f2
  d4 UNBLKGRAD
  (p1 ph0):f1 (p3 ph0):f2
  3u
  p16:gp1*0.333333
  d16
  p1 ph1
  d5
  d10
```

```
  (p3 ph3):f2
  d0
  p2 ph2
  d0
  3u
  p16:gp1*EA1
  d16
  (p4 ph0):f2
  3u
  p16:gp1*EA2
  d16
  d6
  (p3 ph4):f2
  d10
  go=2 ph31
  d1 mc #0 to 2
  10u BLKGRAD
  F1EA(igrad EA1 & igrad EA2, id0 & dd10 & ip3*2 & ip31*2)

exit


ph0=0
ph1=0 0 0 0 2 2 2 2
ph2=0 0 0 0 0 0 0 0 1 1 1 1 1 1 1 1
ph3=2 0
ph4=0 0 2 2
ph31=0 2 2 0 2 0 0 2
     2 0 0 2 0 2 2 0



;pl1 : f1 channel - power level for pulse (default)
;pl2 : f2 channel - power level for pulse (default)
;p1 : f1 channel -  90 degree high power pulse
;p2 : f1 channel - 180 degree high power pulse
;p3 : f2 channel -  90 degree high power pulse
;p4 : f2 channel - 180 degree high power pulse
;p16: homospoil/gradient pulse
;d0 : incremented delay (2D)                    [3 usec]
;d10 : decremented delay (2D), (in0*td1)/2
;d1 : relaxation delay; 1-5 * T1
;d5 : HMBC transfer delay (normally 1/(2J)XH long range)
```

```
;d4 : inept delay (normally 1/(4J)XH long range)
;d11: delay for disk I/O                                    [30 msec]
;d13: short delay                                           [4 usec]
;d16: delay for homospoil/gradient recovery
;cnst4 : 1^J(XH)
;cnst5 : J(XH) long-range
;in0: 1/(2 * SW(X)) = DW(X)
;in10: =in0
;nd0: 2
;NS: 1 * n
;DS: >=16
;td1: number of experiments
;FnMODE: echo-antiecho
;cnst22: 0.5 for C-13, gradient multiplier
;cnst23: 0.3 for C-13, gradient multiplier


;use gradient files:
;gpnam1: SINE.100
```

4.3.2 Reference constant-time HSQC

```
;CT-HSQC.ref
;Reference experiment to the constant-time HMBC (CT-HMBC)
;for the measurement of long-range heteronuclear couplings.
;avance-version
;K. Kobzar, B. Luy, J. Magn. Reson. 186, 131-141 (2007)

#include <Avance.incl>
#include <Grad.incl>

define list<gradient> EA1 = { cnst22 cnst23 }
define list<gradient> EA2 = { -cnst23 -cnst22 }


"p2=p1*2"
"p4=p3*2"
"d4=1/4*cnst4"
"d5=1/2*cnst5"
"l0=td1/2"
"d0=3u"
"d10=(in0*td1)/4"
"in10=in0/2"
"d6=d0*2+p2"

1 ze
  100u UNBLKGRAD
2 d1 BLKGRAD
3 d11
4 p1 ph0
  d4
  (p2 ph0):f1 (p4 ph0):f2
  d4 UNBLKGRAD
  (p1 ph5):f1
  3u
  p16:gp1*0.333333
  d16
  (p1 ph1):f1 (p3 ph3):f2 ;produce MQ-terms that do not evolve
  d5*0.5
  d10
  (p4 ph3):f2
  d5*0.5
  d10
```

```
  d0
  p2 ph2
  d0
  3u
  p16:gp1*EA1
  d16
  d10
  (p4 ph0):f2
  3u
  p16:gp1*EA2
  d16
  d10
  d6
  (p3 ph4):f2
  go=2 ph31
  d1 mc #0 to 2
  10u BLKGRAD
  F1EA(igrad EA1 & igrad EA2, id0 & dd10 & ip3*2 & ip31*2)

exit


ph0=0
ph1=1 1 1 1 3 3 3 3
ph2=0 0 0 0 0 0 0 0 1 1 1 1 1 1 1 1
ph3=2 0
ph4=0 0 2 2
ph5=1
ph31=0 2 2 0 2 0 0 2
     2 0 0 2 0 2 2 0


;pl1 : f1 channel - power level for pulse (default)
;pl2 : f2 channel - power level for pulse (default)
;p1 : f1 channel -  90 degree high power pulse
;p2 : f1 channel - 180 degree high power pulse
;p3 : f2 channel -  90 degree high power pulse
;p4 : f2 channel -  180 degree high power pulse
;p16: homospoil/gradient pulse
;d0 : incremented delay (2D)                    [3 usec]
;d10 : decremented delay (2D), (in0*td1)/4
;d1 : relaxation delay; 1-5 * T1
;d5 : HMBC transfer delay (normally 1/(2J)XH long range)
```

```
;d4 : inept delay (normally 1/(4J)XH long range)
;d11: delay for disk I/O                              [30 msec]
;d13: short delay                                     [4 usec]
;d16: delay for homospoil/gradient recovery
;cnst4 : 1^J(XH)
;cnst5 : J(XH) long-range
;in0: 1/(2 * SW(X)) = DW(X)
;in10: =in0/2
;nd0: 2
;NS: 1 * n
;DS: >=16
;td1: number of experiments
;FnMODE: echo-antiecho
;cnst22: 0.5 for C-13, gradient multiplier
;cnst23: 0.3 for C-13, gradient multiplier


;use gradient files:
;gpnam1: SINE.100
```

4.3.3   CAGEBIRD^{r,X}-CPMG-HSQMBC (CBC-HSQMBC)

```
;CBC-HSQMBC
;K. Kobzar, B. Luy, J. Magn. Reson. 186, 131-141 (2007)

#include <Avance.incl>
#include <Grad.incl>
#include <Delay.incl>


"p2=p1*2"

"p4=p3*2"

"d0=3u"

"d9=1s/(cnst1*2)"

"d13=4u"
"d11=30m"

"DELTA=p16+d16+d13"


"FACTOR1=(d9/((p21+d20*2)*16))/2+0.5"
"d10=32*FACTOR1*(p21+d20*2)"
"l1=FACTOR1*2"

1 ze
  d10 UNBLKGRAD
2 d1 pl1:f1 pl2:f2
 10u BLKGRAD
 (p1 ph1)

;first part of CPMG-transfer

4 d20 pl19:f1 pl20:f2
  (center (p20 ph20):f1 (p21 ph20):f2)
   d20
   d20
  (center (p20 ph21):f1 (p21 ph21):f2)
   d20
   d20
```

```
(center (p20 ph20):f1 (p21 ph20):f2)
 d20
 d20
(center (p20 ph21):f1 (p21 ph21):f2)
 d20
 d20
(center (p20 ph21):f1 (p21 ph21):f2)
 d20
 d20
(center (p20 ph20):f1 (p21 ph20):f2)
 d20
 d20
(center (p20 ph21):f1 (p21 ph21):f2)
 d20
 d20
(center (p20 ph20):f1 (p21 ph20):f2)
 d20
 d20
(center (p20 ph22):f1 (p21 ph22):f2)
 d20
 d20
(center (p20 ph23):f1 (p21 ph23):f2)
 d20
 d20
(center (p20 ph22):f1 (p21 ph22):f2)
 d20
 d20
(center (p20 ph23):f1 (p21 ph23):f2)
 d20
 d20
(center (p20 ph23):f1 (p21 ph23):f2)
 d20
 d20
(center (p20 ph22):f1 (p21 ph22):f2)
 d20
 d20
(center (p20 ph23):f1 (p21 ph23):f2)
 d20
 d20
(center (p20 ph22):f1 (p21 ph22):f2)
 d20 pl1:f1 pl2:f2
 lo to 4 times l1
```

```
;CAGEBIRD-R,X-Filter

  d13
  p16:gp1
  d16

  (p1 ph2):f1

8  d20 pl19:f1 pl20:f2
  (center (p20 ph20):f1 (p21 ph20):f2)
   d20
   d20
  (center (p20 ph21):f1 (p21 ph21):f2)
   d20
   d20
  (center (p20 ph20):f1 (p21 ph20):f2)
   d20
   d20
  (center (p20 ph21):f1 (p21 ph21):f2)
   d20
   d20
  (center (p20 ph21):f1 (p21 ph21):f2)
   d20
   d20
  (center (p20 ph20):f1 (p21 ph20):f2)
   d20
   d20
  (center (p20 ph21):f1 (p21 ph21):f2)
   d20
   d20
  (center (p20 ph20):f1 (p21 ph20):f2)
   d20 pl1:f1 pl2:f2
  lo to 8 times l8

  (center (p2 ph2):f1 (p4 ph2):f2)

9 d20 pl19:f1 pl20:f2
  (center (p20 ph20):f1 (p21 ph20):f2)
   d20
   d20
  (center (p20 ph21):f1 (p21 ph21):f2)
   d20
```

```
  d20
  (center (p20 ph20):f1 (p21 ph20):f2)
   d20
   d20
  (center (p20 ph21):f1 (p21 ph21):f2)
   d20
   d20
  (center (p20 ph21):f1 (p21 ph21):f2)
   d20
   d20
  (center (p20 ph20):f1 (p21 ph20):f2)
   d20
   d20
  (center (p20 ph21):f1 (p21 ph21):f2)
   d20
   d20
  (center (p20 ph20):f1 (p21 ph20):f2)
   d20 pl1:f1 pl2:f2
  lo to 9 times l8

  (p1 ph4):f1

  d13
  p16:gp1
  d16

;second part of CPMG-transfer

5  d20 pl19:f1 pl20:f2
  (center (p20 ph20):f1 (p21 ph20):f2)
   d20
   d20
  (center (p20 ph21):f1 (p21 ph21):f2)
   d20
   d20
  (center (p20 ph20):f1 (p21 ph20):f2)
   d20
   d20
  (center (p20 ph21):f1 (p21 ph21):f2)
   d20
   d20
  (center (p20 ph21):f1 (p21 ph21):f2)
   d20
```

```
 d20
(center (p20 ph20):f1 (p21 ph20):f2)
 d20
 d20
(center (p20 ph21):f1 (p21 ph21):f2)
 d20
 d20
(center (p20 ph20):f1 (p21 ph20):f2)
 d20
 d20
(center (p20 ph22):f1 (p21 ph22):f2)
 d20
 d20
(center (p20 ph23):f1 (p21 ph23):f2)
 d20
 d20
(center (p20 ph22):f1 (p21 ph22):f2)
 d20
 d20
(center (p20 ph23):f1 (p21 ph23):f2)
 d20
 d20
(center (p20 ph23):f1 (p21 ph23):f2)
 d20
 d20
(center (p20 ph22):f1 (p21 ph22):f2)
 d20
 d20
(center (p20 ph23):f1 (p21 ph23):f2)
 d20
 d20
(center (p20 ph22):f1 (p21 ph22):f2)
 d20 pl1:f1 pl2:f2
lo to 5 times l1

p28 ph1
d13

(p1 ph2)
50u UNBLKGRAD
d13
p16:gp3
d16
```

```
  (p3 ph5):f2
  d0
  (p2 ph1)
  d0
  d13
  p16:gp4*-1*EA
  d16
  (p4 ph1):f2
  DELTA
  (p3 ph6):f2
  d13
  p16:gp5
  d16
  (p1 ph1)
  d13
  p16:gp6
  d16
  (p2 ph1)
  DELTA
  go=2 ph31
  d11 mc #0 to 2 F1EA(igrad EA, id0 & ip5*2 & ip31*2)
  10u BLKGRAD
exit


ph1=0
ph2=1
ph3=2
ph4=3
ph5=0 2
ph6=0 0 2 2
ph20=0
ph21=1
ph22=2
ph23=3
ph31=0 2 2 0


;pl1 : f1 channel - power level for pulse (default)
;pl2 : f2 channel - power level for pulse (default)
;pl19 : f1 channel - power level for MOCCA
;pl20 : f2 channel - power level for MOCCA
;p1 : f1 channel -  90 degree high power pulse
```

```
;p2 : f1 channel - 180 degree high power pulse
;p3 : f2 channel -  90 degree high power pulse
;p4 : f2 channel - 180 degree high power pulse
;p20 : f1 channel - 180 degree low power pulse
;p21 : f2 channel - 180 degree low power pulse
;p16: homospoil/gradient pulse
;p28: f1 channel - trim pulse
;d0 : incremented delay (2D)                 [3 usec]
;d1 : relaxation delay; 1-5 * T1
;d9 : Long-range polarization transfer delay
;d11: delay for disk I/O                      [30 msec]
;d13: short delay                            [4 usec]
;d16: delay for homospoil/gradient recovery   [100 usec]
;d20: MOCCA delay                            [200 usec]
;cnst1: = J(XH) Long-range
;in0: 1/(2 * SW(X)) = DW(X)
;nd0: 2
;NS: 1 * n
;DS: >= 16
;td1: number of experiments
;FnMODE: echo-antiecho


;use gradient ratio: gp 1 : gp 2 : gp 3 : gp 4 : gp 5 : gp 6
;    61  : 70.3 :  50  : 80   : 41.7 : 20.1

;for z-only gradients:
;gpz1: 61%
;gpz2: 70.3%
;gpz3: 50%
;gpz4: 80%
;gpz5: 41.7%
;gpz6: 20.1%

;use gradient files:
;gpnam1: SINE.100
;gpnam2: SINE.100
;gpnam3: SINE.100
;gpnam4: SINE.100
;gpnam5: SINE.100
;gpnam6: SINE.100
```

4.3.4 HSQC-TOCSY-IPAP

Pulse program for in-phase spectra

```
;HSQC-TOCSY-IP
;K. Kobzar, B. Luy, J. Magn. Reson. 186, 131-141 (2007)

#include <Avance.incl>
#include <Grad.incl>
#include <Delay.incl>



"p2=p1*2"

"p4=p3*2"

"d0=3u"

"d4=1s/(cnst2*4)"

"d11=30m"

"d13=4u"


"DELTA=p16+d16+p2+d0*2"
"DELTA1=d4-p16-d13-p3"
"FACTOR1=(d9/(p6*115.112))/2+0.5"
"l1=FACTOR1*2"

1 ze
  10u UNBLKGRAD
  d11 pl12:f2
2 d1 BLKGRAD
3 (p1 ph1)
  d4 pl2:f2
  (p2 ph1) (p4 ph6):f2
  d4 UNBLKGRAD
  p28 ph1
  d13
  (p1 ph2) (p3 ph3):f2
  d0
  p2 ph5
```

```
    d0
    p16:gp1
    d16
    (p4 ph4):f2
    DELTA
    (p1 ph1) (p3 ph4):f2
    d4
    (p2 ph1) (p4 ph1):f2
    d13
    p16:gp2
    DELTA1
    (p1 ph10) (p3 ph8):f2



    10u pl0:f1
    300u gron0
    p11:sp1:f1 ph1
    100u groff
    d16
    10u pl10:f1



                                                        ;begin DIPSI2
4 p6*3.556 ph23
  p6*4.556 ph25
  p6*3.222 ph23
  p6*3.167 ph25
  p6*0.333 ph23
  p6*2.722 ph25
  p6*4.167 ph23
  p6*2.944 ph25
  p6*4.111 ph23

  p6*3.556 ph25
  p6*4.556 ph23
  p6*3.222 ph25
  p6*3.167 ph23
  p6*0.333 ph25
  p6*2.722 ph23
  p6*4.167 ph25
  p6*2.944 ph23
  p6*4.111 ph25
```

```
  p6*3.556 ph25
  p6*4.556 ph23
  p6*3.222 ph25
  p6*3.167 ph23
  p6*0.333 ph25
  p6*2.722 ph23
  p6*4.167 ph25
  p6*2.944 ph23
  p6*4.111 ph25

  p6*3.556 ph23
  p6*4.556 ph25
  p6*3.222 ph23
  p6*3.167 ph25
  p6*0.333 ph23
  p6*2.722 ph25
  p6*4.167 ph23
  p6*2.944 ph25
  p6*4.111 ph23
  lo to 4 times l1
                                                    ;end DIPSI2
;------------------------------------------------------------

  10u pl0:f1
  300u gron0
  p12:sp2:f1 ph1
  100u groff
  d16

  10u pl1:f1
  p1 ph1
  go=2 ph31
  d1 mc #0 to 2  F1PH(id0 & ip3)
  100u BLKGRAD
exit


ph1=0
ph2=1
ph10=3
ph3=0 2
ph4=0 0 0 0 2 2 2 2
```

```
ph5=0 0 2 2
ph6=0
ph8=0 2
ph23=3
ph25=1
ph31=0 2 0 2 2 0 2 0
```

```
;pl1 : f1 channel - power level for pulse (default)
;pl2 : f2 channel - power level for pulse (default)
;pl10: DIPSI-2 power
;p1 : f1 channel -  90 degree high power pulse
;p2 : f1 channel - 180 degree high power pulse
;p3 : f2 channel -  90 degree high power pulse
;p4 : f2 channel - 180 degree high power pulse
;p6  : 90 degree low power pulse
;p16: homospoil/gradient pulse
;p28: f1 channel - trim pulse
;p11 : duration of first sweep
;p12 : duration of second sweep
;sp1 : strength for first sweep
;sp2 : strength for second sweep
;gpz0: gradient strength for ZQ suppression
;d0 : incremented delay (2D)                     [3 usec]
;d1 : relaxation delay; 1-5 * T1
;d9  : TOCSY mixing time
;d4 : 1/(4J)XH
;d11: delay for disk I/O                         [30 msec]
;d13: short delay                                [4 usec]
;d16: delay for homospoil/gradient recovery
;cnst2: = J(XH)
;in0: 1/(2 * SW(X)) = DW(X)
;nd0: 2
;NS: 1 * n
;DS: >= 16
;td1: number of experiments
;FnMODE: TPPI
```

```
;use gradient ratio: gp 1 : gp 2
;   80 : 20.1    for C-13
;   80 :  8.1    for N-15
```

```
;for z-only gradients:
;gpz1: 80%
;gpz2: 20.1% for C-13, 8.1% for N-15

;use gradient files:
;gpnam1: SINE.100
;gpnam2: SINE.100
```

Pulse program for anti-phase spectra

```
;HSQC-TOCSY-AP
;K. Kobzar, B. Luy, J. Magn. Reson. 186, 131-141 (2007)

#include <Avance.incl>
#include <Grad.incl>
#include <Delay.incl>



"p2=p1*2"

"p4=p3*2"

"d0=3u"

"d4=1s/(cnst2*4)"

"d11=30m"

"d13=4u"


"DELTA=p16+d16+p2+d0*2"
"DELTA1=d4-p16-d13-p3"
"FACTOR1=(d9/(p6*115.112))/2+0.5"
"l1=FACTOR1*2"

1 ze
  10u UNBLKGRAD
  d11 pl12:f2
2 d1 BLKGRAD
3 (p1 ph1)
  d4 pl2:f2
```

```
(p2 ph1) (p4 ph6):f2
d4 UNBLKGRAD
p28 ph1
d13
(p1 ph2) (p3 ph3):f2
d0
p2 ph5
d0
p16:gp1
d16
(p4 ph4):f2
DELTA
(p1 ph1) (p3 ph4):f2
d4
(p2 ph1) ;(p4 ph1):f2
d13
p16:gp2
DELTA1
(p1 ph10) (p3 ph8):f2
(p3 ph9):f2


10u pl0:f1
300u gron0
p11:sp1:f1 ph1
100u groff
d16
10u pl10:f1



                                                        ;begin DIPSI2
4 p6*3.556 ph23
  p6*4.556 ph25
  p6*3.222 ph23
  p6*3.167 ph25
  p6*0.333 ph23
  p6*2.722 ph25
  p6*4.167 ph23
  p6*2.944 ph25
  p6*4.111 ph23

  p6*3.556 ph25
  p6*4.556 ph23
```

```
  p6*3.222 ph25
  p6*3.167 ph23
  p6*0.333 ph25
  p6*2.722 ph23
  p6*4.167 ph25
  p6*2.944 ph23
  p6*4.111 ph25

  p6*3.556 ph25
  p6*4.556 ph23
  p6*3.222 ph25
  p6*3.167 ph23
  p6*0.333 ph25
  p6*2.722 ph23
  p6*4.167 ph25
  p6*2.944 ph23
  p6*4.111 ph25

  p6*3.556 ph23
  p6*4.556 ph25
  p6*3.222 ph23
  p6*3.167 ph25
  p6*0.333 ph23
  p6*2.722 ph25
  p6*4.167 ph23
  p6*2.944 ph25
  p6*4.111 ph23
  lo to 4 times l1
                                                  ;end DIPSI2
;------------------------------------------------------------

  10u pl0:f1
  300u gron0
  p12:sp2:f1 ph1
  100u groff
  d16
  10u pl1:f1

  p1 ph1
  go=2 ph31
  d1 mc #0 to 2 F1PH(id0 & ip3)
  100u BLKGRAD
exit
```

```
ph1=0
ph2=1
ph10=3
ph3=0 2
ph4=0 0 0 0 2 2 2 2
ph5=0 0 2 2
ph6=0
ph8=0 0 2 2
ph9=0
ph23=3
ph25=1
ph31=0 2 2 0 2 0 0 2


;pl1 : f1 channel - power level for pulse (default)
;pl2 : f2 channel - power level for pulse (default)
;pl10: DIPSI-2 power
;p1 : f1 channel -  90 degree high power pulse
;p2 : f1 channel - 180 degree high power pulse
;p3 : f2 channel -  90 degree high power pulse
;p4 : f2 channel - 180 degree high power pulse
;p6  : 90 degree low power pulse
;p16: homospoil/gradient pulse
;p28: f1 channel - trim pulse
;p11 : duration of first sweep
;p12 : duration of second sweep
;sp1 : strength for first sweep
;sp2 : strength for second sweep
;gpz0: gradient strength for ZQ suppression
;d0 : incremented delay (2D)                    [3 usec]
;d1 : relaxation delay; 1-5 * T1
;d9  : TOCSY mixing time
;d4 : 1/(4J)XH
;d11: delay for disk I/O                        [30 msec]
;d13: short delay                               [4 usec]
;d16: delay for homospoil/gradient recovery
;d20: first z-filter delay                      [2 msec]
;d21: second z-filter delay                     [3 msec]
;cnst2: = J(XH)
;in0: 1/(2 * SW(X)) = DW(X)
;nd0: 2
```

```
;NS: 1 * n
;DS: >= 16
;td1: number of experiments
;FnMODE: TPPI


;use gradient ratio: gp 1 : gp 2
;   80 : 20.1    for C-13
;   80 :  8.1    for N-15

;for z-only gradients:
;gpz1: 80%
;gpz2: 20.1% for C-13, 8.1% for N-15

;use gradient files:
;gpnam1: SINE.100
;gpnam2: SINE.100
```

Bibliography

[1] Freeman, R. Beg, borrow, or steal. Finding ideas for new NMR experiments, *Concepts in Magnetic Resonance Part A* **2003**, *17A*, 71–85.

[2] Conolly, S.; Nishimura, D.; Macovski, A. Optimal-Control Solutions to the Magnetic-Resonance Selective Excitation Problem, *IEEE Transactions on Medical Imaging* **1986**, *5*, 106–115.

[3] Mao, J. T.; Mareci, T. H.; Scott, K. N.; Andrew, E. R. Selective Inversion Radiofrequency Pulses by Optimal-Control, *Journal of Magnetic Resonance* **1986**, *70*, 310–318.

[4] Rosenfeld, D.; Zur, Y. Design of adiabatic selective pulses using optimal control theory, *Magnetic Resonance in Medicine* **1996**, *36*, 401–409.

[5] Khaneja, N.; Glaser, S. J. Efficient transfer of coherence through Ising spin chains, *Physical Review A* **2002**, *66*.

[6] Khaneja, N.; Glaser, S. J.; Brockett, R. Sub-Riemannian geometry and time optimal control of three spin systems: Quantum gates and coherence transfer, *Physical Review A* **2002**, *65*.

[7] Khaneja, N.; Luy, B.; Glaser, S. J. Boundary of quantum evolution under decoherence, *Proceedings of the National Academy of Sciences of the United States of America* **2003**, *100*, 13162–13166.

[8] Khaneja, N.; Reiss, T.; Luy, B.; Glaser, S. J. Optimal control of spin dynamics in the presence of relaxation, *Journal of Magnetic Resonance* **2003**, *162*, 311–319.

[9] Reiss, T. O.; Khaneja, N.; Glaser, S. J. Time-optimal coherence-order-selective transfer of in-phase coherence in heteronuclear IS spin systems, *Journal of Magnetic Resonance* **2002**, *154*, 192–195.

[10] Reiss, T. O.; Khaneja, N.; Glaser, S. J. Broadband geodesic pulses for three spin systems: time-optimal realization of effective trilinear coupling terms and indirect SWAP gates, *Journal of Magnetic Resonance* **2003**, *165*, 95–101.

[11] Stefanatos, D.; Khaneja, N.; Glaser, S. J. Optimal control of coupled spins in the presence of longitudinal and transverse relaxation, *Physical Review A* **2004**, *69*.

[12] Kehlet, C. *Design of optimum liquid-state NMR experiments in the presence of relaxation.* master thesis, TU Mnchen, 2003.

[13] Khaneja, N.; Reiss, T.; Kehlet, C.; Schulte-Herbrüggen, T.; Glaser, S. J. Optimal control of coupled spin dynamics: design of NMR pulse sequences by gradient ascent algorithms, *Journal of Magnetic Resonance* **2005**, *172*, 296–305.

[14] Reiss, T. O. *Anwendung der Steuerungstheorie auf die kernmagnetische Resonanzspektroskopie - von der Entwicklung computergestüzter Optimierungsmethoden bis zur experimentellen Umsetzung.* Ph.d. thesis, TU München, 2002.

[15] Bryson Jr., A.; Ho, Y.-C. *Applied Optimal Control.* Hemisphere: Washington DC, 1975.

[16] Krotov, V. F. *Global Methods in Optimal Control.* Marcel Decker: New York, 1996.

[17] Ernst, R. R.; Bodenhausen, G.; Wokaun, A. *Principles of Nuclear Magnetic Resonance in One and Two Dimensions.* Clarendon Press: Oxford, 1987.

[18] Levitt, M. H. Composite Pulses, *Progress in Nuclear Magnetic Resonance Spectroscopy* **1986**, *18*, 61–122.

[19] Levitt, M. H. In Grant, D.; Harris, R. E.-i.-C., editors, *Encyclopedia of Nuclear Magnetic Resonance*, pp. 1396–1411. Wiley: Chichester New York Brisbane Singapore, 1996.

[20] Emsley, L.; Bodenhausen, G. Gaussian Pulse Cascades - New Analytical Functions for Rectangular Selective Inversion and in-Phase Excitation in NMR, *Chemical Physics Letters* **1990**, *165*, 469–476.

[21] Ewing, B.; Glaser, S. J.; Drobny, G. P. Development and Optimization of Shaped NMR Pulses for the Study of Coupled Spin Systems, *Chemical Physics* **1990**, *147*, 121–129.

[22] Zax, D. B.; Goelman, G.; Vega, S. Amplitude-Modulated Composite Pulses, *Journal of Magnetic Resonance* **1988**, *80*, 375–382.

[23] Press, W. H.; Teukolsky, S.; Vetterling, W.; Flannery, B. *Numerical Recipes in C.* Cambridge University Press: New York, 1988.

[24] Geen, H.; Freeman, R. Band-Selective Radiofrequency Pulses, *Journal of Magnetic Resonance* **1991**, *93*, 93–141.

[25] Garwood, M.; Yong, K. Symmetrical Pulses to Induce Arbitrary Flip Angles with Compensation for Rf Inhomogeneity and Resonance Offsets, *Journal of Magnetic Resonance* **1991**, *94*, 511–525.

[26] Emsley, L.; Bodenhausen, G. Optimization of Shaped Selective Pulses for NMR Using a Quaternion Description of Their Overall Propagators, *Journal of Magnetic Resonance* **1992**, *97*, 135–148.

[27] Wigner, E. P. *Gruppentheorie und ihre Anwendung in der Quantenmechanik der Atomspektren.* Vieweg: Braunschweig, 1931.

[28] Rose, M. E. *Elementary theory of Angular Momentum.* Wiley: New York, 1957.

[29] Brink, D. M.; Satchler, G. R. *Angular Momentum.* Oxford University Press: London, 1962.

[30] Tinkham, M. *Group Theory and Quantum Mechanics.* McGraw-Hill: New York, 1964.

[31] Hamilton, W. R. *Lectures on Quaternions.* Hodges & Smith: Dublin, 1853.

[32] Hamilton, W. R. *Elements of Quaternions.* Chelsea: New York, 1969.

[33] Blümich, B.; Spiess, H. W. Quaternions as a Practical Tool for the Evaluation of Composite Rotations, *Journal of Magnetic Resonance* **1985**, *61*, 356–362.

[34] Skinner, T. E.; Reiss, T. O.; Luy, B.; Khaneja, N.; Glaser, S. J. Application of optimal control theory to the design of broadband excitation pulses for high-resolution NMR, *Journal of Magnetic Resonance* **2003**, *163*, 8–15.

[35] Cano, K. E.; Smith, M. A.; Shaka, A. J. Adjustable, broadband, selective excitation with uniform phase, *Journal of Magnetic Resonance* **2002**, *155*, 131–139.

[36] Skinner, T. E.; Reiss, T. O.; Luy, B.; Khaneja, N.; Glaser, S. J. Reducing the duration of broadband excitation pulses using optimal control with limited RF amplitude, *Journal of Magnetic Resonance* **2004**, *167*, 68–74.

[37] Carravetta, M.; Eden, M.; Johannessen, O. G.; Luthman, H.; Verdegem, P. J. E.; Lugtenburg, J.; Sebald, A.; Levitt, M. H. Estimation of carbon-carbon bond lengths and medium-range internuclear: Distances by solid-state nuclear magnetic resonance, *Journal of the American Chemical Society* **2001**, *123*, 10628–10638.

[38] Carravetta, M.; Eden, M.; Zhao, X.; Brinkmann, A.; Levitt, M. H. Symmetry principles for the design of radiofrequency pulse sequences in the nuclear magnetic resonance of rotating solids, *Chemical Physics Letters* **2000**, *321*, 205–215.

[39] Smith, M. A.; Hu, H.; Shaka, A. J. Improved broadband inversion performance for NMR in liquids, *Journal of Magnetic Resonance* **2001**, *151*, 269–283.

[40] Freeman, R.; Friedrich, J.; Wu, X. L. A Pulse for All Seasons - Fourier-Transform Spectra without a Phase Gradient, *Journal of Magnetic Resonance* **1988**, *79*, 561–567.

[41] Shaka, A. J.; Pines, A. Symmetrical Phase-Alternating Composite Pulses, *Journal of Magnetic Resonance* **1987**, *71*, 495–503.

[42] Keniry, M. A.; Sanctuary, B. C. Experimental-Verification of Composite Inversion Pulses Obtained by Series Expansion of the Offset Angle, *Journal of Magnetic Resonance* **1992**, *97*, 382–384.

[43] Lurie, D. J. Numerical Design of Composite Radiofrequency Pulses, *Journal of Magnetic Resonance* **1986**, *70*, 11–20.

[44] Shaka, A. J. Composite Pulses for Ultra-Broadband Spin Inversion, *Chemical Physics Letters* **1985**, *120*, 201–205.

[45] Shaka, A. J.; Freeman, R. Composite Pulses with Dual Compensation, *Journal of Magnetic Resonance* **1983**, *55*, 487–493.

[46] Tesiram, Y. A.; Bendall, M. R. Universal equations for linear adiabatic pulses and characterization of partial adiabaticity, *Journal of Magnetic Resonance* **2002**, *156*, 26–40.

[47] Hull, W. E. In Croasmun, W.; Carlson, R., editors, *Two-dimensional NMR Spectroscopy - Applications for Chemists and Biochemists*, pp. 67–456. VCH Publishers: New York, 1994.

[48] Kupče, E.; Freeman, R. Wide-Band Excitation with Polychromatic Pulses, *Journal of Magnetic Resonance Series A* **1994**, *108*, 268–273.

[49] Barker, P. B.; Golay, X.; Artemov, D.; Ouwerkerk, R.; Smith, M. A.; Shaka, A. J. Broadband proton decoupling for in vivo brain spectroscopy in humans, *Magnetic Resonance in Medicine* **2001**, *45*, 226–232.

[50] Abramovich, D.; Vega, S. Derivation of Broad-Band and Narrow-Band Excitation Pulses Using the Floquet Formalism, *Journal of Magnetic Resonance Series A* **1993**, *105*, 30–48.

[51] Emsley, L. In Grant, D.; Harris, R. E.-i.-C., editors, *Encyclopedia of Nuclear Magnetic Resonance*, pp. 4228–4236. Wiley: Chichester New York Brisbane Singapore, 1996.

[52] Freeman, R. Shaped radiofrequency pulses in high resolution NMR, *Progress in Nuclear Magnetic Resonance Spectroscopy* **1998**, *32*, 59–106.

[53] Warren, W. The art of pulse crafting: applications to magnetic resonance and laser spectroscopy, *Advances in Magnetic Resonance* **1988**, *12*, 247–384.

[54] Tannor, D. J.; Rice, S. A. Control of Selectivity of Chemical-Reaction Via Control of Wave Packet Evolution, *Journal of Chemical Physics* **1985**, *83*, 5013–5018.

[55] Charmont, P.; Sakellariou, D.; Emsley, L. Sample restriction using radiofrequency field selective pulses in high-resolution solid-state NMR, *Journal of Magnetic Resonance* **2002**, *154*, 136–141.

[56] Kobzar, K.; Skinner, T. E.; Khaneja, N.; Glaser, S. J.; Luy, B. Exploring the limits of broadband excitation and inversion pulses, *Journal of Magnetic Resonance* **2004**, *170*, 236–243.

[57] Skinner, T. E.; Reiss, T. O.; Luy, B.; Khaneja, N.; Glaser, S. J. Tailoring the optimal control cost function to a desired output: application to minimizing phase errors in short broadband excitation pulses, *Journal of Magnetic Resonance* **2005**, *172*, 17–23.

[58] Bendall, M. R.; Gordon, R. E. Depth and Refocusing Pulses Designed for Multipulse NMR with Surface Coils, *Journal of Magnetic Resonance* **1983**, *53*, 365–385.

[59] Cory, D. G. A Dante-Based Method for Radiofrequency-Field Selection, *Journal of Magnetic Resonance Series A* **1993**, *103*, 23–26.

[60] Hoult, D. I. Solution of the Bloch Equations in the Presence of a Varying B_1 Field - Approach to Selective Pulse Analysis, *Journal of Magnetic Resonance* **1979**, *35*, 69–86.

[61] KempHarper, R.; Styles, P.; Wimperis, S. B_1-selective pulses, *Journal of Magnetic Resonance Series A* **1996**, *123*, 230–236.

[62] Scheffler, K. Design of B_1-Insensitive and B_1-Selective Rf Pulses by Means of Stochastic Optimization, *Journal of Magnetic Resonance Series B* **1995**, *109*, 175–183.

[63] Shaka, A. J.; Freeman, R. A Composite 180-Degrees Pulse for Spatial Localization, *Journal of Magnetic Resonance* **1985**, *63*, 596–600.

[64] Shaka, A. J.; Freeman, R. Prepulses for Spatial Localization, *Journal of Magnetic Resonance* **1985**, *64*, 145–150.

[65] Tycko, R.; Pines, A. Spatial Localization of NMR Signals by Narrowband Inversion, *Journal of Magnetic Resonance* **1984**, *60*, 156–160.

[66] Wimperis, S. Broad-Band, Narrow-Band, and Passband Composite Pulses for Use in Advanced NMR Experiments, *Journal of Magnetic Resonance Series A* **1994**, *109*, 221–231.

[67] Belle, V.; Cros, G.; Lahrech, H.; Devoulon, P.; Decorps, M. A Rapid Phase-Sensitive Method for Measurement of the Excitation Profile of a Shaped Pulse, *Journal of Magnetic Resonance Series A* **1995**, *112*, 122–125.

[68] Berger, S. NMR techniques employing selective radiofrequency pulses in combination with pulsed field gradients, *Progress in Nuclear Magnetic Resonance Spectroscopy* **1997**, *30*, 137–156.

[69] Kobzar, K.; Luy, B.; Khaneja, N.; Glaser, S. J. Pattern pulses: design of arbitrary excitation profiles as a function of pulse amplitude and offset, *Journal of Magnetic Resonance* **2005**, *173*, 229–235.

[70] Shaka, A. J.; Keeler, J. Broadband spin decoupling in isotropic liquids, *Progress in Nuclear Magnetic Resonance Spectroscopy* **1987**, *19*, 47–129.

[71] Roberts, T. P. L.; Carpenter, T. A.; Hall, L. D. A Simple Method for the Construction of 180-Degrees Refocusing Rf Pulses for Use in Nuclear-Magnetic-Resonance Imaging, *Journal of Magnetic Resonance Series B* **1993**, *101*, 78–82.

[72] Ngo, J. T.; Morris, P. G. NMR Pulse Symmetry, *Journal of Magnetic Resonance* **1987**, *74*, 122–133.

[73] Meriles, C. A.; Sakellariou, D.; Heise, H.; Moule, A. J.; Pines, A. Approach to high-resolution ex situ NMR spectroscopy, *Science* **2001**, *293*, 82–85.

[74] Yan, H.; Gore, J. C. The Equivalence of Spin Inversion and Phase Reversal Using Symmetric Pulses, *Journal of Magnetic Resonance* **1987**, *75*, 427–433.

[75] Bohlen, J. M.; Bodenhausen, G. Experimental Aspects of Chirp NMR-Spectroscopy, *Journal of Magnetic Resonance Series A* **1993**, *102*, 293–301.

[76] Bohlen, J. M.; Rey, M.; Bodenhausen, G. Refocusing with Chirped Pulses for Broad-Band Excitation without Phase Dispersion, *Journal of Magnetic Resonance* **1989**, *84*, 191–197.

[77] Freeman, R.; Kempsell, S. P.; Levitt, M. H. Radiofrequency Pulse Sequences Which Compensate Their Own Imperfections, *Journal of Magnetic Resonance* **1980**, *38*, 453–479.

[78] Hallenga, K.; Lippens, G. M. A Constant-Time ^{13}C-^{1}H HSQC with Uniform Excitation over the Complete ^{13}C Chemical-Shift Range, *Journal of Biomolecular NMR* **1995**, *5*, 59–66.

[79] Hwang, T. L.; van Zijl, P. C. M.; Garwood, M. Broadband adiabatic refocusing without phase distortion, *Journal of Magnetic Resonance* **1997**, *124*, 250–254.

[80] Levitt, M. H. Symmetrical Composite Pulse Sequences for NMR Population-Inversion. 1. Compensation of Radiofrequency Field Inhomogeneity, *Journal of Magnetic Resonance* **1982**, *48*, 234–264.

[81] Levitt, M. H.; Ernst, R. R. Composite Pulses Constructed by a Recursive Expansion Procedure, *Journal of Magnetic Resonance* **1983**, *55*, 247–254.

[82] Tycko, R.; Cho, H. M.; Schneider, E.; Pines, A. Composite Pulses without Phase-Distortion, *Journal of Magnetic Resonance* **1985**, *61*, 90–101.

[83] Bodenhausen, G.; Ruben, D. J. Natural Abundance ^{15}N NMR by Enhanced Heteronuclear Spectroscopy, *Chemical Physics Letters* **1980**, *69*, 185–189.

[84] Davis, A. L.; Keeler, J.; Laue, E. D.; Moskau, D. Experiments for Recording Pure-Absorption Heteronuclear Correlation Spectra Using Pulsed Field Gradients, *Journal of Magnetic Resonance* **1992**, *98*, 207–216.

[85] Bax, A.; Summers, M. F. ^{1}H and ^{13}C Assignments from Sensitivity-Enhanced Detection of Heteronuclear Multiple-Bond Connectivity by 2D Multiple Quantum NMR, *Journal of the American Chemical Society* **1986**, *108*, 2093–2094.

[86] Verdier, L.; Sakhaii, P.; Zweckstetter, M.; Griesinger, C. Measurement of long range H,C couplings in natural products in orienting media: a tool for structure elucidation of natural products, *Journal of Magnetic Resonance* **2003**, *163*, 353–359.

[87] Ogura, K.; Terasawa, H.; Inagaki, F. Fully ^{13}C-refocused multidimensional ^{13}C-edited pulse schemes using broadband shaped inversion and refocusing pulses, *Journal of Magnetic Resonance Series B* **1996**, *112*, 63–68.

[88] van Zijl, P. C. M.; Hwang, T. L.; Johnson, M. O.; Garwood, M. Optimized excitation and automation for high-resolution NMR using B_1-insensitive rotation pulses, *Journal of the American Chemical Society* **1996**, *118*, 5510–5511.

[89] Kupče, E.; Freeman, R. Adiabatic Pulses for Wide-Band Inversion and Broad-Band Decoupling, *Journal of Magnetic Resonance Series A* **1995**, *115*, 273–276.

[90] Saupe, A.; Englert, G. High-Resolution Nuclear Magnetic Resonance Spectra of Orientated Molecules, *Physical Review Letters* **1963**, *11*, 462–464.

[91] Saupe, A. Kernresonanzen in Kristallinen Flüssigkeiten + in Kristallinflüssigen Lösungen .I, *Zeitschrift Fur Naturforschung Part A: Astrophysik Physik Und Physikalische Chemie* **1964**, *A 19*, 161–171.

[92] Kramer, F.; Deshmukh, M. V.; Kessler, H.; Glaser, S. J. Residual dipolar coupling constants: An elementary derivation of key equations, *Concepts in Magnetic Resonance Part A* **2004**, *21A*, 10–21.

[93] Prestegard, J. H.; Al-Hashimi, H. M.; Tolman, J. R. NMR structures of biomolecules using field oriented media and residual dipolar couplings, *Quarterly Reviews of Biophysics* **2000**, *33*, 371–424.

[94] Snyder, L. C. Analysis of Nuclear Magnetic Resonance Spectra of Molecules in Liquid-Crystal Solvents, *Journal of Chemical Physics* **1965**, *43*, 4041–4050.

[95] Tjandra, N.; Bax, A. Direct measurement of distances and angles in biomolecules by NMR in a dilute liquid crystalline medium, *Science* **1997**, *278*, 1111–1114.

[96] Losonczi, J. A.; Andrec, M.; Fischer, M. W. F.; Prestegard, J. H. Order matrix analysis of residual dipolar couplings using singular value decomposition, *Journal of Magnetic Resonance* **1999**, *138*, 334–342.

[97] Domaille, P. J. Direct Measurement of the Electron Susceptibility Anisotropy in Paramagnetic-Complexes Using High-Field Deuterium NMR, *Journal of the American Chemical Society* **1980**, *102*, 5392–5393.

[98] Bothnerby, A. A.; Domaille, P. J.; Gayathri, C. Ultra-High-Field NMR-Spectroscopy - Observation of Proton-Proton Dipolar Coupling in Paramagnetic Bis Tolyltris(Pyrazolyl)Borato Cobalt(II), *Journal of the American Chemical Society* **1981**, *103*, 5602–5603.

[99] Tolman, J. R.; Flanagan, J. M.; Kennedy, M. A.; Prestegard, J. H. Nuclear Magnetic Dipole Interactions in Field-Oriented Proteins - Information for Structure Determination in Solution, *Proceedings of the National Academy of Sciences of the United States of America* **1995**, *92*, 9279–9283.

[100] Bertini, I.; Del Bianco, C.; Gelis, I.; Katsaros, N.; Luchinat, C.; Parigi, G.; Peana, M.; Provenzani, A.; Zoroddu, M. A. Experimentally exploring the conformational space sampled by domain reorientation in calmodulin, *Proceedings of the National Academy of Sciences of the United States of America* **2004**, *101*, 6841–6846.

[101] Emsley, J. W.; Lindon, J. C. *NMR Spectroscopy using liquid crystal solvents*. Pergamon Press: Oxford, U.K., 1975.

[102] Luckhurs, G. R. Liquid Crystals as Solvents in Nuclear Magnetic Resonance, *Quarterly Reviews* **1968**, *22*, 179–198.

[103] Sackmann, E.; Meiboom, S.; Snyder, L. C. On Relation of Nematic to Cholesteric Mesophases, *Journal of the American Chemical Society* **1967**, *89*, 5981–5982.

[104] Yannoni, C. S.; Ceasar, G. P.; Dailey, B. P. Nuclear Magnetic Resonance Spectrum of Oriented (Cyclobutadiene)Iron Tricarbonyl, *Journal of the American Chemical Society* **1967**, *89*, 2833–2836.

[105] Luz, Z.; Meiboom, S. Nuclear Magnetic-Resonance Studies of Smectic Liquid-Crystals, *Journal of Chemical Physics* **1973**, *59*, 275–295.

[106] Taylor, T. R.; Arora, S. L.; Fergason, J. L. Temperature-Dependent Tilt Angle in Smectic C Phase of a Liquid Crystal, *Physical Review Letters* **1970**, *25*, 722–726.

[107] Yannoni, C. S. Oriented Smectic Liquid Crystal Solutions, *Journal of the American Chemical Society* **1969**, *91*, 4611–4612.

[108] Panar, M.; Phillips, W. D. Magnetic Ordering of Poly-Gamma-Benzyl-L-Glutamate Solutions, *Journal of the American Chemical Society* **1968**, *90*, 3880–3882.

[109] Lawson, K. D.; Flautt, T. J. Magnetically Oriented Lyotropic Liquid Crystalline Phases, *Journal of the American Chemical Society* **1967**, *89*, 5489–5491.

[110] Long, R. C. New Lyotropic Nematic Mesophase for NMR-Spectroscopy, *Journal of Magnetic Resonance* **1973**, *12*, 216–217.

[111] Thiele, C. M.; Berger, S. Probing the diastereotopicity of methylene protons in strychnine using residual dipolar couplings, *Organic Letters* **2003**, *5*, 705–708.

[112] Aroulanda, C.; Boucard, V.; Guibe, F.; Courtieu, J.; Merlet, D. Weakly oriented liquid-crystal NMR solvents as a general tool to determine relative configurations, *Chemistry-a European Journal* **2003**, *9*, 4536–4539.

[113] Bendiak, B. Sensitive through-space dipolar correlations between nuclei of small organic molecules by partial alignment in a deuterated liquid solvent, *Journal of the American Chemical Society* **2002**, *124*, 14862–14863.

[114] Thiele, C. M. Simultaneous assignment of all diastereotopic protons in strychnine using RDCs: PELG as alignment medium for organic molecules, *Journal of Organic Chemistry* **2004**, *69*, 7403–7413.

[115] Prestegard, J. H. New techniques in structural NMR - anisotropic interactions, *Nature Structural Biology* **1998**, *5*, 517–522. Suppl. S.

[116] Hansen, M. R.; Mueller, L.; Pardi, A. Tunable alignment of macromolecules by filamentous phage yields dipolar coupling interactions, *Nature Structural Biology* **1998**, *5*, 1065–1074.

[117] Ruckert, M.; Otting, G. Alignment of biological macromolecules in novel nonionic liquid crystalline media for NMR experiments, *Journal of the American Chemical Society* **2000**, *122*, 7793–7797.

[118] Fleming, K.; Gray, D.; Prasannan, S.; Matthews, S. Cellulose crystallites: A new and robust liquid crystalline medium for the measurement of residual dipolar couplings, *Journal of the American Chemical Society* **2000**, *122*, 5224–5225.

[119] Martin-Pastor, M.; Bush, C. A. Refined structure of a flexible heptasaccharide using ^{1}H-^{13}C and ^{1}H-^{1}H NMR residual dipolar couplings in concert with NOE and long range scalar coupling constants, *Journal of Biomolecular NMR* **2001**, *19*, 125–139.

[120] Neubauer, H.; Meiler, J.; Peti, W.; Griesinger, C. NMR structure determination of saccharose and raffinose by means of homo- and heteronuclear dipolar couplings, *Helvetica Chimica Acta* **2001**, *84*, 243–258.

[121] Azurmendi, H. F.; Bush, C. A. Conformational studies of blood group A and blood group B oligosaccharides using NMR residual dipolar couplings, *Carbohydrate Research* **2002**, *337*, 905–915.

[122] Freedberg, D. I. An alternative method for pucker determination in carbohydrates from residual dipolar couplings: A solution NMR study of the fructofuranosyl ring of sucrose, *Journal of the American Chemical Society* **2002**, *124*, 2358–2362.

[123] Yan, J. L.; Kline, A. D.; Mo, H. P.; Shapiro, M. J.; Zartler, E. R. A novel method for the determination of stereochemistry in six-membered chairlike rings using residual dipolar couplings, *Journal of Organic Chemistry* **2003**, *68*, 1786–1795.

[124] Yan, J. L.; Delaglio, F.; Kaerner, A.; Kline, A. D.; Mo, H. P.; Shapiro, M. J.; Smitka, T. A.; Stephenson, G. A.; Zartler, E. R. Complete relative stereochemistry of multiple stereocenters using only residual dipolar couplings, *Journal of the American Chemical Society* **2004**, *126*, 5008–5017.

[125] Deloche, B.; Samulski, E. T. Short-Range Nematic-Like Orientational Order in Strained Elastomers - a Deuterium Magnetic-Resonance Study, *Macromolecules* **1981**, *14*, 575–581.

[126] Tycko, R.; Blanco, F. J.; Ishii, Y. Alignment of biopolymers in strained gels: A new way to create detectable dipole-dipole couplings in high-resolution biomolecular NMR, *Journal of the American Chemical Society* **2000**, *122*, 9340–9341.

[127] Ishii, Y.; Markus, M. A.; Tycko, R. Controlling residual dipolar couplings in high-resolution NMR of proteins by strain induced alignment in a gel, *Journal of Biomolecular NMR* **2001**, *21*, 141–151.

[128] Sass, H. J.; Musco, G.; Stahl, S. J.; Wingfield, P. T.; Grzesiek, S. Solution NMR of proteins within polyacrylamide gels: Diffusional properties and residual alignment by mechanical stress or embedding of oriented purple membranes, *Journal of Biomolecular NMR* **2000**, *18*, 303–309.

[129] Mangoni, A.; Esposito, V.; Randazzo, A. Configuration assignment in small organic molecules via residual dipolar couplings, *Chemical Communications* **2003**, 154–155.

[130] Meier, S.; Haussinger, D.; Grzesiek, S. Charged acrylamide copolymer gels as media for weak alignment, *Journal of Biomolecular NMR* **2002**, *24*, 351–356.

[131] Chou, J. J.; Gaemers, S.; Howder, B.; Louis, J. M.; Bax, A. A simple apparatus for generating stretched polyacrylamide gels, yielding uniform alignment of proteins and detergent micelles, *Journal of Biomolecular NMR* **2001**, *21*, 377–382.

[132] Lipsitz, R. S.; Tjandra, N. Residual dipolar couplings in NMR structure analysis, *Annual Review of Biophysics and Biomolecular Structure* **2004**, *33*, 387–413.

[133] Freudenberger, J. C.; Spiteller, P.; Bauer, R.; Kessler, H.; Luy, B. Stretched poly(dimethylsiloxane) gels as NMR alignment media for apolar and weakly polar organic solvents: An ideal tool for measuring RDCs at low molecular concentrations, *Journal of the American Chemical Society* **2004**, *126*, 14690–14691.

[134] Zweckstetter, M.; Bax, A. Prediction of sterically induced alignment in a dilute liquid crystalline phase: Aid to protein structure determination by NMR, *Journal of the American Chemical Society* **2000**, *122*, 3791–3792.

[135] Meddour, A.; Canet, I.; Loewenstein, A.; Pechine, J. M.; Courtieu, J. Observation of Enantiomers, Chiral by Virtue of Isotopic-Substitution, through Deuterium NMR in a Polypeptide Liquid-Crystal, *Journal of the American Chemical Society* **1994**, *116*, 9652–9656.

[136] Cormier, R. J.; Kilfoil, M. L.; Callaghan, P. T. Biaxial deformation of a polymer under shear: NMR test of the Doi-Edwards model with convected constraint release, *Physical Review E* **2001**, *6405*. Part 1.

[137] Medick, P.; Vogel, M.; Rossler, E. Large angle jumps of small molecules in amorphous matrices analyzed by 2D exchange NMR, *Journal of Magnetic Resonance* **2002**, *159*, 126–136.

[138] Sentosa, P.; Fujara, F.; Sillescu, H. ^{2}H-NMR-Study of Solvent and Solute Mobility in Polymer-Solution, Gel and Glass States, *Makromolekulare Chemie-Macromolecular Chemistry and Physics* **1992**, *193*, 2421–2431.

[139] ter Beek, L. C.; Linseisen, F. M. Shear-induced orientational order in a polystyrene/benzene-d(6) solution as observed by ^{2}H-NMR, *Macromolecules* **1998**, *31*, 4986–4989.

[140] Fuchs, O. In *Polymer Handbook*, pp. 379–407. J. Wiley & Sons: New York, 1989.

[141] Kay, L. E.; Keifer, P.; Saarinen, T. Pure Absorption Gradient Enhanced Heteronuclear Single Quantum Correlation Spectroscopy with Improved Sensitivity, *Journal of the American Chemical Society* **1992**, *114*, 10663–10665.

[142] Palmer, A. G.; Cavanagh, J.; Wright, P. E.; Rance, M. Sensitivity Improvement in Proton-Detected 2-Dimensional Heteronuclear Correlation NMR-Spectroscopy, *Journal of Magnetic Resonance* **1991**, *93*, 151–170.

[143] Schleucher, J.; Schwendinger, M.; Sattler, M.; Schmidt, P.; Schedletzky, O.; Glaser, S. J.; Sørensen, O. W.; Griesinger, C. A General Enhancement Scheme in Heteronuclear Multidimensional NMR Employing Pulsed-Field Gradients, *Journal of Biomolecular NMR* **1994**, *4*, 301–306.

[144] Kneller, D. G.; Kuntz, I. D. UCSF Sparky - an NMR Display, Annotation and Assignment Tool, *Journal of Cellular Biochemistry* **1993**, 254–254. Suppl. 17C.

[145] Braun, S.; Kalinowski, H.-O.; Berger, S. *150 and More Basic NMR Experiments.* Wiley-VCH: Weinheim, 2nd edition, 1998.

[146] Zweckstetter, M.; Hummer, G.; Bax, A. Prediction of charge-induced molecular alignment of biomolecules dissolved in dilute liquid-crystalline phases, *Biophysical Journal* **2004**, *86*, 3444–3460.

[147] Bernheim, R. A.; Krugh, T. R. Chemical Shift Anisotropies from Nuclear Magnetic Resonance Studies in Liquid Crystals, *Journal of the American Chemical Society* **1967**, *89*, 6784–6785.

[148] Bhattach, P. K.; Dailey, B. P. Structural Parameters and ^{13} and ^{19}F Magnetic Shielding Anisotropies in $^{13}CH_3F$ from Nematic Phase Studies, *Journal of Magnetic Resonance* **1974**, *13*, 317–327.

[149] Buckingh, A. D.; Burnell, E. E. Chemical Shift Anisotropies from Nuclear Magnetic Resonance Studies of Oriented Molecules, *Journal of the American Chemical Society* **1967**, *89*, 3341.

[150] Buckingh, A. D.; Burnell, E. E.; Delange, C. A. Determination of Nuclear Magnetic Shielding Anisotropies of Solutes in Liquid-Crystal Solvents, *Journal of the American Chemical Society* **1968**, *90*, 2972–2974.

[151] Lee, S.; Mesleh, M. F.; Opella, S. J. Structure and dynamics of a membrane protein in micelles from three solution NMR experiments, *Journal of Biomolecular NMR* **2003**, *26*, 327–334.

[152] Haberz, P.; Farjon, J.; Griesinger, C. A DMSO-compatible orienting medium: Towards the investigation of the stereochemistry of natural products, *Angewandte Chemie-International Edition* **2005**, *44*, 427–429.

[153] Kummerlöwe, G.; Auernheimer, J.; Lendlein, A.; Luy, B. Stretched poly(acrylonitrile) as a scalable alignment medium for DMSO, *Journal of the American Chemical Society* **in press**.

[154] Ellestad, G. A.; Kunstman, M. P.; Morton, G. O.; Mirando, P. Structures of Fungal Diterpene Antibiotics Ll-S491beta and Gamma, *Journal of the American Chemical Society* **1972**, *94*, 6206–6208.

[155] Evidente, A.; Sparapano, L.; Fierro, O.; Bruno, G.; Giordano, F.; Motta, A. Sphaeropsidone and episphaeropsidone, phytotoxic dimedone methyl ethers produced by Sphaeropsis sapinea f. sp. cupressi grown in liquid culture, *Phytochemistry* **1998**, *48*, 1139–1143.

[156] Wenzel, T. J.; Wilcox, J. D. Chiral reagents for the determination of enantiomeric excess and absolute configuration using NMR spectroscopy, *Chirality* **2003**, *15*, 256–270.

[157] Parker, D. NMR Determination of Enantiomeric Purity, *Chemical Reviews* **1991**, *91*, 1441–1457.

[158] Sackmann, E.; Meiboom, S.; Snyder, L. C. Nuclear Magnetic Resonance Spectra of Enantiomers in Optically Active Liquid Crystals, *Journal of the American Chemical Society* **1968**, *90*, 2183.

[159] Sarfati, M.; Lesot, P.; Merlet, D.; Courtieu, J. Theoretical and experimental aspects of enantiomeric differentiation using natural abundance multinuclear nmr spectroscopy in chiral polypeptide liquid crystals, *Chemical Communications* **2000**, 2069–2081.

[160] Sarfati, M.; Courtieu, J.; Lesot, P. First successful enantiomeric discrimination of chiral alkanes using NMR spectroscopy, *Chemical Communications* **2000**, 1113–1114.

[161] Aroulanda, C.; Merlet, D.; Courtieu, J.; Lesot, P. NMR experimental evidence of the differentiation of enantiotopic directions in C$_s$ and C$_{2v}$ molecules using partially oriented, chiral media, *Journal of the American Chemical Society* **2001**, *123*, 12059–12066.

[162] Merlet, D.; Emsley, J. W.; Lesot, P.; Courtieu, J. The relationship between molecular symmetry and second-rank orientational order parameters for molecules in chiral liquid crystalline solvents, *Journal of Chemical Physics* **1999**, *111*, 6890–6896.

[163] Baczko, K.; Larpent, C.; Lesot, P. New amino acid-based anionic surfactants and their use as enantiodiscriminating lyotropic liquid crystalline NMR solvents, *Tetrahedron-Asymmetry* **2004**, *15*, 971–982.

[164] Tracey, A. S. Orientations of Molecules Dissolved in Lyotropic Surfactant Solutions - Monohalogenated Benzenes, *Molecular Physics* **1977**, *33*, 339–350.

[165] Tracey, A. S.; Diehl, P. Interaction of D-Alanine and L-Alanine with an Optically-Active Model Membrane System, *Febs Letters* **1975**, *59*, 131–132.

[166] Aroulanda, C.; Sarfati, M.; Courtieu, J.; Lesot, P. Investigation of the enantioselectivity of three polypeptide liquid-crystalline solvents using NMR spectroscopy, *Enantiomer* **2001**, *6*, 281–287.

[167] Canet, I.; Courtieu, J.; Loewenstein, A.; Meddour, A.; Pechine, J. M. Enantiomeric Analysis in a Polypeptide Lyotropic Liquid-Crystal by Deuterium NMR, *Journal of the American Chemical Society* **1995**, *117*, 6520–6526.

[168] Lafontaine, E.; Bayle, J. P.; Courtieu, J. High-Resolution NMR in Cholesteric Medium - Visualization of Enantiomers, *Journal of the American Chemical Society* **1989**, *111*, 8294–8296.

[169] Lafontaine, E.; Pechine, J. M.; Courtieu, J.; Mayne, C. L. Visualization of Enantiomers in Cholesteric Solvents through Deuterium NMR, *Liquid Crystals* **1990**, *7*, 293–298.

[170] Weiss-Lopez, B. E.; Azocar, M.; Montecinos, R.; Cassels, B. K.; Araya-Maturana, R. Differential incorporation of L- and D-N-acyl-1-phenyl-d(5)-2-aminopropane in a cesium N-dodecanoyl-L-alaninate cholesteric nematic lyomesophase, *Langmuir* **2001**, *17*, 6910–6914.

[171] Pechine, J. M.; Meddour, A.; Courtieu, J. Monitoring the differential ordering of enantiomers included into cyclodextrins through deuterium NMR in lyotropic liquid crystals, *Chemical Communications* **2002**, 1734–1735.

[172] Canet, I.; Meddour, A.; Courtieu, J.; Canet, J. L.; Salaun, J. New, and Accurate Method to Determine the Enantiomeric Purity of Amino-Acids Based on Deuterium NMR in a Cholesteric Lyotropic Liquid-Crystal, *Journal of the American Chemical Society* **1994**, *116*, 2155–2156.

[173] Lesot, P.; Merlet, D.; Loewenstein, A.; Courtieu, J. Enantiomeric visualization using proton-decoupled natural abundance deuterium NMR in poly(gamma-benzyl-L-glutamate) liquid crystalline solutions, *Tetrahedron-Asymmetry* **1998**, *9*, 1871–1881.

[174] Lesot, P.; Merlet, D.; Sarfati, M.; Courtieu, J.; Zimmermann, H.; Luz, Z. Enantiomeric and enantiotopic analysis of cone-shaped compounds with C_3 and C_{3v} symmetry using NMR Spectroscopy in chiral anisotropic solvents, *Journal of the American Chemical Society* **2002**, *124*, 10071–10082.

[175] Meddour, A.; Berdague, P.; Hedli, A.; Courtieu, J.; Lesot, P. Proton-decoupled carbon-13 NMR spectroscopy in a lyotropic chiral nematic solvent as an analytical tool for the measurement of the enantiomeric excess, *Journal of the American Chemical Society* **1997**, *119*, 4502–4508.

[176] Smadja, W.; Auffret, S.; Berdague, P.; Merlet, D.; Canlet, C.; Courtieu, J.; Legros, J. Y.; Boutros, A.; Fiaud, J. C. Visualisation of axial chirality using ^{2}H-^{1}H NMR in poly(gamma-benzyl L-glutamate), a chiral liquid crystal solvent, *Chemical Communications* **1997**, 2031–2032.

[177] Solgadi, A.; Meddour, A.; Courtieu, J. Enantiomeric discrimination of water soluble compounds using deuterium NMR in a glucopon/buffered water/n-hexanol chiral lyotropic liquid crystal, *Tetrahedron-Asymmetry* **2004**, *15*, 1315–1318.

[178] Tavasli, M.; Courtieu, J.; Goss, R. J. M.; Meddour, A.; O'Hagan, D. Extreme enantiomeric discrimination of fluoroalkanes using deuterium NMR in chiral liquid crystalline media, *Chemical Communications* **2002**, 844–845.

[179] Farjon, J.; Merlet, D.; Lesot, P.; Courtieu, J. Enantiomeric excess measurements in weakly oriented chiral liquid crystal solvents through 2D ^{1}H selective refocusing experiments, *Journal of Magnetic Resonance* **2002**, *158*, 169–172.

[180] Lesot, P.; Sarfati, M.; Courtieu, J. Natural abundance deuterium NMR spectroscopy in polypeptide liquid crystals as a new and incisive means for the enantiodifferentiation of chiral hydrocarbons, *Chemistry-a European Journal* **2003**, *9*, 1724–1745.

[181] Merlet, D.; Ancian, B.; Courtieu, J.; Lesot, P. Two-dimensional deuterium NMR spectroscopy of chiral molecules oriented in a polypeptide liquid crystal: Applications for the enantiomeric analysis through natural abundance deuterium NMR, *Journal of the American Chemical Society* **1999**, *121*, 5249–5258.

[182] Farjon, J.; Baltaze, J. P.; Lesot, P.; Merlet, D.; Courtieu, J. Heteronuclear selective refocusing 2D NMR experiments for the spectral analysis of enantiomers in chiral oriented solvents, *Magnetic Resonance in Chemistry* **2004**, *42*, 594–599.

[183] Uhrin, D.; Liptaj, T.; Kover, K. E. Modified Bird Pulses and Design of Heteronuclear Pulse Sequences, *Journal of Magnetic Resonance Series A* **1993**, *101*, 41–46.

[184] Luy, B.; Hauser, G.; Kirschning, A.; Glaser, S. J. Optimized NMR spectroscopic method for the configurational analysis of chemically equivalent vicinal protons, *Angewandte Chemie-International Edition* **2003**, *42*, 1300–1302.

[185] Luy, B.; Marino, J. P. JE-TROSY: combined J- and TROSY-spectroscopy for the measurement of one-bond couplings in macromolecules, *Journal of Magnetic Resonance* **2003**, *163*, 92–98.

[186] Ward, A.; Courts, A., editors. *The Science and Technology of Gelatin.* Academic Press: New York, 1977.

[187] Freudenberger, J. C.; Knör, S.; Kobzar, K.; Heckmann, D.; Paululat, T.; Kessler, H.; Luy, B. Stretched poly(vinyl acetate) gels as NMR alignment media for the measurement of residual dipolar couplings in polar organic solvents, *Angewandte Chemie-International Edition* **2005**, *44*, 423–426.

[188] Luy, B.; Kobzar, K.; Kessler, H. An easy and scalable method for the partial alignment of organic molecules for measuring residual dipolar couplings, *Angewandte Chemie-International Edition* **2004**, *43*, 1092–1094.

[189] Meissner, A.; Duus, J. O.; Sørensen, O. W. Integration of spin-state-selective excitation into 2D NMR correlation experiments with heteronuclear ZQ/2Q π rotations for $^1J_{XH}$-resolved E.COSY-type measurement of heteronuclear coupling constants in proteins, *Journal of Biomolecular NMR* **1997**, *10*, 89–94.

[190] Meissner, A.; Duus, J. O.; Sørensen, O. W. Spin-state-selective excitation. Application for E.COSY-type measurement of J_{HH} coupling constants, *Journal of Magnetic Resonance* **1997**, *128*, 92–97.

[191] Sørensen, M. D.; Meissner, A.; Sørensen, O. W. Spin-state-selective coherence transfer via intermediate states of two-spin coherence in IS spin systems: Application to E.COSY-type measurement of J coupling constants, *Journal of Biomolecular NMR* **1997**, *10*, 181–186.

[192] Ottiger, M.; Delaglio, F.; Bax, A. Measurement of J and dipolar couplings from simplified two-dimensional NMR spectra, *Journal of Magnetic Resonance* **1998**, *131*, 373–378.

[193] Tjandra, N.; Bax, A. Measurement of dipolar contributions to $^1J_{CH}$ splittings from magnetic-field dependence of J modulation in two-dimensional NMR spectra, *Journal of Magnetic Resonance* **1997**, *124*, 512–515.

[194] Vuister, G. W.; Bax, A. Quantitative J correlation - a new approach for measuring homonuclear 3-bond $J(H^N H^\alpha))$ coupling constants in ^{15}N-enriched proteins, *Journal of the American Chemical Society* **1993**, *115*, 7772–7777.

[195] Carlomagno, T.; Peti, W.; Griesinger, C. A new method for the simultaneous measurement of magnitude and sign of $^1D_{CH}$ and $^1D_{HH}$ dipolar couplings in methylene groups, *Journal of Biomolecular NMR* **2000**, *17*, 99–109.

[196] Garbow, J. R.; Weitekamp, D. P.; Pines, A. Bilinear Rotation Decoupling of Homonuclear Scalar Interactions, *Chemical Physics Letters* **1982**, *93*, 504–509.

[197] Feher, K.; Berger, S.; Kover, K. E. Accurate determination of small one-bond heteronuclear residual dipolar couplings by F1 coupled HSQC modified with a G-BIRD^r module, *Journal of Magnetic Resonance* **2003**, *163*, 340–346.

[198] Klochkov, V. V.; Klochkov, A. V.; Thiele, C. M.; Berger, S. A novel liquid crystalline system for partial alignment of polar organic molecules, *Journal of Magnetic Resonance* **2006**, *179*, 58–63.

[199] Eberstadt, M.; Gemmecker, G.; Mierke, D. F.; Kessler, H. Scalar Coupling-Constants - Their Analysis and Their Application for the Elucidation of Structures, *Angewandte Chemie-International Edition in English* **1995**, *34*, 1671–1695.

[200] Eberstadt, M.; Mierke, D. F.; Kock, M.; Kessler, H. Peptide Conformation from Coupling-Constants - Scalar Couplings as Restraints in MD Simulations, *Helvetica Chimica Acta* **1992**, *75*, 2583–2592.

[201] Köck, M.; Kessler, H.; Seebach, D.; Thaler, A. Novel Backbone Conformation of Cyclosporine A: the Complex with Lithium-Chloride, *Journal of the American Chemical Society* **1992**, *114*, 2676–2686.

[202] Matsumori, N.; Kaneno, D.; Murata, M.; Nakamura, H.; Tachibana, K. Stereochemical determination of acyclic structures based on carbon-proton spin-coupling constants. A method of configuration analysis for natural products, *Journal of Organic Chemistry* **1999**, *64*, 866–876.

[203] Matsumori, N.; Murata, M.; Tachibana, K. Conformational-Analysis of Natural-Products Using Long-Range Carbon-Proton Coupling-Constants - 3-Dimensional Structure of Okadaic Acid in Solution, *Tetrahedron* **1995**, *51*, 12229–12238.

[204] Milligan, K. E.; Marquez, B.; Williamson, R. T.; Davies-Coleman, M.; Gerwick, W. H. Two new malyngamides from a Madagascan Lyngbya majuscula, *Journal of Natural Products* **2000**, *63*, 965–968.

[205] Murata, M.; Matsuoka, S.; Matsumori, N.; Paul, G. K.; Tachibana, K. Absolute configuration of amphidinol 3, the first complete structure determination from amphidinol homologues: Application of a new configuration analysis based on carbon-hydrogen spin-coupling constants, *Journal of the American Chemical Society* **1999**, *121*, 870–871.

[206] Murata, M.; Yasumoto, T. The structure elucidation and biological activities of high molecular weight algal toxins: maitotoxin, prymnesins and zooxanthellatoxins, *Natural Product Reports* **2000**, *17*, 293–314.

[207] Rundlof, T.; Kjellberg, A.; Damberg, C.; Nishida, T.; Widmalm, G. Long-range proton-carbon coupling constants in conformational analysis of oligosaccharides, *Magnetic Resonance in Chemistry* **1998**, *36*, 839–847.

[208] Seebach, D.; Ko, S. Y.; Kessler, H.; Kock, M.; Reggelin, M.; Schmieder, P.; Walkinshaw, M. D.; Bolsterli, J. J.; Bevec, D. Thiocyclosporins - Preparation, Solution and Crystal-Structure, and Immunosuppressive Activity, *Helvetica Chimica Acta* **1991**, *74*, 1953–1990.

[209] Tvaroska, I.; Taravel, F. R. In *Advances in Carbohydrate Chemistry and Biochemistry*, volume 51 of *Advances in Carbohydrate Chemistry and Biochemistry*, pp. 15–61. 1995.

[210] Wu, M.; Okino, T.; Nogle, L. M.; Marquez, B. L.; Williamson, R. T.; Sitachitta, N.; Berman, F. W.; Murray, T. F.; McGough, K.; Jacobs, R.; Colsen, K.; Asano, T.;

Yokokawa, F.; Shioiri, T.; Gerwick, W. H. Structure, synthesis, and biological properties of kalkitoxin, a novel neurotoxin from the marine cyanobacterium Lyngbya majuscula, *Journal of the American Chemical Society* **2000**, *122*, 12041–12042.

[211] Marquez, B. L.; Gerwick, W. H.; Williamson, R. T. Survey of NMR experiments for the determination of $^{n}J_{CH}$ heteronuclear coupling constants in small molecules, *Magnetic Resonance in Chemistry* **2001**, *39*, 499–530. Sp. Iss. SI.

[212] Koskela, H.; Kilpelainen, I.; Heikkinen, S. LR-CAHSQC: an application of a Carr-Purcell-Meiboom-Gill-type sequence to heteronuclear multiple bond correlation spectroscopy, *Journal of Magnetic Resonance* **2003**, *164*, 228–232.

[213] Kover, K. E.; Batta, G.; Feher, K. Accurate measurement of long-range heteronuclear coupling constants from undistorted multiplets of an enhanced CPMG-HSQMBC experiment, *Journal of Magnetic Resonance* **2006**, *181*, 89–97.

[214] Lacerda, V.; da Silva, G. V. J.; Constantino, M. G.; Tormena, C. F.; Williamson, R. T.; Marquez, B. L. Long-range J_{CH} heteronuclear coupling constants in cyclopentane derivatives, *Magnetic Resonance in Chemistry* **2006**, *44*, 95–98.

[215] Kozminski, W. Simplified multiplet pattern HSQC-TOCSY experiment for accurate determination of long-range heteronuclear coupling constants, *Journal of Magnetic Resonance* **1999**, *137*, 408–412.

[216] Kurz, M.; Schmieder, P.; Kessler, H. HETLOC, an Efficient Method for Determining Heteronuclear Long-Range Couplings with Heteronuclei in Natural Abundance, *Angewandte Chemie-International Edition in English* **1991**, *30*, 1329–1331.

[217] Edden, R. A. E.; Keeler, J. Development of a method for the measurement of long-range ^{13}C-^{1}H coupling constants from HMBC spectra, *Journal of Magnetic Resonance* **2004**, *166*, 53–68.

[218] Titman, J. J.; Neuhaus, D.; Keeler, J. Measurement of Long-Range Heteronuclear Coupling-Constants, *Journal of Magnetic Resonance* **1989**, *85*, 111–131.

[219] Claridge, T. D. W.; Perez-Victoria, I. Enhanced ^{13}C resolution in semi-selective HMBC: a band-selective, constant-time HMBC for complex organic structure elucidation by NMR, *Organic & Biomolecular Chemistry* **2003**, *1*, 3632–3634.

[220] Furihata, K.; Seto, H. Constant time HMBC (CT-HMBC), a new HMBC technique useful for improving separation of cross peaks, *Tetrahedron Letters* **1998**, *39*, 7337–7340.

[221] Koskela, H.; Kilpelainen, I.; Heikkinen, S. CAGEBIRD: improving the GBIRD filter with a CPMG sequence, *Journal of Magnetic Resonance* **2004**, *170*, 121–126.

[222] Luy, B.; Marino, J. P. ^{1}H-^{31}P CPMG-correlated experiments for the assignment of nucleic acids, *Journal of the American Chemical Society* **2001**, *123*, 11306–11307.

[223] Gullion, T.; Baker, D. B.; Conradi, M. S. New, Compensated Carr-Purcell Sequences, *Journal of Magnetic Resonance* **1990**, *89*, 479–484.

[224] Lizak, M. J.; Gullion, T.; Conradi, M. S. Measurement of Like-Spin Dipole Couplings, *Journal of Magnetic Resonance* **1991**, *91*, 254–260.

[225] Furrer, J.; Kramer, F.; Marino, J. P.; Glaser, S. J.; Luy, B. Homonuclear Hartmann-Hahn transfer with reduced relaxation losses by use of the MOCCA-XY16 multiple pulse sequence, *Journal of Magnetic Resonance* **2004**, *166*, 39–46.

[226] Kramer, F.; Peti, W.; Griesinger, C.; Glaser, S. J. Optimized homonuclear Carr-Purcell-type dipolar mixing sequences, *Journal of Magnetic Resonance* **2001**, *149*, 58–66.

[227] Luy, B.; Kobzar, K.; Skinner, T. E.; Khaneja, N.; Glaser, S. J. Construction of universal rotations from point-to-point transformations, *Journal of Magnetic Resonance* **2005**, *176*, 179–186.

[228] Glaser, S. J.; Quant, J. In Warren, W. S., editor, *Advances in Magnetic and Optical Resonance*, volume 19, pp. 59–252. Academic Press: San Diego, 1996.

[229] Luy, B.; Glaser, S. J. Negative polarization transfer between a spin 1/2 and a spin 1, *Chemical Physics Letters* **2000**, *323*, 377–381.

[230] Rance, M. Sign Reversal of Resonances Via Isotropic Mixing in NMR-Spectroscopy, *Chemical Physics Letters* **1989**, *154*, 242–247.

[231] Luy, B.; Glaser, S. J. Superposition of scalar and residual dipolar couplings: Analytical transfer functions for three spins 1/2 under cylindrical mixing conditions, *Journal of Magnetic Resonance* **2001**, *148*, 169–181.

[232] Taylor, D. M.; Ramamoorthy, A. Analysis of dipolar-coupling-mediated coherence transfer in a homonuclear two spin-1/2 solid-state system, *Journal of Magnetic Resonance* **1999**, *141*, 18–28.

[233] Griesinger, C.; Sørensen, O. W.; Ernst, R. R. Correlation of Connected Transitions by Two-Dimensional NMR-Spectroscopy, *Journal of Chemical Physics* **1986**, *85*, 6837–6852.

[234] Bax, A.; Subramanian, S. Sensitivity-Enhanced Two-Dimensional Heteronuclear Shift Correlation NMR-Spectroscopy, *Journal of Magnetic Resonance* **1986**, *67*, 565–569.

[235] Edison, A. S.; Westler, W. M.; Markley, J. L. Elucidation of Amino-Acid Spin Systems in Proteins and Determination of Heteronuclear Coupling-Constants by Carbon Proton Proton 3-Dimensional NMR, *Journal of Magnetic Resonance* **1991**, *92*, 434–438.

[236] Otting, G.; Senn, H.; Wagner, G.; Wüthrich, K. Editing of 2D ^{1}H-NMR Spectra Using X Half-Filters - Combined Use with Residue-Selective ^{15}N Labeling of Proteins, *Journal of Magnetic Resonance* **1986**, *70*, 500–505.

[237] Uhrin, D.; Batta, G.; Hruby, V. J.; Barlow, P. N.; Kover, K. E. Sensitivity- and gradient-enhanced hetero (ω) half-filtered TOCSY experiment for measuring long-range coupling constants, *Journal of Magnetic Resonance* **1998**, *130*, 155–161.

[238] Wollborn, U.; Leibfritz, D. Measurements of Heteronuclear Long-Range Coupling-Constants from Inverse Homonuclear-2D NMR-Spectra, *Journal of Magnetic Resonance* **1992**, *98*, 142–146.

[239] Xu, G. Z.; Evans, J. S. Determination of long-range J_{XH} couplings using "excitation-sculpting" gradient-enhanced heteronuclear correlation experiments, *Journal of Magnetic Resonance Series A* **1996**, *123*, 105–110.

[240] Nolis, P.; Parella, T. Spin-edited 2D HSQC-TOCSY experiments for the measurement of homonuclear and heteronuclear coupling constants: Application to carbohydrates and peptides, *Journal of Magnetic Resonance* **2005**, *176*, 15–26.

[241] Ross, A.; Czisch, M.; Holak, T. A. Selection of simultaneous coherence pathways with gradient pulses, *Journal of Magnetic Resonance Series A* **1996**, *118*, 221–226.

[242] Thrippleton, M. J.; Keeler, J. Elimination of zero-quantum interference in two-dimensional NMR spectra, *Angewandte Chemie-International Edition* **2003**, *42*, 3938–3941.

[243] Luy, B. Spin state selectivity and heteronuclear Hartmann-Hahn transfer, *Journal of Magnetic Resonance* **2004**, *168*, 210–216.

[244] Carlomagno, T.; Prasch, T.; Glaser, S. J. COIN TACSY, a novel approach to tailored correlation spectroscopy, *Journal of Magnetic Resonance* **2001**, *149*, 52–57.

[245] Quant, J.; Prasch, T.; Ihringer, S.; Glaser, S. J. Tailored Correlation Spectroscopy for the Enhancement of Fingerprint Cross Peaks in Peptides and Proteins, *Journal of Magnetic Resonance Series B* **1995**, *106*, 116–121.

[246] Shaka, A. J.; Lee, C. J.; Pines, A. Iterative Schemes for Bilinear Operators - Application to Spin Decoupling, *Journal of Magnetic Resonance* **1988**, *77*, 274–293.

[247] Bolinger, L.; Leigh, J. S. Hadamard Spectroscopic Imaging (Hsi) for Multivolume Localization, *Journal of Magnetic Resonance* **1988**, *80*, 162–167.

[248] deGraaf, R. A.; Nicolay, K. Multislice imaging with adiabatic pulses using transverse Hadamard encoding, *Journal of Magnetic Resonance Series B* **1996**, *113*, 97–101.

[249] Goelman, G.; Leigh, J. S. B_1-Insensitive Hadamard Spectroscopic Imaging Technique, *Journal of Magnetic Resonance* **1991**, *91*, 93–101.

[250] Goelman, G.; Subramanian, V. H.; Leigh, J. S. Transverse Hadamard Spectroscopic Imaging Technique, *Journal of Magnetic Resonance* **1990**, *89*, 437–454.

[251] Blechta, V.; Delrioportilla, F.; Freeman, R. Long-Range Carbon Proton Couplings in Strychnine, *Magnetic Resonance in Chemistry* **1994**, *32*, 134–137.

[252] Blechta, V.; Freeman, R. Multisite Hadamard NMR-Spectroscopy, *Chemical Physics Letters* **1993**, *215*, 341–346.

[253] Krishnamurthy, K. Hadamard excitation sculpting, *Journal of Magnetic Resonance* **2001**, *153*, 144–150.

[254] Ma, L.; Bigler, P. Simultaneous Measurement of One-Bond and Long-Range Carbon Carbon Coupling-Constants in Cembrene, *Magnetic Resonance in Chemistry* **1992**, *30*, 1247–1254.

[255] Mueller, C.; Bigler, P. Increased Efficiency for the Selective Detection and Measurement of Carbon-Carbon Couplings, *Journal of Magnetic Resonance Series A* **1993**, *102*, 42–48.

[256] Nishida, T.; Widmalm, G.; Sandor, P. Hadamard Long-Range Proton Carbon Coupling-Constant Measurements with Band-Selective Proton Decoupling, *Magnetic Resonance in Chemistry* **1995**, *33*, 596–599.

[257] Schraml, J.; van Halbeek, H.; DeBruyn, A.; Contreras, R.; Maras, M.; Herdewijn, P. Hadamard 1D ^{1}H TOCSY and its application to oligosaccharides, *Magnetic Resonance in Chemistry* **1997**, *35*, 883–888.

[258] Hadamard, J. Résolution d'une question relative aux déterminants, *Bulletin des Sciences Mathématiques* **1893**, *17*, 240–248.

[259] Kupče, E.; Nishida, T.; Freeman, R. Hadamard NMR spectroscopy, *Progress in Nuclear Magnetic Resonance Spectroscopy* **2003**, *42*, 95–122.

[260] Kupče, E.; Freeman, R. Fast multi-dimensional NMR of proteins, *Journal of Biomolecular NMR* **2003**, *25*, 349–354.

[261] Kupče, E.; Freeman, R. Frequency-domain Hadamard spectroscopy, *Journal of Magnetic Resonance* **2003**, *162*, 158–165.

[262] Chiarparin, E.; Pelupessy, P.; Bodenhausen, G. Selective cross-polarization in solution state NMR, *Molecular Physics* **1998**, *95*, 759–767.

[263] Hartmann, S. R.; Hahn, E. L. Nuclear Double Resonance in Rotating Frame, *Physical Review* **1962**, *128*, 2042–2053.

[264] Pelupessy, P.; Chiarparin, E. Hartmann-Hahn polarization transfer in liquids: An ideal tool for selective experiments, *Concepts in Magnetic Resonance* **2000**, *12*, 103–124.

[265] Chiarparin, E.; Pelupessy, P.; Cutting, B.; Eykyn, T. R.; Bodenhausen, G. Normalized one-dimensional NOE measurements in isotopically labeled macromolecules using two-way cross-polarization, *Journal of Biomolecular NMR* **1999**, *13*, 61–65.

[266] Cutting, B.; Bodenhausen, G. Attenuation of cross-peak intensities in QUIET-BIRD-NOESY experiments, *Journal of Magnetic Resonance* **1999**, *140*, 289–292.

[267] Eykyn, T. R.; Ghose, R.; Bodenhausen, G. Offset profiles of selective pulses in isotopically labeled macromolecules, *Journal of Magnetic Resonance* **1999**, *136*, 211–213.

[268] Millet, O.; Chiarparin, E.; Pelupessy, P.; Pons, M.; Bodenhausen, G. Measurement of relaxation rates of N^H and H^α backbone protons in proteins with tailored initial conditions, *Journal of Magnetic Resonance* **1999**, *139*, 434–438.

[269] Pelupessy, P.; Chiarparin, E.; Bodenhausen, G. Excitation of selected proton signals in NMR of isotopically labeled macromolecules, *Journal of Magnetic Resonance* **1999**, *138*, 178–181.

[270] Parella, T. Spin-state-selective excitation in gradient-selected heteronuclear cross-polarization NMR experiments, *Journal of Magnetic Resonance* **2004**, *167*, 266–272.

[271] Parella, T.; Belloc, J.; Sanchez-Ferrando, F. Measurement of the sign and the magnitude of heteronuclear coupling constants from spin-state-edited J-cross-polarization NMR experiments, *Magnetic Resonance in Chemistry* **2004**, *42*, 852–862.

[272] Fesik, S. W.; Eaton, H. L.; Olejniczak, E. T.; Zuiderweg, E. R. P.; McIntosh, L. P.; Dahlquist, F. W. 2D and 3D NMR-Spectroscopy Employing ^{13}C-^{13}C Magnetization Transfer by Isotropic Mixing - Spin System-Identification in Large Proteins, *Journal of the American Chemical Society* **1990**, *112*, 886–888.

[273] Glaser, S. J.; Drobny, G. P. In Warren, W. S., editor, *Advances in Magnetic Resonance*, volume 14, pp. 35–58. Academic Press: New York, 1990.

[274] Schulte-Herbrüggen, T.; Madi, Z. L.; Sørensen, O. W.; Ernst, R. R. Reduction of Multiplet Complexity in COSY-Type NMR-Spectra - the Bilinear and Planar COSY Experiments, *Molecular Physics* **1991**, *72*, 847–871.

[275] Kupče, E.; Freeman, R. Fast multi-dimensional Hadamard spectroscopy, *Journal of Magnetic Resonance* **2003**, *163*, 56–63.

[276] Kupče, E.; Freeman, R. Two-dimensional Hadamard spectroscopy, *Journal of Magnetic Resonance* **2003**, *162*, 300–310.

[277] Luy, B.; Barchi, J. J.; Marino, J. P. S^{3}E-E.COSY methods for the measurement of ^{19}F associated scalar and dipolar coupling constants, *Journal of Magnetic Resonance* **2001**, *152*, 179–184.

[278] Parella, T. A complete set of novel 2D correlation NMR experiments based on heteronuclear J-cross polarization, *Journal of Biomolecular NMR* **2004**, *29*, 37–55.

[279] Ferrage, F.; Eykyn, T. R.; Bodenhausen, G. Highly selective excitation in biomolecular NMR by frequency-switched single-transition cross-polarization, *Journal of the American Chemical Society* **2002**, *124*, 2076–2077.

[280] Ferrage, F.; Eykyn, T. R.; Bodenhausen, G. Frequency-switched single-transition cross-polarization: A tool for selective experiments in biomolecular NMR, *ChemPhysChem* **2004**, *5*, 76–84.

[281] Carlomagno, T.; Maurer, M.; Sattler, M.; Schwendinger, M. G.; Glaser, S. J.; Griesinger, C. PLUSH TACSY: Homonuclear planar TACSY with two-band selective shaped pulses applied to C$_\alpha$,C' transfer and C$_\beta$,C$_{aromatic}$ correlations, *Journal of Biomolecular NMR* **1996**, *8*, 161–170.

[282] Carlomagno, T.; Luy, B.; Glaser, S. J. "Kin" HEHAHA sequences, heteronuclear Hartmann-Hahn transfer with different bandwidths for spins I and S, *Journal of Magnetic Resonance* **1997**, *126*, 110–119.

[283] Khaneja, N.; Brockett, R.; Glaser, S. J. Time optimal control in spin systems, *Physical Review A* **2001**, *6303*.

[284] Skinner, T. E.; Kobzar, K.; Luy, B.; Bendall, M. R.; Bermel, W.; Khaneja, N.; Glaser, S. J. Optimal control design of constant amplitude phase-modulated pulses: Application to calibration-free broadband excitation, *Journal of Magnetic Resonance* **2006**, *179*, 241–249.

[285] Frueh, D. P.; Ito, T.; Li, J. S.; Wagner, G.; Glaser, S. J.; Khaneja, N. Sensitivity enhancement in NMR of macromolecules by application of optimal control theory, *Journal of Biomolecular NMR* **2005**, *32*, 23–30.

[286] Kehlet, C. T.; Sivertsen, A. C.; Bjerring, M.; Reiss, T. O.; Khaneja, N.; Glaser, S. J.; Nielsen, N. C. Improving solid-state NMR dipolar recoupling by optimal control, *Journal of the American Chemical Society* **2004**, *126*, 10202–10203.

[287] Kehlet, C.; Vosegaard, T.; Khaneja, N.; Glaser, S. J.; Nielsen, N. C. Low-power homonuclear dipolar recoupling in solid-state NMR developed using optimal control theory, *Chemical Physics Letters* **2005**, *414*, 204–209.

[288] Khaneja, N.; Li, J. S.; Kehlet, C.; Luy, B.; Glaser, S. J. Broadband relaxation-optimized polarization transfer in magnetic resonance, *Proceedings of the National Academy of Sciences of the United States of America* **2004**, *101*, 14742–14747.

[289] Vosegaard, T.; Kehlet, C.; Khaneja, N.; Glaser, S. J.; Nielsen, N. C. Improved excitation schemes for multiple-quantum magic-angle spinning for quadrupolar nuclei designed using optimal control theory, *Journal of the American Chemical Society* **2005**, *127*, 13768–13769.

[290] Kupče, E.; Freeman, R. Multisite Correlation Spectroscopy with Soft Pulses - a New Phase-Encoding Scheme, *Journal of Magnetic Resonance Series A* **1993**, *105*, 310–315.